TRACING GALAXY EVOLUTION THROUGH SPATIAL AND KINEMATIC PROBES OF THE MgII CIRCUMGALACTIC MEDIUM

BY

NIKOLE MARIE NIELSEN, B.S., M.S.

A dissertation submitted to the Graduate School

in partial fulfillment of the requirements

for the degree

Doctor of Philosophy

Major Subject: Astronomy

New Mexico State University

Las Cruces, New Mexico

May 2015

"Tracing Galaxy Evolution Through Spatial and Kinematic Probes of the Mg II Circumgalactic Medium," a dissertation prepared by Nikole M. Nielsen in partial fulfillment of the requirements for the degree, Doctor of Philosophy, has been approved and accepted by the following:

Lou-Vicente Reyes
Dean of the Graduate School

Christopher W. Churchill
Chair of the Examining Committee

Date

Committee in charge:

Dr. Christopher W. Churchill, Chair

Dr. Jon A. Holtzman

Dr. René A. M. Walterbos

Dr. Michael Engelhardt

DEDICATION

To my parents, Jeff and Rachel, for encouraging me to do what I love most.

And to Trixie, MAGiiCAT incarnate.

VITA

EDUCATION

2009-2013	M.S., Astronomy
	New Mexico State University
	Las Cruces, New Mexico, USA
2005-2009	B.S., Astrophysics
	Michigan State University
	East Lansing, Michigan, USA

AWARDS AND GRANTS

2015	NMSU Alumni Association Outstanding Graduate Award for the Graduate School, Ph.D.
2012-2015	NMSU Graduate Research Enhancement Grant ($45,000)
2014	NMSU College of Arts and Sciences Graduate Travel Award ($550)
2013	NMSU Astronomy Zia Award for Outstanding Research ($750)
2012	NSF East Asia and Pacific Summer Institutes Fellowship ($11,500)
2012-2013	New Mexico Space Grant Graduate Research Fellowship ($10,000)
2010-2011	New Mexico Space Grant Graduate Research Fellowship ($10,000)

PROFESSIONAL ORGANIZATIONS & SERVICE

Scientific referee for the Astrophysical Journal

American Astronomical Society

NMSU Astronomy Department Graduate Awards Committee

President of NMSU Astronomy Graduate Student Organization

Vice President of NMSU Astronomy Graduate Student Organization

PUBLICATIONS

Nielsen, N. M., Churchill, C. W., Kacprzak, G. G., Murphy, M. T., & Evans, J. L. 2015, ApJ, submitted. MAGII*CAT V. Kinematic Probes of Outflows and Accretion with Galaxy Orientation*

Nielsen, N. M., Churchill, C. W., Kacprzak, G. G., Murphy, M. T., & Evans, J. L. 2015, ApJ, submitted. MAGII*CAT IV. Quenching Quandaries in the* MgII *Circumgalactic Medium*

Churchill, C. W., Kacprzak, G. G., **Nielsen, N. M.**, Steidel, C. C., & Murphy, M. T. 2015, ApJ, submitted. *The Highly Structured Anatomy of Gaseous Halos Inferred from Extremely Weak* MgII *Absorption and Galaxy Orientation*

Mathes, N. L., Churchill, C. W., Kacprzak, G. G., **Nielsen, N. M.**, Trujillo-Gomez, S., Charlton, J., & Muzahid, S. 2014, ApJ, 792, 128. *Halo Mass Dependence of* HI *and* OVI *Absorption: Evidence for Differential Kinematics*

Churchill, C. W., Trujillo-Gomez, S., **Nielsen, N. M.**, & Kacprzak, G. G. 2013, ApJ, 779, 87. MAGII*CAT III. Interpreting Self-Similarity of the Circumgalactic Medium with Virial Mass using* MgII *Absorption*

Kacprzak, G. G., Cooke, J., Churchill, C. W., Ryan-Weber, E. V., & **Nielsen, N. M.** 2013, ApJ, 777, L11. *The Smooth* MgII *Gas Distribution Through the Interstellar/Extra-planar/Halo Interface*

Nielsen, N. M., Churchill, C. W., & Kacprzak, G. G. 2013, ApJ, 776, 115. MAGII*CAT II. General Characteristics of the* MgII *Absorbing Circumgalactic Medium*

Nielsen, N. M., Churchill, C. W., Kacprzak, G. G., & Murphy, M. T. 2013, ApJ, 776, 114. MAGII*CAT I. The* MgII *Absorber-Galaxy Catalog*

Evans, J. L., Churchill, C. W., Murphy, M. T., **Nielsen, N. M.**, & Klimek, E. S. 2013, ApJ, 768, 3. *The Redshift Distribution of Intervening Weak* MgII *Quasar Absorbers and a Curious Dependence on Quasar Luminosity*

Churchill, C. W., **Nielsen, N. M.**, Kacprzak, G. G., & Trujillo-Gomez, S. 2013, ApJ, 763, L42. *The Self-Similarity of the Circumgalactic Medium with Galaxy Virial Mass: Implications for Cold-Mode Accretion*

Kacprzak, G. G., Churchill, C. W., & **Nielsen, N. M.** 2012, ApJ, 760, L7. *Tracing Outflows and Accretion: A Bimodal Azimuthal Dependence of* Mg II *Absorption*

Churchill, C. W., Kacprzak, G. G., Steidel, C. C., Spitler, L. R., Holtzman, J. A., **Nielsen, N. M.**, & Trujillo-Gomez, S. 2012, ApJ, 760, 68. *Quenched Accretion of a Large Scale Metal-Poor Filament due to Virial Shocking in the Halo of a Massive* $z = 0.7$ *Galaxy*

FIELD OF STUDY

Major Field: Galaxy Evolution & Quasar Absorption Lines

ABSTRACT

TRACING GALAXY EVOLUTION THROUGH SPATIAL AND KINEMATIC PROBES OF THE MgII CIRCUMGALACTIC MEDIUM

BY

NIKOLE MARIE NIELSEN, B.S., M.S.

Doctor of Philosophy

New Mexico State University

Las Cruces, New Mexico, 2015

Dr. Christopher W. Churchill, Chair

Understanding how galaxies form and evolve is a paramount question today. While it is generally understood that galaxies are built by accreting gas and forming stars, mechanisms which are eventually shut off to form passively evolving red galaxies, the detailed physics are still not completely understood. What has become clear is that the baryon cycle is a key to understanding galaxy evolution and can be studied via the circumgalactic medium (CGM), or the massive, metal-enriched, extended gaseous reservoir surrounding galaxies. Extensive work has gone into examining the CGM using quasar absorption lines in which a background quasar sightline probes the CGM of a foreground galaxy. In this dissertation,

we employ nearly three decades of absorber-galaxy survey data focusing on low-ionization Mg II absorption to examine the basic structure of the CGM for galaxies in various stages of evolution.

We compiled the Mg II Absorber-Galaxy Catalog (MAGIICAT) consisting of 182 absorber-galaxy pairs ranging from $0.07 < z_{\rm gal} < 1.1$, where the CGM has been probed out to nearly $D = 200$ kpc. With MAGIICAT, we examined the extent, distribution, and patchiness of gas traced by Mg II in the CGM and found that the Mg II absorption strength and covering fraction decrease with increasing impact parameter. We find differential properties of the CGM such that bluer, more luminous, and higher redshift galaxies host gaseous halos with a larger radius and covering fraction. By examining the kinematics of Mg II absorbers in high-resolution quasar spectra, we also find a dependence of the velocity structure and distribution of column densities on galaxy properties and orientation modeled using *HST* images. The velocity structure of absorbers hosted by passive, red galaxies appears to evolve with redshift, while this is not the case for blue galaxies which tend to have ongoing star formation. We further find larger absorber velocity dispersions in blue galaxies consistent with bipolar, outflowing winds, while the velocity dispersions for red galaxies are very narrow, indicating a lack of outflows from quenched star formation. These results indicate that the CGM and the host galaxy are intimately linked and examining both is necessary for understanding how galaxies evolve over time.

Contents

LIST OF TABLES

LIST OF FIGURES

1. INTRODUCTION

1.1. Background

Our understanding of how galaxies form and evolve has improved drastically over time since Eggen et al. (1962) first suggested that galaxies form via the monolithic collapse of a large cloud of gas and dust from the intergalactic medium (IGM) into a rotating disk. Later work by Searle & Zinn (1978) proposed a "bottom up" formation scenario in which galaxies form and grow by smaller clouds of gas and dust (or smaller galaxies) which coalesce to create larger galaxies. Current models of galaxy formation and evolution combine aspects of both works to form a scenario in which dark matter, the dominant matter in the universe in the cold dark matter model (Blumenthal et al. 1984), forms the underlying structures along which baryons move by gravitational collapse of early density perturbations in the dark matter. Gas is accreted into the centers of dark matter halos where it forms stars (e.g., White & Rees 1978; Silk & Norman 1981; Blumenthal et al. 1986; White & Frenk 1991; Mo & Miralda-Escude 1996; Maller & Bullock 2004), the basis of the visible galaxy structure. These galaxies then merge to form larger galaxies and continue to accrete pristine IGM material over time. This build-up occurs repeatedly to form the galaxies we observe today.

As both observations and simulations of galaxies have improved, we have found that the process by which galaxies evolve is complex, where gas and stars are key components in the cycling of baryons into and through galaxies. In the baryon cycle, gas is accreted onto galaxies via dark matter filaments or deposited into galaxies by mergers, then forms stars, which then drive galactic-scale outflowing winds (e.g., Kereš et al. 2005, 2009; Ceverino & Klypin 2009; Dekel et al. 2009;

Oppenheimer et al. 2010; Ceverino et al. 2014). The material in these winds may remain bound to the galaxy and eventually fall back as recycled accretion for future star formation. Much of this baryon cycling occurs in the interface between the interstellar medium (ISM) within galaxies and the IGM between galaxies. Extended gaseous halos which act as this interface were initially theorized as hot halos ($T \sim 10^6$ K) by Spitzer (1956) but are now commonly known as the circumgalactic medium (CGM), a diffuse, multiphase reservoir of gas.

Foreground galaxies with extended gaseous galaxy halos (i.e., the CGM) were first predicted to be the source of metal absorption lines found in distant quasar spectra nearly 50 years ago by Bahcall & Spitzer (1969). Observations confirmed this prediction decades later (Bergeron 1988; Bergeron & Boissé 1991) by comparing the redshift of nearby (projected on the sky) galaxies to the absorption redshift. The CGM is now known to be massive, containing a gas mass of roughly $M_{\rm CGM} > 10^9 M_\odot$ (e.g., Thom et al. 2011; Tumlinson et al. 2011; Werk et al. 2013), comparable to that of the ISM, and consistent with the mass predictions of Bahcall & Spitzer (1969).

Since the observational confirmation of gaseous halos surrounding galaxies, the study of quasar absorption lines has proliferated to include the study of galaxies in the Local Group (e.g., Lehner et al. 2012; Fox et al. 2014, 2015) and nearby universe (e.g., Keeney et al. 2013), at $0.1 < z < 1$ (e.g., Steidel et al. 1994; Guillemin & Bergeron 1997; Steidel et al. 1997; Barton & Cooke 2009; Chen et al. 2010a; Gauthier & Chen 2011; Kacprzak et al. 2011b; Stocke et al. 2013; Tumlinson et al. 2013; Werk et al. 2013; Bordoloi et al. 2014b), at $2 < z < 3.5$ (e.g., Steidel et al. 2010; Rudie et al. 2012; Lehner et al. 2014), and up to $z = 6$ (e.g., Matejek et al. 2013, although the galaxies hosting these absorbers have yet to be

identified for this sample) for a wide range of ions in the CGM.

Figure 1.1 presents the redshift distribution for the largest quasar absorption line surveys to date. The blue shaded regions indicate the COS-Dwarfs (Bordoloi et al. 2014b) and COS-Halos (Tumlinson et al. 2013) surveys, which examined HI, CIV, OVI, and absorption from a variety of other ions. The green shaded region is the Keck Baryonic Structure Survey (KBSS, Rudie et al. 2012), focusing on HI absorption. The red histogram indicates the collection of MgII absorbers detected in high resolution quasar spectra by Evans (2011), while the histogram in orange represents the distribution of MgII absorbers observed in infrared wavelengths by Matejek & Simcoe (2012). Both Evans (2011) and Matejek & Simcoe (2012) have not identified the galaxies giving rise to the absorption, but are a rich source of MgII absorbers to explore. Finally, the purple histogram represents the sample presented in this dissertation (MAGIICAT, described in Chapter 2), which consists of MgII absorber-galaxy pairs from Steidel et al. (1994), Guillemin & Bergeron (1997), Steidel et al. (1997), Chen & Tinker (2008), Barton & Cooke (2009), Chen et al. (2010a), Kacprzak et al. (2010b), Gauthier & Chen (2011), Kacprzak et al. (2011a), Kacprzak et al. (2011b), and Churchill et al. (2013a).

Recently, the advent of large galaxy surveys such as the Sloan Digital Sky Survey (SDSS) has allowed for much larger (on the order of tens of thousands of galaxies) examining the CGM-galaxy connection (e.g., Zhu & Ménard 2013; Lan et al. 2014). Absorption line studies have also expanded to use not only background quasars, but also the host galaxy itself in a "down-the-barrel" approach, though the galaxy spectra have to be stacked in most cases due to their lower luminosity in order to detect absorption due to the CGM (e.g., Weiner et al. 2009; Bordoloi et al. 2011; Martin et al. 2012; Rubin et al. 2010; Bordoloi et al. 2014c;

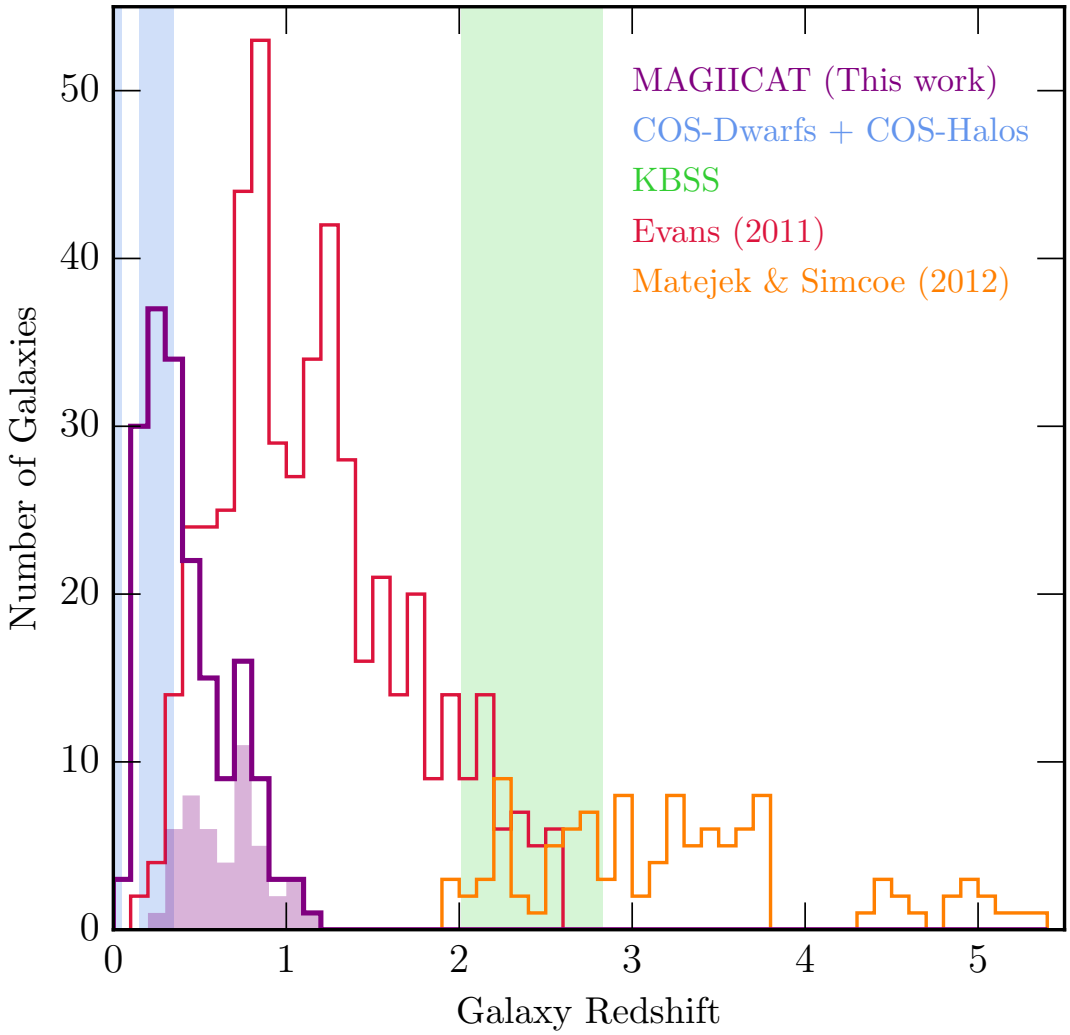

Fig. 1.1.— Redshift distribution for the largest Mg II surveys to date, excluding large databases such as SDSS and BOSS which can only be examined on a statistical basis. Absorber-galaxy surveys COS-Dwarfs and COS-Halos are plotted as the blue shaded region while the Keck Baryonic Structure Survey is plotted as the green shaded region. The Mg II absorber catalog compiled by Evans (2011) is plotted as the red histogram and the Matejek & Simcoe (2012) FIRE sample is plotted as the orange histogram. The work presented in this dissertation is plotted as the purple histogram, where the shaded purple histogram represents the subsample of galaxies with high resolution spectra for kinematics study.

Rubin et al. 2014).

By far, the vast majority of studies of focused on Mg II $\lambda\lambda 2796, 2803$ absorption, which probes the photoionized CGM at $T \sim 10^{4.5}$ K. The Mg II ion is well-suited as a tracer of gas in the CGM since it is easily observed from the ground in optical wavelengths over redshifts $0.1 < z < 0.25$ and traces metal-enriched, low ionization gas over a large range of H I column densities, $10^{16} \lesssim N(\mathrm{H\,I}) \lesssim 10^{22}$ cm^{-2} (Bergeron & Stasińska 1986; Steidel & Sargent 1992; Churchill et al. 1999, 2000; Rao & Turnshek 2000; Rigby et al. 2002). Mg II absorption has been found out to projected distances of nearly 150 kpc (e.g., Kacprzak et al. 2008; Chen et al. 2010a; Kacprzak et al. 2011b; Churchill et al. 2013a) and traces a wide range of environments including infalling gas (Kacprzak et al. 2010a, 2011b, 2012b; Ribaudo et al. 2011; Stewart et al. 2011; Martin et al. 2012; Rubin et al. 2012) and bipolar, outflowing galactic-scale winds (Bouché et al. 2006, 2012; Tremonti et al. 2007; Martin & Bouché 2009; Weiner et al. 2009; Chelouche & Bowen 2010; Rubin et al. 2010; Bordoloi et al. 2011; Coil et al. 2011; Martin et al. 2012; Bordoloi et al. 2014c; Rubin et al. 2014). Some evidence also shows that Mg II absorption is due to merging satellite galaxies in the halo of the host galaxy (e.g., Martin et al. 2012).

1.2. Motivation

The wealth of data available in the literature for Mg II absorption is clearly extensive and the observations span several decades. However, this results in various selection methods employed in the surveys, and photometric properties and quasar-galaxy impact parameters which have been calculated with a variety

of cosmological parameters (many of which are long outdated and incorrect). Different observing facilities and filter sets were available and used over time, and the proliferation of several absorber-galaxy pairs throughout the literature in an effort to analyze the largest sample possible resulted in duplicates with different published values. Despite the field having identified nearly 200 absorber-galaxy pairs, the largest survey only consisted of ~ 80 galaxies, with a plethora of smaller ($\lesssim 30$ absorber-galaxy pairs) surveys.

In spite of this, these surveys presented a picture in which the CGM is patchy and extends out to $100 - 200$ kpc, where more luminous galaxies have a larger CGM, and the strongest absorbing gas lies nearest to the galaxy. As surveys grew in size, the results became more statistically significant and hints of trends with other galaxy properties started to show, leading to the following questions: How does the structure of the CGM change over time? Does the star formation rate impact the basic properties of the CGM? What is the source of CGM material and what is its fate? Do galaxies of different masses have similar CGM properties?

Focusing on the Mg II absorption profiles, several works have studied the detailed gas kinematics (e.g., Sargent et al. 1988; Petitjean & Bergeron 1990; Churchill 1997; Churchill & Vogt 2001; Churchill et al. 2003; Evans 2011). Thus far, the kinematics of the absorbers have been observed but have not been observationally tied to galaxy properties (though suggestions and predictions have been made). Understanding the variations in the gas kinematics is important to not only constrain the precise gas motions in the CGM, but also to understand how the cycling of baryons occurs. This leads to several questions: Do we see signatures of the basic evolutionary processes in the kinematics of Mg II absorption? What are those signatures? Where do these evolutionary processes occur

with respect to the galaxy? How does accreting and outflowing material depend on galaxy properties, or rather, what galaxy properties do we obtain when the baryon cycle is active as opposed to inactive (i.e., star-forming vs. passive)?

1.3. Goals

The general goal of this dissertation is to further illuminate the role the circumgalactic medium plays in the baryon cycle and how it helps govern the evolution of galaxies. More specifically, we have aimed to do the following:

1. Compile and standardize all Mg II absorber-galaxy pairs from the literature, only including pairs in which the galaxy has been spectroscopically confirmed and Mg II absorption has either been detected or an upper limit on absorption has been measured. This is the sample from which we draw for our analysis. A catalog such as this will serve as a uniform database available to the CGM community for easy comparison between present surveys and as a building block for present and future large statistical surveys such as the Sloan Digital Sky Survey. The redshift distribution for this catalog is plotted as the purple histogram in Figure 1.1.

2. Explore the basic structure of the circumgalactic medium in a statistical sense to determine the radial extent and patchiness for galaxies in different evolutionary stages as defined by their luminosity, color, and redshift. These basic quantities constrain the general properties of the CGM in simulations and provide an overall picture to which we can compare more detailed observations.

3. Examine, for the first time, the kinematics of Mg II absorbing gas, includ-

ing the internal absorber velocity structure and the velocities with respect to the galaxy systemic velocity, as a function of galaxy properties such as color, redshift, impact parameter, and orientation. This will allow us to understand the motions of the gas that is cycling in and out of (and possibly between) galaxies. The redshift distribution for the absorber-galaxy pairs with high-resolution quasar spectra (the sample we use in this dissertation) is plotted as the shaded purple histogram in Figure 1.1.

Simulations are just now becoming powerful enough to accurately model the CGM and its role in galaxy evolution. By observing the detailed CGM properties and kinematics as a function of galaxy properties, we can provide important constraints on the simulations to better understand galaxy evolution.

This dissertation is organized such that each chapter is a self-contained paper consisting, in general, of an introduction, methods, results, discussion, and conclusions. Chapter 2 was published as Nielsen et al. (2013b, Paper I) and details the absorber-galaxy catalog used throughout this dissertation. Chapter 3, published as Nielsen et al. (2013a, Paper II), explores the general characteristics of the Mg II CGM in terms of absorption strength, covering fraction, and radial extent. In Chapter 4, which has been submitted to the Astrophysical Journal as Nielsen et al. (2015b, Paper IV), we detail our absorption kinematics sample, the methods, and an analysis of pixel velocity two-point correlation functions as a function of galaxy color, redshift, and radius at which absorption is found. Chapter 5 also examines the kinematics of Mg II absorption, but for galaxy color and orientation, providing constraints on the motions of the gas involved in galaxy evolutionary processes. This chapter has been submitted to the Astrophysical

Journal as Nielsen et al. (2015a, Paper V). Finally, Chapter 6 summarizes and concludes this dissertation, placing our results in the context of the broader field of galaxy evolution and providing avenues for future work. We note that Appendices A, B, and C were published as appendices in Paper I (Nielsen et al. 2013b), while Appendix D has been submitted as an appendix in Paper IV (Nielsen et al. 2015b).

2. MAGIICAT I. THE MgII ABSORBER-GALAXY CATALOG

The contents of this chapter were originally published as Nielsen, N. M., Churchill, C. W., Kacprzak, G. G., & Murphy, M. T. 2013, ApJ, 776, 114.

We describe the Mg II Absorber-Galaxy Catalog, MAGIICAT, a compilation of 182 spectroscopically identified intermediate redshift ($0.07 \leq z \leq 1.1$) galaxies with measurements of Mg II $\lambda\lambda 2796, 2803$ absorption from their circumgalactic medium within projected distances of 200 kpc from background quasars. In this work, we present "isolated" galaxies, which are defined as having no spectroscopically identified galaxy within a projected distance of 100 kpc and a line of sight velocity separation of 500 km s^{-1}. We standardized all galaxy properties to the ΛCDM cosmology and galaxy luminosities, absolute magnitudes, and rest-frame colors to the B- and K-band on the AB system. We present galaxy properties and rest-frame Mg II equivalent width, $W_r(2796)$, versus galaxy redshift. The well-known anti-correlation between $W_r(2796)$ and quasar-galaxy impact parameter, D, is significant to the 8σ level. The mean color of MAGIICAT galaxies is consistent with an Sbc galaxy for all redshifts. We also present B- and K-band luminosity functions for different $W_r(2796)$ and redshift subsamples: "weak absorbing" [$W_r(2796) < 0.3$ Å], "strong absorbing" [$W_r(2796) \geq 0.3$ Å], low redshift ($z < \langle z \rangle$), and high redshift ($z \geq \langle z \rangle$), where $\langle z \rangle = 0.359$ is the median galaxy redshift. Rest-frame color $B - K$ correlates with M_K at the 8σ level for the whole sample but is driven by the strong absorbing, high redshift subsample (6σ). Using M_K as a proxy for stellar mass and examining the luminosity functions, we infer that in lower stellar mass galaxies, Mg II absorption is preferentially detected in blue galaxies and the absorption is more likely to be weak.

2.1. Introduction

Galaxies are known to harbor large, extended reservoirs of gas referred to as the circumgalactic medium (CGM). This region contains the material through which filaments accrete, galactic-scale winds outflow, and merging galaxies are tidally stripped – mechanisms which are critical to the growth and transformation of galaxies given that the CGM harbors a gas mass which may rival that of the galaxy itself (Tumlinson et al. 2011; Stocke et al. 2013; Werk et al. 2013). Additionally, theoretical works have established that the baryons in the CGM depend on the dark matter halo mass and various processes such as stellar and active galactic nucleus feedback (Birnboim & Dekel 2003; Maller & Bullock 2004; Kereš et al. 2005; Dekel & Birnboim 2006; Birnboim et al. 2007; Ocvirk et al. 2008; Kereš et al. 2009; Oppenheimer et al. 2010; Stewart et al. 2011; van de Voort et al. 2011; van de Voort & Schaye 2012). As such, the evolution of galaxies is intimately tied to the origin, processing, and fate of gas in their halos, making studies of the CGM key to understanding galaxy evolution.

Campaigns to study the CGM in absorption at $z \leq 1$ have targeted various ions that probe a range of gas densities and temperatures. For $z < 0.3$, O VI absorption (e.g., Tumlinson et al. 2011; Stocke et al. 2013) traces gas with $n_{\rm H} \sim 10^{-4}$ g cm^{-3} between $T = 10^{4.8}$ K (photoionized) and $T = 10^{5.5}$ K (collisionally ionized). At $z < 1$, C IV absorption (e.g., Chen et al. 2001a) probes $10^{-2} \leq n_{\rm H} \leq 10^{-4}$ g cm^{-3} gas with temperatures in the range of $\sim 10^{4.6}$ K (photoionized) and $\sim 10^{5.0}$ K (collisionally ionized). The neutral hydrogen component of the CGM has been observed using Lyα absorption (e.g., Lanzetta et al. 1995; Chen et al. 2001b; Stocke et al. 2013). However, by far the vast majority of surveys have

focused on Mg II absorption (e.g., Bergeron & Boissé 1991; Steidel et al. 1994; Churchill et al. 2005; Chen et al. 2010a; Kacprzak et al. 2011b), which samples photoionized CGM gas with $n_{\rm H} \sim 10^{-1}$ g cm^{-3} and $T \sim 10^{4.5}$ K. Further details of $z < 1$ absorbing gas properties are discussed in Bergeron et al. (1994).

The Mg II $\lambda\lambda 2796, 2803$ absorption doublet is well-suited to studying the processes occurring in the CGM since it is easily observed from the ground in the optical at redshifts $0.1 < z < 2.5$. Mg II traces metal-enriched, low ionization gas over a large range of H I column densities, $16 \lesssim \log N({\rm H\,I}) \lesssim 22$ (Bergeron & Stasińska 1986; Steidel & Sargent 1992; Churchill et al. 1999, 2000; Rao & Turnshek 2000; Rigby et al. 2002), corresponding to a wide range of environments out to projected distances of ~ 150 kpc (Kacprzak et al. 2008; Chen et al. 2010a; Churchill et al. 2013a). Detailed information on the gas kinematics with Mg II have indicated the presence of infalling gas (Kacprzak et al. 2010a, 2011b; Ribaudo et al. 2011; Stewart et al. 2011; Martin et al. 2012; Rubin et al. 2012; Kacprzak et al. 2012b) and outflowing galactic-scale winds (Bouché et al. 2006; Tremonti et al. 2007; Martin & Bouché 2009; Weiner et al. 2009; Chelouche & Bowen 2010; Rubin et al. 2010; Bordoloi et al. 2011; Coil et al. 2011; Bouché et al. 2012; Martin et al. 2012).

The various methods employed for surveys of Mg II absorbing galaxies present challenges in understanding the CGM-galaxy interaction. The largest survey has no more than ~ 80 isolated galaxies, yet some 200 are known. Galaxy absolute photometric properties and quasar-galaxy impact parameters were computed using a variety of cosmological parameters (the accepted cosmology at the time a given survey was published), which have changed over the last ~ 20 years. Different observing facilities have been used, resulting in various filter sets. Different

magnitude systems were employed. Even the selection methods from survey to survey are diverse, and in some cases different surveys report the same absorber-galaxy pairs, causing duplicates throughout the literature. All these factors result in difficulties when synthesizing the galaxy properties and results between studies.

Motivated by the potential that combining the data from our work and other surveys may further illuminate the CGM-galaxy connection, we have endeavored to assemble a database of the extant works focused on MgII absorption from the CGM of intermediate redshift galaxies. We aim to provide a large uniform data suite based upon a single cosmological parameter set and to standardize all absolute magnitudes to two filters on the AB system. We consolidate the measurements of given absorber-galaxy pairs duplicated in various works to include the highest-quality data available for each absorber-galaxy pair. Such a compilation holds the promise of yielding higher statistical significance in the already published results, and of providing greater leverage for exploring the dependence of CGM MgII absorption on various galaxy properties.

In this paper we present the construction of the MgII Absorber-Galaxy Catalog, MAGIICAT (pronounced magic-cat). We also present the data and general characteristics of the "isolated galaxy" sample. In several works from which the absorber-galaxy pairs were drawn, group galaxies (which we define below) were identified. Since the absorption associated with multi-galaxy pairs may be probing the intragroup medium, or providing a single absorption measurement from the overlap of the circumgalactic medium from more than one galaxy, we defer presentation and analysis of these pairs for future work. Our aim here is to focus on the CGM-galaxy connection for cases in which the data are consistent, to the best of our knowledge, with the absorption arising in the CGM of a single domi-

nant host galaxy. In a future paper, we will present the "group galaxy" subsample of MAGIICAT and will examine the intragroup medium environment.

We also leave further detailed analysis of the CGM-galaxy connection for other papers in this series, e.g., Paper II (Nielsen et al. 2013a), in which we studied the general characteristics of the CGM with galaxy luminosity, color, and redshift, and Paper III (Churchill et al. 2013c), in which we studied the behavior of the CGM with galaxy virial mass. An additional series paper is planned in which we will study the kinematics of the Mg II absorbing CGM. We have also presented additional analysis of the "isolated" galaxy subsample in Kacprzak et al. (2012a) and Churchill et al. (2013b).

In section 2.2 we provide the selection criteria for inclusion of galaxies in the catalog and briefly describe each of the works from which the galaxies are drawn and the various selection methods. In section 2.3 we detail the galaxy data we obtained and how we standardized various galaxy and absorption properties. We adopt a ΛCDM cosmology ($H_0 = 70$ km s^{-1} Mpc^{-1}, $\Omega_M = 0.3$, and $\Omega_\Lambda = 0.7$) and report AB absolute magnitudes throughout this paper. In section 2.4 we present characteristics of the sample, tabulated values for MAGIICAT galaxies, and luminosity functions. We summarize the present work and conclude with the potential of MAGIICAT in section 2.5. The catalog is available in its entirety in the on-line journal and has been placed on-line at the NMSU Quasar Absorption Line Group website[1].

[1]http://astronomy.nmsu.edu/cwc/Group/magiicat

2.2. Constructing MAGIICAT

We compiled a catalog of galaxies with spectroscopic redshifts $0.07 \leq z \leq 1.1$ within a projected distance of $D \leq 200$ kpc from a background quasar, with known Mg II absorption or an upper limit on absorption less than 0.3 Å. We chose to include only galaxies with spectroscopic redshifts, excluding galaxies from e.g., Rao et al. (2011) and Bowen & Chelouche (2011), which have photometric redshifts and would have supplied $\sim$ 30 and $\sim$ 10 galaxies to MAGIICAT, respectively. We also limited the sample to galaxies which are not located in group environments (defined in section 2.2.3) to the limits the data indicate. The galaxies were primarily drawn from the works of Steidel et al. (1994), Churchill et al. (1996), Guillemin & Bergeron (1997), Steidel et al. (1997), Chen & Tinker (2008), Barton & Cooke (2009), Chen et al. (2010a), Kacprzak et al. (2010b), Gauthier & Chen (2011), Kacprzak et al. (2011a,b), and Churchill et al. (2013a).

The galaxy discovery methods employed by the aforementioned surveys range from unbiased volume-limited samples with no *a priori* knowledge of Mg II absorption in the background quasar spectrum (Barton & Cooke 2009; Gauthier & Chen 2011; Kacprzak et al. 2011a), to magnitude-limited samples (Steidel et al. 1997; Kacprzak et al. 2010b), one with a luminosity scaled maximum projected separation from the quasar sightline (Chen et al. 2010a), and to samples in which galaxies are searched for at the redshifts of known Mg II absorbers (i.e., absorption selected; Bergeron & Boissé 1991; Steidel et al. 1994; Guillemin & Bergeron 1997; Chen & Tinker 2008; Gauthier & Chen 2011; Kacprzak et al. 2011b). Some quasar fields have been imaged from the ground only (some with and some without subtraction of the quasar), while others have been imaged at high resolution

with the *Hubble Space Telescope* (*HST*). As such, our compilation comprises a catalog of galaxies with heterogeneous selection methods, and a range of sensitivity in magnitude and impact parameter. Though it may be argued that a complete galaxy sample is indicated by always identifying a galaxy at the redshift of known MgII absorption (Steidel et al. 1994; Steidel 1995), it is inherently difficult to demonstrate completeness unless the quasar fields are systematically surveyed to a uniform magnitude limit and projected separation from the quasar.

2.2.1. Overview of Surveys

Here we present a brief overview of the previous works included in MAGIICAT.

2.2.1.1. SDP94 We obtained the data for galaxies presented in Steidel et al. (1994) [hereafter SDP94] with $0.3 \leq z \leq 1.0$ (Steidel, private communication). Their sample is "gas cross section-selected," meaning that the galaxies were selected based on known MgII absorption with rest-frame equivalent widths $W_r \geq 0.3$ Å in the spectra of background quasars. Galaxies were searched for starting at the quasar position and moving outward in angular separation, θ, with most galaxies having an angular separation less than $10''$. Images of the quasar fields were acquired in the R_s band[2] using the 2.1 m and 4 m telescopes at Kitt Peak National Observatory, as well as the 2.4 m Hiltner telescope at the Michigan-Dartmouth-MIT Observatory. Images in the infrared K_s band were obtained with NICMOS III cameras on the Kitt Peak 4 m Mayall telescope and the Las Campanas Observatory 2.5 m DuPont telescope. Galaxy spectroscopy was conducted

[2]Chuck Steidel kindly provided the electronic versions of the R_s and K_s filter response curves.

using the Lens/Grism Spectrograph and the Kast Double Spectrograph on the Lick Observatory 3 m Shane telescope. Roughly 30% of the galaxies identified by SDP94 do not have spectroscopically confirmed redshifts; we did not include those galaxies. Many of the galaxies from SDP94 were studied more extensively in later works, and are therefore listed under the most recent work.

2.2.1.2. Steidel-PC Steidel (private communication) kindly provided the unpublished "interloper" galaxy data briefly discussed as "control fields" in SDP94 and Steidel (1995). These galaxies were targeted because they were not responsible for absorption [to a 5σ upper limit $W_r(2796) < 0.3$ Å] in background quasar spectra during the campaign of SDP94. Galaxy images and spectroscopy were obtained using the same facilities used by SDP94. Later works have obtained HIRES/Keck (Vogt et al. 1994) or UVES/VLT (Dekker et al. 2000) quasar spectra for all galaxies in this sample, therefore the equivalent width limits for these galaxies have been remeasured at the 3σ level by Churchill et al. (2013a) or the present work.

2.2.1.3. GB97 Studying quasar fields with known Mg II absorbers, Guillemin & Bergeron (1997) [hereafter GB97] identified galaxies producing the absorption at $0.07 < z < 1.2$, with $R < 23.5$ and quasar-galaxy angular separations $\theta < 15''$. Imaging in the R band[3] and galaxy spectroscopy were conducted on the European Southern Observatory 3.5 m telescope using the ESO Faint Object Spectrograph and Camera (hereafter the R-band from this work will be referred to as $R_{\rm EFOSC}$).

[3]The electronic version of the ESO Faint Object Spectrograph and Camera R filter response curve was kindly provided by Jacqueline Bergeron.

We did not include the high redshift *candidate* absorbers from GB97.

2.2.1.4. Steidel97 Steidel et al. (1997) [hereafter Steidel97] conducted a deep, magnitude-limited study of the overdense galaxy field within $\theta = 50''$ of 3C 336 (1622+238). Galaxies as faint as $R_s = 24.5$ were imaged in R_s with the Michigan-Dartmouth-MIT 2.4 m Hiltner telescope and F702W with WFPC2 on the *Hubble Space Telescope* (*HST*). Infrared K_s band images were obtained with the Kitt Peak 4 m Mayall telescope, with the final image reaching Vega magnitude $K_s \sim 22$ (AB magnitude $K_s \sim 23.8$). Quasar spectra were collected from various instruments and telescopes: the Faint Object Spectrograph on *HST*, the Kast Double Spectrograph with the Lick Observatory 3 m Shane telescope, the RC Spectrograph at the Kitt Peak 4 m Mayall telescope, and the Low Resolution Imaging Spectrograph (LRIS) on the 10 m Keck-I telescope. Galaxy spectroscopy was conducted with the LRIS/Keck-I combination. The data presented in Steidel97 have been improved upon in later works, in fact a UVES/VLT spectrum is now available, therefore we reference these galaxies according to the work giving updated values, with Steidel97 as the source of the K_s magnitudes.

2.2.1.5. CT08 Chen & Tinker (2008) [hereafter CT08] selected several quasar fields for which about half of the galaxy data was available from prior Mg II surveys (Steidel97), and half from Lyα and C IV surveys (Lanzetta et al. 1995; Chen et al. 1998, 2001a,b). The majority of galaxies were imaged in the F702W band with WFPC2 on *HST*, while galaxies in the field 0226-4110 were imaged in R_J with IMACS on the Magellan Baade telescope. Quasar spectroscopy was obtained with the MIKE Echelle Spectrograph on the Magellan Clay telescope or were obtained

from the ESO data archive where they had been observed with UVES on the Very Large Telescope (VLT).

2.2.1.6. BC09 Working with the Sloan Digital Sky Survey (SDSS) Data Release 4 (DR4) and Data Release 6 (DR6), Barton & Cooke (2009) [hereafter BC09] performed a volume-limited survey of galaxies at $z \sim 0.1$, with a limiting absolute magnitude $M_r \leq -21.3$. Background quasars were selected at projected distances less than or equal to 107 kpc from the galaxies from the SDSS Data Release 6 (DR6) quasar catalog. Galaxy spectra were collected from SDSS while quasar spectra were obtained using the blue channel of LRIS on Keck-I. We obtained apparent SDSS "model" g and r magnitudes from a NASA/IPAC Extragalactic Database (NED)[4] search. The equivalent widths for several of these galaxies were remeasured by Kacprzak et al. (2011a).

2.2.1.7. Chen10 Chen et al. (2010a) [hereafter Chen10] photometrically selected galaxies with $z < 0.5$ from the SDSS DR6 archive with $r' < 22$. Galaxies in quasar fields were targeted with the limitation that the quasar-galaxy impact parameter, D, must be less than the expected gaseous radius for each galaxy, $R = R_*(L_B/L_B^*)^{0.35}$, where $R_* = 130$ kpc. Follow up galaxy and quasar spectroscopy was obtained using the Dual Imaging Spectrograph (DIS) on the 3.5 m telescope at the Apache Point Observatory (APO) or with MagE on the Magellan Clay Telescope at the Las Campanas Observatory. We obtained apparent SDSS model g and r magnitudes from NED. The published $W_r(2796)$ upper limits were converted from 2σ to 3σ upper limits and we included only those galaxies for

[4]http://ned.ipac.caltech.edu

which the upper limit was less than or equal to 0.3 Å.

2.2.1.8. KMC10 Performing a magnitude-limited survey down to F814W$\leq$ 20.3, Kacprzak et al. (2010b) [hereafter KMC10] studied the field 1127-145 which contains many bright galaxies within an angular quasar-galaxy separation of 50″. The field was imaged in the F814W band on *HST* with WFPC2. Spectroscopy of the galaxies was obtained with DIS at the APO 3.5 m telescope, while quasar spectroscopy was conducted with UVES/VLT.

2.2.1.9. GC11 Gauthier & Chen (2011) [hereafter GC11] studied luminous red galaxies (LRGs) that were photometrically identified in SDSS DR4 with $z \approx$ 0.5 and a maximum D corresponding to the fiducial virial radius of LRGs, which is given as 500 kpc. A subset of their LRGs were selected by known Mg II absorbers in quasar spectra, while a larger subset was randomly selected near quasar sightlines with no prior knowledge of Mg II absorption. Galaxy spectra were obtained using DIS on the 3.5 m telescope at APO or with the Boller & Chivens Spectrograph on the Las Campanas DuPont telescope. We obtained apparent SDSS "model" g and r magnitudes from NED and included only those LRGs with impact parameters $D < 200$ kpc in MAGIICAT. We also converted the published upper limits on $W_r(2796)$ from 2σ to 3σ, including only those galaxies with $W_{\rm lim} \leq 0.3$ Å.

2.2.1.10. KCBC11 Kacprzak et al. (2011a) [hereafter KCBC11] built upon the work of BC09 by adding galaxies of somewhat larger redshift, $z \sim 0.13$. Galaxy spectra were obtained with DIS on the 3.5 m APO telescope, while quasar spectra were collected using the blue channel of LRIS on Keck-I. Using NED, we obtained

the SDSS "model" r and 2MASS total K_s apparent magnitudes for all but two galaxies, where K_s was not available. We instead obtained the SDSS "model" g and r magnitudes for those two galaxies.

2.2.1.11. KCEMS11 Galaxies selected by Kacprzak et al. (2011b) [hereafter KCEMS11] are based on known Mg II absorption at $0.3 < z < 1$ in quasar spectra, with many having been originally identified by SDP94. Imaging of the quasar fields was conducted by *HST* with the F702W or F814W filters on WFPC2. Infrared imaging for the SDP94 fields was conducted in the K_s band with the NICMOS III cameras on the Kitt Peak 4 m Mayall telescope and the Las Campanas Observatory 2.5 m DuPont telescope. K' magnitudes were obtained for three galaxies from Chen et al. (2001b), who used NSFCAM on the IRTF 3 m telescope, and F160W magnitudes for two galaxies from David Law (private communication) who observed them with WFC3 on *HST*. Quasar spectroscopy was obtained with HIRES/Keck or UVES/VLT, while galaxy spectroscopic redshifts were collected from the literature (see Table 3 in KCEMS11).

2.2.1.12. Churchill13 Requiring high resolution quasar spectra ($R = 45,000$) and *HST* images, Churchill et al. (2013a) [hereafter Churchill13] studied galaxies with weak [$W_r(2796) < 0.3$ Å] or undetected Mg II absorption. Half of the galaxies in this sample were obtained from Steidel-PC, while the other half were collected from Steidel97, Churchill et al. (2012), CT08, and KMC10. Galaxies were imaged in F702W or F814W with WFPC2 on *HST* and, in some cases, in K_s as detailed in Steidel-PC. Quasar spectra were obtained with HIRES/Keck, UVES/VLT, or with the MIKE Echelle Spectrograph on the Magellan Clay telescope. We included

galaxies listed as the "New Sample" in Table 2 in Churchill13.

2.2.2. Sources of Data

In Table 2.1, we present the sources of data for galaxies in MAGIICAT. We present the work from which galaxies were obtained in column (1). The rest of the columns contain the number of galaxies for which the following data was obtained: (2) the galaxy identification, such as redshift and impact parameter, (3) the observed magnitude used to calculate the B-band absolute magnitude, (4) the observed magnitude used to calculate the K-band absolute magnitude, and (5) the MgII equivalent width, while columns (6) and (7) contain the number of galaxies that have detectable absorption and have an upper limit on absorption, respectively.

We note that for many of the sources from which data were obtained, the images of the quasar fields were not published. In cases in which images were published and/or annotated, we did not have access to the electronic data in order to verify and/or directly characterize the magnitude limits and galaxy detection thresholds. As such, we have not been able to directly inspect the imaged fields around the quasars for a substantial portion of the sample. In addition, in many cases the spectra showing the MgII absorption lines were not published so that we have had to rely upon the published equivalent width measurements.

2.2.3. Defining Isolated and Group Galaxies

In this paper, we present only "isolated" galaxies since we are focused on the CGM of individual systems. We define an isolated galaxy to be one in which there

Table 2.1. Sources of Data in MAGIICAT

		Magnitudes		Absorption		
(1) Survey[a]	(2) Galaxy ID	(3) B	(4) K	(5) $W_r(2796)$	(6) Absorbers	(7) Upper Limits
GB97	9	9	0	3	3	0
Churchill13	18	17	9	20	0	20
KCEMS11	33	33	0	32	32	0
Steidel97	0	0	11	0	0	0
CT08	5	5	0	3	2	1
Chen10	68	0	0	68	47	21
SDP94	18	18	38	7	7	0
Steidel-PC	0	1	1	0	0	0
KMC10	4	4	0	1	0	1
KCBC11	9	0	0	9	9	0
GC11	12	0	0	12	5	7
BC09	6	0	0	6	0	6
This Work	0	95	105	21	18	3
Total	182	182	164	182	123	59

[a]The numbers associated with each "survey" reflect the source from which the data we published are taken. In cases where a "0" appears, this is because all of the galaxy or absorption data was either published elsewhere for the first time or republished with higher quality data in a later work.

is no spectroscopically identified galaxy within 100 kpc (projected) and a line of sight velocity separation of 500 km s^{-1}. Conversely, a group galaxy is defined to have a spectroscopically identified nearest neighbor within a projected separation of 100 kpc and having a line of sight relative velocity less than 500 km s^{-1}. This definition is adopted from Chen et al. (2010a), but modified to include a slightly larger velocity separation.

Since we are unable to examine all images of the quasar fields to search for faint objects near the quasar or the identified absorbing galaxy, we cannot place more stringent limits on the definition separating isolated and group galaxies. In the following section, we present an averaged relationship between limiting absolute magnitude and limiting apparent magnitude based upon the general specifications of the published surveys (see Figures 2.4a and 2.4b). The curves show that the "average" survey is generally not deep enough to extend down to luminous satellites like the Large Magellanic Cloud around the Milky Way, and certainly cannot detect dwarf galaxies in groups. Thus, the definition of isolated and group galaxies refers, on average, to the brighter galaxy population.

Our ability to distinguish a group such as the Local Group based upon its brightest members, M31 and the Milky Way, is, in the end, dependent upon the direction from which the the Local Group would be viewed. Given the $\sim$ 700 kpc distance between M31 and the Milky Way, a line of sight perpendicular to their separation vector would render both galaxies as isolated regardless of their relative sightline velocities. On the other hand, a line of sight more or less parallel to their separation vector in which their projected separation is less than 100 kpc would render their being classified as group galaxies, given that their line of sight velocity separation is on the order of $\sim$ 400 km s^{-1}. As such, there is likely some

level, which is difficult to quantify, to which the isolated sample contains galaxies in environments similar to the Local Group. And, for those galaxies classified as group members, there may be some fraction for which the galaxies are physically separated by a large enough distance that their respective CGM environments do not overlap into an intragroup medium (which is likely the case for M31 and the Milky Way, but would in general depend upon the dynamical history of the group).

As we stated above, we present only isolated galaxies in this paper drawing upon a definition set by precedent in the literature. The intragroup medium of the group galaxy subsample will be studied in a forthcoming paper.

2.3. Methods

For each galaxy, the measured quantities include one or more apparent magnitudes in various photometric bands, the spectroscopic redshift, $z_{\rm gal}$, the galaxy right ascension and declination offsets from the quasar, $\Delta\alpha$ and $\Delta\delta$, and/or the galaxy angular separation from the quasar, θ. Many of the galaxies have multiple measurements from several different studies; we selected the highest quality measurements (usually the most recent).

2.3.1. Galaxy Properties

Galaxy redshifts, $z_{\rm gal}$, were taken directly from published values. The galaxy spectra were not published in most cases and were not available in electronic form for further confirmation or re-measurement. Since the uncertainties of $z_{\rm gal}$ were also not published, the accuracy of the published $z_{\rm gal}$ measurements is reflected

by the number of significant figures.

Due to the application of different cosmologies in the literature over the last ~ 20 years, we calculated new impact parameters, D, and luminous properties for each galaxy using the ΛCDM cosmology ($H_0 = 70$ km s^{-1} Mpc^{-1}, $\Omega_M = 0.3$, and $\Omega_\Lambda = 0.7$).

We first calculated the values $\Delta\alpha$ and $\Delta\delta$ from the right ascensions and declinations of the galaxy and its associated quasar, which were obtained from NED when available. We then determined θ from $\Delta\alpha$ and $\Delta\delta$ using $\theta = [(\Delta\delta)^2 + (\Delta\alpha)^2 \cos^2(\delta_{\rm QSO})]^{1/2}$. We compute the impact parameter from $D = \theta D_{\rm A}(z_{\rm gal})$, where $D_{\rm A}(z_{\rm gal})$ is the angular diameter distance at the galaxy redshift. In cases where $\Delta\alpha$ and $\Delta\delta$ could not be obtained, we used the published values of θ to calculate D. Using these methods, we have measured $\Delta\alpha$ and $\Delta\delta$ for most galaxies and standardized impact parameters for all galaxies in MAGIICAT.

All galaxies have been imaged in the g, r, $R_{\rm EFOSC}$, R_s, $R_{\rm J}$, F702W, or F814W bands. For each galaxy, we determined rest-frame AB absolute B-band magnitudes, M_B, using the equation, $M_B({\rm AB}) = [m_y - K_{By}] - DM$, where m_y is the AB apparent magnitude in the observed band, K_{By} is the appropriate K-correction (e.g., Kim et al. 1996, see Appendix A) for the observed magnitude, and DM is the distance modulus for each galaxy. In cases where m_y is a Vega magnitude, such as F702W and F814W, we add the constant -0.0873 to convert from Vega magnitudes to AB magnitudes. Details on how we determined this constant are given in Appendix A.

To compute the K-corrections, we applied the actual filter response curve for each published apparent magnitude. The K-corrections as a function of redshift

for the F702W- and g-band to the B-band are shown in panels (a) and (c) of Figure A.1, respectively. Using the spectral energy distribution (SED) templates from Bolzonella et al. (2000) who extended the Coleman et al. (1980) SEDs to shorter and longer wavelengths, we adopted a SED for each galaxy. To do this, we compared the observed color of each SED to each galaxy's observed color and chose the SED with the closest color. For 18 galaxies where no observed galaxy color was available, we adopted an Sbc galaxy SED, the average type selected by MgII absorption (SDP94; Zibetti et al. 2007). Figure B.1 in Appendix B presents F702W $- K_s$ and $g - r$, the two most common observed galaxy colors in MAGIICAT, as a function of redshift.

The apparent magnitudes in MAGIICAT have not been Galactic reddening corrected to the extent of our knowledge. We did not apply this correction to the magnitudes as the mean reddening correction in each magnitude band is, on average, a small fraction of the uncertainty in the K-corrections due to SED selections. The greatest reddening correction in MAGIICAT would be applied to the g band, as it is the band measuring the shortest wavelengths. The mean reddening correction in this band is 0.2 magnitudes, while the greatest difference in the K-correction $K_{B,g}$ between an E and an Im SED is 1.5 magnitudes (see Figure A.1).

Galaxies drawn from SDP94 and Steidel97 were imaged in the infrared with the K_s band. Many galaxies in CT08, BC09, KCBC10, KCEMS11, and Churchill13 were imaged in either the 2MASS K_s band and obtained from NED, the K' band from Chen et al. (2001b), or the *HST* F160W band from David Law (private communication). Using these values, we computed M_K(AB) from K-corrected infrared magnitudes using the methods applied for the B-band and the equation,

$M_K(\mathrm{AB}) = [m_y - K_{Ky}] - DM + 1.8266$, where m_y is the Vega apparent magnitude and the value 1.8266 is the constant used to convert from Vega magnitudes to AB magnitudes in all cases. The K-corrections in the K_s band for each SED are presented in panel (b) of Figure A.1 as a function of redshift.

Apparent magnitudes in the K-band were not available for all galaxies drawn from Chen10 and GC11, and many galaxies from BC09 and KCBC11. We used an indirect method to compute M_K by determining rest-frame $B-K$ colors from rest-frame $B-R$ colors. We obtained "model" g and r apparent magnitudes from NED/SDSS. We adopt "model" magnitudes because the galaxy light is measured consistently through the same aperture in all bands, therefore they are the best magnitudes for measuring the colors of galaxies. Using these magnitudes and the methods for M_B above, we calculated M_B from g and M_R from r. The K-corrections for these magnitudes are presented in panels (c) and (d) of Figure A.1, respectively. In order to convert these $B-R$ colors to $B-K$, we computed rest-frame $B-R$ and $B-K$ colors for each galaxy SED, which suggest a linear relationship with the form $(B-K) = 1.86(B-R) + 0.02$, determined from a linear least-squares fit to the rest-frame SED colors. The rest-frame colors of each SED and the linear fit are presented in Figure C.1. We then applied this relation to the $B-R$ colors to obtain $B-K$. Finally, M_K was calculated from M_B and $B-K$. Using these methods, we obtained colors for all but 18 galaxies in MAGIICAT.

B-band luminosities, L_B/L_B^*, were obtained using a linear fit to M_B^* with redshift using the "All" sample in Table 6 from Faber et al. (2007). The K-band luminosities, L_K/L_K^*, were computed using $M_K^*(z)$ as expressed in Eq. 2 from Cirasuolo et al. (2010).

2.3.2. Absorption Properties

Where we have obtained access to HIRES/Keck or UVES/VLT quasar spectra, we have remeasured $W_r(2796)$ using the methods of Schneider et al. (1993) and Churchill et al. (2000). Upper limits on $W_r(2796)$ are quoted at 3σ and must be less than or equal to 0.3 Å, corresponding to an unresolved absorption feature, for a galaxy to be included in MAGIICAT. In cases where HIRES/Keck and/or UVES/VLT spectra do not exist, we adopted the best published values. In most cases, these are measurements are take directly from tabulated data. We have also converted published 2σ upper limits to 3σ where needed. We have not included galaxies with upper limits less stringent than 0.3 Å in order to ensure all non-detections reside below the historical absorption threshold of 0.3 Å (SDP94).

Adopting a 3σ upper limit of $W_r(2796) = 0.3$ Å allows us to distinguish two subsamples by absorption strength based upon historical precedence. Several of the surveys from which MAGIICAT is constructed were conducted on 4-meter class telescopes using moderate resolution (~ 1 Å); the typical equivalent width detection sensitivity of these surveys was $W_r(2796) = 0.3$ Å. Not until the advent of the HIRES spectrograph on Keck I in the early 1990s was it possible to systematically explore equivalent widths below this threshold (Churchill et al. 1999). Absorbers with $W_r(2796) < 0.3$ Å were thus dubbed "weak systems".

Following the historical precedent, we adopt the term "strong" absorption for values in the range $W_r(2796) \geq 0.3$ Å. However, we note that this term has often been applied in the literature to describe absorbers with $W_r(2796) \geq 1.0$ Å or higher. Throughout this work, we also adopt the term "weak" absorption for values in the range $W_r(2796) < 0.3$ Å, regardless of whether absorption was

formally detected or not detected to the varying limits of the HIRES and/or UVES quasar spectra.

The term "non-absorber" is most suitably applied for surveys designed to be complete to a well-defined detection threshold, in which upper limits below the threshold would be described using such a term to indicate "below the survey limit". In a global description of absorption strengths, we must keep in mind that a non-detection does not provide evidence for no absorption. A highly stringent limit on $W_r(2796)$ could indicate that the line of sight passed through a low-density, high-ionization region in which the ionization fraction of Mg II is vanishingly small. Similarly, it could indicate that the line of sight probed a very low H I column density, dense, low-ionization structure, such that even with a high metallicity and a high ionization fraction, Mg II would not be detected to the limits of the data. It is likely extremely rare that gas within 200 kpc (projected) of a galaxy and relative velocity within a few hundred kilometers per second would be entirely devoid of Mg II absorption.

In order to simplify terminology, we adopt the two terms "weak" and "strong" absorption, and remind the reader that "weak" absorption encompasses all measurements below $W_r(2796) = 0.3$ Å and all upper limits, since presumably higher and higher sensitivities would yield "detections" in most all cases.

2.4. Galaxy Sample

Here we present basic characteristics of MAGIICAT, leaving any analysis to future work.

MAGIICAT consists of 182 isolated galaxies along 134 sightlines. The redshift range of the sample is $0.07 \leq z \leq 1.12$, with median $\langle z \rangle = 0.359$.

Observed galaxy properties for MAGIICAT are presented in Table 2.2. The columns include the (1) QSO identifier, (2) Julian 2000 designation (J-Name), (3) galaxy spectroscopic redshift, $z_{\rm gal}$, (4) quasar-galaxy right ascension offset, $\Delta\alpha$, (5) quasar-galaxy declination offset, $\Delta\delta$, (6) quasar-galaxy angular separation, θ, (7) reference for columns 4, 5, and 6, (8) apparent magnitude used to obtain M_B, (9) band for the preceding apparent magnitude, (10) reference for columns 8 and 9, (11) apparent magnitude used to calculate M_K, (12) band for m_K, (13) reference for columns 11 and 12, and (14) galaxy spectral energy distribution type based on the galaxy observed color.

The galaxy right ascension and declination offsets from the quasar, $\Delta\alpha$ and $\Delta\delta$, are presented in Figure 2.1(a). Points are colored by reference, indicating the work from which the galaxy data was drawn. No values for $\Delta\alpha$ and $\Delta\delta$ were originally published for galaxies from SDP94, though later works have obtained the values for many of these galaxies (Steidel, private communication). The plus sign indicates the location of the associated background quasar.

Figure 2.1(b) shows the location of each galaxy in MAGIICAT in physical units (kpc) with respect to the associated background quasar (plus sign). The points are colored by the source of the $\Delta\alpha$ and $\Delta\delta$ measurements.

Table 2.2. Observed Galaxy Properties

			Galaxy ID				B-band			K-band			
(1) QSO	(2) J-Name	(3) $z_{\rm gal}$	(4) $\Delta\alpha$ (arcsec)	(5) $\Delta\delta$ (arcsec)	(6) θ (arcsec)	(7) Ref[a]	(8) m_y[b]	(9) Band[c]	(10) Ref[a]	(11) m_y[d]	(12) Band[c]	(13) Ref[a]	(14) SED[e]
0002−422	J000448.11−415728.8	0.840	−6.4	−3.4	7.10	1	22.60	$R_{\rm EFOSC}$(V)	1	···	···	···	(Sbc)
0002+051	J000520.21+052411.80	0.298	−13.4	0.4	13.45	3	19.86	F702W(V)	3	16.37	K_s(V)	7	E/S0
0002+051	J000520.21+052411.80	0.592	−2.6	−4.8	5.46	3	21.11	F702W(V)	3	17.40	K_s(V)	7	E/S0
0002+051	J000520.21+052411.80	0.85180	−3.3	0.6	3.40	3	22.21	F702W(V)	3	19.30	K_s(V)	7	Im
SDSS	J003340.21−005525.53	0.2124	−5.4	3.2	6.28	6	19.44	g(AB)	14	18.79	r(AB)	14	Scd
SDSS	J003407.34−085452.07	0.3617	6.5	−1.2	6.56	6	22.41	g(AB)	14	21.45	r(AB)	14	Scd
SDSS	J003413.04−010026.86	0.2564	−2.8	7.1	7.63	6	21.68	g(AB)	14	20.25	r(AB)	14	E/S0
0058+019	J010054.15+021136.52	0.6128	···	···	4.40	7	23.25	R_s(AB)	7	19.90	K_s(V)	7	Sbc
0058+019	J010054.15+021136.52	0.680	−3.3	−5.5	6.50	2	22.06	F702W(V)	2	18.65	K_s(V)	8	Sbc
SDSS	J010135.84−005009.08	0.2615	10.2	−7.4	12.60	6	20.91	g(AB)	14	19.57	r(AB)	14	E/S0
SDSS	J010156.32−084401.74	0.1588	−7.7	−7.0	10.36	6	21.08	g(AB)	14	20.32	r(AB)	14	Sbc
SDSS	J010352.47+003739.79	0.3515	−9.7	1.0	9.75	6	22.59	g(AB)	14	21.43	r(AB)	14	Sbc
0102−190	J010516.82−184641.9	1.025	−0.7	−4.9	5.00	1	22.90	$R_{\rm EFOSC}$(V)	1	···	···	···	(Sbc)
0109+200	J011210.18+202021.79	0.534	0.8	7.1	7.13	3	22.27	F702W(V)	3	16.70	K_s(V)	7	E/S0
0117+213	J012017.20+213346.00	0.5763	···	···	1.20	7	20.65	R_s(AB)	7	16.60	K_s(V)	7	E/S0
0117+213	J012017.20+213346.00	0.729	−6.8	−3.6	7.68	3	21.06	F702W(V)	3	16.80	K_s(V)	7	E/S0
0122−003	J012528.84−000555.93	0.3788	−8.7	−12.3	15.07	5	20.60	F702W(AB)	5	17.94	K'(V)	13	Im
0141+339	J014411.70+341157.92	0.4708	···	···	6.50	7	22.86	R_s(AB)	7	20.10	K_s(V)	7	Scd
0150−202	J015227.32−200107.10	0.383	8.5	−7.8	11.47	3	21.15	F702W(V)	3	···	···	···	(Sbc)
0150−202	J015227.32−200107.10	0.603	5.1	−6.4	8.10	2	20.29	F702W(V)	2	17.40	K_s(V)	8	Scd
0150−202	J015227.32−200107.10	0.780	···	···	7.40	7	22.32	R_s(AB)	7	18.90	K_s(V)	7	Scd
SDSS	J015453.03−095535.39	0.5663	−8.7	1.8	8.71	11	22.50	g(AB)	14	21.00	r(AB)	14	Sbc
SDSS	J021558.40−011135.79	0.2103	6.6	4.6	8.04	6	20.13	g(AB)	14	19.43	r(AB)	14	Scd

Table 2.2 (continued)

(1) QSO	(2) J-Name	(3) $z_{\rm gal}$	Galaxy ID (4) $\Delta\alpha$ (arcsec)	(5) $\Delta\delta$ (arcsec)	(6) θ (arcsec)	(7) Ref[a]	B-band (8) m_y[b]	(9) Band[c]	(10) Ref[a]	K-band (11) m_y[d]	(12) Band[c]	(13) Ref[a]	(14) SED[e]
0226−4110	J022815.2-405716	0.2067	−7.9	−7.9	10.00	5	22.20	R_J(AB)	5	···	···	···	(Sbc)
0226−4110	J022815.2-405716	0.2674	11.6	−12.5	15.41	5	20.40	R_J(AB)	5	···	···	···	(Sbc)
SDSS	J022950.32−074256.77	0.3866	−5.2	0.9	5.25	6	22.08	g(AB)	14	21.03	r(AB)	14	Scd
0229+131	J023145.89+132254.71	0.4167	−5.5	4.0	6.74	3	19.72	F702W(V)	3	16.45	K_s(V)	7	E/S0
0235+164	J023838.93+163659.27	0.524	0.2	−1.9	1.95	3	20.31	F702W(V)	3	17.30	K_s(V)	7	Sbc
0235+164	J023838.93+163659.27	0.852	···	···	1.00	7	21.93	R_s(AB)	7	17.80	K_s(V)	7	Sbc
0302−223	J030450.10−221157.00	0.418	−18.0	−15.0	23.00	1	18.40	$R_{\rm EFOSC}$(V)	1	···	···	···	(Sbc)
0302−223	J030450.10−221157.00	1.000	−2.6	−7.2	7.70	1	23.10	$R_{\rm EFOSC}$(V)	1	···	···	···	(Sbc)
SDSS	J032232.58+003649.13	0.2185	−0.4	−4.5	4.52	6	22.48	g(AB)	14	21.51	r(AB)	14	Sbc
0334−204	J033626.90−201940.00	1.120	2.9	−7.3	7.90	1	22.60	$R_{\rm EFOSC}$(V)	1	···	···	···	(Sbc)
0349−146	J035128.54−142908.71	0.3236	12.2	−24.1	27.02	2	19.92	F702W(V)	2	16.54	K'(V)	13	E/S0
0349−146	J035128.54−142908.71	0.3567	−9.9	10.4	14.35	3	20.44	F702W(V)	3	18.54	K'(V)	13	Im
SDSS	J035242.12+001307.32	0.3671	−1.9	9.8	9.98	6	22.54	g(AB)	14	20.99	r(AB)	14	E/S0
0454−220	J045608.92−215909.40	0.2784	10.6	5.6	11.99	2	21.18	F702W(V)	2	19.14	K'(V)	13	Im
0454−220	J045608.92−215909.40	0.3818	0.2	−19.8	19.79	2	20.41	F702W(V)	2	17.24	K'(V)	13	Sbc
0454−220	J045608.92−215909.40	0.48382	−1.2	−17.9	17.98	3	20.09	F702W(V)	3	16.94	K'(V)	13	Sbc
0454+039	J045647.17+040052.94	0.072	3.8	1.4	4.00	1	20.50	$R_{\rm EFOSC}$(V)	1	···	···	···	(Sbc)
0454+039	J045647.17+040052.94	0.201	2.1	−26.8	26.60	2	18.42	F702W(V)	2	15.24	K_s(V)	8	E/S0
0454+039	J045647.17+040052.94	0.8596	···	···	2.10	7	24.60	R_s(AB)	7	···	···	···	(Sbc)
SDSS	J075001.85+161305.05	0.1466	−7.3	−3.1	7.66	6	21.30	g(AB)	14	20.75	r(AB)	14	Scd
SDSS	J075450.04+184952.79	0.2856	1.0	12.5	12.54	6	21.25	g(AB)	14	19.82	r(AB)	14	E/S0
SDSS	J075525.51+172836.59	0.2541	−5.4	−10.8	11.97	6	20.57	g(AB)	14	19.57	r(AB)	14	Sbc
SDSS	J080004.56+184935.15	0.2544	7.8	−1.8	7.60	6	20.76	g(AB)	14	20.05	r(AB)	14	Scd
SDSS	J081420.19+383408.3	0.09801	28.4	−19.0	29.18	10	16.76	r(AB)	14	13.91	K_s(V)	15	Sbc

Table 2.2 (continued)

(1) QSO	(2) J-Name	(3) $z_{\rm gal}$	Galaxy ID (4) $\Delta\alpha$ (arcsec)	(5) $\Delta\delta$ (arcsec)	(6) θ (arcsec)	(7) Ref[a]	B-band (8) m_y[b]	(9) Band[c]	(10) Ref[a]	K-band (11) m_y[d]	(12) Band[c]	(13) Ref[a]	(14) SED[e]
SDSS	J082340.18+074801.68	0.1864	5.6	−10.6	11.96	6	19.74	g(AB)	14	18.61	r(AB)	14	E/S0
0827+243	J083052.08+241059.82	0.258	5.1	16.9	17.50	2	20.20	F702W(V)	2	17.12	K_s(V)	8	E/S0
0827+243	J083052.08+241059.82	0.5247	5.6	2.0	5.98	3	20.64	F702W(V)	3	16.95	K_s(V)	7	E/S0
0836+113	J083933.01+111203.82	0.78682	0.9	3.5	3.61	3	22.63	F702W(V)	3	19.70	K_s(V)	7	Scd
SDSS	J084119.78+012621.75	0.4091	12.1	7.1	14.03	6	21.51	g(AB)	14	20.27	r(AB)	14	Sbc
SDSS	J084456.06+004708.95	0.1551	−7.2	9.2	11.68	6	19.71	g(AB)	14	18.97	r(AB)	14	Sbc
SDSS	J085826.93+022604.49	0.1097	44.2	11.6	45.66	6	19.34	g(AB)	14	18.89	r(AB)	14	Scd
SDSS	J090519.70+084917.32	0.1499	0.3	−3.3	3.31	6	22.90	g(AB)	14	22.54	r(AB)	14	Im
SDSS	J090519.70+084917.32	0.3856	−10.2	16.4	19.25	6	21.66	g(AB)	14	20.57	r(AB)	14	Scd
SDSS	J090519.70+084917.32	0.4545	−1.3	14.9	14.96	6	21.91	g(AB)	14	21.19	r(AB)	14	Im
SDSS	J091119.16+031152.9	0.09616	−35.4	17.8	39.57	10	16.75	r(AB)	14	13.69	K_s(V)	15	Sbc
SDSS	J091845.91+060226.09	0.1849	−12.1	−23.2	26.13	6	19.98	g(AB)	14	18.77	r(AB)	14	E/S0
SDSS	J092300.67+075108.2	0.10385	4.3	−3.1	5.30	10	16.42	r(AB)	14	13.10	K_s(V)	15	E/S0
SDSS	J093251.82+073729.11	0.3876	6.4	2.5	6.82	6	21.42	g(AB)	14	20.40	r(AB)	14	Scd
SDSS	J093536.98+112408.03	0.2808	4.0	2.6	4.70	6	21.35	g(AB)	14	20.49	r(AB)	14	Scd
SDSS	J100807.51+014448.97	0.2173	46.5	−2.8	46.56	6	18.79	g(AB)	14	17.98	r(AB)	14	Sbc
SDSS	J100906.36+023555.31	0.2523	8.2	2.5	8.56	6	20.70	g(AB)	14	19.30	r(AB)	14	E/S0
SDSS	J102218.98+013218.82	0.1369	25.9	−35.3	43.78	6	18.69	g(AB)	14	17.63	r(AB)	14	E/S0
1019+309	J102230.29+304105.11	0.346	−6.5	6.9	9.44	3	20.46	F702W(V)	3	17.73	K_s(V)	7	Scd
SDSS	J102751.62+104532.61	0.1093	−24.4	32.6	40.49	12	16.25	r(AB)	14	13.41	K_s(V)	15	Sbc
SDSS	J102847.00+391800.5	0.11348	−6.6	42.3	42.59	10	17.07	g(AB)	14	17.07	r(AB)	14	Scd
SDSS	J103607.51+015659.14	0.3571	−33.7	−4.3	33.95	6	20.00	g(AB)	14	18.98	r(AB)	14	Scd
SDSS	J103836.50+095138.85	0.1742	−1.8	4.8	5.12	6	21.26	g(AB)	14	20.46	r(AB)	14	Sbc
1038+064	J104117.16+061016.92	0.3157	−4.5	−10.8	11.70	2	21.44	F702W(V)	2	17.80	K_s(V)	8	E/S0

Table 2.2 (continued)

(1) QSO	(2) J-Name	(3) $z_{\rm gal}$	Galaxy ID (4) $\Delta\alpha$ (arcsec)	(5) $\Delta\delta$ (arcsec)	(6) θ (arcsec)	(7) Ref[a]	B-band (8) m_y[b]	(9) Band[c]	(10) Ref[a]	K-band (11) m_y[d]	(12) Band[c]	(13) Ref[a]	(14) SED[e]
1038+064	J104117.16+061016.92	0.4432	9.7	2.1	9.86	3	20.59	F702W(V)	3	16.50	K_s(V)	7	E/S0
SDSS	J104935.99+075813.74	0.4793	−18.0	−23.6	29.58	11	22.80	g(AB)	14	20.50	r(AB)	14	E/S0
SDSS	J105033.08−001354.84	0.1155	−34.4	21.8	40.68	12	16.59	r(AB)	14	13.73	K_s(V)	15	Sbc
1100−264	J110325.29−264515.7	0.359	5.7	−10.8	12.20	1	20.40	$R_{\rm EFOSC}$(V)	1	···	···	···	(Sbc)
SDSS	J111342.42−000730.80	0.1094	1.5	−24.9	24.95	12	16.22	r(AB)	14	12.95	K_s(V)	15	E/S0
SDSS	J111850.13−002100.7	0.13159	−6.9	−9.4	11.67	10	17.22	g(AB)	14	17.22	r(AB)	14	Sbc
SDSS	J112016.66+093323.53	0.4933	−0.4	−5.6	5.61	6	21.67	g(AB)	14	20.64	r(AB)	14	Scd
SDSS	J112613.52+352002.60	0.1117	−55.8	−15.4	48.06	12	17.05	r(AB)	14	13.89	K_s(V)	15	E/S0
1127−145	J113007.05−144927.38	0.20735	−12.9	31.4	33.91	9	19.85	F814W(V)	9	···	···	···	(Sbc)
1127−145	J113007.05−144927.38	0.27921	25.0	−12.5	27.92	9	20.22	F814W(V)	9	···	···	···	(Sbc)
1127−145	J113007.05−144927.38	0.30515	−23.6	36.2	43.23	9	19.50	F814W(V)	9	···	···	···	(Sbc)
1127−145	J113007.05−144927.38	0.33293	···	···	38.12	9	19.76	F814W(V)	9	···	···	···	(Sbc)
SDSS	J113757.02+085017.21	0.3356	−3.9	5.2	6.47	6	21.76	g(AB)	14	20.81	r(AB)	14	Scd
SDSS	J114144.62+080614.79	0.2290	3.1	−20.7	20.93	6	20.12	g(AB)	14	19.44	r(AB)	14	Scd
SDSS	J114144.62+080614.79	0.3583	7.7	−9.5	12.18	6	21.24	g(AB)	14	20.14	r(AB)	14	Sbc
SDSS	J114444.63+071443.75	0.4906	10.1	12.7	16.15	11	22.07	g(AB)	14	20.23	r(AB)	14	E/S0
SDSS	J114518.47+451601.4	0.13389	21.6	6.1	16.38	10	17.04	r(AB)	14	14.58	K_s(V)	15	Im
SDSS	J114657.91+020712.69	0.5437	11.1	4.2	11.72	11	22.11	g(AB)	14	20.53	r(AB)	14	E/S0
SDSS	J114803.17+565411.4	0.10451	10.1	14.5	15.51	10	16.49	r(AB)	14	13.06	K_s(V)	15	E/S0
1148+387	J115129.37+382552.35	0.5536	−0.2	3.2	3.20	3	20.94	F702W(V)	3	18.10	K_s(V)	7	Scd
SDSS	J120932.26+004555.92	0.2533	−9.7	−9.7	13.72	6	21.86	g(AB)	14	20.62	r(AB)	14	E/S0
1209+107	J121140.59+103002.02	0.392	5.3	4.8	7.12	3	21.74	F702W(V)	3	19.20	K_s(V)	7	Scd
1222+228	J122527.39+223513.0	0.5502	4.5	3.9	5.92	3	22.50	F702W(V)	3	18.80	K_s(V)	7	E/S0
1229−021	J123200.01−022405.27	0.7546	···	···	1.70	7	22.90	R_s(AB)	7	19.20	K_s(V)	7	Sbc

Table 2.2 (continued)

(1) QSO	(2) J-Name	(3) $z_{\rm gal}$	Galaxy ID (4) $\Delta\alpha$ (arcsec)	(5) $\Delta\delta$ (arcsec)	(6) θ (arcsec)	(7) Ref[a]	B-band (8) m_y[b]	(9) Band[c]	(10) Ref[a]	K-band (11) m_y[d]	(12) Band[c]	(13) Ref[a]	(14) SED[e]
1241+176	J124410.82+172104.52	0.550	3.3	0.5	3.31	3	21.39	F702W(V)	3	18.43	K_s(V)	7	Sbc
1245+345	J124727.83+341509.56	0.941	···	···	3.50	7	22.90	R_s(AB)	7	19.53	K_s(V)	7	Im
1246−057	J124913.85−055919.07	0.637	−4.0	1.6	4.25	3	22.21	F702W(V)	3	18.80	K_s(V)	7	Sbc
1248+401	J125048.32+395139.48	0.7725	···	···	4.80	7	23.35	R_s(AB)	7	19.70	K_s(V)	7	Scd
1254+047	J125659.92+042734.39	0.9341	···	···	1.60	7	24.30	R_s(AB)	7	20.20	K_s(V)	7	Sbc
SDSS	J125739.22+144806.26	0.4648	−4.2	−4.1	5.77	6	21.03	g(AB)	14	20.39	r(AB)	14	Im
SDSS	J130554.17+014929.82	0.1747	43.2	−7.5	43.82	6	19.04	g(AB)	14	17.81	r(AB)	14	E/S0
SDSS	J130554.17+014929.82	0.2258	19.8	−1.2	19.83	6	20.30	g(AB)	14	19.39	r(AB)	14	Sbc
SDSS	J131815.12+012450.67	0.5405	10.6	−12.9	16.66	11	22.65	g(AB)	14	21.01	r(AB)	14	E/S0
1317+277	J131956.23+272808.22	0.6610	−6.3	−13.5	14.88	3	21.34	F702W(V)	3	18.07	K_s(V)	7	Sbc
1317+277	J131956.23+272808.22	0.6719	−6.9	4.6	8.27	2	20.95	F702W(V)	2	17.57	K_s(V)	7	Sbc
1321+294	J132320.55+291007.15	0.231	···	···	4.70	7	20.09	R_s(AB)	7	16.64	K_s(V)	7	E/S0
SDSS	J132757.41+101141.78	0.2557	−2.8	−5.8	6.42	6	21.63	g(AB)	14	20.77	r(AB)	14	Scd
SDSS	J132831.08+075942.01	0.2358	24.7	10.6	26.66	6	20.15	g(AB)	14	19.52	r(AB)	14	Im
SDSS	J132831.08+075942.01	0.3323	6.8	1.0	6.81	6	20.64	g(AB)	14	19.57	r(AB)	14	Sbc
1331+170	J133335.78+164904.01	0.7443	···	···	4.20	7	23.25	R_s(AB)	7	18.54	K_s(V)	7	E/S0
1332+552	J133411.70+550124.98	0.373	−2.6	4.7	5.42	3	19.39	F702W(V)	3	16.15	K_s(V)	7	E/S0
1354+195	J135704.43+191907.37	0.44060	−21.7	−12.1	24.82	2	20.96	F702W(V)	2	18.04	K'(V)	13	Sbc
1354+195	J135704.43+191907.37	0.4592	1.4	7.7	7.80	3	21.08	F702W(V)	3	18.17	K_s(V)	7	Sbc
1354+195	J135704.43+191907.37	0.8031	26.2	−0.1	25.70	2	22.13	F702W(V)	2	17.65	K_s(V)	8	E/S0
SDSS	J140619.61+130106.82	0.1748	−18.6	36.8	41.02	6	19.07	g(AB)	14	18.13	r(AB)	14	Sbc
SDSS	J140619.61+130106.82	0.2220	4.8	−1.6	4.94	6	20.65	g(AB)	14	19.96	r(AB)	14	Scd
SDSS	J140843.77+004730.46	0.1146	−22.9	4.6	23.40	12	17.41	r(AB)	14	13.67	K_s(V)	15	E/S0
SDSS	J141654.33−000520.35	0.4746	2.4	−13.9	14.11	11	22.53	g(AB)	14	20.36	r(AB)	14	E/S0

Table 2.2 (continued)

(1) QSO	(2) J-Name	(3) $z_{\rm gal}$	Galaxy ID (4) $\Delta\alpha$ (arcsec)	(5) $\Delta\delta$ (arcsec)	(6) θ (arcsec)	(7) Ref[a]	B-band (8) m_y[b]	(9) Band[c]	(10) Ref[a]	K-band (11) m_y[d]	(12) Band[c]	(13) Ref[a]	(14) SED[e]
SDSS	J142310.50+093357.14	0.6139	22.6	12.4	25.55	11	21.81	g(AB)	14	20.15	r(AB)	14	E/S0
SDSS	J142556.40−001818.79	0.1382	54.7	0.7	54.70	6	17.21	g(AB)	14	16.09	r(AB)	14	E/S0
1424−118	J142738.10−120350.00	0.3404	−0.4	17.8	17.83	3	20.18	F702W(V)	3	17.04	K'(V)	13	Sbc
SDSS	J143216.78+095519.29	0.3293	2.8	2.9	4.00	6	21.89	g(AB)	14	20.65	r(AB)	14	Sbc
SDSS	J150339.98+064259.96	0.1809	2.5	8.2	8.57	6	21.80	g(AB)	14	20.65	r(AB)	14	E/S0
SDSS	J150339.98+064259.96	0.2333	−5.4	−24.9	25.47	6	21.09	g(AB)	14	20.43	r(AB)	14	Scd
SDSS	J151228.82−011223.12	0.1284	−8.5	7.0	11.01	6	19.88	g(AB)	14	19.28	r(AB)	14	Scd
1511+103	J151329.29+101105.54	0.437	5.0	4.5	6.76	3	21.23	F702W(V)	3	18.59	K_s(V)	7	Scd
SDSS	J151541.23+334739.49	0.1156	−7.0	12.9	14.17	12	17.31	r(AB)	14	14.23	K_s(V)	15	Sbc
SDSS	J153112.98+091138.78	0.2659	0.4	−11.8	11.81	6	22.03	g(AB)	14	20.85	r(AB)	14	Sbc
SDSS	J153112.98+091138.78	0.3265	−3.1	−19.1	19.34	6	22.02	g(AB)	14	21.01	r(AB)	14	Scd
SDSS	J153715.34+023049.73	0.2151	4.9	6.7	8.30	6	20.27	g(AB)	14	19.70	r(AB)	14	Im
1548+092	J155103.39+090849.25	0.339	8.2	20.3	21.60	2	19.67	F702W(V)	2	16.45	K_s(V)	8	E/S0
1548+092	J155103.39+090849.25	0.554	−7.8	6.5	10.10	2	21.31	F702W(V)	2	17.61	K_s(V)	8	E/S0
1548+092	J155103.39+090849.25	0.7703	···	···	5.50	7	23.60	R_s(AB)	7	20.60	K_s(V)	7	Im
1548+092	J155103.39+090849.25	0.803	3.6	16.1	16.20	2	20.68	F702W(V)	2	17.02	K_s(V)	8	Sbc
SDSS	J155336.46+053423.97	0.3227	4.6	14.3	15.01	6	20.41	g(AB)	14	19.36	r(AB)	14	Sbc
SDSS	J155557.07−003608.41	0.3006	−7.9	−7.2	10.69	6	21.81	g(AB)	14	21.31	r(AB)	14	Im
SDSS	J160726.77+471251.37	0.4980	−13.3	−29.6	30.96	11	22.07	g(AB)	14	20.70	r(AB)	14	Sbc
SDSS	J160749.34−002219.86	0.3985	3.0	−8.6	9.11	6	21.34	g(AB)	14	19.99	r(AB)	14	Sbc
SDSS	J160905.42+071337.29	0.2075	14.0	−6.6	15.38	6	20.10	g(AB)	14	19.04	r(AB)	14	Sbc
SDSS	J161714.12+243255.63	0.5703	−7.8	−0.9	7.15	11	22.07	g(AB)	14	20.34	r(AB)	14	E/S0
SDSS	J161940.56+254323.0	0.12438	−18.1	10.5	19.42	10	17.15	r(AB)	14	13.95	K_s(V)	15	E/S0
1622+238	J162439.08+234512.20	0.261	25.7	17.7	31.21	2	21.28	F702W(V)	2	17.27	K_s(V)	4	E/S0

Table 2.2 (continued)

(1) QSO	(2) J-Name	(3) $z_{\rm gal}$	Galaxy ID (4) $\Delta\alpha$ (arcsec)	(5) $\Delta\delta$ (arcsec)	(6) θ (arcsec)	(7) Ref[a]	B-band (8) m_y[b]	(9) Band[c]	(10) Ref[a]	K-band (11) m_y[d]	(12) Band[c]	(13) Ref[a]	(14) SED[e]
1622+238	J162439.08+234512.20	0.2800	12.7	−31.2	33.30	5	22.90	F702W(AB)	5	19.74	K_s(V)	4	Sbc
1622+238	J162439.08+234512.20	0.3181	−6.7	9.7	11.82	3	20.00	F702W(V)	3	16.06	K_s(V)	4	E/S0
1622+238	J162439.08+234512.20	0.4720	−4.3	−3.9	5.79	3	22.27	F702W(V)	3	19.78	K_s(V)	4	Scd
1622+238	J162439.08+234512.20	0.565	−2.8	9.1	9.57	2	23.42	F702W(V)	2	21.28	K_s(V)	4	Im
1622+238	J162439.08+234512.20	0.635	−5.5	7.6	9.40	2	23.78	F702W(V)	2	21.91	K_s(V)	4	Im
1622+238	J162439.08+234512.20	0.6560	1.6	14.3	14.37	3	22.55	F702W(V)	3	19.81	K_s(V)	4	Scd
1622+238	J162439.08+234512.20	0.7016	−12.4	9.8	15.81	3	21.62	F702W(V)	3	18.10	K_s(V)	4	Sbc
1622+238	J162439.08+234512.20	0.7975	−9.0	3.1	9.57	3	22.37	F702W(V)	3	18.59	K_s(V)	4	Sbc
1622+238	J162439.08+234512.20	0.8280	7.9	−17.0	18.47	5	24.20	F702W(AB)	5	19.31	K_s(V)	4	E/S0
1622+238	J162439.08+234512.20	0.8909	3.0	−0.0	3.01	3	22.64	F702W(V)	3	20.00	K_s(V)	4	Im
1704+710	J170426.08+705734.7	0.7123	···	···	3.10	7	23.42	R_s(AB)	7	19.80	K_s(V)	7	Sbc
2000−330	J200324.11−325145.13	0.791	1.2	−6.6	6.70	1	21.60	$R_{\rm EFOSC}$(V)	1	···	···	···	(Sbc)
SDSS	J204303.55−010126.05	0.1329	11.8	−11.9	16.76	6	20.44	g(AB)	14	19.73	r(AB)	14	Sbc
SDSS	J204303.55−010126.05	0.2356	−0.3	−13.0	13.00	6	19.49	g(AB)	14	18.99	r(AB)	14	Im
SDSS	J210230.72+094125.08	0.3565	2.1	−4.0	4.50	6	22.30	g(AB)	14	21.22	r(AB)	14	Sbc
SDSS	J211626.32−062437.44	0.5237	−6.0	22.0	22.79	11	22.27	g(AB)	14	20.70	r(AB)	14	E/S0
SDSS	J212938.59−063801.85	0.2782	5.8	3.0	6.51	6	22.29	g(AB)	14	21.15	r(AB)	14	Sbc
2128−123	J213135.26−120704.79	0.430	6.7	5.4	8.63	3	20.43	F702W(V)	3	17.12	K_s(V)	7	E/S0
2145+067	J214805.45+065738.60	0.790	0.4	−5.5	5.50	1	22.50	$R_{\rm EFOSC}$(V)	1	18.70	K_s(V)	7	Sbc
2206−199	J220852.07−194359.0	0.752	···	···	1.60	7	22.80	R_s(AB)	7	···	···	···	(Sbc)
2206−199	J220852.07−194359.0	0.948	−6.2	9.2	11.08	3	21.92	F702W(V)	3	19.74	F160W(V)	16	Im
2206−199	J220852.07−194359.0	1.01655	−12.4	−4.2	13.08	3	20.99	F702W(V)	3	18.87	F160W(V)	16	Im
SDSS	J221126.76+124458.16	0.4872	−5.0	1.8	5.20	6	22.33	g(AB)	14	20.46	r(AB)	14	E/S0
SDSS	J221526.74+011356.47	0.1952	2.1	−9.3	9.53	6	22.06	g(AB)	14	21.50	r(AB)	14	Im

Table 2.2 (continued)

(1) QSO	(2) J-Name	(3) $z_{\rm gal}$	Galaxy ID (4) $\Delta\alpha$ (arcsec)	(5) $\Delta\delta$ (arcsec)	(6) θ (arcsec)	(7) Ref[a]	B-band (8) m_y[b]	(9) Band[c]	(10) Ref[a]	K-band (11) m_y[d]	(12) Band[c]	(13) Ref[a]	(14) SED[e]
SDSS	J221526.74+011356.47	0.3203	−10.5	−2.7	10.84	6	21.35	g(AB)	14	20.38	r(AB)	14	Scd
SDSS	J223246.80+134702.04	0.3221	−5.2	−6.7	8.39	6	20.41	g(AB)	14	19.34	r(AB)	14	Sbc
SDSS	J223316.87+133309.90	0.2138	−7.7	5.5	9.29	6	19.82	g(AB)	14	19.09	r(AB)	14	Scd
SDSS	J223359.93−003315.79	0.1162	−2.8	−5.0	5.73	6	20.70	g(AB)	14	20.01	r(AB)	14	Sbc
2231−002	J223408.99+000001.69	0.8549	···	···	3.10	7	23.80	R_s(AB)	7	···	···	···	(Sbc)
SDSS	J224704.78−081617.54	0.4270	−11.4	16.5	20.00	6	21.23	g(AB)	14	19.96	r(AB)	14	Sbc
SDSS	J225036.72+000759.49	0.14826	14.4	−14.4	20.39	10	17.50	r(AB)	14	13.34	K_s(V)	15	E/S0
SDSS	J230225.49−082154.12	0.3618	−6.4	−2.5	6.82	6	21.90	g(AB)	14	20.38	r(AB)	14	E/S0
SDSS	J230845.60−091449.45	0.2147	−1.0	3.5	3.64	6	21.42	g(AB)	14	20.00	r(AB)	14	E/S0
SDSS	J232735.98+153309.57	0.4756	23.9	14.6	27.22	11	22.68	g(AB)	14	21.18	r(AB)	14	Sbc
SDSS	J232925.18−100722.43	0.4606	−15.8	−6.5	16.81	11	22.17	g(AB)	14	20.48	r(AB)	14	E/S0
2342+089	J234433.00+091039.4	0.7233	···	···	4.80	7	20.76	R_s(AB)	7	17.22	K_s(V)	7	Scd
2343+125	J234628.21+124859.9	0.7148	···	···	11.80	8	21.70	R_s(AB)	8	18.20	K_s(V)	8	Scd
2343+125	J234628.21+124859.9	0.7313	···	···	4.50	7	23.80	R_s(AB)	7	20.30	K_s(V)	7	Scd
SDSS	J234949.61+003535.39	0.2778	−2.8	7.0	7.54	6	21.71	g(AB)	14	20.45	r(AB)	14	Sbc

[a]Galaxy Identification and Apparent Magnitude Reference: (1) Guillemin & Bergeron (1997), (2) Churchill et al. (2013a), (3) Kacprzak et al. (2011b), (4) Steidel et al. (1997), (5) Chen & Tinker (2008), (6) Chen et al. (2010a), (7) Steidel et al. (1994), (8) Steidel-PC, (9) Kacprzak et al. (2010b), (10) Kacprzak et al. (2011a), (11) Gauthier & Chen (2011), (12) Barton & Cooke (2009), (13) Chen et al. (2001b), (14) NED/SDSS, (15) NED/2MASS, and (16) David Law, personal communication.

[b]Apparent magnitude used to obtain M_B.

[c]Magnitude Band and Type: (AB) AB magnitude, and (V) Vega magnitude.

[d]Apparent magnitude used to obtain M_K.

[e]Galaxy Spectral Energy Distributions: (Sbc) No color information – Sbc used.

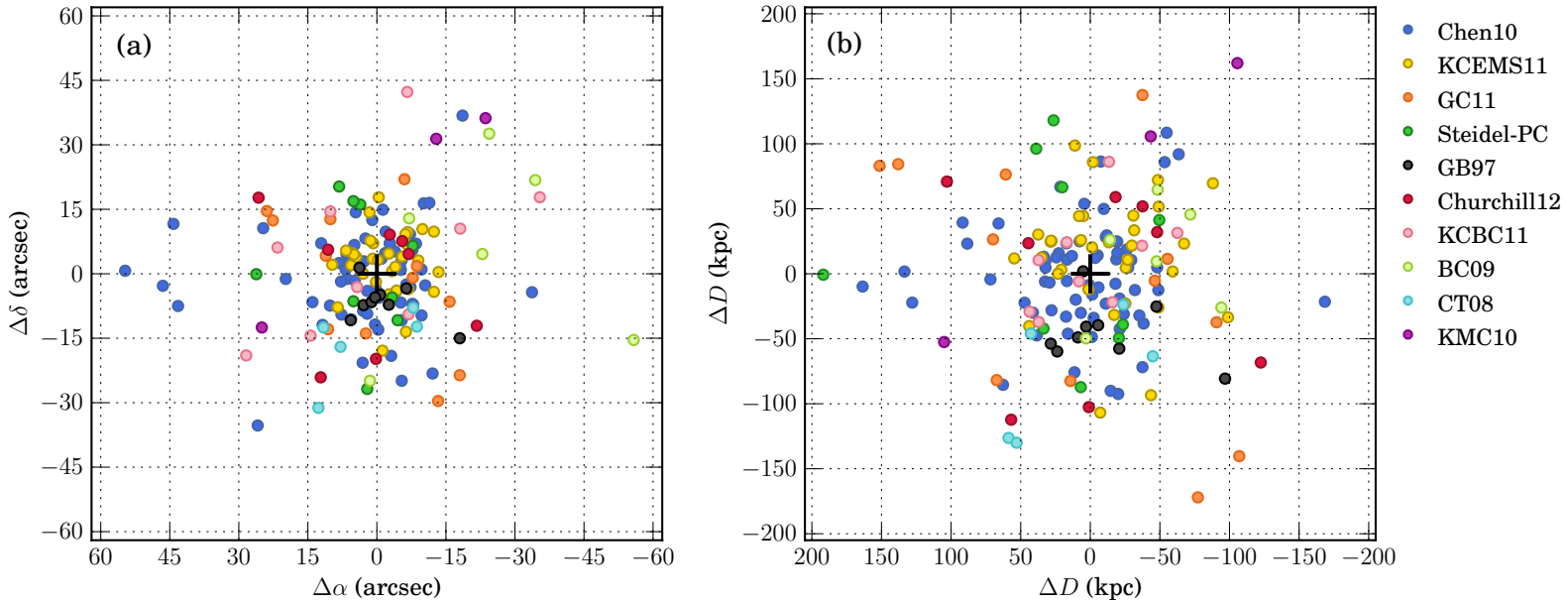

Fig. 2.1.— (a) Angular offsets (arcsec) of each galaxy for which we have $\Delta\alpha$ and $\Delta\delta$ from the associated background quasar. (b) Physical offsets (kpc) of each galaxy from the associated background quasar. Points are color coded by the work from which the galaxy was obtained. The plus sign indicates the location of the background quasar.

Impact parameter, D, as a function of galaxy redshift, $z_{\rm gal}$, is presented in Figure 2.2. Points are colored by $W_r(2796)$, with 3σ upper limits on $W_r(2796)$ represented as open points. Histograms of the data collapsed along the axes show the distribution of impact parameters and galaxy redshifts. Impact parameters range from $5.4 \leq D \leq 194$ kpc, where the median impact parameter is $\langle D \rangle = 48.7$ kpc.

From Figure 2.2, it is apparent that most galaxies with upper limits on absorption are found at larger impact parameters. This anti-correlation between $W_r(2796)$ and D is a commonly known property of Mg II galaxies (e.g., Lanzetta & Bowen 1990; Bergeron & Boissé 1991; Steidel 1995; Bouché et al. 2006; Kacprzak et al. 2008; Chen et al. 2010a; Churchill et al. 2013a). We performed a non-parametric Kendall's τ rank correlation test on $W_r(2796)$ and D, allowing for upper limits on $W_r(2796)$ (see Brown et al. 1974; Wang & Wells 2000). We find that $W_r(2796)$ is anti-correlated with D at the 7.9σ level. We present the anti-correlation in Figure 3.1, leaving any analysis for future work in which we explore the scatter in the relationship as a function of galaxy properties (see Paper II and Churchill et al. 2013b). Galaxies with measured absorption are shown as blue points, while upper limits on absorption are open red circles with downward arrows. The distributions of $W_r(2796)$ and D for absorbers (thin blue lines), and galaxies with upper limits on absorption (dotted red lines) are presented in histograms.

The equivalent width detections and upper limits on absorption of MAGIICAT galaxies have a range of $0.003 \leq W_r(2796) \leq 4.42$ Å, where the weakest confirmed absorption is $W_r(2796) = 0.03$ Å. Of the 182 galaxies, 59 have upper limits on $W_r(2796)$ where the most stringent upper limit is 3 mÅ. To a 3σ $W_r(2796)$ thresh-

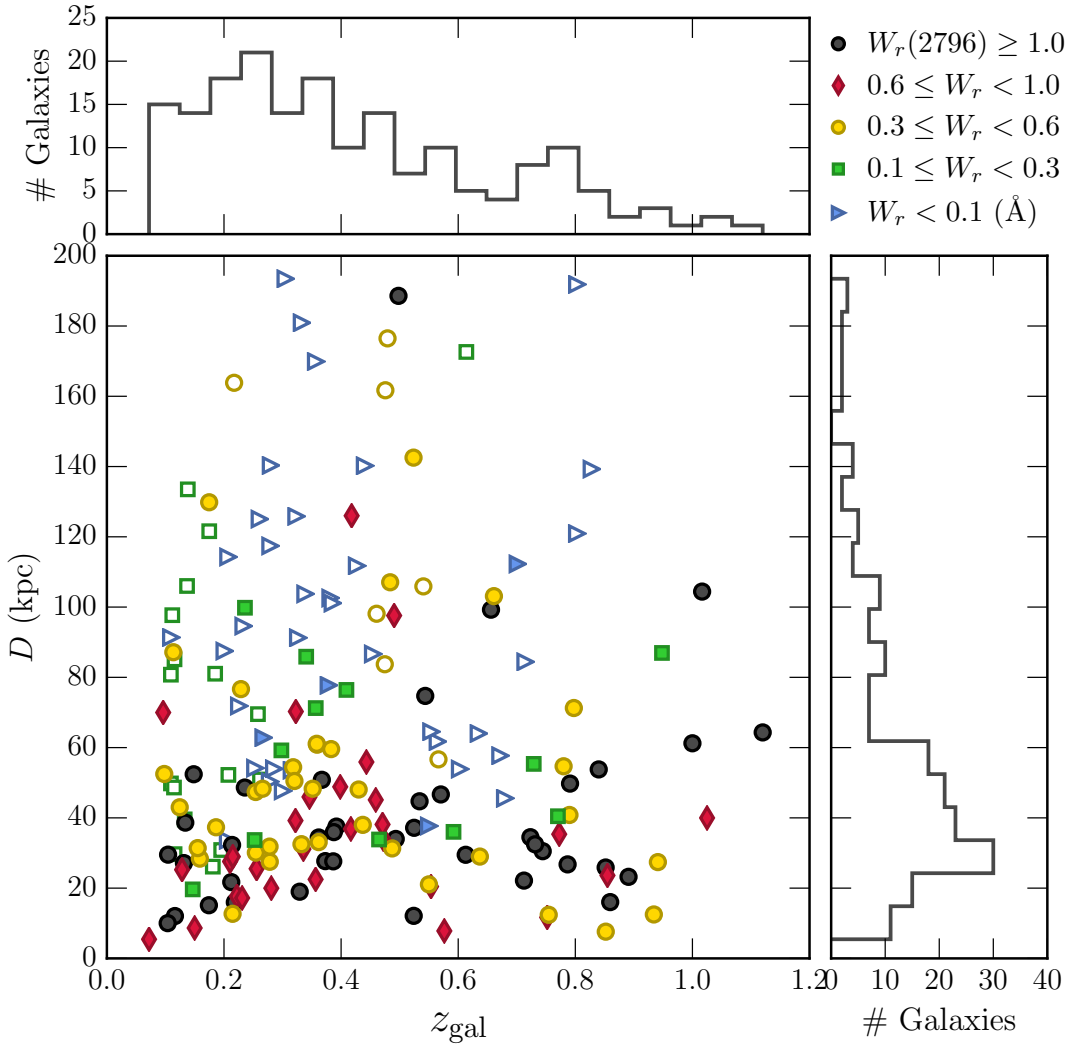

Fig. 2.2.— Quasar-galaxy impact parameter, D, as a function of galaxy redshift, $z_{\rm gal}$. Points are colored by $W_r(2796)$, with open points representing 3σ upper limits on $W_r(2796)$. Open yellow circles indicate galaxies with an upper limit of $W_r(2796) = 0.3$ Å, the largest upper limit in MAGIICAT. Histograms show the distribution of D and $z_{\rm gal}$ for the full sample.

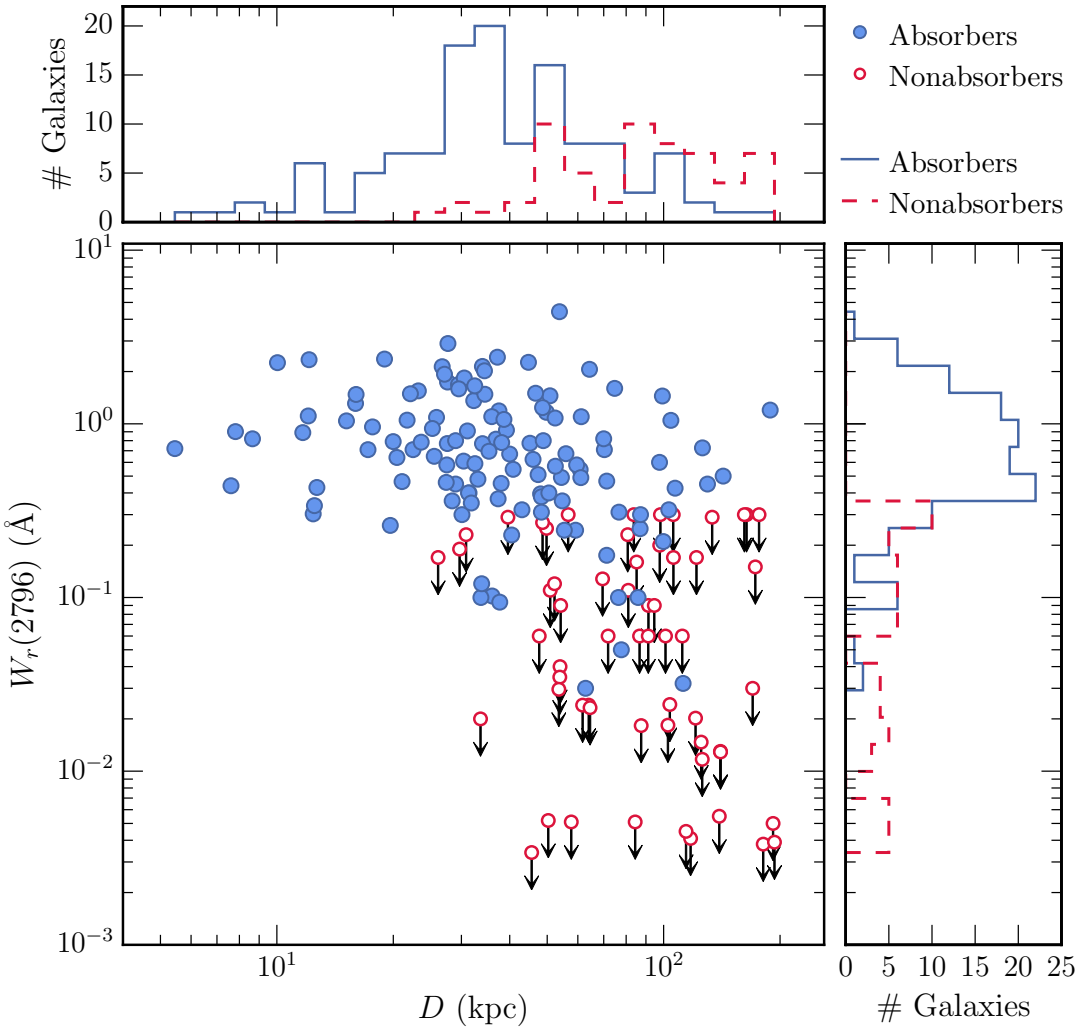

Fig. 2.3.— Rest-frame Mg II equivalent width, $W_r(2796)$, vs. impact parameter, D. Points are colored based on $W_r(2796)$ absorption, with solid blue points representing galaxies with measured absorption and red open points with downward arrows representing 3σ upper limits on $W_r(2796)$. The histograms show the D and $W_r(2796)$ distributions for absorbers (thin blue line) and an upper limit on absorption (dotted red line). The anti-correlation between $W_r(2796)$ and D is significant at the 7.9σ level.

old, MAGIICAT is 100% complete to 0.3 Å, 90% complete to 0.2 Å, 80% complete to 0.05 Å, and 70% complete to 0.01 Å.

The absolute B-band magnitudes range from $-16.1 \geq M_B \geq -23.1$. Figure 2.4(a) shows M_B as a function of $z_{\rm gal}$. Points are colored by $W_r(2796)$, with open points representing upper limits on $W_r(2796)$. Histograms show the distribution of galaxies in redshift and M_B.

Absolute K-band magnitudes range from $-17.0 \geq M_K \geq -25.3$. Figure 2.4(b) presents M_K against $z_{\rm gal}$. Points are colored by $W_r(2796)$, with upper limits on $W_r(2796)$ shown as open points. Histograms present the distribution of redshift and M_K of the sample.

The completeness limits of the magnitudes are complicated due to the heterogeneous imaging campaigns described in section 2.2.1. For the B-band, the majority of galaxies at low redshift ($z < \langle z \rangle$, where $\langle z \rangle = 0.359$ is the median redshift of the sample) were selected by SDSS r magnitudes with a limiting magnitude of $r = 22$. However, we used the SDSS g band for these galaxies to calculate M_B, which is sensitive to the threshold $g \simeq 23$ (AB magnitude; dotted line in Figure 2.4(a)). At the mean redshift of the low redshift subsample, $z = 0.23$, this corresponds to $M_B \simeq -17.5$. The majority of galaxies at high redshift ($z \geq \langle z \rangle$) were imaged in the F702W-band. This subsample has a threshold of F702W $\simeq 24$ (Vega magnitude; dashed line in Figure 2.4(a)), corresponding to $M_B \simeq -18$ at the mean redshift, $z = 0.61$.

In the infrared, the galaxy magnitudes are generally sensitive to the threshold $K_s \simeq 21$ (Vega magnitude), with the exception of the extensive campaign on the field 1622+268 (Steidel97) which is sensitive to $K_s \simeq 22$ (Vega magnitude; dashed

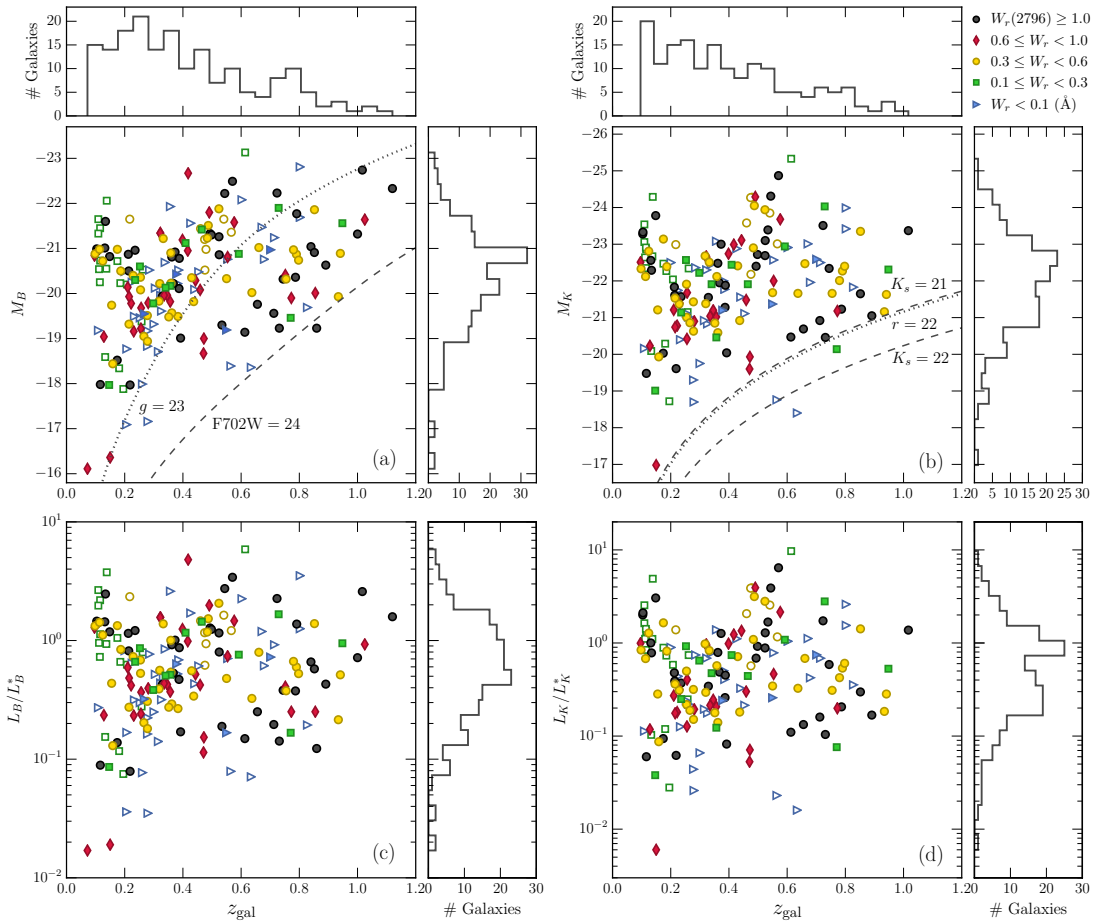

Fig. 2.4.— Galaxy luminous properties, M_B, M_K, L_B/L_B^*, and L_K/L_K^*, as a function of redshift. Point types indicate the strength of Mg II absorption, $W_r(2796)$. Open points represent upper limits on absorption. The distributions of redshift and luminous properties are shown in histograms along the respective axes. (a) The B-band AB absolute magnitude, M_B, as a function of galaxy redshift, $z_{\rm gal}$. M_B is calculated at all redshifts from apparent magnitudes of $g = 23$ (AB magnitude; dotted line) and F702W = 24 (Vega magnitude; dashed line), representing the limiting magnitudes for the surveys in which many of the galaxies were observed. The value of g comes from the Sloan Digital Sky Survey, whereas the F702W-band was observed with WFPC2 on *HST*. (b) The K-band AB absolute magnitude, M_K, vs. galaxy redshift, $z_{\rm gal}$. M_K is calculated at all redshifts from apparent K_s- and r-band magnitudes to indicate the limiting magnitudes associated with the various samples in MAGIICAT. The majority of galaxies imaged with the K_s-band have a limiting magnitude of $K_s = 21$ (Vega magnitude; dashed line), while those obtained from Steidel97 were imaged more deeply down to $K_s = 22$ (Vega magnitude; dashed line). Galaxies imaged in the r-band with SDSS have a limiting magnitude of $r = 22$ (dotted line). We translated M_r into M_K using the relationship between $B - R$ and $B - K$ colors in section 2.3.1 and Appendix C. (*c*) The B-band luminosity, L_B/L_B^*, as a function of galaxy redshift, $z_{\rm gal}$. (d) The K-band luminosity, L_K/L_K^*, vs. galaxy redshift, $z_{\rm gal}$.

lines in Figure 2.4(b)). For the high redshift subsample, $K_s \simeq 21$ corresponds $M_K \simeq -20$ at the mean redshift, $z = 0.61$. The majority of galaxies at low redshift were imaged in the r-band with SDSS. This subsample has a threshold of $r \simeq 22$ (AB magnitude; dotted line in Figure 2.4(b)), which, when converted to M_K using the conversion between $B-R$ and $B-K$, is roughly equal to $K_s \simeq 21$.

B-band luminosities have a range of $0.02 \leq L_B/L_B^* \leq 5.87$, with median $L_B/L_B^* = 0.611$. L_B/L_B^* as a function of $z_{\rm gal}$ is presented in Figure 2.4(c). Point colors represent $W_r(2796)$, with open points indicating upper limits on $W_r(2796)$. Histograms show the distributions of B-band luminosity and galaxy redshift.

Luminosities in the K-band range from $0.006 \leq L_K/L_K^* \leq 9.71$ and have a median of $L_K/L_K^* = 0.493$. K-band Luminosity as a function of $z_{\rm gal}$ is presented in Figure 2.4(d) with point colors indicating $W_r(2796)$ and upper limits on $W_r(2796)$ as open points. The distributions of L_K/L_K^* and $z_{\rm gal}$ are presented in histograms along their respective axes.

Galaxy rest-frame $B-K$ colors have a range of $0.04 \leq B-K \leq 4.09$, with median $B-K = 1.48$. $B-K$ as a function of $z_{\rm gal}$ is shown in Figure 2.5 and point colors represent $W_r(2796)$ strength, with open points indicating upper limits on $W_r(2796)$. Color and redshift distributions are shown in histograms. The mean and standard deviations in $B-K$ for three equal-sized redshift bins ($z < 0.403$, $0.403 \leq z < 0.709$, and $z \geq 0.709$) are plotted as black error bars. Horizontal error bars indicate the range in redshift for each bin. The horizontal dashed lines indicate the rest-frame $B-K$ color for each SED, where all three redshift bins are consistent with an Sbc galaxy. This is in agreement with SDP94 and Zibetti et al. (2007), who find that galaxies with Mg II absorption have, on average, an

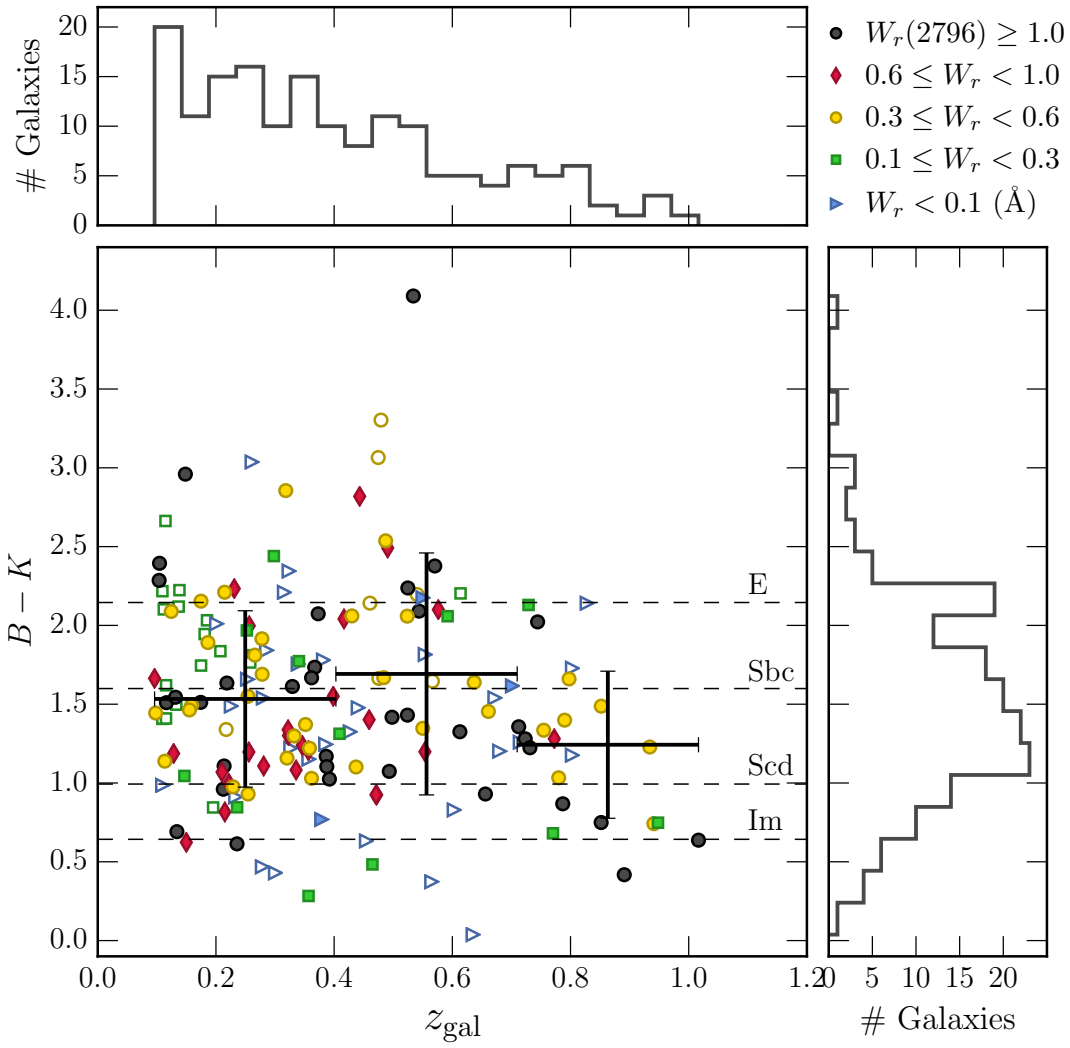

Fig. 2.5.— Rest-frame galaxy color, $B-K$, against galaxy redshift, $z_{\rm gal}$. Points are colored by $W_r(2796)$, with open points representing upper limits on $W_r(2796)$. The dashed lines mark the rest-frame $B-K$ colors for the spectral energy distributions of E, Sbc, Scd, and Im galaxies. Crosses indicate the average color in three redshift bins ($z < 0.403$, $0.403 \leq z < 0.709$, and $z \geq 0.709$). Horizontal error bars show the range in redshift for each bin while vertical error bars are the standard deviations in $B-K$ for each bin. The average colors in all three redshift bins are consistent with an Sbc galaxy. Color and redshift distributions for MAGIICAT are presented as histograms. From the color histogram, the most common galaxy type is slightly redder than an Scd galaxy.

Sbc SED type. The most common galaxy color is slightly redder than an Scd SED type.

Table 2.3 presents calculated galaxy and absorption properties for galaxies in MAGIICAT. The listed columns are the (1) QSO identifier, (2) Julian 2000 designation (J-Name), (3) galaxy spectroscopic redshift, $z_{\rm gal}$, (4) Mg II absorption redshift, $z_{\rm abs}$, (5) Mg II equivalent width, $W_r(2796)$, (6) Mg II doublet ratio, (7) reference for columns 4, 5, and 6, (8) quasar-galaxy impact parameter, D, (9) K-correction to obtain M_B, (10) absolute B-band magnitude, M_B, (11) B-band luminosity, L_B/L_B^*, (12) K-correction to obtain M_K, (13) absolute K-band magnitude, M_K, (14) K-band luminosity, L_K/L_K^*, and (15) rest-frame color, $B-K$.

A summary of the absorption and galaxy properties of MAGIICAT is presented in Table 2.4. We list the minimum, maximum, mean, and median values for each property.

Table 2.3. Calculated Galaxy and Absorption Properties

			Mg II Absorption					B-band			K-band			
(1) QSO	(2) J-Name	(3) $z_{\rm gal}$	(4) $z_{\rm abs}$	(5) $W_r(2796)$ Å	(6) DR	(7) Ref[a]	(8) D (kpc)	(9) K_{By}[b]	(10) M_B[c]	(11) L_B/L_B^*	(12) K_{Ky}[d]	(13) M_K[c]	(14) L_K/L_K^*	(15) $B-K$
0002−422	J000448.11−415728.8	0.840	0.836627	4.422 ± 0.002	1.12 ± 0.09	13	53.8	−0.08	−21.04	0.66	···	···	···	···
0002+051	J000520.21+052411.80	0.298	0.298059	0.244 ± 0.003	1.336 ± 0.029	3	59.2	−1.39	−19.78	0.38	−0.52	−22.22	0.64	2.43
0002+051	J000520.21+052411.80	0.592	0.591365	0.102 ± 0.002	1.539 ± 0.039	3	36.0	−0.80	−20.88	0.76	−0.53	−22.94	1.08	2.05
0002+051	J000520.21+052411.80	0.85180	0.851393	1.089 ± 0.008	1.160 ± 0.013	3	25.9	−0.64	−20.91	0.58	−0.88	−21.65	0.29	0.74
SDSS	J003340.21−005525.53	0.2124	0.2121	1.05 ± 0.03	···	6	21.7	0.20	−20.87	1.15	0.06	−21.83	0.47	0.96
SDSS	J003407.34−085452.07	0.3617	0.3616	0.48 ± 0.05	···	6	33.1	0.54	−19.57	0.29	0.13	−20.59	0.14	1.02
SDSS	J003413.04−010026.86	0.2564	0.2564	0.61 ± 0.06	···	6	30.4	0.80	−19.68	0.37	0.43	−21.68	0.40	1.99
0058+019	J010054.15+021136.52	0.6128	0.612586	1.684 ± 0.004	1.06 ± 0.09	13	29.5	−0.40	−19.14	0.15	−0.59	−20.47	0.11	1.32
0058+019	J010054.15+021136.52	0.680	0.680	< 0.0034	···	2	45.6	−0.34	−20.76	0.61	−0.63	−21.96	0.42	1.20
SDSS	J010135.84−005009.08	0.2615	0.2615	< 0.11	···	6	50.9	0.82	−20.53	0.80	0.44	−22.34	0.74	1.81
SDSS	J010156.32−084401.74	0.1588	0.1586	0.36 ± 0.03	···	6	28.4	0.11	−18.44	0.13	0.14	−19.93	0.08	1.49
SDSS	J010352.47+003739.79	0.3515	0.3508	0.38 ± 0.03	···	6	48.3	0.71	−19.48	0.27	0.27	−20.85	0.17	1.37
0102−190	J010516.82−184641.9	1.025	1.0262	0.67 ± 0.05	0.971 ± 0.1	1	40.0	0.28	−21.64	0.93	···	···	···	···
0109+200	J011210.18+202021.79	0.534	0.5346	2.26 ± 0.05	1.32 ± 0.09	3	44.7	−0.95	−19.30	0.19	−0.51	−23.39	1.68	4.09
0117+213	J012017.20+213346.00	0.5763	0.576398	0.902 ± 0.007	1.070 ± 0.01	13	7.8	−0.40	−21.58	1.47	−0.52	−23.68	2.14	2.09
0117+213	J012017.20+213346.00	0.729	0.729077	0.244 ± 0.005	1.839 ± 0.088	3	55.4	−0.38	−21.90	1.67	−0.59	−24.03	2.79	2.12
0122−003	J012528.84−000555.93	0.3788	0.3791	0.05 ± 0.01	···	5	77.7	−0.52	−20.43	0.64	−0.58	−21.20	0.24	0.76
0141+339	J014411.70+341157.92	0.4708	0.4708	0.78 ± 0.07	1.200 ± 0.17	7	38.1	−0.57	−18.67	0.11	−0.57	−19.60	0.05	0.92
0150−202	J015227.32−200107.10	0.383	0.3887	0.58 ± 0.05	1.81 ± 0.09	3	59.6	−1.02	−19.49	0.27	···	···	···	···
0150−202	J015227.32−200107.10	0.603	0.603	< 0.0348	···	2	53.9	−0.47	−22.08	2.25	−0.61	−22.91	1.04	0.82
0150−202	J015227.32−200107.10	0.780	0.780	0.36 ± 0.04	1.710 ± 0.38	7	54.7	−0.14	−20.97	0.67	−0.70	−22.01	0.42	1.03
SDSS	J015453.03−095535.39	0.5663	0.5663	< 0.30	···	11	56.7	1.27	−21.36	1.21	0.64	−23.01	1.16	1.64
SDSS	J021558.40−011135.79	0.2103	0.2108	0.77 ± 0.05	···	6	27.6	0.20	−20.14	0.59	0.05	−21.21	0.27	1.06
0226−4110	J022815.2-405716	0.2067	0.2067	< 0.02	···	5	33.6	−0.75	−17.09	0.04	···	···	···	···

Table 2.3 (continued)

			Mg II Absorption					B-band			K-band			
(1) QSO	(2) J-Name	(3) $z_{\rm gal}$	(4) $z_{\rm abs}$	(5) $W_r(2796)$ Å	(6) DR	(7) Ref[a]	(8) D (kpc)	(9) K_{By}[b]	(10) M_B[c]	(11) L_B/L_B^*	(12) K_{Ky}[d]	(13) M_K[c]	(14) L_K/L_K^*	(15) $B-K$
0226−4110	J022815.2-405716	0.2674	0.2678	0.03 ± 0.01	···	5	62.8	−0.72	−19.55	0.32	···	···	···	···
SDSS	J022950.32−074256.77	0.3866	0.3861	1.74 ± 0.04	···	6	27.6	0.59	−20.11	0.47	0.16	−21.28	0.25	1.16
0229+131	J023145.89+132254.71	0.4167	0.417338	0.816 ± 0.02	1.163 ± 0.042	3	36.9	−1.21	−20.95	0.99	−0.52	−22.99	1.23	2.04
0235+164	J023838.93+163659.27	0.524	0.524	2.34 ± 0.05	1.06 ± 0.09	3	12.1	−0.90	−21.26	1.16	−0.56	−22.69	0.88	1.43
0235+164	J023838.93+163659.27	0.852	0.852	0.44 ± 0.05	···	7	7.6	0.12	−21.86	1.39	−0.69	−23.35	1.41	1.48
0302−223	J030450.10−221157.00	0.418	0.42041	0.727 ± 0.028	1.154 ± 0.063	14	126.0	−0.81	−22.67	4.80	···	···	···	···
0302−223	J030450.10−221157.00	1.000	1.009382	1.099 ± 0.036	1.100 ± 0.04	13	61.2	0.24	−21.32	0.72	···	···	···	···
SDSS	J032232.58+003649.13	0.2185	0.2183	1.31 ± 0.12	···	6	16.0	0.28	−17.97	0.08	0.18	−19.61	0.06	1.63
0334−204	J033626.90−201940.00	1.120	1.1174	2.06 ± 0.05	1.177 ± 0.04	1	64.3	0.44	−22.33	1.59	···	···	···	···
0349−146	J035128.54−142908.71	0.3236	0.3236	< 0.0117	···	2	125.8	−1.36	−19.96	0.44	−0.47	−22.30	0.68	2.34
0349−146	J035128.54−142908.71	0.3567	0.357168	0.175 ± 0.007	1.171 ± 0.069	3	71.3	−0.87	−20.17	0.52	−0.56	−20.46	0.12	0.28
SDSS	J035242.12+001307.32	0.3671	0.3677	1.45 ± 0.05	···	6	50.8	1.30	−20.22	0.53	0.66	−21.95	0.48	1.73
0454−220	J045608.92−215909.40	0.2784	0.2784	< 0.0052	···	2	50.3	−0.85	−18.83	0.16	−0.50	−19.30	0.04	0.46
0454−220	J045608.92−215909.40	0.3818	0.3818	< 0.0184	···	2	102.6	−1.02	−20.22	0.52	−0.49	−22.00	0.50	1.78
0454−220	J045608.92−215909.40	0.48382	0.483337	0.426 ± 0.007	1.331 ± 0.037	3	107.1	−0.94	−21.23	1.18	−0.51	−22.90	1.09	1.66
0454+039	J045647.17+040052.94	0.072	0.072	0.72 ± 0.05	1.10 ± 0.09	1	5.4	−1.04	−16.11	0.02	···	···	···	···
0454+039	J045647.17+040052.94	0.201	0.201	< 0.0183	···	2	87.5	−1.15	−20.49	0.82	−0.40	−22.50	0.89	2.01
0454+039	J045647.17+040052.94	0.8596	0.859569	1.476 ± 0.009	1.030 ± 0.01	13	16.0	0.14	−19.23	0.12	···	···	···	···
SDSS	J075001.85+161305.05	0.1466	0.1469	0.26 ± 0.08	···	6	19.6	0.06	−17.97	0.09	0.05	−19.01	0.03	1.04
SDSS	J075450.04+184952.79	0.2856	0.2856	< 0.04	···	6	54.0	0.93	−20.52	0.77	0.49	−22.36	0.74	1.84
SDSS	J075525.51+172836.59	0.2541	0.2546	0.51 ± 0.02	···	6	47.4	0.38	−20.36	0.69	0.20	−21.91	0.49	1.54
SDSS	J080004.56+184935.15	0.2544	0.2536	0.30 ± 0.04	···	6	30.1	0.29	−20.08	0.53	0.07	−21.01	0.21	0.92
SDSS	J081420.19+383408.3	0.09801	0.09833	0.57 ± 0.05	2.040 ± 0.37	10	52.5	−0.62	−20.88	1.33	−0.20	−22.33	0.84	1.44
SDSS	J082340.18+074801.68	0.1864	0.1863	0.37 ± 0.04	···	6	37.3	0.45	−20.50	0.84	0.32	−22.39	0.81	1.89

Table 2.3 (continued)

			Mg II Absorption					B-band			K-band			
(1) QSO	(2) J-Name	(3) $z_{\rm gal}$	(4) $z_{\rm abs}$	(5) $W_r(2796)$ Å	(6) DR	(7) Ref[a]	(8) D (kpc)	(9) K_{By}[b]	(10) M_B[c]	(11) L_B/L_B^*	(12) K_{Ky}[d]	(13) M_K[c]	(14) L_K/L_K^*	(15) $B-K$
0827+243	J083052.08+241059.82	0.258	0.258	< 0.128	···	2	69.5	−1.08	−19.38	0.28	−0.48	−21.15	0.24	1.76
0827+243	J083052.08+241059.82	0.5247	0.524966	2.419 ± 0.012	1.041 ± 0.009	3	37.2	−0.98	−20.86	0.80	−0.51	−23.10	1.28	2.23
0836+113	J083933.01+111203.82	0.78682	0.786725	2.133 ± 0.019	1.050 ± 0.013	3	26.8	−0.56	−20.36	0.38	−0.70	−21.23	0.20	0.86
SDSS	J084119.78+012621.75	0.4091	0.4084	0.10 ± 0.02	···	6	76.4	0.89	−21.12	1.16	0.34	−22.44	0.74	1.31
SDSS	J084456.06+004708.95	0.1551	0.1554	0.40 ± 0.05	···	6	31.4	0.10	−19.74	0.44	0.14	−21.21	0.28	1.46
SDSS	J085826.93+022604.49	0.1097	0.1097	< 0.09	···	6	91.4	−0.01	−19.18	0.27	0.05	−20.16	0.11	0.98
SDSS	J090519.70+084917.32	0.1499	0.1501	0.82 ± 0.1	···	6	8.6	−0.00	−16.36	0.02	−0.04	−16.98	0.00	0.62
SDSS	J090519.70+084917.32	0.3856	0.3856	< 0.06	···	6	101.1	0.59	−20.52	0.69	0.16	−21.77	0.40	1.24
SDSS	J090519.70+084917.32	0.4545	0.4545	< 0.06	···	6	86.7	0.37	−20.48	0.61	−0.01	−21.11	0.21	0.63
SDSS	J091119.16+031152.9	0.09616	0.09636	0.82 ± 0.1	2.410 ± 0.59	10	70.0	−0.63	−20.84	1.28	−0.20	−22.51	0.99	1.66
SDSS	J091845.91+060226.09	0.1849	0.1849	< 0.11	···	6	81.0	0.45	−20.23	0.66	0.32	−22.27	0.73	2.03
SDSS	J092300.67+075108.2	0.10385	0.10423	2.25 ± 0.14	1.610 ± 0.17	10	10.0	−0.99	−20.99	1.46	−0.19	−23.28	2.00	2.28
SDSS	J093251.82+073729.11	0.3876	0.3876	1.10 ± 0.02	···	6	35.9	0.60	−20.78	0.87	0.16	−21.88	0.45	1.10
SDSS	J093536.98+112408.03	0.2808	0.2811	0.79 ± 0.04	···	6	20.0	0.35	−19.79	0.40	0.07	−20.90	0.19	1.10
SDSS	J100807.51+014448.97	0.2173	0.2173	< 0.30	···	6	163.8	0.28	−21.65	2.34	0.17	−22.99	1.38	1.33
SDSS	J100906.36+023555.31	0.2523	0.2521	0.10 ± 0.01	···	6	33.7	0.78	−20.60	0.86	0.42	−22.57	0.92	1.96
SDSS	J102218.98+013218.82	0.1369	0.1369	< 0.17	···	6	106.0	0.19	−20.55	0.94	0.26	−22.67	1.10	2.11
1019+309	J102230.29+304105.11	0.346	0.346247	0.624 ± 0.017	1.484 ± 0.068	14	46.0	−0.98	−19.96	0.43	−0.56	−21.20	0.24	1.23
SDSS	J102751.62+104532.61	0.1093	0.1093	< 0.23	···	12	80.8	−0.62	−21.65	2.66	−0.22	−23.06	1.63	1.40
SDSS	J102847.00+391800.5	0.11348	0.11411	0.30 ± 0.02	2.230 ± 0.36	10	87.2	−0.01	−20.98	1.42	0.05	−22.12	0.68	1.13
SDSS	J103607.51+015659.14	0.3571	0.3571	< 0.03	···	6	169.9	0.53	−21.93	2.60	0.12	−23.08	1.38	1.15
SDSS	J103836.50+095138.85	0.1742	0.1744	1.04 ± 0.06	···	6	15.1	0.16	−18.52	0.14	0.15	−20.03	0.09	1.51
1038+064	J104117.16+061016.92	0.3157	0.3157	< 0.0296	···	2	53.6	−1.02	−18.71	0.14	−0.53	−20.92	0.19	2.20
1038+064	J104117.16+061016.92	0.4432	0.441453	0.673 ± 0.011	1.338 ± 0.041	3	55.9	−1.16	−20.29	0.52	−0.51	−23.11	1.35	2.81

Table 2.3 (continued)

			Mg II Absorption					B-band			K-band			
(1) QSO	(2) J-Name	(3) $z_{\rm gal}$	(4) $z_{\rm abs}$	(5) $W_r(2796)$ Å	(6) DR	(7) Ref[a]	(8) D (kpc)	(9) K_{By}[b]	(10) M_B[c]	(11) L_B/L_B^*	(12) K_{Ky}[d]	(13) M_K[c]	(14) L_K/L_K^*	(15) $B-K$
SDSS	J104935.99+075813.74	0.4793	0.4793	< 0.30	···	11	176.5	1.62	−20.98	0.94	1.09	−24.28	3.91	3.30
SDSS	J105033.08−001354.84	0.1155	0.1155	< 0.16	···	12	85.1	−0.62	−21.45	2.19	−0.24	−22.86	1.34	1.40
1100−264	J110325.29−264515.7	0.359	0.358989	0.545 ± 0.001	1.255 ± 0.004	14	60.8	−0.86	−20.23	0.54	···	···	···	···
SDSS	J111342.42−000730.80	0.1094	0.1094	< 0.25	···	12	49.8	−0.98	−21.33	1.97	−0.20	−23.54	2.54	2.21
SDSS	J111850.13−002100.7	0.13159	0.13158	1.93 ± 0.08	1.060 ± 0.06	10	27.1	0.05	−21.01	1.44	0.13	−22.56	1.00	1.54
SDSS	J112016.66+093323.53	0.4933	0.4933	2.14 ± 0.03	···	6	34.0	0.77	−21.33	1.28	0.30	−22.40	0.68	1.07
SDSS	J112613.52+352002.60	0.1117	0.1117	< 0.20	···	12	97.7	−0.98	−20.54	0.96	−0.21	−22.64	1.10	2.10
1127−145	J113007.05−144927.38	0.20735	0.20735	< 0.0045	···	2	114.3	−1.51	−18.77	0.17	···	···	···	···
1127−145	J113007.05−144927.38	0.27921	0.27921	< 0.0041	···	2	117.4	−1.48	−19.17	0.22	···	···	···	···
1127−145	J113007.05−144927.38	0.30515	0.30515	< 0.0039	···	2	193.5	−1.47	−20.12	0.52	···	···	···	···
1127−145	J113007.05−144927.38	0.33293	0.33293	< 0.0038	···	9	180.9	−1.45	−20.09	0.49	···	···	···	···
SDSS	J113757.02+085017.21	0.3356	0.336	0.91 ± 0.06	···	6	31.1	0.49	−19.96	0.43	0.10	−21.04	0.21	1.08
SDSS	J114144.62+080614.79	0.2290	0.2286	0.31 ± 0.03	···	6	76.7	0.24	−20.40	0.73	0.06	−21.37	0.31	0.97
SDSS	J114144.62+080614.79	0.3583	0.3585	0.49 ± 0.02	···	6	61.1	0.73	−20.90	1.00	0.28	−22.12	0.57	1.22
SDSS	J114444.63+071443.75	0.4906	0.4906	0.60 ± 0.1	···	11	97.6	1.66	−21.80	1.98	1.14	−24.29	3.92	2.49
SDSS	J114518.47+451601.4	0.13389	0.13402	1.06 ± 0.06	0.990 ± 0.07	10	38.6	−0.36	−21.60	2.47	−0.29	−22.29	0.78	0.69
SDSS	J114657.91+020712.69	0.5437	0.5437	1.60 ± 0.2	···	11	74.7	1.85	−22.22	2.74	1.38	−24.31	3.89	2.09
SDSS	J114803.17+565411.4	0.10451	0.10433	1.59 ± 0.06	1.270 ± 0.07	10	29.5	−0.99	−20.94	1.39	−0.19	−23.33	2.10	2.39
1148+387	J115129.37+382552.35	0.5536	0.553363	0.64 ± 0.013	1.749 ± 0.067	3	20.4	−0.87	−20.81	0.74	−0.59	−22.00	0.46	1.19
SDSS	J120932.26+004555.92	0.2533	0.2533	< 0.09	···	6	54.2	0.78	−19.46	0.30	0.42	−21.12	0.24	1.65
1209+107	J121140.59+103002.02	0.392	0.392924	1.187 ± 0.005	1.437 ± 0.012	3	37.5	−0.97	−19.01	0.17	−0.56	−20.04	0.08	1.02
1222+228	J122527.39+223513.0	0.5502	0.550198	0.094 ± 0.009	1.562 ± 0.242	3	37.7	−0.91	−19.19	0.17	−0.51	−21.37	0.25	2.17
1229−021	J123200.01−022405.27	0.7546	0.756903	0.303 ± 0.003	1.280 ± 0.02	13	12.4	−0.12	−20.32	0.38	−0.66	−21.66	0.31	1.33
1241+176	J124410.82+172104.52	0.550	0.550482	0.465 ± 0.011	1.290 ± 0.043	3	21.1	−0.87	−20.33	0.48	−0.57	−21.68	0.34	1.34

Table 2.3 (continued)

			Mg II Absorption					B-band			K-band			
(1) QSO	(2) J-Name	(3) $z_{\rm gal}$	(4) $z_{\rm abs}$	(5) $W_r(2796)$ Å	(6) DR	(7) Ref[a]	(8) D (kpc)	(9) K_{By}[b]	(10) M_B[c]	(11) L_B/L_B^*	(12) K_{Ky}[d]	(13) M_K[c]	(14) L_K/L_K^*	(15) $B-K$
1245+345	J124727.83+341509.56	0.941	0.941	0.46 ± 0.04	1.210 ± 0.17	7	27.4	−0.15	−20.89	0.51	−0.94	−21.63	0.28	0.74
1246−057	J124913.85−055919.07	0.637	0.639909	0.450 ± 0.004	1.178 ± 0.016	3	29.0	−0.75	−20.02	0.33	−0.61	−21.66	0.32	1.63
1248+401	J125048.32+395139.48	0.7725	0.772957	0.695 ± 0.005	1.280 ± 0.02	13	35.4	−0.15	−19.90	0.25	−0.69	−21.18	0.19	1.28
1254+047	J125659.92+042734.39	0.9341	0.934231	0.338 ± 0.005	1.500 ± 0.04	13	12.5	0.32	−19.93	0.21	−0.72	−21.16	0.18	1.22
SDSS	J125739.22+144806.26	0.4648	0.4644	0.12 ± 0.02	···	6	33.8	0.38	−21.42	1.44	−0.01	−21.91	0.44	0.48
SDSS	J130554.17+014929.82	0.1747	0.174	0.45 ± 0.03	···	6	129.8	0.39	−20.98	1.33	0.30	−23.14	1.64	2.15
SDSS	J130554.17+014929.82	0.2258	0.2258	< 0.06	···	6	71.9	0.30	−20.25	0.64	0.18	−21.74	0.43	1.48
SDSS	J131815.12+012450.67	0.5405	0.5405	< 0.30	···	11	105.9	1.84	−21.65	1.64	1.36	−23.85	2.55	2.19
1317+277	J131956.23+272808.22	0.6610	0.660049	0.320 ± 0.006	1.611 ± 0.057	3	103.1	−0.72	−21.02	0.80	−0.62	−22.47	0.68	1.45
1317+277	J131956.23+272808.22	0.6719	0.6719	< 0.0051	···	2	57.7	−0.70	−21.47	1.19	−0.62	−23.01	1.11	1.54
1321+294	J132320.55+291007.15	0.231	0.231	0.71 ± 0.05	···	7	17.2	−1.06	−19.16	0.23	−0.45	−21.39	0.31	2.23
SDSS	J132757.41+101141.78	0.2557	0.2553	0.65 ± 0.04	···	6	25.5	0.29	−19.22	0.24	0.07	−20.42	0.12	1.19
SDSS	J132831.08+075942.01	0.2358	0.2362	0.21 ± 0.05	···	6	99.8	0.09	−20.30	0.66	−0.09	−21.14	0.25	0.84
SDSS	J132831.08+075942.01	0.3323	0.3326	0.59 ± 0.04	···	6	32.5	0.65	−21.22	1.38	0.25	−22.51	0.83	1.29
1331+170	J133335.78+164904.01	0.7443	0.744642	1.836 ± 0.003	1.30 ± 0.09	13	30.5	0.26	−20.32	0.38	−0.59	−22.34	0.58	2.02
1332+552	J133411.70+550124.98	0.373	0.374	2.90 ± 0.05	1.00 ± 0.09	3	27.7	−1.28	−20.92	1.01	−0.53	−23.00	1.26	2.07
1354+195	J135704.43+191907.37	0.44060	0.4406	< 0.013	···	2	140.2	−0.98	−20.09	0.43	−0.50	−21.56	0.32	1.47
1354+195	J135704.43+191907.37	0.4592	0.456598	0.773 ± 0.015	1.333 ± 0.044	3	45.1	−0.97	−20.08	0.42	−0.55	−21.48	0.30	1.40
1354+195	J135704.43+191907.37	0.8031	0.8031	< 0.005	···	2	191.8	0.22	−21.69	1.26	−0.61	−23.42	1.54	1.72
SDSS	J140619.61+130106.82	0.1748	0.1748	< 0.17	···	6	121.6	0.16	−20.72	1.05	0.15	−22.47	0.89	1.74
SDSS	J140619.61+130106.82	0.2220	0.2222	0.96 ± 0.06	···	6	17.7	0.22	−19.78	0.42	0.06	−20.78	0.18	0.99
SDSS	J140843.77+004730.46	0.1146	0.1146	< 0.27	···	12	48.6	−0.97	−20.25	0.73	−0.21	−22.91	1.41	2.66
SDSS	J141654.33−000520.35	0.4746	0.4746	< 0.30	···	11	83.7	1.61	−21.20	1.16	1.07	−24.27	3.87	3.06
SDSS	J142310.50+093357.14	0.6139	0.6139	< 0.15	···	11	172.6	2.14	−23.13	5.87	1.65	−25.33	9.71	2.20

Table 2.3 (continued)

			Mg II Absorption					B-band			K-band			
(1) QSO	(2) J-Name	(3) $z_{\rm gal}$	(4) $z_{\rm abs}$	(5) $W_r(2796)$ Å	(6) DR	(7) Ref[a]	(8) D (kpc)	(9) K_{By}[b]	(10) M_B[c]	(11) L_B/L_B^*	(12) K_{Ky}[d]	(13) M_K[c]	(14) L_K/L_K^*	(15) $B-K$
SDSS	J142556.40−001818.79	0.1382	0.1382	< 0.29	···	6	133.5	0.20	−22.06	3.76	0.26	−24.29	4.90	2.22
1424−118	J142738.10−120350.00	0.3404	0.341716	0.100 ± 0.015	1.869 ± 0.394	3	85.9	−1.05	−20.13	0.51	−0.49	−21.91	0.47	1.77
SDSS	J143216.78+095519.29	0.3293	0.3296	2.36 ± 0.04	···	6	19.0	0.64	−19.94	0.43	0.25	−21.55	0.34	1.61
SDSS	J150339.98+064259.96	0.1809	0.1809	< 0.17	···	6	26.1	0.43	−18.34	0.12	0.31	−20.29	0.11	1.94
SDSS	J150339.98+064259.96	0.2333	0.2333	< 0.09	···	6	94.6	0.25	−19.49	0.32	0.06	−20.40	0.12	0.91
SDSS	J151228.82−011223.12	0.1284	0.1284	0.94 ± 0.16	···	6	25.2	0.02	−19.04	0.23	0.05	−20.23	0.11	1.18
1511+103	J151329.29+101105.54	0.437	0.4369	0.454 ± 0.046	1.29 ± 0.09	3	38.0	−0.95	−19.82	0.34	−0.57	−20.92	0.18	1.10
SDSS	J151541.23+334739.49	0.1156	0.1156	< 0.19	···	12	29.7	−0.62	−20.73	1.13	−0.24	−22.35	0.84	1.62
SDSS	J153112.98+091138.78	0.2659	0.266	0.31 ± 0.03	···	6	48.3	0.42	−19.05	0.20	0.21	−20.86	0.18	1.81
SDSS	J153112.98+091138.78	0.3265	0.3265	< 0.06	···	6	91.3	0.46	−19.61	0.32	0.09	−20.83	0.17	1.22
SDSS	J153715.34+023049.73	0.2151	0.2151	0.80 ± 0.02	···	6	29.0	0.06	−19.93	0.48	−0.08	−20.74	0.17	0.81
1548+092	J155103.39+090849.25	0.339	0.339	< 0.0242	···	2	103.8	−0.98	−20.69	0.85	−0.53	−22.45	0.77	1.75
1548+092	J155103.39+090849.25	0.554	0.554	< 0.0232	···	2	64.5	−0.55	−20.76	0.71	−0.51	−22.57	0.78	1.81
1548+092	J155103.39+090849.25	0.7703	0.770643	0.229 ± 0.018	1.117 ± 0.129	14	40.5	−0.34	−19.46	0.17	−0.83	−20.14	0.07	0.68
1548+092	J155103.39+090849.25	0.803	0.803	< 0.0202	···	2	120.9	−0.11	−22.81	3.52	−0.67	−23.99	2.60	1.17
SDSS	J155336.46+053423.97	0.3227	0.324	0.71 ± 0.01	···	6	70.3	0.61	−21.34	1.57	0.25	−22.64	0.94	1.30
SDSS	J155557.07−003608.41	0.3006	0.3006	< 0.06	···	6	47.7	0.17	−19.32	0.25	−0.11	−19.75	0.06	0.42
SDSS	J160726.77+471251.37	0.4980	0.498	1.20 ± 0.2	···	11	188.6	1.12	−21.30	1.24	0.50	−22.72	0.92	1.41
SDSS	J160749.34−002219.86	0.3985	0.3993	0.80 ± 0.01	···	6	48.8	0.86	−21.19	1.25	0.32	−22.74	0.98	1.55
SDSS	J160905.42+071337.29	0.2075	0.2075	< 0.12	···	6	52.2	0.25	−20.20	0.63	0.17	−22.04	0.58	1.83
SDSS	J161714.12+243255.63	0.5703	0.5703	1.50 ± 0.3	···	11	46.7	1.95	−22.49	3.41	1.49	−24.87	6.43	2.37
SDSS	J161940.56+254323.0	0.12438	0.12501	0.32 ± 0.03	1.120 ± 0.18	10	43.0	−0.95	−20.72	1.11	−0.23	−22.81	1.27	2.08
1622+238	J162439.08+234512.20	0.261	0.261	< 0.0147	···	2	125.0	−1.43	−17.99	0.08	−0.48	−21.02	0.22	3.03
1622+238	J162439.08+234512.20	0.2800	0.280	< 0.0129	···	14	140.3	−0.72	−17.16	0.04	−0.51	−18.70	0.02	1.53

Table 2.3 (continued)

			Mg II Absorption					B-band			K-band			
(1) QSO	(2) J-Name	(3) $z_{\rm gal}$	(4) $z_{\rm abs}$	(5) $W_r(2796)$ Å	(6) DR	(7) Ref[a]	(8) D (kpc)	(9) K_{By}[b]	(10) M_B[c]	(11) L_B/L_B^*	(12) K_{Ky}[d]	(13) M_K[c]	(14) L_K/L_K^*	(15) $B-K$
1622+238	J162439.08+234512.20	0.3181	0.317597	0.491 ± 0.010	1.230 ± 0.044	3	54.4	−1.36	−19.83	0.39	−0.53	−22.68	0.97	2.85
1622+238	J162439.08+234512.20	0.4720	0.471930	0.769 ± 0.006	1.187 ± 0.016	3	34.0	−0.93	−19.00	0.15	−0.57	−19.93	0.07	0.92
1622+238	J162439.08+234512.20	0.565	0.565	< 0.024	···	2	61.7	−0.86	−18.39	0.08	−0.71	−18.76	0.02	0.37
1622+238	J162439.08+234512.20	0.635	0.635	< 0.024	···	2	64.0	−0.83	−18.36	0.07	−0.74	−18.40	0.01	0.03
1622+238	J162439.08+234512.20	0.6560	0.656106	1.446 ± 0.006	1.098 ± 0.007	3	99.3	−0.75	−19.76	0.25	−0.64	−20.69	0.13	0.93
1622+238	J162439.08+234512.20	0.7016	0.702902	0.032 ± 0.003	1.607 ± 0.27	3	112.3	−0.65	−20.97	0.72	−0.64	−22.59	0.74	1.61
1622+238	J162439.08+234512.20	0.7975	0.797078	0.468 ± 0.008	1.617 ± 0.049	3	71.3	−0.47	−20.74	0.53	−0.67	−22.40	0.60	1.66
1622+238	J162439.08+234512.20	0.8280	0.828	< 0.0055	···	14	139.3	0.30	−19.69	0.19	−0.62	−21.83	0.35	2.14
1622+238	J162439.08+234512.20	0.8909	0.891276	1.548 ± 0.004	1.093 ± 0.005	3	23.2	−0.61	−20.63	0.43	−0.91	−21.05	0.16	0.41
1704+710	J170426.08+705734.7	0.7123	0.7123	1.49 ± 0.05	···	7	22.1	−0.21	−19.56	0.20	−0.64	−20.92	0.16	1.35
2000−330	J200324.11−325145.13	0.791	0.791669	1.165 ± 0.002	1.159 ± 0.003	14	49.8	−0.19	−21.77	1.38	···	···	···	···
SDSS	J204303.55−010126.05	0.1329	0.1329	< 0.29	···	6	39.6	0.05	−18.59	0.15	0.13	−20.09	0.10	1.49
SDSS	J204303.55−010126.05	0.2356	0.235	1.24 ± 0.05	···	6	48.6	0.09	−20.96	1.21	−0.09	−21.57	0.37	0.61
SDSS	J210230.72+094125.08	0.3565	0.3563	0.71 ± 0.04	···	6	22.5	0.73	−19.82	0.37	0.28	−21.02	0.20	1.20
SDSS	J211626.32−062437.44	0.5237	0.5237	0.50 ± 0.1	···	11	142.5	1.77	−21.88	2.06	1.29	−23.94	2.80	2.05
SDSS	J212938.59−063801.85	0.2782	0.2779	0.58 ± 0.03	···	6	27.5	0.46	−18.94	0.18	0.21	−20.63	0.15	1.69
2128−123	J213135.26−120704.79	0.430	0.429735	0.395 ± 0.01	1.166 ± 0.047	3	48.1	−1.18	−20.35	0.56	−0.51	−22.41	0.71	2.06
2145+067	J214805.45+065738.60	0.790	0.790866	0.547 ± 0.005	1.520 ± 0.02	13	40.8	−0.19	−20.87	0.60	−0.67	−22.27	0.53	1.39
2206−199	J220852.07−194359.0	0.752	0.751923	0.890 ± 0.002	1.10 ± 0.09	13	11.7	−0.13	−20.41	0.41	···	···	···	···
2206−199	J220852.07−194359.0	0.948	0.948361	0.249 ± 0.002	1.331 ± 0.015	3	86.9	−0.56	−21.56	0.95	−0.07	−22.31	0.52	0.74
2206−199	J220852.07−194359.0	1.01655	1.017038	1.047 ± 0.003	1.143 ± 0.005	3	104.4	−0.50	−22.74	2.59	−0.07	−23.37	1.37	0.63
SDSS	J221126.76+124458.16	0.4872	0.484	0.40 ± 0.02	···	6	31.3	1.65	−21.51	1.53	1.13	−24.05	3.15	2.53
SDSS	J221526.74+011356.47	0.1952	0.1952	< 0.23	···	6	30.9	0.04	−17.88	0.07	−0.07	−18.72	0.02	0.84
SDSS	J221526.74+011356.47	0.3203	0.3201	0.40 ± 0.05	···	6	50.5	0.45	−20.22	0.56	0.09	−21.38	0.29	1.15

Table 2.3 (continued)

(1) QSO	(2) J-Name	(3) $z_{\rm gal}$	Mg II Absorption (4) $z_{\rm abs}$	(5) $W_r(2796)$ Å	(6) DR	(7) Ref[a]	(8) D (kpc)	B-band (9) K_{By}[b]	(10) M_B[c]	(11) L_B/L_B^*	K-band (12) K_{Ky}[d]	(13) M_K[c]	(14) L_K/L_K^*	(15) $B-K$
SDSS	J223246.80+134702.04	0.3221	0.3225	0.92 ± 0.05	···	6	39.2	0.61	−21.34	1.56	0.25	−22.67	0.96	1.33
SDSS	J223316.87+133309.90	0.2138	0.2139	1.36 ± 0.06	···	6	32.3	0.20	−20.50	0.82	0.06	−21.61	0.39	1.10
SDSS	J223359.93−003315.79	0.1162	0.1162	1.11 ± 0.09	···	6	12.1	0.01	−17.98	0.09	0.12	−19.48	0.06	1.50
2231−002	J223408.99+000001.69	0.8549	0.855069	0.784 ± 0.004	1.310 ± 0.02	13	23.6	0.13	−20.01	0.25	···	···	···	···
SDSS	J224704.78−081617.54	0.4270	0.427	< 0.06	···	6	111.7	0.94	−21.56	1.71	0.36	−22.88	1.11	1.32
SDSS	J225036.72+000759.49	0.14826	0.14837	1.08 ± 0.07	0.970 ± 0.09	10	52.4	−0.92	−20.82	1.18	−0.29	−23.78	3.04	2.95
SDSS	J230225.49−082154.12	0.3618	0.362	2.02 ± 0.06	···	6	34.4	1.28	−20.81	0.92	0.64	−22.48	0.79	1.66
SDSS	J230845.60−091449.45	0.2147	0.2139	0.43 ± 0.07	···	6	12.7	0.60	−19.32	0.27	0.36	−21.53	0.36	2.21
SDSS	J232735.98+153309.57	0.4756	0.4756	< 0.30	···	11	161.7	1.07	−20.52	0.62	0.45	−22.18	0.56	1.66
SDSS	J232925.18−100722.43	0.4606	0.4606	< 0.30	···	11	98.1	1.56	−21.44	1.47	1.00	−23.58	2.06	2.14
2342+089	J234433.00+091039.4	0.7233	0.7233	1.48 ± 0.05	1.44 ± 0.09	7	34.5	−0.24	−22.23	2.26	−0.67	−23.51	1.73	1.28
2343+125	J234628.21+124859.9	0.7148	0.7148	< 0.0051	···	14	84.4	−0.26	−21.24	0.92	−0.67	−22.50	0.68	1.25
2343+125	J234628.21+124859.9	0.7313	0.731219	1.655 ± 0.006	1.190 ± 0.01	13	32.5	−0.23	−19.23	0.14	−0.68	−20.46	0.10	1.22
SDSS	J234949.61+003535.39	0.2778	0.2776	0.35 ± 0.02	···	6	31.8	0.46	−19.51	0.31	0.21	−21.43	0.31	1.91

[a]Mg II Absorption Measurements: (1) Guillemin & Bergeron (1997), (2) Churchill et al. (2013a), (3) Kacprzak et al. (2011b), (4) Steidel et al. (1997), (5) Chen & Tinker (2008), (6) Chen et al. (2010a), (7) Steidel et al. (1994), (8) Steidel-PC, (9) Kacprzak et al. (2010b), (10) Kacprzak et al. (2011a), (11) Gauthier & Chen (2011), (12) Barton & Cooke (2009), (13) Evans (2011), and (14) This work.

[b]K-correction used to obtain M_B from column (8) in Table 2.2.

[c]Absolute magnitudes are AB magnitudes.

[d]K-correction used to obtain M_K from column (11) in Table 2.2.

Table 2.4. MAGIICAT Properties

Property	Min	Max	Mean	Median
$W_r(2796)$ (Å)	0.003	4.422	0.629	0.400
$z_{\rm gal}$	0.072	1.120	0.418	0.359
D (kpc)	5.4	193.5	61.1	48.7
M_B	−16.1	−23.1	−20.3	−20.4
M_K	−17.0	−25.3	−21.9	−22.0
L_B/L_B^*	0.017	5.869	0.855	0.611
L_K/L_K^*	0.006	9.712	0.883	0.493
$B-K$	0.04	4.09	1.54	1.48

2.4.1. Luminosity Functions

Prior to measurements of galaxy luminosity functions, $\Phi(M)$, out to $z = 1$ (e.g., Lilly et al. 1995; Lin et al. 1999; Fried et al. 2001; Wolf et al. 2003; Faber et al. 2007; Cirasuolo et al. 2010), selecting galaxies by Mg II absorption provided a compelling technique for compiling a presumably complete sample of intermediate redshift galaxies SDP94. Using absorption selection, SDP94 presented the B- and K-band luminosity functions of intermediate redshift galaxies associated with $W_r(2796) \geq 0.3$ Å.

In order to compare to and expand upon the work of SDP94, we measured the B- and K-band luminosity functions for MAGIICAT galaxies. We divided the galaxies at all redshifts into two subsamples bifurcated by $W_r(2796) = 0.3$ Å. We also divided the galaxies into four subsamples bifurcated by $W_r(2796) = 0.3$ Å and $z = 0.359$ (the median redshift). The average redshift is $z = 0.23$ for the low redshift subsample and $z = 0.61$ for the high redshift subsample. These averages translate to a 3.2 Gyr time spread.

Since the majority of the galaxies are absorption selected, we followed SDP94 and applied a gas cross section correction, $\langle R_{\rm gas} \rangle^{-2}$, to the number of galaxies in each luminosity bin, where $\langle R_{\rm gas} \rangle \propto \langle L/L^* \rangle^{\beta}$, where $\langle L/L^* \rangle$ is the mean luminosity of the bin and where β gives the empirically determined luminosity dependence. For the MAGIICAT galaxies, we determined $\beta = 0.38$ for the B-band, and $\beta = 0.27$ for the K-band, as described in Paper II (Nielsen et al. 2013a). The correction factor rectifies the relative volume probed by absorption line surveys at fixed luminosity under the assumption of completeness.

In Figures 2.6 and 2.7, we present the B- and K-band luminosity functions for

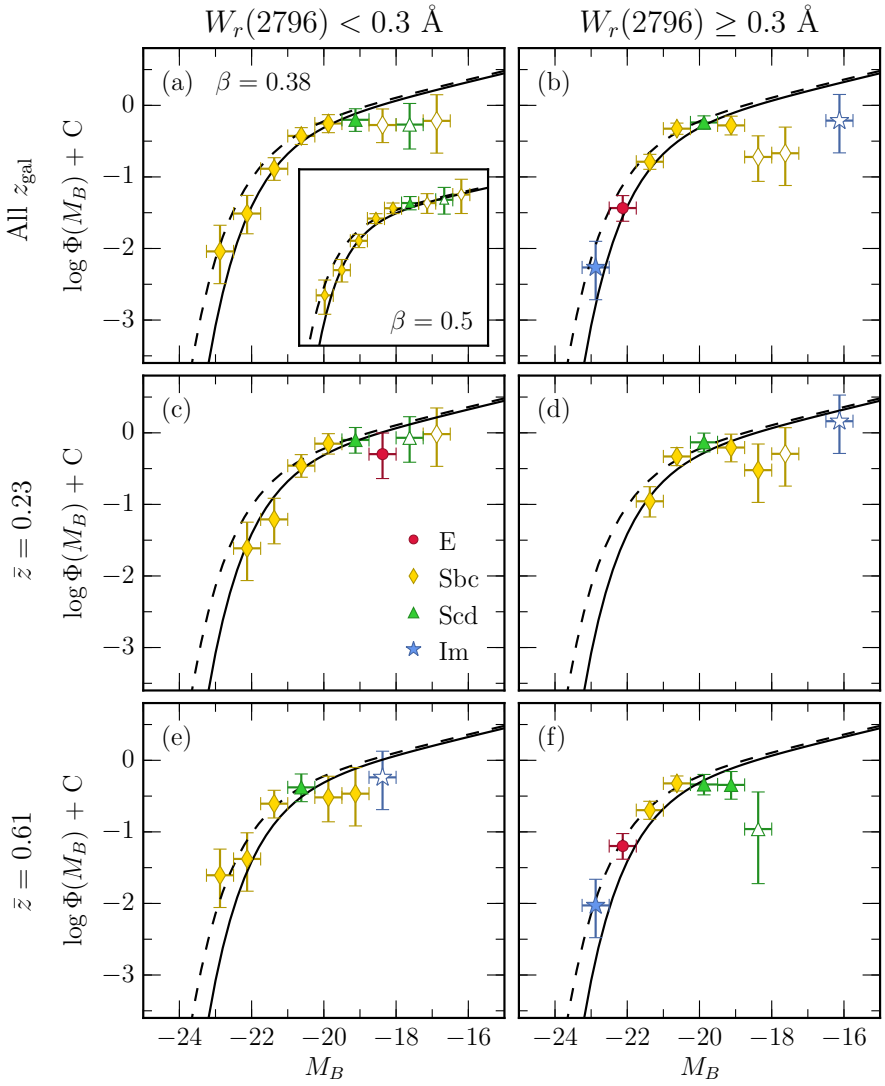

Fig. 2.6.— B-band luminosity functions for $W_r(2796) < 0.3$ ((a), (c), and (e)) and $W_r(2796) \geq 0.3$ ((b), (d), and (f)). Galaxies at all redshifts are included in panels (a) and (b), while galaxies with $z < \langle z \rangle$ are in panels (c) and (d) (mean $z = 0.22$), and galaxies with $z \geq \langle z \rangle$ are in panels (e) and (f) (mean $z = 0.61$), where $\langle z \rangle = 0.359$. The solid and dashed curves are $z = 0.3, 1.1$ Schechter functions, respectively, from Faber et al. (2007). Data point colors and types are assigned according to the mean color of the galaxies in the bin. Red circles indicate the mean color in the bin is closest to an elliptical (E) SED type, yellow diamonds indicate Sbc, green triangles indicate Scd, and blue stars indicates a Magellanic-type irregular (Im) SED type. Open points are where the completeness of the sample declines. The inset of panel ((a)) illustrates how the observed luminosity function changes with the gas cross section correction $\langle R_{\rm gas} \rangle^{-2} \propto \langle L/L_B^* \rangle^{-2\beta}$.

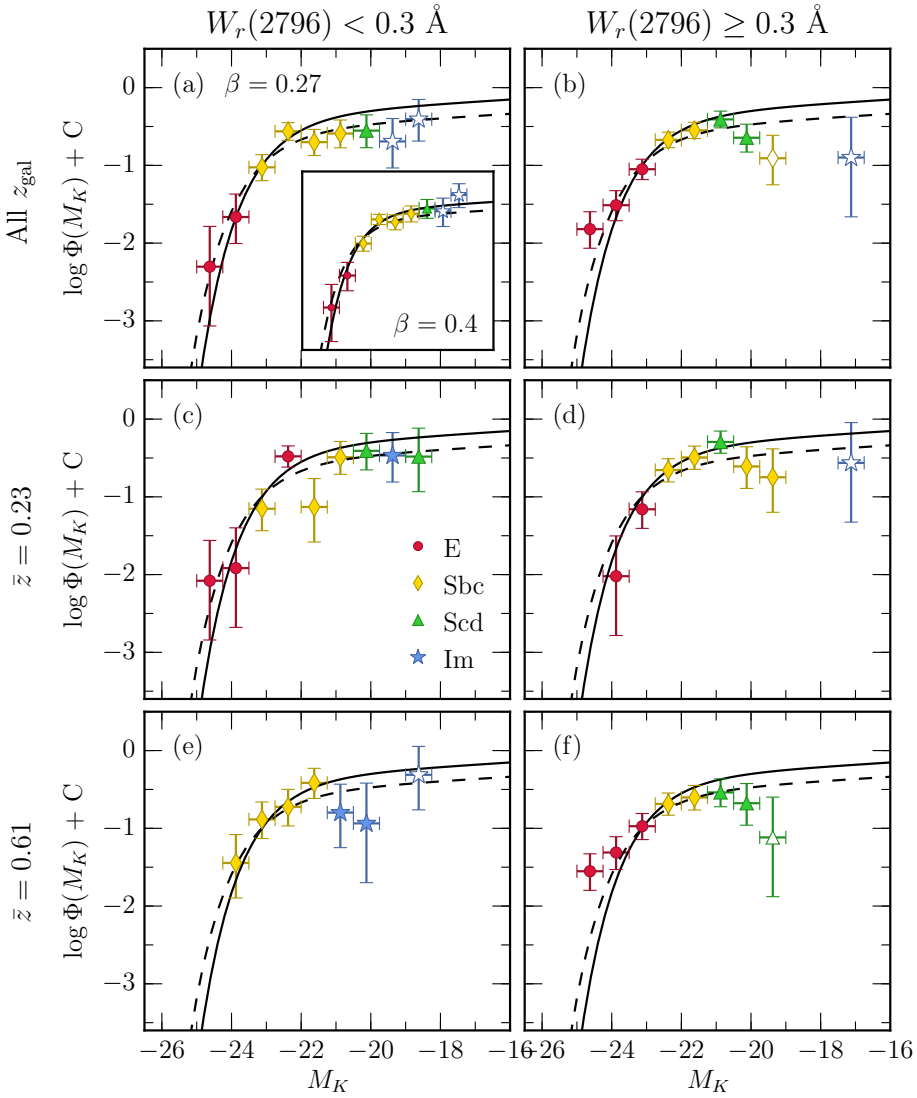

Fig. 2.7.— K-band luminosity functions for $W_r(2796) < 0.3$ ((a), (c), and (e)) and $W_r(2796) \geq 0.3$ ((b), (d), and (f)). Galaxies at all redshifts are included in panels (a) and (b), while galaxies with $z < \langle z \rangle$ are in panels (c) and (d) (mean $z = 0.22$), and galaxies with $z \geq \langle z \rangle$ are in panels (e) and (f) (mean $z = 0.61$), where $\langle z \rangle = 0.359$. The solid and dashed curves are $z = 0.3, 1.1$ Schechter functions, respectively, from Cirasuolo et al. (2010). Point types and colors are the same as described in Figure 2.6. The inset of panel (a) illustrates how the observed luminosity function changes with the gas cross section correction $\langle R_{\rm gas} \rangle^{-2} \propto \langle L/L_K^* \rangle^{-2\beta}$.

MAGiiCAT galaxies. For reference, we have overplotted empirically determined Schechter luminosity functions from deep galaxy surveys (plus a single additive constant to roughly match the data at M_*). We show the $z = 0.3$ (solid curve) and $z = 1.1$ (dashed curve) luminosity functions from Faber et al. (2007) for the B-band using their "all galaxy sample" and Cirasuolo et al. (2010) for the K-band of galaxies in the UKIDSS UDF field. These curves roughly bracket the low and high redshift subsamples. For the B-band, the appropriate characteristic luminosities are $M_B^* = -21.1$ for $z = 0.3$ and $M_B^* = -21.5$ for $z = 1.1$. For the K-band, the appropriate characteristic luminosities are $M_K^* = -22.7$ for $z = 0.3$ and $M_K^* = -23.1$ for $z = 1.1$.

For each binned data point, we computed the mean $B - K$ rest-frame color of the galaxies contributing to the bin and then color coded the point based upon the closest matching SED type (see Figure 2.5). Red data points indicate an average SED type for an elliptical (E) galaxy, yellow indicates Sbc on average, green indicates Scd on average, and blue indicates Magellanic-type irregular (Im) on average.

If we adopt the view that the galaxy surveys are magnitude-limited, we estimate that the completeness of MAGiiCAT begins to decline for $M_B > -18$ and $M_K > -17.5$ for the low redshift subsample and $M_B > -19$ and $M_K > -20$ for the high redshift subsample (see Figures 2.4(a) and 2.4(b)). We conservatively plotted the data in these luminosity bins as open points.

2.4.1.1. $W_r(2796)$ and Redshift Differences For all MAGIICAT galaxies with "weak" absorption or non-detections [$W_r(2796) < 0.3$ Å][5] (Figures 2.6(a) and 2.7(a)), the luminosity functions are more or less consistent with those of Faber et al. (2007) and Cirasuolo et al. (2010), though there is a trend for a flattening of the faint-end slopes, especially in $\Phi(M_B)$. The faint-end slopes of the "strong" absorbing galaxies [$W_r(2796) \geq 0.3$ Å] (Figures 2.6(b) and 2.7(b)), are less certain, but suggestive of a flattening of the faint-end slope relative to the Faber et al. (2007) and Cirasuolo et al. (2010) luminosity functions.

For the subsamples over the full redshift interval, we find no statistical differences between the $\Phi(M_B)$ for weak and strong absorbers (panel (a) vs. (b) of Figure 2.6) as deduced from a KS test on the unbinned luminosities. The same result applies for $\Phi(M_K)$ for weak and strong absorbers (panel (a) vs. (b) of Figure 2.7). Similarly, there are no statistical differences between the $\Phi(M_B)$ of weak and strong absorbing galaxies in the low redshift subsample (panel (c) vs. (d) of Figure 2.6) nor in the $\Phi(M_B)$ in the high redshift subsample (panel (e) vs. (f) of Figure 2.6). The same result holds for the $\Phi(M_K)$ of weak and strong absorbing galaxies for both the low and high redshift subsamples.

For each band, we examined for redshift evolution for the subsample with weak absorption or non-detections (panels (c) vs. (e) of Figures 2.6 and 2.7) and for the subsample with strong absorption (panels (d) vs. (f) of Figures 2.6 and 2.7). For $\Phi(M_B)$ of the weak absorbing galaxies, we find redshift evolution at a

[5]By examining gas defined by $W_r(2796) < 0.3$ Å, whether Mg II absorption is detected or not detected to the sensitivities afforded by the data, we are probing a well-defined gas regime, i.e., gas that does not give rise to Mg II absorption with $W_r(2796) \geq 0.3$ Å. The only assumption is that there is gas probed by the quasar line of sight within the region we would consider to be the CGM.

3.4σ significance level in the sense that the luminosity function at low redshift is shifted ~ 0.5 magnitudes dimmer relative to high redshift for galaxies with $M_B < -18$. We find only a suggestive trend for redshift evolution of $\Phi(M_B)$ of the strong absorbing galaxies (2.4σ). There is also a possible trend for redshift evolution in the K-band of the strong absorbing galaxies (2.4σ), but no evidence for the weak absorbing galaxies.

For the B-band luminosities, we note that the observed trends from lower to higher redshift (i.e., flattening of the faint-end slope and relative overabundance at higher luminosity) are reminiscent of the Malmquist bias that plagues magnitude-limited surveys. Given the heterogeneous selection methods used by the various works from which we constructed MAGIICAT, it is difficult to quantify the degree to which this may be an issue.

2.4.1.2. Color Sequence Along $\Phi(M_B)$ and $\Phi(M_K)$ The MAGIICAT galaxies (full catalog) exhibit a significant correlation between $B-K$ and M_K (7.8σ), but only a weak trend between $B-K$ and M_B (2.0σ). For the subsample of strong absorbing galaxies (Figure 2.7(b)) the correlation between $B-K$ and M_K is significant to 6.6σ and for the weak absorbing galaxy subsample (Figure 2.7(a)) the correlation is 3.6σ. The weak trend between $B-K$ and M_B is dominated by strong absorbing galaxies (2.0σ, Figure 2.6(f)).

The weakest trends (less than 3σ) between $B-K$ and M_K are found for the strong absorbing galaxies at low redshift (Figure 2.7(d)) and the weak absorbing galaxies at high redshift (Figure 2.7(e)), even though the mean colors suggest a strong trend. $B-K$ and M_K are correlated at the 3.2σ level for weak absorbing galaxies at low redshift (Figure 2.7(c)) and 6.4σ for strong absorbing galaxies at

high redshift (Figure 2.7(f)). There is no correlation between $B-K$ color and M_B for any of the subsamples presented in Figures 2.6 except for Figure 2.6(f), where there is a 3.0σ correlation.

The trends and strong correlations between $B-K$ and M_K are reflected in the color sequence of the data points for $\Phi(M_K)$ in Figure 2.7; the higher the infrared luminosity, the redder the mean galaxy color. Interestingly, for both the B-band and the K-band, KS tests reveal no significant differences in the distribution of $B-K$ between the weak and strong absorbing galaxies at low redshift, at high redshift, nor for all redshifts.

Though the overall color distribution may not differ between the galaxy subsamples, the average SED of the bright end of the K-band luminosity function corresponds to early-type E galaxies and the faint end corresponds to late-type galaxies (Sbc, Scd, and Im). On the contrary, there is no clear color differential along the luminosity sequence of $\Phi(M_B)$. The average color in virtually all B-band luminosity bins is that of an Sbc or Scd SED.

2.4.1.3. The $W_r(2796) \geq 0.3$ Å High-Redshift Subsample The strong absorbing [$W_r(2796) \geq 0.3$ Å] high redshift subsamples (Figures 2.6(f) and 2.7(f)) are most appropriately compared to the SDP94 luminosity functions, which correspond to $\langle z \rangle = 0.65$.

SDP94 find that $\Phi(M_B)$ for Mg II absorption selected galaxies turns down (or "rolls off") relative to the faint-end slope of $\Phi(M_B)$ for field galaxies starting roughly at 1.5 magnitudes below M_B^*, whereas $\Phi(M_K)$ for Mg II absorption selected galaxies is consistent with $\Phi(M_K)$ of field galaxies to roughly 3.1 magnitudes

below M_K^* (i.e., $L_K/L_K^* \simeq 0.05$). They infer that the absorption selected galaxies "missing" from the faint end of $\Phi(M_B)$ are Sd types and later.

SDP94 also report a strong correlation between $B-K$ and M_K in that fainter galaxies in the K-band are bluer, and also find no such correlation between $B-K$ and M_B. Incorporating the correlation between $B-K$ and M_K, they argue that faint blue galaxies (e.g., Ellis 1997) do not typically exhibit Mg II absorption with $W_r(2796) \geq 0.3$ Å and that this explains the difference in the behavior of the faint-end slopes of $\Phi(M_B)$ and $\Phi(M_K)$. They further conclude that the gas cross section is more likely to be governed by galaxy mass ($\propto L_K$) than by star formation. We note that this latter statement is inconsistent with our finding that the covering fraction of Mg II absorption is invariant with galaxy halo mass for multiple $W_r(2796)$ thresholds (Churchill et al. 2013b).

For MAGIICAT galaxies, the measured $\Phi(M_B)$ for strong absorbing galaxies at high redshift (Figure 2.6(f)) is suggestive of a faint-end roll off around 1.5 magnitudes below M_B^*, consistent with the SDP94 result. Similarly, we find a possible faint-end roll off in $\Phi(M_K)$ for the strong absorbing galaxies at high redshift (Figure 2.7(f)) starting at roughly 2 magnitudes below M_K^*. This latter result is contrary to the findings of SDP94. Note that, for this subsample of the MAGIICAT galaxies, the data extend roughly an additional magnitude below M_K^* as compared to the SDP94 sample.

2.4.1.4. Interpreting $\Phi(M_B)$ and $\Phi(M_K)$ Interpreting and comparing the functional forms of $\Phi(M_B)$ and $\Phi(M_K)$ is rendered difficult due to the heterogeneous selection methods of the galaxies in MAGIICAT. The majority of galaxies are "absorption selected", whereas some galaxies are magnitude-limited or volume-

limited selected. We have applied "gas cross section" corrections to all galaxies in the sample, which is a correct procedure for absorption selected galaxies.

In the cases where galaxies are searched for and identified based upon prior knowledge of a MgII absorption redshift, there can be ambiguity as to whether the galaxy is the only galaxy connected to the MgII absorption. It is always possible that an additional galaxy is in close projection with the background quasar; given the clustering properties of galaxies, this would be more rare for two galaxies at the bright end of the luminosity function, but it could be more probable as fainter galaxies are considered. These can be found only with careful point spread function subtraction of the quasar, which has been performed for all of the quasar fields surveyed from the ground by GB97 and for the majority of the fields originally surveyed by SDP94 (in both ground-based and *HST* images, where the latter was performed by A. Shapley, private communication, unpublished). However, such analysis has not been performed for the remainder of the galaxies in MAGIICAT. Furthermore, the absorption selection approach usually entails an incomplete survey of the galaxies in the quasar field. If an additional galaxy (or galaxies) might be discovered in a given quasar field to have a redshift consistent with the MgII absorption, the galaxies would reclassify as a "group" and would not be included in the present work.

In the cases where galaxies are identified in apparent magnitude- or volume-limited surveys, the point spread function issue is just as relevant. Furthermore, apparent magnitude-limited surveys would suffer from faint-end incompleteness and/or Malmquist bias.

Though the shapes of the luminosity functions presented in Figures 2.6 and

2.7 are suggestive of a relative paucity of sub-L^* galaxies as compared to field galaxies, or perhaps even a roll over in the faint-end slopes, the above considerations make it difficult to assess whether selection effects are at play. Though the gas cross section corrections we applied act to reduce the value of $\Phi(M)$ for $L > L^*$ galaxies, the corrections *increase* the value of $\Phi(M)$ for sub-L^* galaxies; the correction factor increases with decreasing luminosity. Thus, discrepancies between the observed luminosity functions and a Schechter function could result from our not applying the proper cross section correction.

As an exercise, we could attempt to recover the Schechter function (under the assumption that the luminosity function of *all* galaxies follows this functional form) by varying the β in the gas cross section correction $\langle R_{\rm gas}\rangle^{-2} \propto \langle L/L^*\rangle^{-2\beta}$. In essence, we then learn something about the gas cross sections of galaxies as a function of luminosity. In the insets of Figures 2.6(a) and 2.7(a), we provide examples of a $\simeq 0.1$ increase in β for the $W_r(2796) < 0.3$ Å subsamples over all redshifts. This illustrates that if we have a steeper luminosity dependence on the gas cross section, especially at the faint end, the data can be better matched to a Schechter function. That is, matching the observed luminosity function of absorption selected galaxies to the Schechter function can, in principle, be used to constrain the luminosity dependence of the gas cross section. Most importantly, with an increased sample size (larger than MAGIICAT), we might be able to determine that the gas cross section does not follow a constant power law, that the slope β is also luminosity dependent. For example, it is possible to have all subsamples conform to a Schechter function if we parameterize β to have luminosity dependence such that the gas cross section of low luminosity galaxies declines more rapidly with decreasing luminosity than it does for high luminosity

galaxies.

Even using the presented luminosity functions, we can still infer that, in general, galaxy $B-K$ color is independent of galaxy B-band luminosity. Regardless of the B-band luminosity, the *average* color is consistent with that of an Sbc/Scd galaxy. However, there is a $B-K$ color sequence in that the greater the infrared luminosity, the redder the $B-K$ color. This is a highly significant result. If M_K serves as a very crude proxy for *stellar* mass, the luminosity functions suggest that galaxies with lower stellar masses with detectable Mg II absorbing gas comprise bluer (younger) stellar populations.

This might suggest that a detectable Mg II absorbing CGM may not be present in low stellar mass red galaxies; only the lower stellar mass galaxies with bluer (younger) stellar populations give rise to detectable Mg II absorption. Since the roll over at the faint-end is more pronounced for galaxies with $W_r(2796) \geq 0.3$ Å absorbing gas, we might infer that weaker Mg II absorption is preferentially found in the lower stellar mass galaxies.

2.5. Summary and Conclusions

We compiled, from our own work and the literature, the Mg II Absorbing-Galaxy Catalog, MAGIICAT, consisting of galaxies with intermediate redshifts to study the galaxy-circumgalactic medium interaction as probed by Mg II $\lambda\lambda 2796, 2803$ absorption. The catalog presented here contains 182 isolated galaxies with spectroscopic redshifts $0.07 \leq z \leq 1.1$, impact parameters $D < 200$ kpc from a background quasar, and known Mg II absorption or a 3σ upper limit on absorption less than or equal to 0.3 Å. A summary of the minimum, maximum, mean, and

median values for absorption and galaxy properties in MAGIICAT is presented in Table 2.4.

All values that depend on cosmological parameters have been recalculated, including quasar-galaxy impact parameters, absolute magnitudes, and luminosities. This standardizes the galaxy properties and allows for a comparison of galaxies whose properties were placed on different cosmologies over the last $\sim$ 20 years. Absolute magnitudes and luminosities were calculated in the B-band for all galaxies and in the K-band for all but 18. We find that the average rest-frame $B-K$ color of MAGIICAT galaxies is consistent with an Sbc galaxy, though the most common galaxy color is slightly redder than an Scd galaxy. The average color agrees with SDP94 and Zibetti et al. (2007).

We present the B- and K-band luminosity functions, $\Phi(M)$, for subsamples split by $W_r(2796) < 0.3$ Å ("weak") and $W_r(2796) \geq 0.3$ Å ("strong"), and by low redshift and high redshift, cut by $z = 0.359$. We find that the luminosity functions in both bands for galaxies with weak absorption or non-detections are more-or-less consistent with Faber et al. (2007) and Cirasuolo et al. (2010), while the strong absorbing galaxies may be flatter in the faint-end slope. Comparing the strong, high redshift subsample to SDP94, we find the suggestive faint-end roll off of the luminosity function in the B-band consistent, while the possible roll off in the K-band is contrary. No statistical difference between weak and strong subsamples for all, low redshift, and high redshift galaxies is present in either the B- or the K-band. The B-band may show redshift evolution in both the weak and strong subsamples, but in the K-band, evolution may only be present in the strong subsample. These above statements depend upon the gas cross section correction factor that we have applied to the data. We discussed how the

luminosity functions can, in principle, be used to constrain the dependence of the gas cross section on galaxy luminosity.

We find a correlation between $B-K$ and M_K for the full sample (7.8σ), but only a weak correlation between $B-K$ and M_B (2.0σ), consistent with the findings of SDP94. Splitting MAGIICAT into weak absorbers, strong absorbers, low redshift, and high redshift subsamples, we find the correlations in both bands are dominated by the high redshift, strong absorbing galaxies. As M_K becomes brighter, the mean galaxy color becomes redder. On the other hand, the mean color of most magnitude bins in the B-band luminosity functions is consistent with an Sbc/Scd SED.

The behavior of the luminosity functions suggest that only the lower stellar mass galaxies with bluer (younger) stellar populations give rise to detectable Mg II absorption. Comparing the faint-end roll over between galaxies with $W_r(2796) \geq 0.3$ Å and $W_r(2796) < 0.3$ Å absorbing gas, it would seem that in lower stellar mass galaxies, weaker Mg II absorption would be observed more commonly.

Further analysis has already been conducted with all or a portion of the galaxies in MAGIICAT. Kacprzak et al. (2012a) studied the effect of galaxy orientation on Mg II absorption. They found that Mg II gas is preferentially found along the galaxy major and minor axes, where the covering fraction of Mg II absorption as a function of orientation is enhanced by as much as $20\% - 30\%$ along the major and minor axes. This bimodality was found to be driven by blue galaxies and may indicate outflowing gas with an opening angle of 100° and inflowing gas with an opening angle of 40°.

Using halo abundance matching, Churchill et al. (2013b,c) obtained the galaxy

virial masses for all galaxies in MAGIICAT and studied the $W_r(2796)$-D anti-correlation and Mg II covering fractions, both as a function of galaxy virial mass. They found that the Mg II CGM has projected absorption profile that follows $(D/R_{\rm vir})^{-2}$, where $R_{\rm vir}$ is the virial radius, indicating a self-similar behavior with virial mass. They also find that $W_r(2796)$ increases with virial mass in finite ranges of D but is constant in finite ranges of $D/R_{\rm vir}$, and that covering fractions are unchanged as a function of galaxy virial mass within a given D or $D/R_{\rm vir}$. Their results are contrary to the theoretical prediction that cold-mode accretion is shut down in high-mass galaxies (Birnboim & Dekel 2003; Dekel & Birnboim 2006; Stewart et al. 2011).

Nielsen et al. (2013a) [Paper II of this series] presented an analysis of how $W_r(2796)$, covering fractions, and the radial extent of the Mg II CGM depend on impact parameter, galaxy redshift, B- and K-band luminosities, and $B-K$ color. They found that the anti-correlation between $W_r(2796)$ and D can be characterized by a log-linear fit which levels off at low D. The scatter on the $W_r(2796)-D$ plane may be due to galaxy luminosity, where more luminous galaxies have larger $W_r(2796)$ at a fixed D. They also found that the covering fraction decreases with increasing D and increasing $W_r(2796)$ threshold. More luminous, bluer, and higher redshift galaxies have larger covering fractions than less luminous, redder, and lower redshift galaxies at a given D. The luminosity-scaled radial extent of the Mg II CGM is more sensitive to luminosity in the B-band than in the K-band. The radial extent has a steeper luminosity dependence for red galaxies than blue galaxies, and for low redshift than high redshift galaxies.

In future work we intend to apply multivariate analysis methods to MAGIICAT, incorporating the galaxy virial mass estimates of the galaxies from Churchill et al.

(2013c) as well as Mg II kinematics and the low- and high-ionization absorption strengths of the CGM. We also plan to utilize the sample of group galaxies we obtained with the present work, comparing the group galaxies to the isolated galaxies. Mining the *Hubble Space Telescope* archive for H I and UV low- and high-ionization metal-line transitions will be useful for developing a more complete understanding of the CGM properties of MAGIICAT galaxies.

We thank the referee for helpful comments which improved the manuscript. We also thank Jacqueline Bergeron for providing details on the observations conducted in Guillemin & Bergeron (1997), Chuck Steidel for communicating detailed aspects relating to the work by Steidel et al. (1994), including access to unpublished materials, and David Law for additional magnitudes. We extend our gratitude to all the researchers whose hard work over the last two decades resulted in the growing database of published galaxies in quasar fields. Without their efforts, this work would not have been possible. This research was primarily supported through grant HST-AR-12646 provided by NASA via the Space Telescope Science Institute, which is operated by the Association of Universities for Research in Astronomy (AURA) under NASA contract NAS 5-26555. This work was also supported by the Research Enhancement Program provided by NASA's New Mexico Space Grant Consortium (NMSGC). N.M.N. was also partially supported through a NMSGC Graduate Fellowship and a Graduate Research Enhancement Grant (GREG) sponsored by the Office of the Vice President for Research at New Mexico State University. M.T.M. thanks the Australian Research Council for a QEII Research Fellowship (DP0877998) and Discovery Project grant (DP130100568). This research has made extensive use of the SAO/NASA Astrophysics Database System (ADS), operated by the Smithsonian Astrophysical Ob-

servatory under contract with NASA, the NASA/IPAC Extragalactic Database (NED), operated by the Jet Propulsion Laboratory and California Institute of Technology, under contract with NASA, and the SIMBAD database, operated at Centre de Données, Strasbourg, France. This research has also made use of the Spanish Virtual Observatory (http://svo.cab.inta-csic.es) supported from the Spanish MICINN / MINECO through grants AyA2008-02156, AyA2011-24052

3. MAGIICAT II. GENERAL CHARACTERISTICS OF THE MgII ABSORBING CIRCUMGALACTIC MEDIUM

The contents of this chapter were originally published as Nielsen, N. M., Churchill, C. W., & Kacprzak, G. G. 2013, ApJ, 776, 115.

We examine the Mg II absorbing circumgalactic medium (CGM) for the 182 intermediate redshift ($0.072 \leq z \leq 1.120$) galaxies in the "Mg II Absorber-Galaxy Catalog" (MAGIICAT, Nielsen et al.). We parameterize the anti-correlation between equivalent width, $W_r(2796)$, and impact parameter, D, with a log-linear fit, and show that a power law poorly describes the data. We find that higher luminosity galaxies have larger $W_r(2796)$ at larger D (4.3σ). The covering fractions, f_c, decrease with increasing D and $W_r(2796)$ detection threshold. Higher luminosity galaxies have larger f_c; no absorption is detected in lower luminosity galaxies beyond 100 kpc. Bluer and redder galaxies have similar f_c for $D < 100$ kpc, but for $D > 100$ kpc, bluer galaxies have larger f_c, as do higher redshift galaxies. The "absorption radius," $R(L) = R_*(L/L^*)^\beta$, which we examine for four different $W_r(2796)$ detection thresholds, is more luminosity sensitive to the B-band than the K-band, more sensitive for redder galaxies than for bluer galaxies, and does not evolve with redshift for the K-band, but becomes more luminosity sensitive towards lower redshift for the B-band. These trends clearly indicate a more extended Mg II absorbing CGM around higher luminosity, bluer, and higher redshift galaxies. Several of our findings are in conflict with other works. We address these conflicts and discuss the implications of our results for the low-ionization, intermediate redshift CGM.

3.1. Introduction

Understanding the formation and evolution of galaxies is one of the foremost problems facing extragalactic research. Over the last decade, theoretical activity has been focused on studying how galaxies form and evolve in the context of the response of baryonic gas to dark matter halos of various masses and to physical processes such as stellar and AGN feedback (e.g., Birnboim & Dekel 2003; Maller & Bullock 2004; Kereš et al. 2005; Dekel & Birnboim 2006; Birnboim et al. 2007; Ocvirk et al. 2008; Kereš et al. 2009; Oppenheimer et al. 2010; Stewart et al. 2011; van de Voort et al. 2011; van de Voort & Schaye 2012). These theoretical works have established that the circumgalactic medium (CGM) is a dynamic environment comprising inflowing accretion, outflowing winds, and gas that recycles between the halo and galaxy.

What has become clear is that the CGM is intimately linked to galaxy morphology, stellar populations and kinematics, and chemical evolution. The detailed physics governing the heating and cooling of baryonic gas regulates the formation and galactic-scale dynamical motions of stars, which in turn feedback and govern the physics of the gas in the CGM (e.g., Dekel & Silk 1986; Ceverino & Klypin 2009). Since this paradigm of galaxy evolution suggests a strong CGM-galaxy connection, many investigators have taken a phenomenological approach to developing models that predict the observable geometric distribution and kinematics of baryonic gas in and around galaxies (e.g., Weisheit 1978; Lanzetta & Bowen 1992; Charlton & Churchill 1996; Mo & Miralda-Escude 1996; Benjamin & Danly 1997; Charlton & Churchill 1998; Tinker & Chen 2008; Chelouche & Bowen 2010; Bouché et al. 2012).

As such, the CGM is an astrophysical environment which, at any point in the evolution of a galaxy, yields clues to both its historical development and future evolution. Therefore, observations of the CGM around individual galaxies promise to provide highly sought constraints on the physics governing the global properties of galaxies. In practice, the CGM is almost exclusively accessible via absorption lines present in the spectra of background objects (traditionally using the technique of quasar absorption lines). Studying the CGM-galaxy connection is desirable over all redshifts, with the vast majority of work to date having been focused on $z \leq 1$ (however, cf., Adelberger et al. 2005; Simcoe et al. 2006; Steidel et al. 2010; Rudie et al. 2012). At these redshifts, galaxy photometric and spectral properties can be measured with relatively high accuracy and modest investment in telescope time with Mg II absorption (e.g., Bergeron & Boissé 1991; Steidel et al. 1994; Churchill et al. 2005; Chen et al. 2010a; Kacprzak et al. 2011b).

The Mg II $\lambda\lambda 2796, 2803$ doublet is especially well suited at intermediate redshifts since the absorption is observable in the optical. Furthermore, Mg II absorption is ideal for tracing low ionization, metal-enriched CGM gas in that it arises in a wide range of H I environments, from $\log N(\mathrm{H\,I}) \simeq 16.5$ to greater than 21.5 (Bergeron & Stasińska 1986; Steidel & Sargent 1992; Churchill et al. 1999, 2000; Rao & Turnshek 2000; Rigby et al. 2002). It is also well established that Mg II absorption probes key CGM structures such as outflow gas (e.g., Tremonti et al. 2007; Weiner et al. 2009; Martin & Bouché 2009; Rubin et al. 2010) and inflow gas (e.g., Ribaudo et al. 2011; Rubin et al. 2012; Thom et al. 2011; Kacprzak et al. 2012b) associated with galaxies.

Through the efforts of the aforementioned studies, the behavior of Mg II CGM absorption in relation to various galaxy properties has been incrementally char-

acterized over the last two decades. Examples of some of the findings include relationships between the strength of Mg II absorption and galaxy luminosity (Kacprzak et al. 2008; Chen et al. 2010a), galaxy mass (Bouché et al. 2006; Gauthier et al. 2009; Churchill et al. 2013b), star formation or specific star formation rate (Chen et al. 2010b; Ménard et al. 2011), galaxy color (Zibetti et al. 2007; Bordoloi et al. 2011), galaxy morphology (Kacprzak et al. 2007), and galaxy orientation (Bordoloi et al. 2011; Bouché et al. 2012; Kacprzak et al. 2011b, 2012a; Churchill et al. 2013a).

Generally speaking, these investigations have yielded results that appear to be converging on an observational portrait of the Mg II absorbing CGM that is more or less consistent with the broad scenario forwarded by theory and simulations. For example, evidence is mounting that accretion may preferentially reside in a coplanar geometry (e.g., Steidel et al. 1997; Kacprzak et al. 2010a; Stewart et al. 2011; Kacprzak et al. 2011b), whereas winds may outflow along the galaxy minor axis (Bordoloi et al. 2011; Bouché et al. 2012; Churchill et al. 2013a; Kacprzak et al. 2012a). However, due to the complex ionization structure, non-uniform metal enrichment, and dynamical processes of the CGM, and due to the wide range of galaxy properties, such as luminosity, color, mass, and morphology, the data exhibit substantial scatter. As such, while some works have found statistically significant correlations between two quantities or between combined/scaled quantities, many works have reported connections between galaxy and Mg II absorption CGM properties either based on general trends (i.e., correlations that are not statistically significant above the 3σ level) or on slight reductions in the scatter of certain relationships by combining/scaling one or more measured quantity.

We compiled the "Mg II Absorber-Galaxy Catalog" (MAGIICAT) which is

described in detail in Paper I of this series (Nielsen et al. 2013b), with the aim to further illuminate the CGM-galaxy connection at higher statistical significance and over a wide range of galaxy properties. In this paper, we utilize the data to address several long-standing questions with regard to the Mg II CGM-galaxy connection. In section 3.2, we briefly describe the galaxy sample, which has uniform photometric properties and impact parameters for a ΛCDM cosmology ($H_0 = 70$ km s^{-1} Mpc^{-1}, $\Omega_M = 0.3$ and $\Omega_\Lambda = 0.7$). In section 3.3, we present an examination of (1) galaxy color and absolute magnitude evolution, (2) the dependence of $W_r(2796)$ on galaxy color, (3) the dependence of $W_r(2796)$ on impact parameter, (4) covering fraction as a function of impact parameter and $W_r(2796)$ for luminosity, color, and redshift subsamples, and (5) the luminosity scaling of "halo absorption radius" and the behavior of covering fraction with $W_r(2796)$, galaxy color, and redshift. In section 3.4, we discuss the implications of our results and give concluding remarks in section 3.5.

3.2. Galaxy Sample and Subsamples

From an exhaustive literature search, we compiled a catalog of galaxies with spectroscopic redshifts $0.07 \leq z \leq 1.1$ within a projected distance of $D \leq 200$ kpc from a background quasar, with known Mg II absorption or an upper limit on absorption less than 0.3 Å. We distinguish between isolated and group galaxies, where group galaxies have a nearest neighbor within 100 kpc and have a velocity separation no greater than 500 km s^{-1}, and focus only on isolated galaxies in the present work. The total catalog consists of 182 isolated galaxies. Full details of all galaxies and Mg II absorption properties as well as the various selection methods used are presented in Paper I. Here we briefly describe the general properties of

MAGIICAT.

The sample presented here comprises 182 isolated galaxies toward 134 sightlines, covering a redshift range $0.072 \leq z_{\rm gal} \leq 1.120$, with a median of $\langle z \rangle = 0.359$. The impact parameter range is $5.4 \leq D \leq 194$ kpc, with median $\langle D \rangle = 49$ kpc.

For each galaxy, we determined rest-frame AB absolute magnitudes, M_B and M_K, by computing k-corrections appropriate for the observed magnitudes (e.g., Kim et al. 1996) using the extended Coleman et al. (1980) spectral energy distribution (SED) templates from Bolzonella et al. (2000). We selected a galaxy SED by comparing the observed galaxy colors to the redshifted SEDs. Luminosities, L_B/L_B^* and L_K/L_K^*, were obtained using a linear fit to M_B^* with redshift from Faber et al. (2007) (B-band) and using $M_K^*(z)$ as expressed in Eq. 2 from Cirasuolo et al. (2010) (K-band). Absolute B-band magnitudes range from $-16.1 \geq M_B \geq -23.1$, corresponding to luminosities of $0.02 \leq L_B/L_B^* \leq 5.87$, with median $L_B/L_B^* = 0.611$. Absolute K-band magnitudes range from $-17.0 \geq M_K \geq -25.3$, corresponding to $0.006 \leq L_K/L_K^* \leq 9.7$. Rest-frame $B-K$ colors range from $0.04 \leq B-K \leq 4.09$, with median $B-K = 1.48$. We obtain K-band absolute magnitudes and luminosities, and $B-K$ colors for all but 18 of the galaxies.

Galaxies in MAGIICAT were bifurcated into several subsamples for analysis. When dividing the galaxy-absorber pairs into subsamples, we either took a sample driven approach by splitting the sample at the median value of a given observed quantity, or dividing the sample based upon historical precedent, such as $W_r(2796)$ cuts. The full sample was sliced by the median galaxy redshift, L_B/L_B^*, L_K/L_K^*, or $B-K$. Table 3.1 presents the characteristics of the full sample and each subsample, including the number of galaxies, the median value by which the

catalog was cut, and the minimum, maximum, and mean values of galaxy redshift, B- and K-band luminosity, and $B-K$ color. The subsample names listed will be used throughout this paper.

Table 3.1. Subsample Characteristics

			$z_{\rm gal}$			L_B/L_B^*			L_K/L_K^*			$B-K$		
Subsample	# Gals	Cut[a]	Min	Max	Mean	Min	Max	Mean	Min[b]	Max[b]	Mean[b]	Min[b]	Max[b]	Mean[b]
All	182	···	0.072	1.120	0.418	0.017	5.869	0.855	0.006	9.712	0.883	0.038	4.090	1.537
Low z	91	0.359	0.072	0.358	0.225	0.017	3.759	0.734	0.006	4.901	0.654	0.283	3.037	1.554
High z	91	0.359	0.359	1.120	0.612	0.071	5.869	0.976	0.016	9.712	1.123	0.038	4.090	1.520
Low L_B/L_B^*	91	0.611	0.072	0.941	0.411	0.017	0.610	0.306	0.006	1.680	0.271	0.038	4.090	1.410
High L_B/L_B^*	91	0.611	0.096	1.120	0.425	0.613	5.869	1.405	0.241	9.712	1.452	0.483	3.303	1.655
Low L_K/L_K^*	82	0.493	0.110	0.941	0.396	0.019	1.440	0.376	0.006	0.487	0.222	0.038	3.037	1.231
High L_K/L_K^*	82	0.493	0.096	1.017	0.410	0.189	5.869	1.359	0.499	9.712	1.544	0.637	4.090	1.843
Blue	82	1.482	0.098	1.017	0.444	0.019	3.522	0.803	0.006	2.602	0.454	0.038	1.478	1.047
Red	82	1.482	0.096	0.852	0.362	0.035	5.869	0.931	0.026	9.712	1.312	1.487	4.090	2.027

[a]The median value by which each subsample was bifurcated. The cut is inclusive to the "high" bins and red bin.
[b]Only including galaxies with a value for M_K.

3.3. Results

In this section, we report on the luminous properties of the galaxies and directly compare them to the properties of the Mg II absorbing CGM. The analysis presented here is based upon direct observables. We do not scale or combine measured quantities. We also do not scale or fit the data to models of the CGM. Our aim is to characterize the Mg II CGM-galaxy connection directly with no assumptions and to provide information that can be directly interpreted in terms of primary observables. We examine only bivariate relationships, reserving further analysis, such as multivariate techniques for future work to appear in later papers of this series.

3.3.1. Galaxy Magnitudes, Luminosities, and Colors Versus Redshift

Since the CGM as probed by Mg II may depend upon galaxy stellar populations, and these populations are known to evolve, we examined whether the galaxy magnitudes and rest-frame colors evolve with redshift for the sample. A Kendall-τ rank correlation test yielded a 4.4σ significance that M_B correlates with $z_{\rm gal}$ (i.e., galaxies at higher redshift are brighter in the B-band), whereas M_K shows a weak trend for redshift evolution (2.2σ). Faber et al. (2007) found that M_B^* brightens with increasing redshift from the DEEP2+COMBO-17 surveys. The average M_B of the sample presented here increases with redshift more rapidly than M_B^*. Similarly, Cirasuolo et al. (2010) found that M_K^* tends to brighten with increasing redshift from UKIDSS, whereas the average M_K of the sample presented here does not exhibit redshift evolution. As such, we may be seeing that galaxies associated with Mg II absorption or an upper limit on absorption are characterized by bluer

colors at higher redshift. However, selection effects may be important. Virtually all the galaxies were selected or discovered (for a summary of the selection methods used, see Nielsen et al. 2013b) using the red band in the observer frame, which probes further toward the B-band in the galaxy rest frame with increasing redshift. However, this cannot explain the lack of evolution in the K-band.

We also conducted a rank correlation test on galaxy luminosities versus redshift, $z_{\rm gal}$, since we calculate the luminosities from the absolute magnitudes. In the B-band, we find no redshift evolution of L_B/L_B^* to the 1.2σ level. Similarly in the K-band, we find that L_K/L_K^* does not correlate with redshift at the 0.9σ level. The lack of correlations here are due to the fact that we take into account the redshift evolution of M_B^* from Faber et al. (2007) and M_K^* from Cirasuolo et al. (2010) in our luminosity calculations.

A rank correlation test on $B-K$ versus $z_{\rm gal}$ shows that the null hypothesis of no correlation can be ruled out to a confidence level (CL) no better than 1.8σ, indicating that the $B-K$ rest-frame color of galaxies in MAGIICAT does not evolve with redshift. This result is consistent with Zibetti et al. (2007) who use statistical methods in which individual galaxies were not directly identified with absorbers for $0.4 \leq z \leq 1$ using observed g, r, i, and z band magnitudes for $W_r(2796) \geq 0.8$ Å. A direct comparison is difficult because we use optical B-band and 2.2μm infrared (K-band) absolute magnitudes to determine rest-frame colors and we study systems with much smaller $W_r(2796)$ than represented by their sample. Slicing the sample presented here at $W_r(2796) = 0.8$ Å to compare to the Zibetti et al. (2007) sample, we obtain 0.8σ for $W_r(2796) \geq 0.8$ Å and for $W_r(2796) < 0.8$ Å we obtain 1.7σ.

3.3.2. Galaxy Luminosities and Colors Versus $W_r(2796)$

To determine whether $W_r(2796)$ exhibits some dependency on galaxy luminosity, we performed a non-parametric Kendall's τ rank correlation test that allows for upper limits on either the dependent or independent variable for bivariate data (see Brown et al. 1974; Wang & Wells 2000) with $W_r(2796)$ as the dependent variable. The null hypothesis of no correlation could not be ruled out for $W_r(2796)$ against L_B/L_B^* (0.2σ), L_K/L_K^* (0.6σ), M_B (0.9σ), and M_K (0.5σ). The lack of correlations found here are interesting in view of the arguments by Bouché et al. (2006), who derive an anti-correlation between $W_r(2796)$ and galaxy luminosity with a dependence on the faint-end slope of the galaxy luminosity function and a proportionality between galaxy luminosity and the cross-section of the absorbing CGM.

To determine if $W_r(2796)$ has any dependency on galaxy color, we performed the non-parametric Kendall's τ rank correlation test on $W_r(2796)$ against $B-K$. The test indicates that $W_r(2796)$ does not directly correlate with galaxy color for the full sample (1.3σ). A Kendall's τ rank correlation test between $W_r(2796)$ and $B-K$ for the subsample with $D \leq 50$ kpc indicates that $W_r(2796)$ is also not correlated with color at smaller impact parameters (0.5σ).

The lack of a correlation between $W_r(2796)$ and $B-K$ is consistent with the findings of Chen et al. (2010a), who examined $B-R$ colors for $0.1 \leq z \leq 0.5$. However, the result is contrary to the statistically based results of Zibetti et al. (2007), who find bluer colors from the integrated light selected by stronger Mg II absorbers and redder colors selected by weaker absorbers for $0.4 \leq z \leq 1$, where the minimum $W_r(2796)$ of their sample is 0.8 Å. A direct comparison with the work

of Zibetti et al. (2007) is difficult due to its statistical nature. However, a Kendall's τ test examining the $W_r(2796) \geq 0.8$ Å subsample of MAGIICAT yielded a slight trend between $W_r(2796)$ and $B-K$ (2.1σ) such that larger equivalent widths may show a weak trend with galaxy color. Bifurcating the full galaxy sample at $W_{\rm cut} = 0.1$, 0.3, 0.6, and 1.0 Å, we find a 2.5σ significance for a correlation between $W_r(2796)$ and $B-K$ for galaxies hosting $W_r(2796) \geq 1.0$ Å absorption; for the very strongest absorbers, the redder the galaxy, the greater the Mg II equivalent width. As mentioned, this is contrary to the findings of Zibetti et al. (2007).

To examine the possible Mg II equivalent width distribution dependence on $B-K$ color, we also performed a Kolmogorov-Smirnov (KS) test comparing the cumulative $W_r(2796)$ distribution functions of red ($B-K \geq 1.48$) and blue ($B-K < 1.48$) galaxies. We limited the test to include only those galaxies with detected Mg II absorption. The two subsamples are statistically consistent with having been drawn from the same parent distribution ($\simeq 0.5\sigma$). Limiting the sample to galaxies with $D \leq 50$ kpc, the KS test results remain below 1σ. Though the distribution for red galaxies has power beyond the largest and smallest $W_r(2796)$ of the blue galaxies, the statistics do not ferret out a difference between the two galaxy subsamples; the average and maximum $W_r(2796)$ for $D \leq 50$ kpc associated with red galaxies and blue galaxies are consistent (average 1.02 and 0.92 Å, with maximum 2.9 and 2.3 Å, respectively).

Our findings that the $W_r(2796)$ distributions from the CGM within $D = 50$ kpc of blue and red galaxies are indistinguishable is at odds with the dramatic finding of Bordoloi et al. (2011). They report a factor of eight times larger equivalent width associated with blue galaxies compared to red galaxies in stacked spectra for which the CGM is probed within $D = 50$ kpc.

3.3.3. $W_r(2796)$ and Impact Parameter

A commonly known property of Mg II galaxies is the anti-correlation between $W_r(2796)$ and impact parameter, D, (e.g., Lanzetta & Bowen 1990; Bergeron & Boissé 1991; Steidel 1995; Bouché et al. 2006; Kacprzak et al. 2008; Chen et al. 2010a; Churchill et al. 2013a). In Figure 3.1, we present $W_r(2796)$ versus D. Galaxies with detected Mg II absorption are plotted as solid blue points and those with upper limits on absorption are plotted as open blue points with downward arrows.

We performed a non-parametric Kendall's τ rank correlation test on $W_r(2796)$ against D, allowing for upper limits on $W_r(2796)$. For this sample, $W_r(2796)$ is anti-correlated with D at the 7.9σ level. Since $W_r(2796)$ correlates with the number of clouds (Voigt profile components, Petitjean & Bergeron 1990; Churchill et al. 2003; Evans 2011), this result indicates that either the column densities, velocity spreads, or both, diminish with projected distance from the galaxy.

To parameterize the general behavior of the anti-correlation, we used the Expectation-Maximization maximum-likelihood method (Wolynetz 1979) accounting for upper limits on $W_r(2796)$ to fit a power law, $\log W_r(2796) = \alpha_1 \log D + \alpha_2$, and a log-linear fit, $\log W_r(2796) = \alpha_1 D + \alpha_2$, to the data. The data are poorly described by a power law [green, long dashed curve in Figure 3.1, from Chen et al. (2010a)] due to the substantial population of $W_r(2796) < 0.1$ Å absorbers and upper limits. We present the log-linear fit and its 1σ uncertainties in Figure 3.1 (solid black curve) for $\alpha_1 = -0.015 \pm 0.002$ and $\alpha_2 = 0.27 \pm 0.11$.

The considerable scatter about this relation *may* suggest that $W_r(2796)$ is governed by physical processes related to the galaxy such as luminosity (cf.,

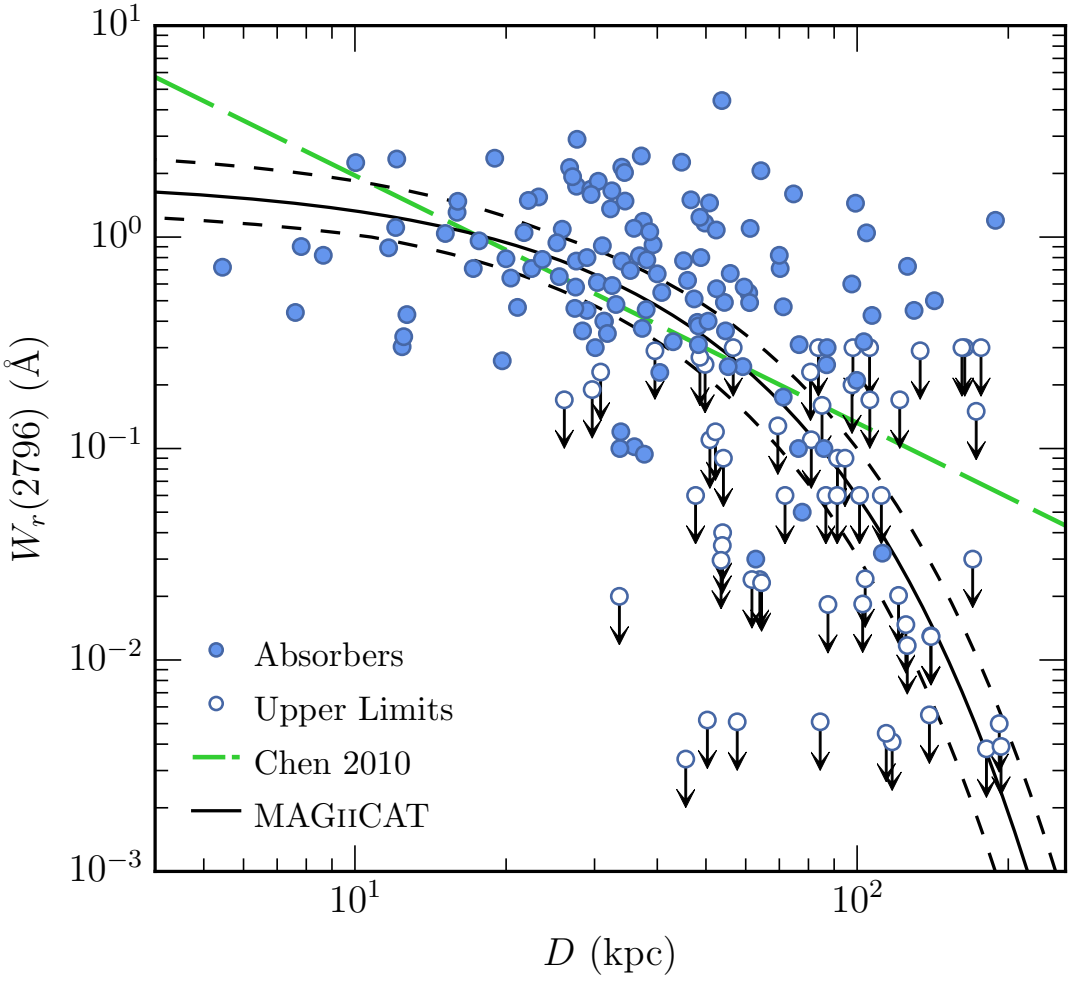

Fig. 3.1.— Mg II λ2796 rest-frame equivalent width, $W_r(2796)$, vs. impact parameter, D. Galaxies with detected Mg II absorption are presented as solid blue points, whereas those with upper limits on absorption are open blue points with downward arrows. The full sample comprises 182 galaxies with a 7.9σ anti-correlation between $W_r(2796)$ and D. The green, long dashed curve is the power law fit obtained by Chen et al. (2010a) for their data. The solid curve is a log-linear maximum likelihood fit to the data presented here, $\log W_r(2796) = \alpha_1 D + \alpha_2$, where $\alpha_1 = -0.015 \pm 0.002$ and $\alpha_2 = 0.27 \pm 0.11$. Short dashed curves provide 1 σ uncertainties in the fit.

Kacprzak et al. 2008; Chen et al. 2010a), mass (cf., Bouché et al. 2006; Gauthier et al. 2009; Lundgren et al. 2009; Churchill et al. 2013b), star formation (cf., Chen et al. 2010b; Ménard et al. 2011), or orientation (cf., Bordoloi et al. 2011; Bouché et al. 2012; Kacprzak et al. 2011b, 2012a; Churchill et al. 2013a). Alternatively, the CGM is inherently patchy (Churchill et al. 2007, 2013a).

To examine possible trends and/or sources of this scatter in the distribution of $W_r(2796)$ versus D, we applied the two-dimensional Kolmogorov-Smirnov (2DKS) test. This test examines if the 2D distribution of $W_r(2796)$ and D from two samples can be ruled out as being consistent.

We first investigated bifurcations of the full sample about the median values of $B-K$, $z_{\rm gal}$, L_B/L_B^*, and L_K/L_K^*, which are presented in Figure 3.2. Performing a 2DKS test on the subsamples, we find that the null hypothesis that blue and red galaxies are drawn from the same population can not be ruled out to the 1.6σ level. Using a redshift cut, the data show a weak trend for larger $W_r(2796)$ at fixed D for high z galaxies (2.2σ). A 2DKS test on the luminosities shows that high L_B/L_B^* and L_K/L_K^* are found with larger $W_r(2796)$ at fixed D than low luminosities at the 4.2σ and 4.3σ level, respectively. We then examined only galaxies with detected absorption in each subsample. In this case, the significance level decreases for all subsamples.

We also divided the sample into quartiles by $B-K$, $z_{\rm gal}$, L_B/L_B^*, and L_K/L_K^* and performed the 2DKS test on the lowest and highest quartiles. We obtained $P(\rm KS) = 0.03$, 0.30, 0.0007, and 0.0006 for $B-K$, $z_{\rm gal}$, L_B/L_B^*, and L_K/L_K^*, respectively. At best, there is a 3.4σ significance that the distribution or scatter of $W_r(2796)$ versus D is due to a dependence on L_K/L_K^*, a 3.4σ significance of a

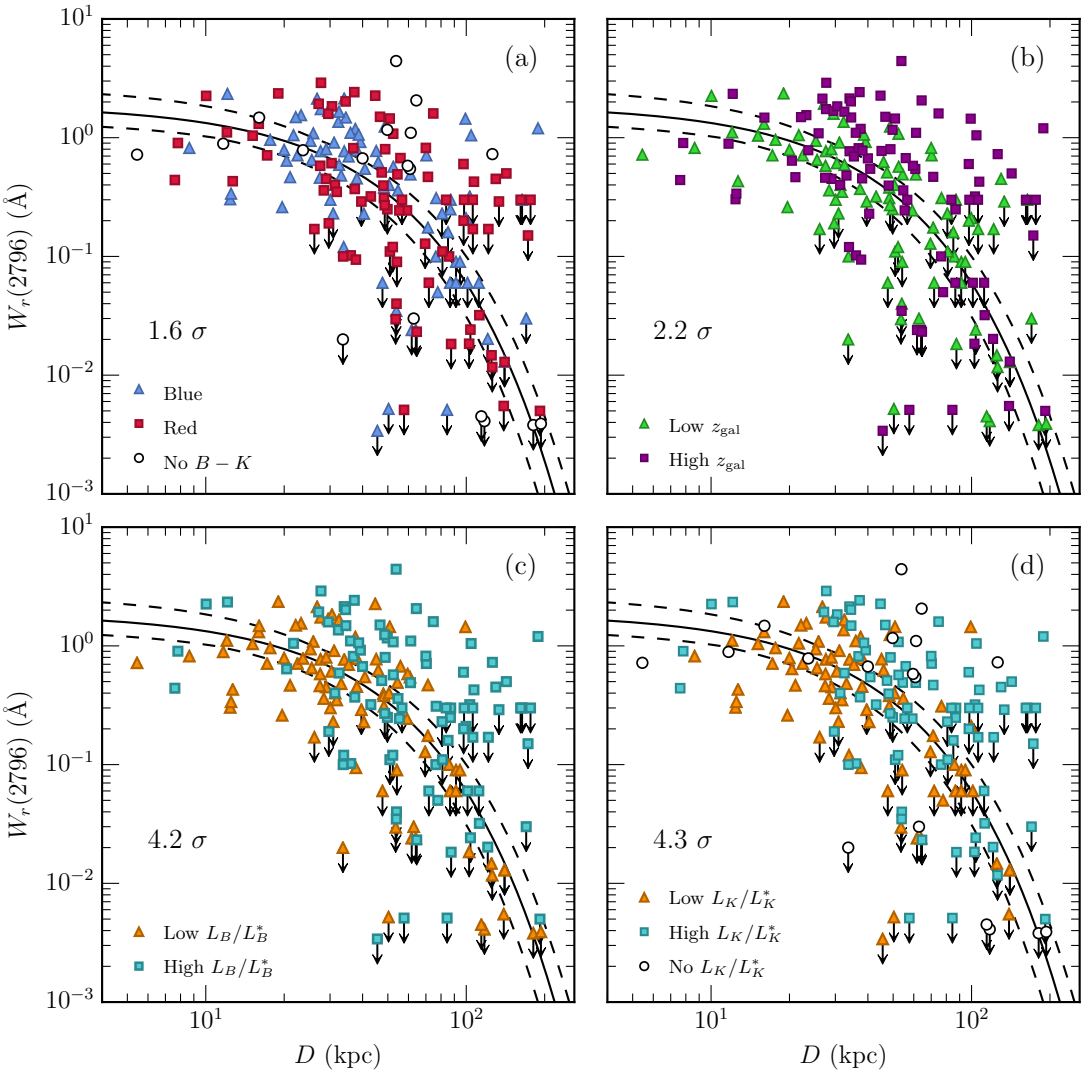

Fig. 3.2.— Mg II equivalent width, $W_r(2796)$, as a function of impact parameter, D, split by median (a) galaxy color, (b) redshift, (c) B-band luminosity, and (d) K-band luminosity. Galaxies with no K-band magnitude are presented as open points in panels a and d. The null hypothesis that two subsamples are drawn from the same population can be ruled out to the 1.6σ ($B-K$), 2.2σ ($z_{\rm gal}$), 4.2σ (L_B/L_B^*), and 4.3σ (L_K/L_K^*) level. The significance level decreases in all cases when we only consider galaxies for which we have detected Mg II absorption.

connection to L_B/L_B^*, and a 2.1σ significance it is connected to $B-K$. There is clearly no redshift dependence. When we examine only galaxies for which we have detectable absorption, we find that the significance level decreases or remains the same for all subsamples.

3.3.4. Covering Fraction and Impact Parameter

Here we examined the dependence of covering fraction directly on impact parameter and galaxy luminosity, color, and redshift. We present directly observable quantities, making no assumptions with regard to the Mg II absorbing CGM density profile or geometry.

3.3.4.1. Covering Fraction Within Fixed Impact Parameters In order to examine the covering fraction within a fixed projected radial distance from the galaxies, we computed the quantity $f_{D\mathrm{max}} \equiv f(W \geq W_{\mathrm{cut}}, D \leq D_{\mathrm{max}})$, which we define as the fraction of absorbers with $W_r(2796) \geq W_{\mathrm{cut}}$ inside a projected separation of D_{max} from the galaxy.

In Figure 3.3, we plot $f_{D\mathrm{max}}$ against D_{max} in 10 kpc intervals. The uncertainties in $f_{D\mathrm{max}}$ are shown as shaded regions. These are the upper and lower limits, calculated using the formalism for binomial statistics (see Gehrels 1986). Values of $f_{D\mathrm{max}}$ at $D_{\mathrm{max}} \leq 10$ kpc are not robust given the small number of galaxies within this impact parameter[1]. Due to the relative undersampling of galaxies at $D_{\mathrm{max}} > 150$ kpc and the cumulative nature of $f_{D\mathrm{max}}$, the covering fraction will

[1]Of the three galaxies at $D \leq 10$ kpc, one is at low redshift where the angular separation from the quasar is much greater than the quasar seeing disk, and the other two were found at higher redshift following point spread function subtraction of the quasar (Steidel et al. 1994), which was not performed in all surveys.

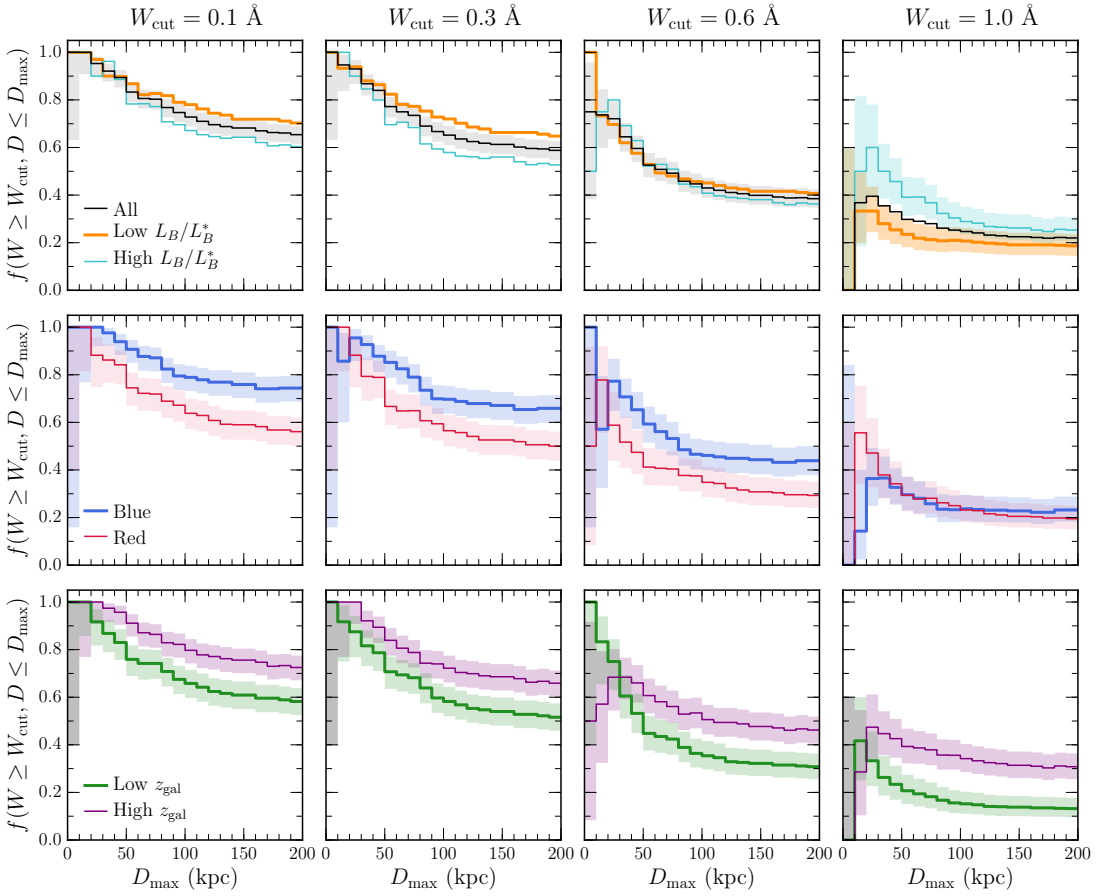

Fig. 3.3.— Covering fraction, $f_{D\rm max}$, inside $D_{\rm max}$ for different bifurcated subsamples split at the median L_B/L_B^*, $B-K$, and $z_{\rm gal}$ and for various $W_r(2796) > W_{\rm cut}$ thresholds. Shaded regions represent 1σ uncertainties based upon binomial statistics. — (upper) The full sample of galaxies (thin black line), the high luminosity galaxies (thin blue line), and the low luminosity galaxies (thick orange line), divided at the median B-band luminosity, $L_B/L_B^* = 0.611$. — (middle) The blue ($B-K < 1.48$) and red ($B-K \geq 1.48$) galaxy subsamples bifurcated at the median galaxy color. — (lower) The high ($z \geq \langle z \rangle$) and low ($z < \langle z \rangle$) redshift galaxy subsamples where $\langle z \rangle = 0.359$.

be virtually unchanging outside this impact parameter; thus the shape of $f_{D\max}$ versus $D_{\max}$ is less robust for $D_{\max} > 150$ kpc.

In Figure 3.3 (upper panels), we present $f_{D\max}$ for the full galaxy sample and for low and high luminosity galaxies. For each $W_{\rm cut}$ subsample, the covering fraction of the MgII absorbing CGM inside $D = D_{\max}$ decreases as $D_{\max}$ is increased. At a given $D_{\max}$, there is a clear trend that as $W_{\rm cut}$ is increased, $f_{D\max}$ decreases, indicating that the covering fraction within a fixed projected separation increases as the minimum absorption threshold is lowered. The covering fraction may exhibit a luminosity dependence for $W_{\rm cut} = 0.1$ and 0.3 Å such that low luminosity galaxies have larger covering fractions than high luminosity galaxies, but this is most apparent outside of $D = 100$ kpc where the covering fraction is less robust. We find no luminosity dependence for $W_{\rm cut} = 0.6$ Å. For $W_{\rm cut} = 1.0$ Å, $f_{D\max}$ is larger for high luminosity galaxies at all $D_{\max}$ than for low luminosity galaxies. This difference is accentuated at $D_{\max} \leq 50$ kpc.

In the middle panels of Figure 3.3, we present $f_{D\max}$ and its uncertainties versus $D_{\max}$ for red and blue galaxies. The mean redshift for red galaxies is $\overline{z} = 0.36$ over the range $0.1 \leq z \leq 0.85$, and for blue galaxies $\overline{z} = 0.44$ over $0.1 \leq z \leq 1.02$. For the $W_{\rm cut} = 0.1$, 0.3, and 0.6 Å subsamples, blue galaxies have higher covering fractions relative to red galaxies for $D_{\max} > 50$ kpc. Within 50 kpc, the larger uncertainties make it difficult to distinguish any possible differences. For $W_{\rm cut} = 1.0$ Å, the covering fractions for red and blue galaxies are indistinguishable outside of $D = 50$ kpc. Within $D = 50$ kpc, red galaxies may have larger covering fractions, though the uncertainties are again large.

In Figure 3.3 (lower panels), we present $f_{D\max}$ and its uncertainties against

$D_{\rm max}$ for the high z and low z galaxy subsamples. For $D_{\rm max} \leq 50$ kpc, it is difficult to distinguish any redshift evolution in $f_{D{\rm max}}$ due to the uncertainties. Beyond 50 kpc, the data suggest that $f_{D{\rm max}}$ may evolve such that at higher redshift, the covering fraction of Mg II absorbing gas is higher than at lower redshift.

Chen et al. (2010a) also examined the luminosity dependence of $f_{D{\rm max}}$ as a function of $W_{\rm cut}$, where their $D_{\rm max}$ is fixed at the luminosity scaled "gas radius", with $R_{\rm gas} \propto (L_B/L_B^*)^{0.35}$, assuming isothermal density profile (Tinker & Chen 2008) and NFW profile (Navarro et al. 1996) models. As such, a direct comparison with our non-parameterized results is difficult. Nonetheless, they found that $f_{D{\rm max}}$ has little to no dependence on galaxy B-band luminosity for $W_{\rm cut} = 0.1$, 0.3, and 0.5 Å, which is consistent with our result; however, for $W_{\rm cut} = 1.0$ Å, we found systematically larger $f_{D{\rm max}}$ for high luminosity galaxies as compared to low luminosity galaxies, especially for $D_{\rm max} \leq 50$ kpc.

3.3.4.2. Covering Fraction Profiles To examine the covering fraction profile with projected distance from the galaxy, we computed $f_{\langle D\rangle} \equiv f(W \geq W_{\rm cut}, \langle D\rangle)$, which we define as the fraction of absorbers with $W_r(2796) \geq W_{\rm cut}$ in fixed impact parameter bins. We select the bins $0 \leq D < 25$ kpc, $25 \leq D < 50$ kpc, $50 \leq D < 100$ kpc, and $100 \leq D < 200$ kpc, for which $\langle D\rangle$ is the average impact parameter of the galaxies in the bin.

In Figure 3.4, we plot $f_{\langle D\rangle}$ against $\langle D\rangle$. The horizontal bars are the impact parameter ranges and the data points are the average impact parameters, $\langle D\rangle$, for each bin. The vertical error bars are the 1σ uncertainties in $f_{\langle D\rangle}$ based upon binomial statistics. The subsamples presented in each panel are identical to the corresponding panels of Figure 3.3.

As can be seen in the upper panels of Figure 3.4, the $f_{\langle D \rangle}$ profile decreases as impact parameter is increased and this behavior is exhibited regardless of $W_{\rm cut}$. Also note that as $W_{\rm cut}$ is increased, $f_{\langle D \rangle}$ is smaller for a given impact parameter bin. This indicates that in a fixed annulus around galaxies, the sky-projected distribution of the Mg II CGM becomes progressively patchier as higher column density material and/or more complex kinematics are selected. For $W_{\rm cut} = 0.1$ Å, the $f_{\langle D \rangle}$ profile decreases from unity within a radius of 25 kpc to 30% in the annulus 100–200 kpc, whereas for $W_{\rm cut} = 1.0$ Å, the covering fraction decreases from 40% to less than 10%.

Also shown in the upper panels of Figure 3.4 is $f_{\langle D \rangle}$ split by $L_B/L_B^* = 0.611$. For low luminosity galaxies, the covering fraction vanishes outside of $D = 100$ kpc for all $W_{\rm cut}$. On the other hand, in the annulus 100–200 kpc, the covering fractions for high luminosity galaxies are approximately 50%, 40%, 15%, and 10% for $W_{\rm cut} = 0.1$, 0.3, 0.6, and 1.0 Å, respectively. Covering fraction profiles for all, low, and, high luminosity galaxies are listed in Table 3.2.

The data are suggestive of a luminosity dependence for the maximum extent of Mg II absorbing gas, such that the CGM of low L_B/L_B^* galaxies extends no further than 100 kpc, whereas high luminosity galaxies have a detectable Mg II CGM beyond 100 kpc. The difference between high and low luminosity galaxies is most prominent outside of 100 kpc for $W_{\rm cut} = 0.1$, and 0.3 Å. As such, high luminosity galaxies exhibit a more extended Mg II CGM, whereas for low luminosity galaxies, the Mg II CGM is more concentrated in the central regions but with relatively lower covering fraction as $W_{\rm cut}$ is increased.

In the middle panels of Figure 3.4, the covering fraction profiles of red and

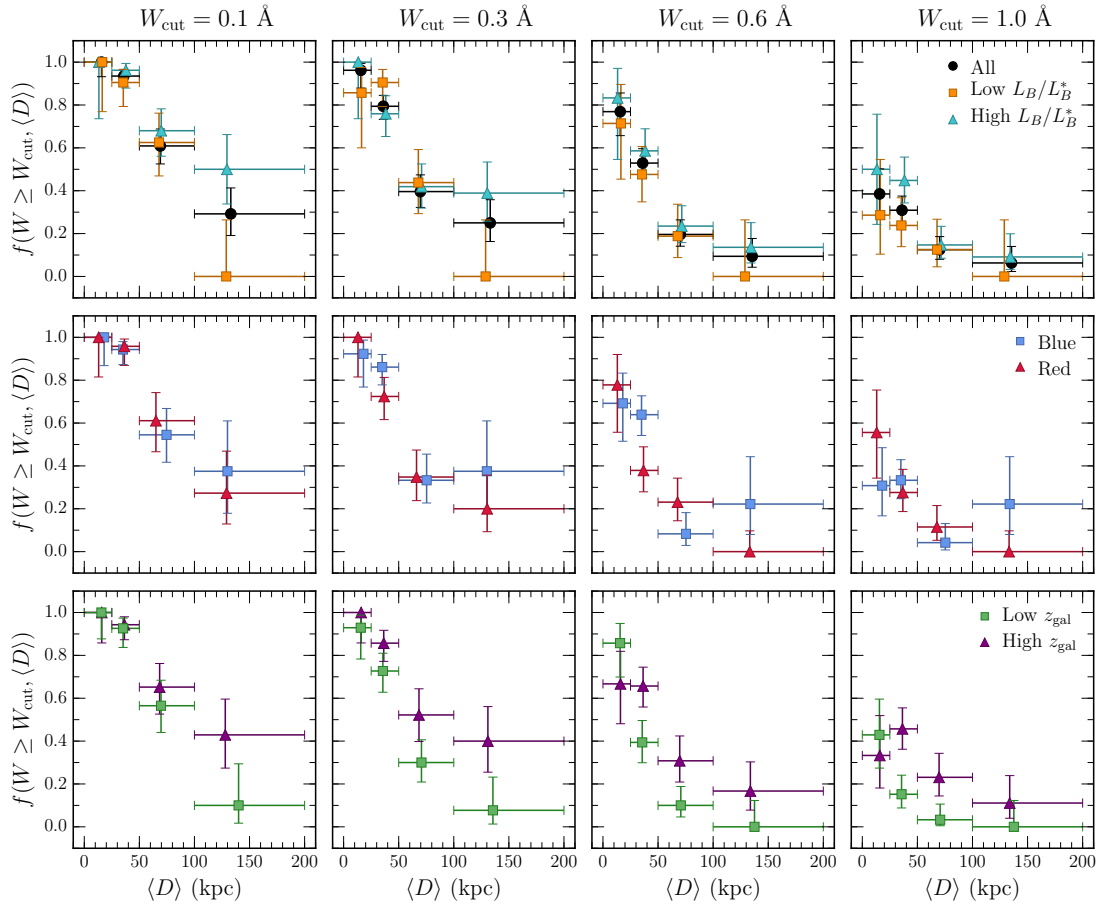

Fig. 3.4.— Covering fraction profile, $f_{\langle D \rangle}$, for the impact parameter bins $0 \leq D < 25$ kpc, $25 \leq D < 50$ kpc, $50 \leq D < 100$ kpc, and $100 \leq D < 200$ kpc for different $W_r(2796)$ thresholds, $W_{\rm cut}$. The horizontal bars indicate the impact parameter bin width and the vertical bars are the 1σ binomial uncertainties. Data points are plotted at the mean impact parameter of the galaxies in the bin. — (upper) The full sample of galaxies (solid black circles), the high luminosity galaxies (blue triangles), and the low luminosity galaxies (orange squares). — (middle) Blue (blue squares) and red (red triangles) galaxy subsamples sliced at the median galaxy color. – (lower) High (purple triangles) and low (green squares) redshift subsamples cut by the median redshift, $\langle z \rangle = 0.359$.

Table 3.2. Luminosity Dependence of Covering Fraction Profiles, $f_{\langle D \rangle}$

$W_{\rm cut}$, Å	(0–25), kpc	[25–50), kpc	[50–100), kpc	[100–200), kpc
		All Galaxies		
0.1	$1.00^{+0.00}_{-0.07}$	$0.94^{+0.03}_{-0.05}$	$0.61^{+0.08}_{-0.08}$	$0.29^{+0.12}_{-0.10}$
0.3	$0.96^{+0.03}_{-0.08}$	$0.79^{+0.05}_{-0.06}$	$0.40^{+0.08}_{-0.07}$	$0.25^{+0.11}_{-0.09}$
0.6	$0.77^{+0.09}_{-0.11}$	$0.53^{+0.07}_{-0.07}$	$0.20^{+0.07}_{-0.06}$	$0.09^{+0.08}_{-0.05}$
1.0	$0.39^{+0.12}_{-0.11}$	$0.31^{+0.07}_{-0.06}$	$0.13^{+0.06}_{-0.05}$	$0.06^{+0.08}_{-0.04}$
		Low L_B/L_B^* Galaxies		
0.1	$1.00^{+0.00}_{-0.23}$	$0.91^{+0.06}_{-0.11}$	$0.63^{+0.14}_{-0.16}$	$0.00^{+0.26}_{-0.00}$
0.3	$0.86^{+0.12}_{-0.26}$	$0.91^{+0.06}_{-0.11}$	$0.44^{+0.15}_{-0.15}$	$0.00^{+0.26}_{-0.00}$
0.6	$0.71^{+0.18}_{-0.26}$	$0.48^{+0.13}_{-0.13}$	$0.19^{+0.15}_{-0.10}$	$0.00^{+0.26}_{-0.00}$
1.0	$0.29^{+0.26}_{-0.18}$	$0.24^{+0.13}_{-0.10}$	$0.13^{+0.14}_{-0.08}$	$0.00^{+0.26}_{-0.00}$
		High L_B/L_B^* Galaxies		
0.1	$1.00^{+0.00}_{-0.26}$	$0.96^{+0.03}_{-0.08}$	$0.68^{+0.10}_{-0.12}$	$0.50^{+0.16}_{-0.16}$
0.3	$1.00^{+0.00}_{-0.26}$	$0.76^{+0.08}_{-0.10}$	$0.42^{+0.11}_{-0.10}$	$0.39^{+0.15}_{-0.13}$
0.6	$0.83^{+0.14}_{-0.29}$	$0.59^{+0.10}_{-0.11}$	$0.24^{+0.10}_{-0.08}$	$0.14^{+0.12}_{-0.07}$
1.0	$0.50^{+0.26}_{-0.26}$	$0.45^{+0.11}_{-0.11}$	$0.15^{+0.09}_{-0.06}$	$0.09^{+0.11}_{-0.06}$

blue galaxies exhibit several differences. Note that for red galaxies, none have absorption with $W_r(2796) \geq 0.6$ Å in the range 100–200 kpc. Blue galaxies consistently have covering fractions of approximately 40% for $W_{\rm cut} \leq 0.3$ Å and 20% for $W_r(2796) \geq 0.6$ Å in the range 100–200 kpc. Within 25 kpc the covering fraction for blue galaxies drops more rapidly than for red galaxies with increasing $W_{\rm cut}$. Moreover, for $W_{\rm cut} = 0.6$ and 1.0 Å there is a hint that the covering fraction of red galaxies drops more rapidly for $D > 25$ kpc relative to the $D = 0$–25 kpc region. This may suggest that the gas in red galaxies is more concentrated near the center while in blue galaxies, the gas is not as highly concentrated.

As shown in the lower panels of Figure 3.4, high redshift galaxies exhibit a trend of higher $f_{\langle D \rangle}$ in the 25–50, 50–100, and 100–200 kpc annuli relative to low redshift galaxies. Within 25 kpc, the covering fraction may be higher in low redshift galaxies for stronger absorption, $W_{\rm cut} = 0.6$ and 1.0 Å. Though the trends are marginal, they may suggest a greater extension of the gas at higher redshift followed by a settling of material into the inner regions at lower redshift.

Chen et al. (2010a) examined $f_{\langle D \rangle}$ for their sample ($\langle z \rangle = 0.25$), and also found that the covering fraction profile, $f_{\langle D \rangle}$, decreases with increasing D and is smaller at a given $\langle D \rangle$ with increasing $W_{\rm cut}$ using $W_{\rm cut} = 0.1$, 0.3, and 0.5 Å. However, a direct comparison with our results is difficult because Chen et al. (2010a) scale D assuming a B-band galaxy luminosity dependent "gas radius" proportional to $(L_B/L_B^*)^{0.35}$.

3.3.5. Luminosity Scaling and Covering Fraction

Our results in the previous section strongly suggest that the Mg II absorbing CGM extends further for weaker absorption than for stronger absorption, and that this behavior has a clear dependence with galaxy luminosity. What is further clear, is that for a given $W_{\rm cut}$, the CGM becomes more "patchy" with increasing D, as indicated by the decreasing covering fractions. *As such, it would seem that the notion of a well-defined* Mg II *CGM "gas radius", or "halo absorption radius" is an oversimplification in that the extent of the gas exhibits a "fuzzy" boundary when averaged over many galaxies.* Nonetheless, for historical comparisons we parameterize the characteristics of an "outer" boundary and its plausible dependence on the galaxy properties and redshift.

Since the work of Bergeron & Boissé (1991), the extent of absorbing gas is commonly assumed to follow a Holmberg-like relation, $R(L) = R_*(L/L^*)^\beta$. We examined whether the halo absorption radius also depends on $W_r(2796)$, and/or galaxy color and redshift.

To examine the dependence on $W_r(2796)$, we adopt $W_{\rm cut} = 0.1$, 0.3, 0.6, and 1.0 Å. To estimate R_* and β, we varied the two parameters over the ranges $0 \leq R_* \leq 300$ kpc and $0 \leq \beta \leq 1$ and computed the function $q(R_*, \beta, L, W_{\rm cut}) = wr_{(\geq)} + r_{(<)}$, where $r_{(\geq)}$ is the fraction of systems with $W_r(2796) \geq W_{\rm cut}$ below $R(L)$, $r_{(<)}$ is the fraction with $W_r(2796) < W_{\rm cut}$ above $R(L)$, and w is a weighting factor[2]. The parameter values are adopted when $q(R_*, \beta, L, W_{\rm cut})$ is a maximum, for which the covering fraction inside $R(L)$ is $f_{R(L)} = 1/(1+x)$, where $x =$

[2]Since we wish to determine the "outer envelope" of the halo absorption radius, we adopt the weight $w = 2$. When $w = 1$, we find β consistent with zero.

$(n_{(\geq)}/n_{(<)})(1 - r_{(<)})/r_{(\geq)}$, and where $n_{(\geq)}$ and $n_{(<)}$ are the number of systems with $W_r(2796) \geq W_{\rm cut}$ and $W_r(2796) < W_{\rm cut}$, respectively.

The downward and upward 1σ uncertainties in R_* were estimated by using the best estimate of β and performing one-sided integration under the $q(R_*, \beta, L, W_{\rm cut})$ curve until 84.13% of the total area was obtained. Similarly, the downward and upward 1σ uncertainties in β were estimated by using the best estimate of R_*. The 1σ uncertainties in $f_{R(L)}$ are computed using binomial statistics by computing the fraction of galaxies with $W_r(2796) \geq W_{\rm cut}$ to all galaxies within $R(L)$.

Our results are presented in Table 3.3 for both B- and K-band luminosities. In the upper panels of Figure 3.5, we present D against L_B/L_B^*. The luminosity scaling increases from $\beta \sim 0.3$ for $W_{\rm cut} = 0.1$ Å to $\beta \sim 0.4$ for $W_{\rm cut} = 0.3$, 0.6, and 1.0 Å. The absorbing gas halo radius, R_*, for an L_B^* galaxy is on the order of ~ 80 kpc for $W_{\rm cut} = 0.1$ and 0.3 Å, while R_* is on the order of ~ 75 kpc (but consistent with 80 kpc, given the uncertainties in R_*) for $W_{\rm cut} = 0.6$ and 1.0 Å. The covering fraction decreases from $f_{R(L)} = 0.85$ for $W_{\rm cut} = 0.1$ Å to $f_{R(L)} = 0.34$ for $W_{\rm cut} = 1.0$ Å.

In the lower panels of Figure 3.5, we present the K-band results. We note that this subsample has 18 fewer galaxies than the B-band subsample. The luminosity scaling varies from ~ 0.2 for $W_{\rm cut} = 0.1$ and 1.0 Å to ~ 0.3 for $W_{\rm cut} = 0.3$ and 0.6 Å. The halo absorption radius also has a range of values where $R_* = 75$ kpc for $W_{\rm cut} = 0.1$ Å, 78 kpc for 0.3 and 0.6 Å, and 62 kpc for 1.0 Å, however, these values are all consistent within uncertainties. The covering fraction behaves similarly to the B-band (see Table 3.3).

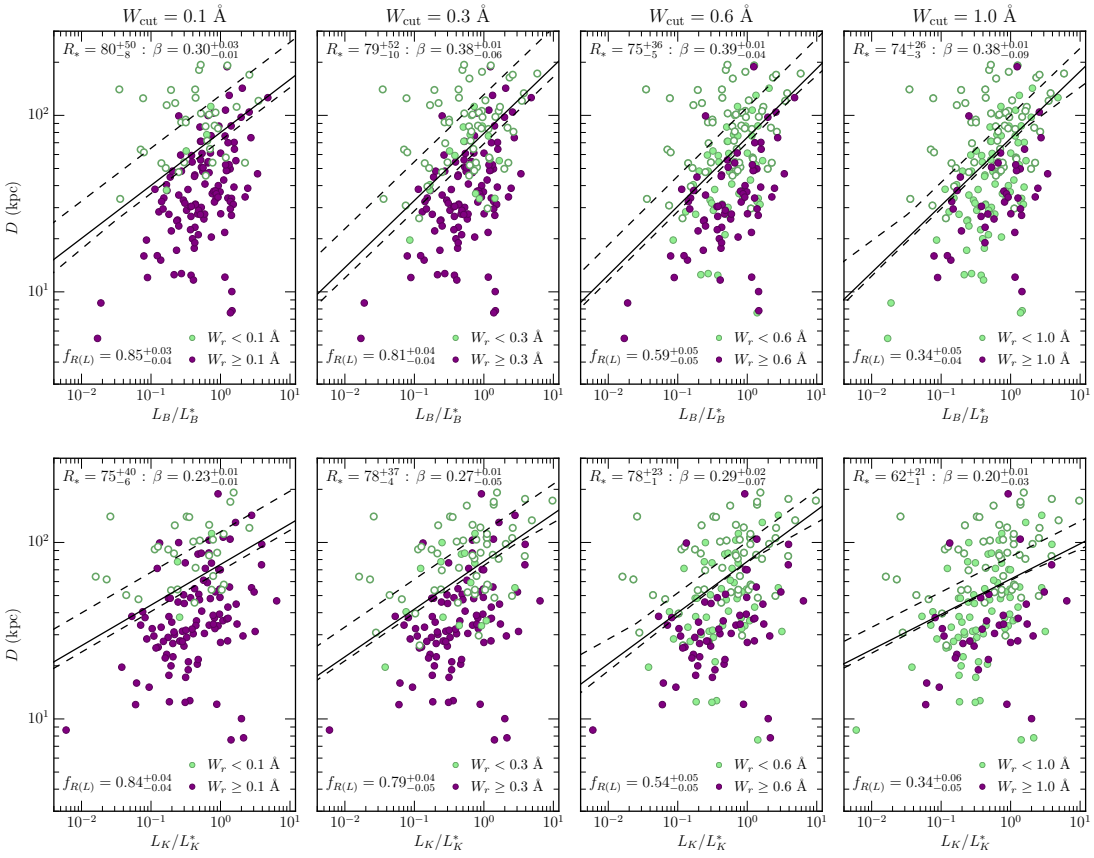

Fig. 3.5.— Impact parameter, D, vs. luminosity for different $W_r(2796)$ bifurcations at $W_{\rm cut}$. Green points are galaxies with $W_r(2796) < W_{\rm cut}$ (solid points) or an upper limit on absorption (open points) and purple points are galaxies with $W_r(2796) \geq W_{\rm cut}$. — (upper) B-band luminosity. — (lower) K-band luminosity. The fit parameters R_*, β, and $f_{R(L)}$ give the absorbing gas halo radius for an L^* galaxy, luminosity scaling power index, and absorption covering fraction, respectively, for each $W_r(2796) = W_{\rm cut}$ threshold (see Table 3.3). Dashed lines provide the envelope 1 σ uncertainties in the fit at fixed L/L^*. For $W_{\rm cut} = 0.1$ Å, galaxies with an upper limit on absorption greater than 0.1 Å were not included in the fitting process and are therefore not plotted.

Table 3.3. Luminosity Scaled Halo Absorption Radii

	B-band			K-band		
$W_{\rm cut}$ [Å]	R_* [kpc]	β	$f_{R(L)}$	R_* [kpc]	β	$f_{R(L)}$
0.1	80^{+50}_{-8}	$0.30^{+0.03}_{-0.01}$	$0.85^{+0.03}_{-0.04}$	75^{+40}_{-6}	$0.23^{+0.01}_{-0.01}$	$0.84^{+0.04}_{-0.04}$
0.3	79^{+52}_{-10}	$0.38^{+0.01}_{-0.06}$	$0.81^{+0.04}_{-0.04}$	78^{+37}_{-4}	$0.27^{+0.01}_{-0.05}$	$0.79^{+0.04}_{-0.05}$
0.6	75^{+36}_{-5}	$0.39^{+0.01}_{-0.04}$	$0.59^{+0.05}_{-0.05}$	78^{+23}_{-1}	$0.29^{+0.02}_{-0.07}$	$0.54^{+0.05}_{-0.05}$
1.0	74^{+26}_{-3}	$0.38^{+0.01}_{-0.09}$	$0.34^{+0.05}_{-0.04}$	62^{+21}_{-1}	$0.20^{+0.01}_{-0.03}$	$0.34^{+0.06}_{-0.05}$

Steidel (1995) reported $\beta \simeq 0.2$ and $R_* = 55$ kpc for the B-band and $\beta \simeq 0.15$ and $R_* = 58$ kpc for the K-band, both for $W_{\rm cut} = 0.3$ Å (the values of R_* quoted here have been converted to a "737" ΛCDM cosmology at the mean redshift, $\langle z \rangle = 0.65$, of his sample). He deduced a covering fraction of $f_{R(L)} \simeq 1$ and that β and R_* for the K-band are slightly smaller than for the B-band. Guillemin & Bergeron (1997) obtained similar results, with $R_* = 47$ kpc (adjusted from $q_0 = 0.05$ and h_{50} at $z = 0.7$) and $\beta = 0.28$ for the B-band with $W_{\rm cut} \simeq 0.3$ Å.

Using the observed Mg II absorber redshift path number density as a constraint, Kacprzak et al. (2008) explored the parameter space of the minimum luminosity of Mg II absorption-selected galaxies; the slope, β; the halo absorption radius, R_*; and covering fraction, $f_{R(L)}$. For $W_{\rm cut} = 0.3$ Å, they constrained R_* to the range 50–110 kpc, β to the range 0.2–0.28, and $f_{R(L)}$ to the range 50–80%. Our values of R_* reside in the range of allowed values from their study.

Chen et al. (2010a) reported $R_* = 107$ kpc with $\beta = 0.35$ for the B-band, where they fitted their data in the context of an isothermal sphere model (see Tinker & Chen 2008) of the Mg II CGM. For these values, they find $f_{R(L)} = 0.7$ for $W_{\rm cut} = 0.3$ Å and $f_{R(L)} = 0.8$ for $W_{\rm cut} = 0.1$ Å, both of which are $\sim 10\%$ smaller than what we find.

Employing the Tinker & Chen (2008) isothermal sphere model, Bordoloi et al. (2011) deduced $R_* = 115$ kpc. Whereas β for this work is consistent with the value reported by Chen et al. (2010a), the larger values of R_* reported by both Chen et al. (2010a) and Bordoloi et al. (2011) may be an artifact of their application of a model to the data. Furthermore, the methods of Bordoloi et al. (2011) involve "averaging" over annuli of fixed impact parameter, which may introduce

an additional systematic.

3.3.5.1. Galaxy Color To examine the dependence of $R(L)$ on galaxy color, we computed R_*, β, and $f_{R(L)}$ for red and blue galaxies, bifurcated by $B - K = 1.48$, in both the B- and K-bands. Due to the smaller number of galaxies in the blue and red subsamples (82 each), we adopted a single equivalent width cut, $W_{\rm cut} = 0.3$ Å (the median $W_r(2796)$ for galaxies with measured colors). As shown in Figure 3.6 and tabulated in Table 3.4, the parameters for $R(L)$ suggest a dependence on galaxy color in both the B- and K-bands.

In the B-band (top panels of Figure 3.6), we find that red galaxies have a steeper luminosity scaling, $\beta \sim 0.7$, than blue galaxies, $\beta \sim 0.5$, but a smaller covering fraction, $f_{R(L)} = 0.6$, than blue galaxies, $f_{R(L)} = 0.9$. The halo absorption radius for red galaxies, $R_* \sim 110$ kpc, is larger than for blue galaxies, $R_* \sim 87$ kpc. However, both values of R_* are consistent within uncertainties. These values are smaller than the model dependent values found by Bordoloi et al. (2011), who report 118 kpc for red galaxies and 107 kpc for blue galaxies, but the behavior of R_* with color is similar in that our red galaxies have larger R_* than blue galaxies.

The $R(L)$ dependence on galaxy color is similar in the K-band (bottom panels of Figure 3.6). The halo absorption radius, R_*, is again larger for red galaxies (though the values are still consistent within uncertainties), with $R_* \sim 75$ kpc and $R_* \sim 105$ kpc for blue and red galaxies, respectively. The luminosity scaling is steeper in red galaxies, $\beta \sim 0.5$, than blue galaxies, $\beta \sim 0.2$, and the covering fraction is larger in blue galaxies than red galaxies ($f_{R(L)} \sim 0.9$ and $f_{R(L)} \sim 0.6$, respectively).

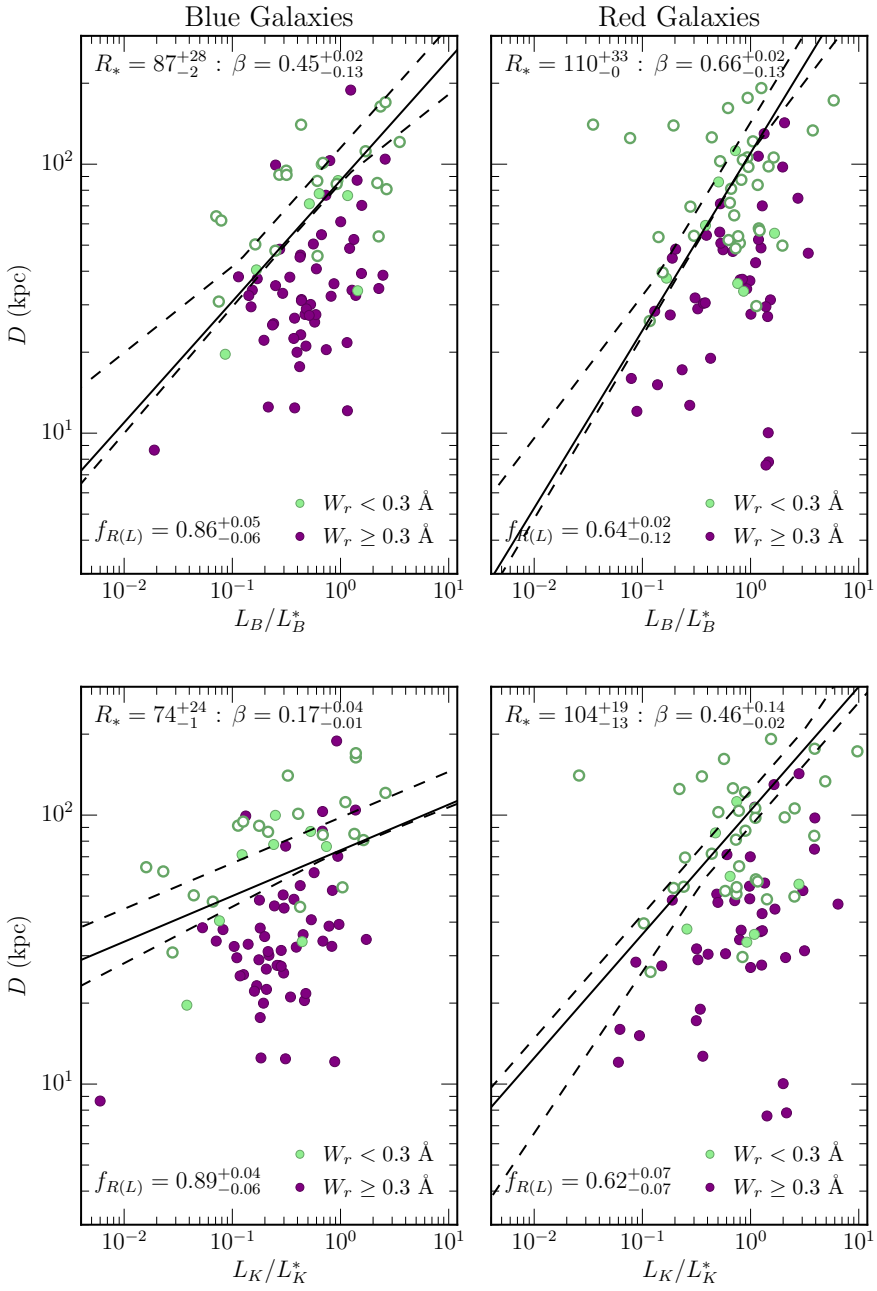

Fig. 3.6.— Impact parameter, D, vs. L_B/L_B^* (top) and L_K/L_K^* (bottom) for blue and red galaxies split by the median color $B-K=1.48$. Point types and curves are the same as Figure 3.5 for $W_{\rm cut}=0.3$ Å. The luminosity scaling, β, and radius, R_*, of the absorbing gas halo radius exhibits a color dependence for this $W_{\rm cut}$. In the B-band, blue galaxies have a steeper luminosity scaling, larger R_*, and larger covering fraction than red galaxies. For the K-band, we find R_* and β to be larger in red galaxies than blue, while blue galaxies still have a larger covering fraction.

Table 3.4. Luminosity Scaling for Subsamples at $W_{\rm cut} = 0.3$ Å

	B-band			K-band		
Sample	R_* [kpc]	β	$f_{R(L)}$	R_* [kpc]	β	$f_{R(L)}$
All	80^{+50}_{-8}	$0.30^{+0.03}_{-0.01}$	$0.85^{+0.03}_{-0.04}$	75^{+40}_{-6}	$0.23^{+0.01}_{-0.01}$	$0.84^{+0.04}_{-0.04}$
Blue	87^{+28}_{-2}	$0.45^{+0.02}_{-0.13}$	$0.86^{+0.05}_{-0.06}$	74^{+24}_{-1}	$0.17^{+0.04}_{-0.01}$	$0.89^{+0.04}_{-0.06}$
Red	110^{+33}_{-0}	$0.66^{+0.02}_{-0.13}$	$0.64^{+0.02}_{-0.12}$	104^{+19}_{-13}	$0.46^{+0.14}_{-0.02}$	$0.62^{+0.07}_{-0.07}$
Low $z_{\rm gal}$	80^{+38}_{-2}	$0.38^{+0.08}_{-0.04}$	$0.75^{+0.06}_{-0.07}$	78^{+32}_{-1}	$0.27^{+0.01}_{-0.04}$	$0.78^{+0.06}_{-0.07}$
High $z_{\rm gal}$	86^{+30}_{-1}	$0.27^{+0.07}_{-0.02}$	$0.85^{+0.05}_{-0.06}$	82^{+35}_{-4}	$0.26^{+0.01}_{-0.06}$	$0.83^{+0.05}_{-0.07}$

3.3.5.2. Galaxy Redshift We also examined the $R(L)$ dependence in both the B- and K-bands on galaxy redshift, slicing the sample into low and high redshift galaxies by the median redshift $\langle z \rangle = 0.359$, and adopting $W_{\rm cut} = 0.3$ Å. Values for R_*, β, and $f_{R(L)}$ are presented in Figure 3.7 and tabulated in Table 3.4.

In the B-band (top panels of Figure 3.7), we find $R_* \sim 80$ kpc, $\beta \sim 0.4$, and $f_{R(L)} \sim 0.75$ in the low z subsample. The high z subsample has similar values for R_* (~ 85 kpc) and $f_{R(L)}$ (~ 0.8), but a much shallower dependence on L_B/L_B^*, with $\beta \sim 0.3$. This difference in β may be due to selection effects in that the lowest luminosity galaxies ($L_B/L_B^* < 0.1$) are being selected against at high redshift. The selection methods for MAGIICAT galaxies are detailed in Paper I (Nielsen et al. 2013b). Additionally, the presence of galaxies at low z and low impact parameter may bias β to a larger value.

On the other hand, the K-band (bottom panels of Figure 3.7) shows no discernable difference within uncertainties between the low and high z subsamples. The values for R_*, β, and $f_{R(L)}$ for both subsamples are ~ 80 kpc, ~ 0.3, and ~ 0.8, respectively. Comparing to the apparent B-band evolution, this may imply that the luminosity dependence of the extent of the Mg II absorbing CGM is unchanged with redshift for the K-band. An alternate explanation is that the K-band is not impacted by selection effects as much as the B-band since K-band absolute magnitudes and luminosities were calculated from apparent K-band magnitudes for half of the sample. The K-band apparent magnitude is not one of the galaxy selection criteria (Nielsen et al. 2013b).

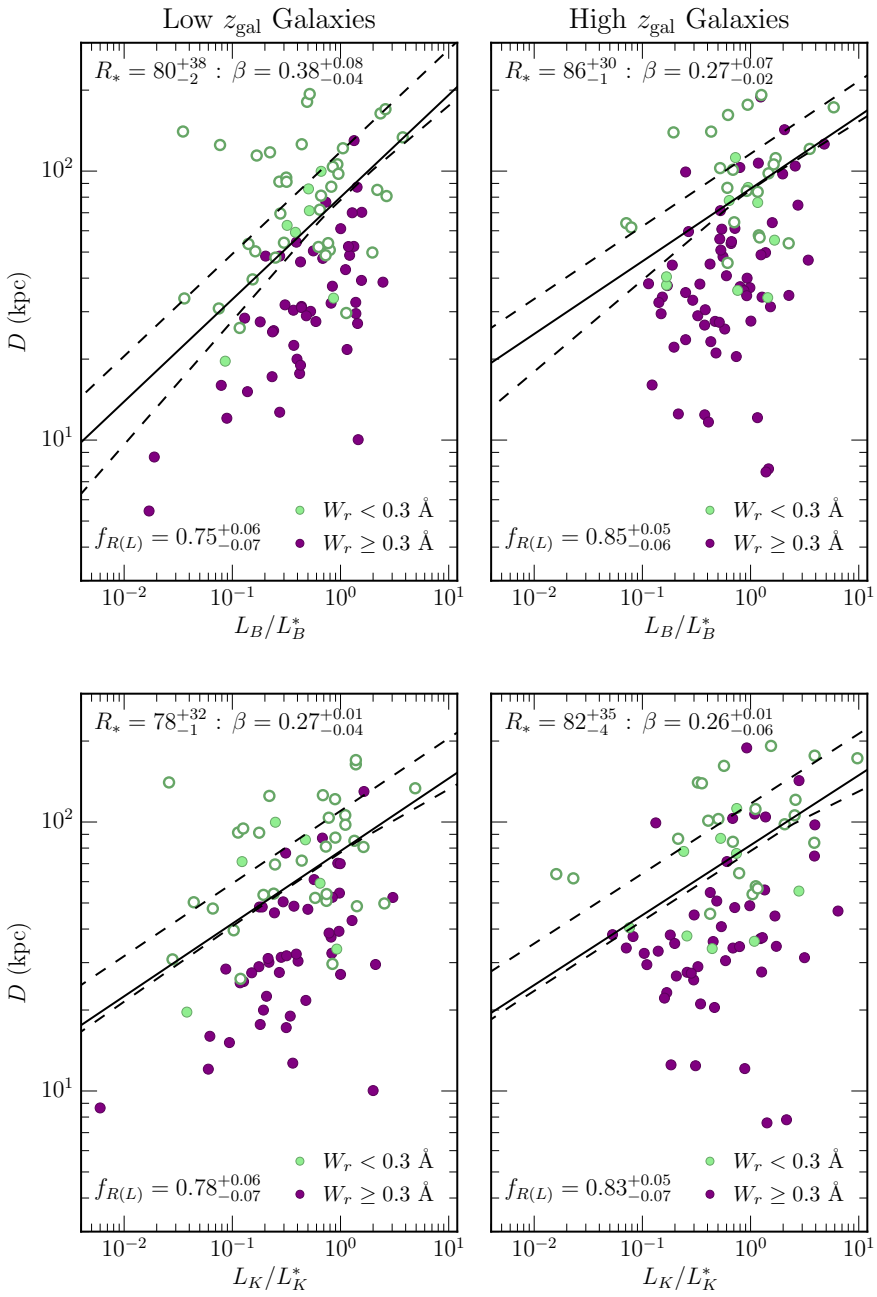

Fig. 3.7.— Impact parameter, D, vs. L_B/L_B^* (top) and L_K/L_K^* (bottom) for low and high redshift galaxies sliced by the median redshift $z_{\rm gal} = 0.359$. Point types and curves are the same as Figure 3.5 for $W_{\rm cut} = 0.3$ Å. The average z for the low redshift subsample is 0.23 and the average for the high redshift subsample is 0.61, which is a ~ 3.2 Gyr difference.

3.4. Discussion

With the larger sample afforded by MAGIICAT, we have obtained additional leverage to probe the dependence of the properties of the MgII absorbing CGM with galaxy color, redshift, luminosity, impact parameter, and $W_r(2796)$ threshold. For our analysis, we have purposely avoided couching the data within the framework of model expectations or scaling various measured quantities with "second parameters", such as scaling the impact parameter by galaxy luminosity, in order to provide a direct view of the CGM-galaxy connection and to interpret the data from a purely observational perspective.

We confirm the well-known anti-correlation between MgII equivalent width, $W_r(2796)$, and impact parameter, D, which is significant to the 7.9σ level. We find that the general behavior of this anti-correlation on the $W_r(2796) - D$ plane is best fit by a log-linear fit to the data, $\log W_r(2796) = \alpha_1 D + \alpha_2$, where $\alpha_1 = -0.015 \pm 0.002$ and $\alpha_2 = 0.27 \pm 0.11$. This is in contrast to the power law fit obtained by Chen et al. (2010a). Our log-linear fit predicts a leveling off of $W_r(2796)$ as D goes to zero, whereas the Chen et al. (2010a) fit does not. In fact, for $D = 5$ kpc, which is roughly the smallest impact parameter in MAGIICAT, our log-linear fit predicts $W_r(2796) \simeq 1.6$ Å, while the power law predicts $W_r(2796) \simeq 4.4$ Å (and continues to increase, for example at $D = 1$ kpc, the power law fit predicts $W_r(2796) \simeq 30$ Å). It would seem reasonable that the equivalent width distribution should flatten as one probes galaxy disks as $W_r(2796) > 10$ Å has yet to be reported in the literature, even for the Milky Way interstellar medium.

As many previous works have noted (see Section 3.3.3 for references), there is considerable scatter in the $W_r(2796) - D$ plane, which we also observe in Figure 3.1.

Slicing MAGIICAT by the median values of $B-K$, $z_{\rm gal}$, L_B/L_B^*, and L_K/L_K^* (see Figure 3.2), we find that the scatter is not related to galaxy color or redshift. However, we do find that the scatter may be related to galaxy luminosities such that higher luminosity galaxies systematically populate the $W_r(2796)-D$ plane at larger $W_r(2796)$ and larger D. Performing a 2DKS test on luminosities in the $W_r(2796)-D$ plane, we find this result to be significant to the 4.2σ level for the B-band and to the 4.3σ level for the K-band. Given that the K-band can be considered a proxy for stellar mass, this result may indicate that the scatter in the $W_r(2796)-D$ plane is actually due to galaxy mass such that more massive galaxies have larger $W_r(2796)$ for a given D. In fact, Churchill et al. (2013b) find this to be true for MAGIICAT galaxies with the galaxy virial mass obtained using halo abundance matching.

Alternatively, the luminosity segregation on the $W_r(2796)-D$ plane may be due to a gas metallicity-luminosity correlation. For damped Lyα systems, Turnshek et al. (2005) found that gas metallicity correlates with Mg II equivalent width. If higher luminosity galaxies have more metal-rich gas, then $W_r(2796)$ would tend to be larger than for lower luminosity galaxies, and the gas would be detectable to larger impact parameters. This behavior on the $W_r(2796)-D$ plane might have some relationship to the observed metallicity bimodality in Lyman limit systems (Lehner et al. 2013).

With regard to the relationship between galaxy color and $W_r(2796)$, our results challenge those of previous studies. For the overall sample, we find no correlation between $W_r(2796)$ and $B-K$. However, we find that for the subsample with $W_r(2796)\geq 1$ Å, redder galaxies have larger $W_r(2796)$ with a significance level of 2.5σ. These findings are contrary to the results of Zibetti et al. (2007)

and Bordoloi et al. (2011), who both report larger $W_r(2796)$ associated with bluer galaxies. It is difficult to rectify the inconsistencies of our findings with those works unless the solution originates in the different experimental methods.

Zibetti et al. (2007) developed an image stacking method in which the individual galaxies are not identified, but light from galaxies in various SDSS photometric bands are measured *relative to control fields* for which the quasars show no Mg II absorption. The color cuts of the galaxies studied by Bordoloi et al. (2011) are based upon a color-mass relation using $u - B$ colors. Furthermore, the equivalent widths measured by Bordoloi et al. (2011) are based on stacked spectra over fixed impact parameter annuli in which the Mg II doublet is not resolved, whereas those measured in this work are based upon pencil-beam probes of the CGM for which all doublets are cleanly resolved. If the CGM is intrinsically patchy (see Churchill et al. 2013a) with covering fraction dependencies on $W_r(2796)$ threshold and galaxy luminosity (as we have demonstrated in this paper), then the two methods (statistical versus case-by-case) may be providing different but complimentary clues to the nature of the CGM.

Our analysis of the covering fraction profile of the Mg II absorbing CGM as a function of impact parameter, galaxy luminosity, and absorption strength threshold provides improved insights on the extent and distribution of the low ionization, metal-enriched CGM (see Figure 3.4 and Table 3.2). The decrease in the covering fraction with increasing absorption threshold indicates that the cross-section of the highest column density and/or most kinematically dispersed gas (plausibly winds material) is smaller than the cumulative cross-section including lower column density, kinematically quiescent gas (plausibly accretion material).

Additional insight is provided by the relative behavior of the covering fraction profile of low and high luminosity galaxies (bifurcated at $L_B/L_B^* = 0.611$). First, the Mg II absorbing CGM appears to extend no further than 100 kpc for low luminosity galaxies. Second, the CGM at $D \geq 100$ kpc surrounding high luminosity galaxies is dominated by lower column density, kinematically quiescent gas traced by $W_r(2796) < 0.6$ Å absorption; the cross-section of this material increases as the equivalent width threshold is decreased to 0.1 Å. In contrast, within $D < 100$ kpc, the observed frequencies of lower and higher column density CGM gas is not strongly dependent on galaxy luminosity for $W_{\rm cut} = 0.1$, 0.3, and 0.6 Å, but for $W_{\rm cut} = 1.0$ Å, high luminosity galaxies have a higher observed frequency of Mg II absorbing CGM. For $D \leq 25$ kpc, the covering fraction is effectively unity for the thresholds $W_r(2796) \geq 0.1$ and 0.3 Å, but declines for $W_r(2796) \geq 0.6$ and 1.0 Å as the threshold is increased.

These results indicate a strong luminosity dependence in cross-sections and extent of the Mg II absorbing CGM such that high luminosity galaxies have both a much more extended diffuse CGM than low luminosity galaxies and higher filling factors of the highest column density material within 50 kpc as compared to low luminosity galaxies. Since the luminosity segregation we are employing is for the B-band, we could be seeing a connection between the CGM and young stars, such that the increased presence of young stars is related to a greater cross-section of higher column density gas in the inner regions of the galaxies and a more extended distribution of the lower column density gas in the outer regions of the galaxies (beyond 100 kpc). This would imply a stellar driven mechanism for distributing the gas further out into the CGM.

We also find a difference in the covering fraction as a function of galaxy color

outside of 100 kpc. In this case, blue galaxies have higher covering fractions than red galaxies, which have no absorption beyond 100 kpc for the highest column density material ($W_r(2796) \geq 0.6$ Å). Blue galaxies are more likely to host the galactic-scale winds which lift more metal-rich material into the halo. Therefore, the larger covering fractions in blue galaxies could be due to more metal-rich material present at large impact parameters. Lehner et al. (2013) concluded that Lyman limit systems, which trace the cool CGM, have a bimodal metallicity distribution where the metal-poor branch is likely probing cold accretion streams while the metal-rich branch could be tracing recycled outflowing winds. Therefore, our implied stellar driven mechanism may be driving more metal-rich material into the CGM. This metal-rich material may result in larger $W_r(2796)$, which in turn could cause higher covering fractions for more luminous galaxies at large impact parameters.

Following previous studies, we have assumed the relation $R(L) = R_*(L/L^*)^\beta$ to describe the "halo absorption radius" dependence on luminosity. For the B-band luminosity, we find that the sensitivity of $R(L)$ to luminosity (the parameter β, see Table 3.3 and Figure 3.5) increases as the equivalent width threshold is raised. For $W_r(2796) \geq 0.1$ Å, we find $\beta \simeq 0.3$, and for $W_r(2797) \geq 0.3$, 0.6, and 1.0 Å, we find $\beta \simeq 0.4$. The extent for an L_B^* galaxy decreases with increasing equivalent width threshold. We find $R_* \simeq 80$ kpc for $W_r(2796) \geq 0.1$ and 0.3 Å, and $R_* \simeq 75$ kpc for $W_r(2796) \geq 0.6$ and 1.0 Å, though these values are consistent within uncertainties. In the K-band, we find similar values of R_* ($\sim$ 80 kpc) for $W_{\rm cut} = 0.1$, 0.3, and 0.6 Å, while the most optically thick gas has a much smaller absorption radius ($R_* \sim 60$ kpc for $W_{\rm cut} = 1.0$ Å). Furthermore, we find a shallower dependence of $R(L)$ on the K-band luminosity, where β ranges

from ~ 0.2 to ~ 0.3. The greater extent in the most optically thick gas for the B-band compared to the K-band and the higher luminosity sensitivity to the B-band relative to the K-band would further strengthen the idea that the geometric extent and morphology of the Mg II absorbing CGM is governed in large part by young stars.

There is an indication that galaxy color directly plays a role in governing the luminosity sensitivity of $R(L)$. For $W_r(2796) \geq 0.3$ Å, red galaxies have a remarkably steeper luminosity dependence than do blue galaxies in the B-band. For red galaxies, we find $\beta = 0.66$, whereas for blue galaxies, we find $\beta = 0.45$. In the B-band, the covering fraction within $R(L)$ of red galaxies is $\simeq 30\%$ lower than for blue galaxies. For the K-band, red galaxies still have a much steeper luminosity dependence ($\beta = 0.46$) than blue galaxies ($\beta = 0.17$), as well as a $\sim 40\%$ smaller covering fraction. In studying the K-band of Figure 3.6, it is apparent that red galaxies are, on average, brighter in the K-band than blue galaxies. Using the K-band luminosity as a proxy for stellar mass, this indicates that red galaxies are, on average, more massive than blue galaxies. Therefore, we may be seeing that the halo absorption radius depends on the mass of the galaxy such that more massive galaxies have larger halo absorption radii resulting in a larger β for redder, more massive galaxies. The dependence of the halo absorption radius on mass is explored in more depth in the third paper of this series (Churchill et al. 2013c).

We strongly caution that the function $R(L)$ should not be viewed as a well-defined outer boundary to the Mg II absorbing CGM. The values of R_* and β are dependent on the sample and may change if we obtain more low luminosity galaxies with $L/L^* < 0.1$. We are confident, however, that larger luminosity galaxies have a more extended CGM, i.e., the value of β is positive for both the

B- and K-bands. Additionally, examination of the data on the D–L/L^* plane shown in Figure 3.5 clearly reveals that a non-negligible number of galaxies with $W_r(2796)$ greater than the threshold cut also reside above the curve. The 1σ upper envelope of the $R(L)$ boundary characterizes the presence of these galaxies. These galaxies also drive the large upward uncertainties in the best fit R_*. Note that this uncertainty increases from $\simeq 26$ to $\simeq 50$ kpc as the absorption threshold is decreased from $W_r(2796) \geq 1.0$ to 0.1 Å. This suggests that the $R(L)$ boundary is less well defined for the lower column density structures of the CGM. Physically, the behavior of the data in this regime of impact parameter and $W_r(2796)$ could either reflect a greater level of patchiness in the low column density material residing in the outskirts of the CGM of individual galaxies or a broad range of CGM properties from galaxy to galaxy.

3.5. Summary

Combining our previous studies and the extant works in the literature, we have compiled a "MgII Absorber-Galaxy Catalog" (MAGIICAT) of intermediate redshift galaxies and their associated circumgalactic medium (CGM) as probed using MgII $\lambda\lambda 2796, 2803$ absorption. Details of the MAGIICAT data are presented in Paper I (Nielsen et al. 2013b). In this paper, we present results from a first analysis in which we compare only direct observables and avoid converting or scaling the data to a preferred CGM model, focusing exclusively on "isolated" galaxies, which are defined to have no neighboring galaxy within a projected distance of 100 kpc and line of sight velocity within 500 km s^{-1}.

The sample presented here comprises 182 galaxies toward 134 quasar sight-

lines over the redshift range $0.072 \leq z_{\rm gal} \leq 1.120$, with median $\langle z \rangle = 0.359$. The rest-frame magnitudes range from $-16.1 \geq M_B \geq -23.1$ ($0.02 \leq L_B/L_B^* \leq 5.87$) and $-17.0 \geq M_K \geq -25.3$ ($0.006 \leq L_K/L_K^* \leq 9.71$) with AB rest-frame colors $0.04 \leq B-K \leq 4.09$. The median B-band luminosity is $L_B/L_B^* = 0.611$ and the median color is $B-K = 1.48$.

The main results are:

1. The mean M_B increases with increasing redshift (4.4σ), whereas M_K exhibits a weak trend to increase with redshift (2.2σ). Galaxy luminosities L_B/L_B^* and L_K/L_K^* do not evolve with redshift. The rest-frame $B-K$ color shows no redshift evolution, consistent with the findings of Zibetti et al. (2007).

2. There is no correlation between $W_r(2796)$ and $B-K$ for the full sample (1.3σ). However, for galaxies associated with $W_r(2796) \geq 1.0$ Å absorption, $B-K$ correlates with $W_r(2796)$ at 2.5σ, indicating a trend that redder galaxies have stronger absorption in this equivalent width regime. In our sample, the distributions of $W_r(2796)$ within $D = 50$ kpc of blue ($B-K < 1.48$) and red ($B-K \geq 1.48$) galaxies are consistent with being drawn from the same parent distribution (0.3σ). The $W_r(2796)$-color correlation in our sample conflicts with the $W_r(2796)$-color anti-correlation reported by Zibetti et al. (2007). Both the $W_r(2796)$-color correlation and the indistinguishable $W_r(2796)$ distributions in our sample are in conflict with the findings of Bordoloi et al. (2011), who report eight times stronger $W_r(2796)$ within $D = 50$ kpc associated with bluer galaxies.

3. Including upper limits on $W_r(2796)$, we find that the significance level of the well-known anti-correlation between $W_r(2796)$ and impact parameter, D, is

7.9σ for this sample. The best parameterization is a log-linear relation, for which we find $\log W_r(2796) = (-0.015 \pm 0.002)D + (0.27 \pm 0.11)$. The scatter in this relation may be due to the redshifts, colors, or luminosities of the galaxies. Splitting the sample by the K-band luminosity yields a 4.3σ significance that low and high L_K/L_K^* galaxies are separate populations on the $W_r(2796) - D$ plane such that higher K-band luminosity galaxies tend to have higher $W_r(2796)$ at a given impact parameter. Dividing the sample into quartiles based on the redshift, color, or luminosity of the galaxies and comparing the lowest and highest quartiles yields at best a 3.4 σ significance with K-band luminosity.

4. The covering fraction profiles with projected distance from the galaxy, $f_{D\max}$ and $f_{\langle D\rangle}$, decrease with both increasing D and increasing minimum $W_r(2796)$ (see Figures 3.3 and 3.4). High luminosity galaxies have higher covering fractions. In terms of $f_{\langle D\rangle}$, this difference is greatest at $100 < D \leq 200$ kpc for absorbing CGM gas with $W_r(2796) \geq 0.1$ Å and at $D \leq 50$ kpc for CGM gas with $W_r(2796) \geq 1.0$ Å. There is no clear difference between the covering fraction profile of blue galaxies versus red galaxies within 100 kpc, though the gas in red galaxies may be more concentrated near the center of the galaxy than in blue galaxies. Outside 100 kpc, red galaxies have smaller covering fractions than blue galaxies and no absorption for $W_r(2796) \geq 0.6$. The high redshift galaxies ($z \geq \langle z\rangle$) have a higher covering fraction than the low redshift galaxies ($z < \langle z\rangle$) at $D > 50$ kpc.

5. We determined the best-fit parameters R_* and β for the luminosity scaling of the outer envelope for absorption, or the "halo absorption radius",

$R(L) = R_*(L/L^*)^\beta$, for both the B- and K-bands as a function of $W_r(2796)$ threshold. For the B-band, the luminosity scaling increases from $\beta \sim 0.3$ to $\beta \sim 0.4$ with increasing $W_{\rm cut}$. We find $R_* \sim 80$ kpc for $W_{\rm cut} = 0.1$ and 0.3 Å, and $R_* \sim 75$ kpc for $W_{\rm cut} = 0.6$ and 1.0 Å. The covering fraction inside $R(L_B)$ decreases from $f_{R(L)} = 0.85$ for $W_{\rm cut} = 0.1$ Å to $f_{R(L)} = 0.34$ for $W_{\rm cut} = 1.0$ Å. For the K-band, the luminosity scaling ranges from $\beta \sim 0.2$ to 0.3, and R_* ranges from ~ 60 kpc to ~ 80 kpc. The covering fraction behaves similarly to the B-band. Though the "outer envelope" for absorption has a clear dependence on both luminosity and $W_r(2796)$ threshold, we note that the scatter in the data in the $W_r(2796)$-D plane, the behavior of the covering fraction profile $f_{\langle D \rangle}$ with increasing D, and the relatively extended upward uncertainties in R_* all indicate that $R(L)$ is not a well-defined quantity, but should be interpreted as a "fuzzy" boundary and that the "fuzziness" increases with decreasing equivalent width threshold.

6. Dividing the galaxies by the median color ($B - K = 1.48$), adopting $W_{\rm cut} = 0.3$ Å, and examining the fit parameters to $R(L) = R_*(L/L^*)^\beta$, we find that red galaxies have a steeper luminosity scaling, β, and larger halo absorption radii, R_*, than blue galaxies in both the B- and K-bands. This behavior of larger R_* for red galaxies is consistent with the results of Bordoloi et al. (2011), though our values are smaller. Using the K-band as a proxy for stellar mass, we may be seeing that the difference in the values of R_* and β between red and blue galaxies is due to the mass of a galaxy such that more massive galaxies have larger halo absorption radii (also see Churchill et al. 2013c).

7. We also examined the $R(L)$ dependence in both the B- and K-bands on galaxy redshift, slicing the sample at the median redshift $z = 0.359$, and adopting $W_{\rm cut} = 0.3$ Å. In the B-band, we find $R_* \sim 80$ kpc, $\beta \sim 0.4$, and $f_{R(L)} \sim 0.8$ in the low z subsample. The high z subsample has similar values for R_* (~ 85 kpc) and $f_{R(L)}$ (~ 0.8), but a much shallower dependence on L_B/L_B^*, with $\beta \sim 0.3$. In the K-band, we find no discernable difference within uncertainties between the low and high z subsamples. The values for R_*, β, and $f_{R(L)}$ for both subsamples are ~ 80 kpc, ~ 0.3, and ~ 0.8, respectively.

This work constitutes our first examination of the relationship of the Mg II absorbing CGM with galaxy properties using MAGIICAT. In particular, we have examined the data by comparing direct observables and have avoided analyzing the quantities based upon converting or scaling the data to a preferred model of the CGM. Our aim has been to provide an unfiltered view of the Mg II absorbing CGM. Nonetheless, the simple bivariate testing we have conducted here does not provide full leverage for probing of the available data. In future work, we will apply multivariate analysis methods in which we also incorporate mass estimates of the galaxies, Mg II kinematics, and both low and high ionization absorption strengths of the CGM for these galaxies. We will also conduct comparative studies of the isolated galaxies and group galaxies in the catalog.

We thank the anonymous referee for a careful reading of the manuscript and for valuable input that improved this work. We also thank Nick Gnedin for reading and providing insightful comments on an earlier draft. This research was primarily supported through grant HST-AR-12646 provided by NASA via

the Space Telescope Science Institute, which is operated by the Association of Universities for Research in Astronomy (AURA) under NASA contract NAS 5-26555. This work was also supported by the Research Enhancement Program provided by NASA's New Mexico Space Grant Consortium (NMSGC). NMN was also partially supported through a NMSGC Graduate Fellowship and a three-year Graduate Research Enhancement Grant (GREG) sponsored by the Office of the Vice President for Research at New Mexico State University.

4. MAGIICAT IV. KINEMATICS OF THE MgII ABSORBING CIRCUMGALACTIC MEDIUM

The contents of this chapter have been submitted for publication in the Astrophysical Journal as Nielsen, N. M., Churchill, C. W., Kacprzak, G. G., Murphy, M. T., & Evans, J. L. 2013, ApJ

We examine the kinematics of the Mg II absorbing circumgalactic medium for 47 galaxies ($0.3 < z_{\rm gal} < 1.0$) as a function of galaxy rest-frame $B-K$ color, redshift, $z_{\rm gal}$, and virial radius-normalized projected impact parameter, $D/R_{\rm vir}$. We find that most absorbers span a velocity range of $v_{\rm cloud} = |150|$ km s^{-1} with respect to the velocity at the optical depth weighted mean and absorbers are mostly located within $v_{\rm cloud-galaxy} = |200|$ km s^{-1} of the host galaxy systemic redshift. We also examine pixel velocity two-point correlation functions (TPCFs) for our galaxy subsamples. We find evidence for the quenching of star formation in red galaxies, where the internal absorber TPCFs for red galaxies are more extended at high redshift than at low redshift, but ongoing evolution in blue galaxies, with no difference in the TPCFs between low and high redshift. The velocities of absorbers around red galaxies at low redshift are large, indicating that the absorbers are unlikely to accrete onto the galaxy. Conversely, we find smaller absorber-galaxy velocities in blue galaxies which suggest that the gas traced by these absorbers may (re-)accrete onto the galaxy. The internal absorber TPCFs of red galaxies comparing low and high $D/R_{\rm vir}$ follow the anticorrelation between Mg II equivalent width and $D/R_{\rm vir}$ such that the velocity dispersions at low $D/R_{\rm vir}$ are larger than at high $D/R_{\rm vir}$, but we do not see this trend in blue galaxies. Large velocity separation peaks in the absorber-galaxy TPCFs of both blue and red galaxies may be indicative of outflows, merging satellite galaxies, or both.

4.1. Introduction

Through extensive observations and detailed simulations, it has become clear that the baryon cycle plays a key role in governing the evolution of galaxies. In this scenario, galaxies grow by accreting pristine gas from the intergalactic medium (IGM), which is the fuel for star formation. Intense star formation and/or supernovae then drive outflowing galactic-scale winds, entraining portions of the interstellar medium (ISM) and coplanar gas along the way. Serving as the interface between the IGM and the ISM, the circumgalactic medium (CGM) contains the gas that is too hot to accrete onto the galaxy itself due to shock heating and stores outflowing material until it re-accretes onto the galaxy. Thus, the CGM is massive, with estimates of $M_{\rm CGM} > 10^9 M_\odot$ (Thom et al. 2011; Tumlinson et al. 2011; Werk et al. 2013), a gas mass comparable to the galaxy itself.

Extensive amounts of work have studied the CGM using quasar absorption lines in which a background quasar sightline pierces the CGM within a few hundred kiloparsecs projected on the sky. Much of this work has been focused on Mg II $\lambda\lambda 2796, 2803$ absorption, which traces gas in a wide range of environments (including accretion and outflows) for a large redshift range ($0.1 < z < 2.5$) at which Mg II is observable from the ground. By examining Mg II absorption in infrared wavelengths using the FIRE spectrograph on Magellan, Matejek & Simcoe (2012) were able to extend this redshift range out to $z < 6$ (however they have yet to identify the host galaxies in each case). They found evidence that the incidence rate, dN/dz, of the strongest Mg II absorbers traces the global star formation rate density, with a peak between $2 < z < 3$, decreasing to lower redshifts. In Matejek et al. (2013), they further stated that the most kinematically complex absorbers

(which tend to be the strongest absorbers) also appear to follow the global star formation rate. Nielsen et al. (2013a, Paper II of the MAGIICAT series) and Churchill et al. (2013b) found that the MgII equivalent width, $W_r(2796)$, anti-correlates with D ($\sim 7\sigma$) and $D/R_{\rm vir}$ ($\sim 9\sigma$), respectively. Given that $W_r(2796)$ correlates with the number of clouds or Voigt profile (VP) components (Petitjean & Bergeron 1990; Churchill et al. 2003; Evans 2011), this indicates that either the column densities, velocity spreads, or both diminish with projected distance from the galaxy. These results indicate that examining the kinematics of the gas traced by MgII absorption over time and space is critical in understanding the detailed physics of the baryon cycle processes occurring in the CGM.

Many works examining MgII kinematics have focused on the clustering of VP components in MgII absorbers by constructing a two-point correlation function (TPCF) for their samples using VP components, but they do not have the properties of the galaxies hosting the absorption (Sargent et al. 1988; Petitjean & Bergeron 1990; Churchill 1997; Churchill & Vogt 2001; Churchill et al. 2003; Evans 2011). Both Petitjean & Bergeron (1990) and Churchill et al. (2003) fit their absorber TPCFs with two Gaussian components. Petitjean & Bergeron (1990) interprets their narrow component as being due to the relative motions of clouds within halos, while Churchill et al. (2003) associate it with vertical dispersions in face-on galaxy disks. The second and more broad component may represent the relative motions of galaxy pairs in the field (Petitjean & Bergeron 1990) or rotational motions in edge-on disks (Churchill et al. 2003).

More recently, Evans (2011) required three components to fit their TPCF because their sample is more than an order of magnitude larger than previous works and therefore more sensitive to an extended tail in the distribution. These

authors did not try to interpret their fitted Gaussian components, stating that doing so would be an oversimplification. This is reasonable since their absorber sample spans a large redshift range ($0.1 < z_{\rm abs} < 2.6$) and likely probes the CGM of a variety of galaxy types. In fact, we show in Papers II and III of the series (Nielsen et al. 2013a; Churchill et al. 2013c), as well as in Churchill et al. (2013b), that typical measures of the CGM via absorption such as $W_r(2796)$, the covering fraction, and the luminosity-scaled radius depend on galaxy color, redshift, impact parameter, and halo mass.

Recent work by Tumlinson et al. (2013) and Werk et al. (2013) who study absorption by HI and intermediate ions (MgII, CII, CIII, and/or SiIII), respectively, examined the full velocity extent and VP component velocities relative to the galaxy systemic velocity as a function of impact parameter, halo mass, and whether the host galaxy is star forming or quiescent. Both works found that most absorption is located within ± 200 km s^{-1} of the galaxy and spans the galaxy systemic velocity, inferring that the material is bound to the galaxy. Tumlinson et al. (2013) also found that the kinematics of HI absorbers do not depend on galaxy type. Also examining HI in addition to OVI, Mathes et al. (2014) found that most absorption is located within ± 500 km s^{-1}, but the kinematics (bound fraction of gas, in particular) depend on $\log(M_{\rm h}/M_{\odot})$ and $D/R_{\rm vir}$, which they call differential kinematics.

What many (but not all) of these previous works lack is connecting the detailed kinematics of these absorbers to the properties of the host galaxy. In this paper, we build upon previous work and examine the kinematics of MgII absorption for both TPCFs and individual VP components as a function of galaxy rest-frame $B-K$ color, redshift, $z_{\rm gal}$, and virial radius-normalized impact param-

eter, $D/R_{\rm vir}$. We organize this paper as follows. Section 4.2 details our sample, including both galaxy properties and quasar spectra. Section 4.3 reviews the literature on characterizing quasar absorption line kinematics in terms of both Voigt profile components and the two-point velocity correlation function. In this section, we also detail our methods for calculating several types of pixel velocity two-point correlation functions (TPCFs) and present our results examining TPCFs for bivariate cuts in galaxy rest-frame color, $B-K$. Section 4.4 presents a multivariate analysis in the TPCFs for cuts in galaxy color, redshift, and virial radius-normalized impact parameter. We discuss our results in Section 4.5, and summarize and conclude our findings in Section 4.6.

4.2. Sample and Data Analysis

4.2.1. Galaxy Properties

All 47 galaxies ($0.3 < z_{\rm gal} < 1.0$) studied here are a subset of the Mg II Absorber-Galaxy Catalog (MAGIICAT) and we refer the reader to Paper I of the series (Nielsen et al. 2013b) for full details on where the data were obtained, the galaxy selection methods, and how the galaxy properties were determined. To summarize, each galaxy is spectroscopically identified to be located at the redshift of an associated Mg II absorber (whether absorption was detected and measured *a priori* or not) and within a projected distance $D < 200$ kpc from a background quasar. All galaxies are isolated to the limits of the data, where isolation is defined as having no spectroscopically identified galaxy within 100 kpc (projected) and within a line of sight velocity separation of 500 km s^{-1}. For each galaxy, we have spectroscopic redshifts, $z_{\rm gal}$, rest-frame B- and K-band AB magnitudes and luminosities, rest-frame $B-K$ colors, and quasar-galaxy impact parameters, D.

We also have halo masses, $\log(M_{\rm h}/M_{\odot})$, virial radii, $R_{\rm vir}$, and maximum circular velocities, $V_{\rm circ}$, from halo abundance matching, the details for which are presented in Paper III (Churchill et al. 2013c).

We slice our sample into various subsamples based on median galaxy rest-frame color, $B-K$, redshift, $z_{\rm gal}$, and impact parameter normalized by the virial radius, $D/R_{\rm vir}$. A summary is presented in Table 4.1, which details the median value(s) by which the subsamples were defined and the number of galaxies in each subsample. The subsample names listed will be used throughout this paper.

We note that, though the focus of this paper is on galaxy $B-K$ colors, we cannot disentangle effects due to color from those due to galaxy halo masses, $\log(M_{\rm h}/M_{\odot})$, which were calculated in Churchill et al. (2013b,c). A Kendall-τ rank correlation test on color and mass results in a 2.8σ correlation such that redder galaxies tend to be more massive. Figure 4.1 presents $B-K$ versus $\log(M_{\rm h}/M_{\odot})$ with points colored by $z_{\rm gal}$. Dashed lines indicate the median color and mass of the sample. Almost all galaxies in our sample lie within the blue, low mass or red, high mass regions of Figure 4.1, with the exception of four blue, high mass galaxies and four red, low mass galaxies. If we instead conduct our analysis with $\log(M_{\rm h}/M_{\odot})$, we find no significant differences in the TPCFs when we compare blue samples to low mass samples or red to high mass samples. Therefore, any differences we find in the TPCFs is due to a color-mass dependence rather than just a color dependence.

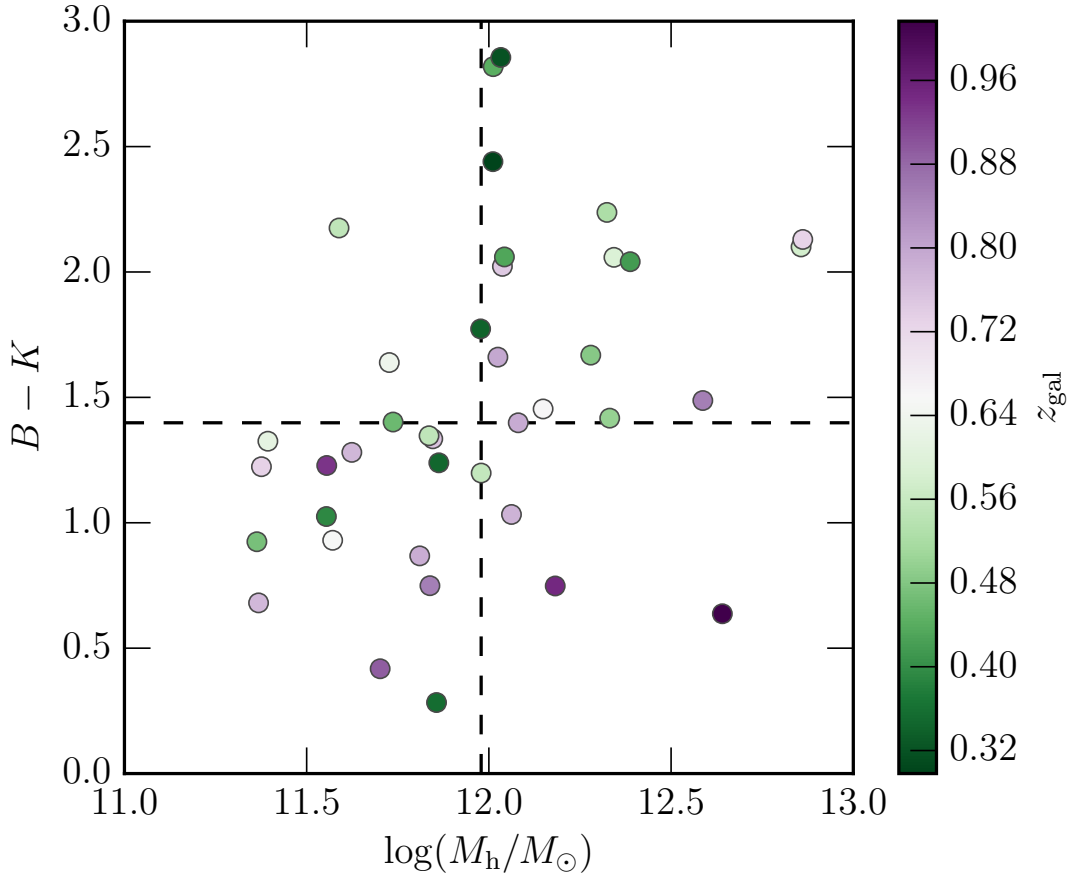

Fig. 4.1.— Galaxy rest-frame $B-K$ color versus halo mass, $\log(M_{\rm h}/M_\odot)$. Point colors indicate the galaxy redshift, $z_{\rm gal}$, where the median redshift is $\langle z_{\rm gal}\rangle = 0.656$, roughly corresponding to the white portion of the color bar. The vertical dashed line represents the median $\log(M_{\rm h}/M_\odot)$ of the sample and the horizontal dashed line is the median $B-K$. A Kendall's τ rank correlation test comparing $B-K$ to $\log(M_{\rm h}/M_\odot)$ found a correlation with a significance of 2.8σ. This is represented as having most points located in the blue, low mass or red, high mass subsamples.

4.2.2. Quasar Spectra

Quasar spectra were observed with HIRES on Keck (Vogt et al. 1994) or UVES on the VLT (Dekker et al. 2000). Most spectra and details of their reduction are published in Churchill (1997), Churchill & Vogt (2001), Evans (2011), and/or Kacprzak et al. (2011b). We obtained two additional reduced HIRES/Keck spectra through private communication with C. C Steidel and J.-R. Gauthier. These spectra were reduced using the Mauna Kea Echelle Extraction (MAKEE[1]) package.

Full explanations of how the MgII absorption systems are identified in the quasar spectra and Voigt profile fitted are presented in great detail in Churchill (1997), Churchill et al. (2003), Evans (2011), and Kacprzak et al. (2011b). We present a summary of the process.

Using SYSANAL (Churchill 1997; Churchill & Vogt 2001; Evans 2011), we detect the MgII $\lambda\lambda 2796, 2803$ in each spectrum with a 5σ (3σ) significance criterion in the equivalent width spectrum for the $\lambda 2796$ ($\lambda 2803$) line by following the formalism of Schneider et al. (1993). SYSANAL then determines equivalent width regions (the velocity or wavelength bounds that define regions of pixels which contribute to the equivalent width), defines the optical depth mean system absorption redshift, $z_{\rm abs}$, and calculates the rest-frame equivalent width, $W_r(2796)$. In Figures 4.2(a) and (b), we present an example spectrum of quasar Q1248+401 with multiple MgII equivalent width regions at $z_{\rm abs} = 0.772957$. The black histogram represents the data for the MgII $\lambda 2796$ line (panel (a)) and for the MgII $\lambda 2803$ line (panel (b)). The shaded region in panel (a) designates one of the two equivalent

[1]http://www.astro.caltech.edu/~tb/makee/

width regions for this system. For our TPCF analysis, we use only the outputs from SYSANAL.

We then fit all MgII systems using Voigt profile (VP) decomposition with MINFIT (Churchill 1997; Churchill & Vogt 2001; Churchill et al. 2003) and adopt the model with the fewest statistically significant VP components. MINFIT defines the VP component (cloud) velocities, column densities, and Dopper b parameters. Full details of MINFIT and the fittin process are described in Evans (2011) and most VP fits are presented in Kacprzak et al. (2011b). An example VP fit is presented in Figures 4.2(a) and (b) as the thick red line. Individual VP components are plotted as thin red lines centered at velocities indicated by the red, vertical ticks. This system was fitted with six components in the shaded region and one component at larger velocities.

To account for differences in the quality of our spectra, we use an equivalent width sensitivity cut. We calculate the mean 3σ $W_r(2796)$ detection threshold in each spectrum, defined as the minimum $W_r(2796)$ an equivalent width region should have in order to be detected. Figure 4.2(c) presents the cumulative distribution function of the detection threshold in each spectrum in our sample, which is 100% complete to roughly 0.07 Å. We adopt this value as our equivalent width sensitivity limit and do not include any equivalent width regions with $W_r(2796) < 0.07$ Å in our analysis. An example equivalent width region that is just below our sensitivity limit with $W_r(2796) = 0.064$ Å is presented in Figure 4.2(a) at $v \sim 225$ km s^{-1}.

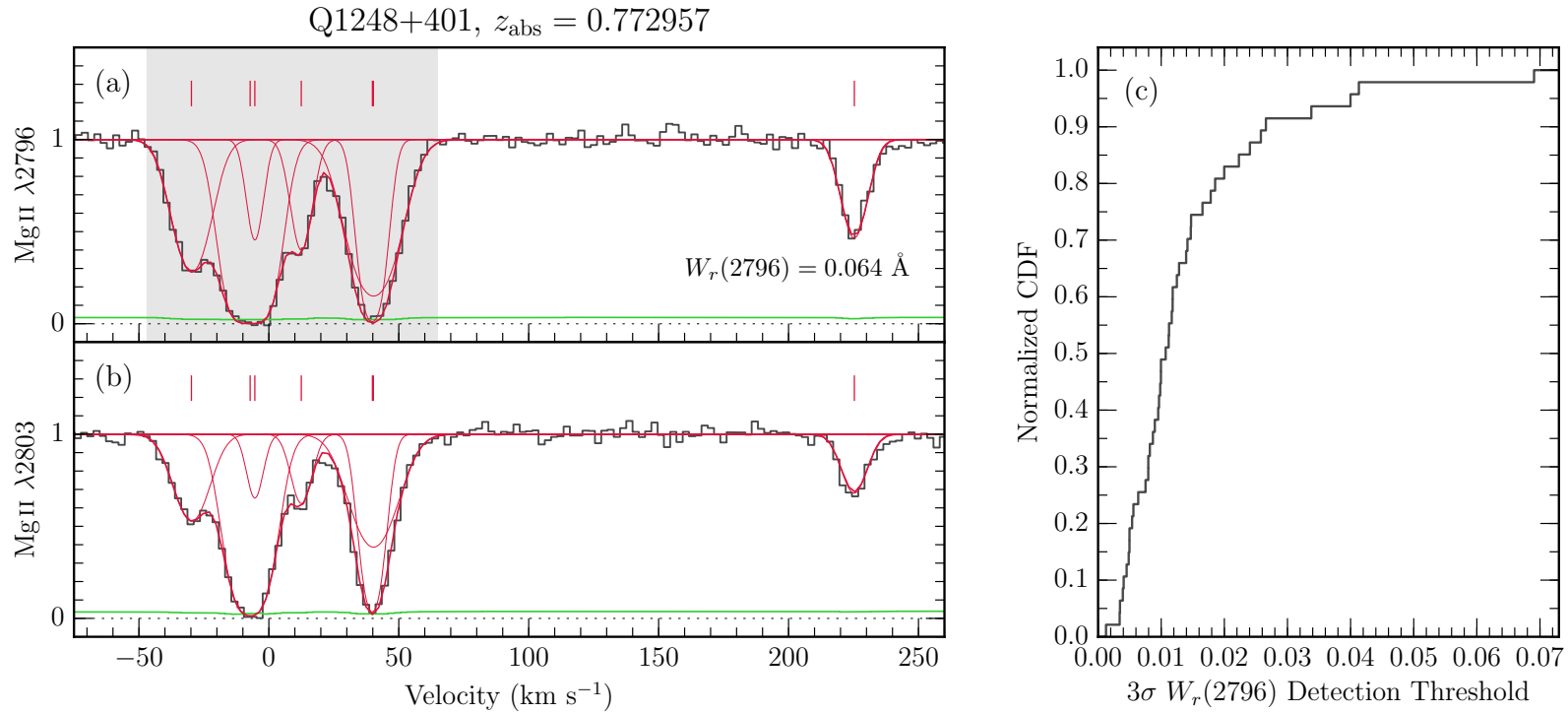

Fig. 4.2.— An example quasar spectrum focused on the Mg II $\lambda\lambda 2796, 2803$ absorption doublet in panels (a) and (b). Black histograms are the data, thick red lines are the full Voigt profile fit to the data, and thin red lines are the individual Voigt profile components that compose the total fit. The VP components are centered on the vertical ticks at the top of each panel. The shaded region indicates the pixels used in the TPCF analysis. (c) Cumulative distribution function showing the equivalent width sensitivity limit for the full kinematics sample. This sample is complete to ~ 0.07 Å, therefore we do not include any equivalent width regions for which $W_r(2796) < 0.07$ Å. An example equivalent width region below this limit is shown at $v \sim 225$ km s^{-1} in panel (a), which has $W_r(2796) = 0.064$ Å.

4.3. Characterizing Kinematics

Several methods to examine the kinematics of Mg II absorbers have been used in the literature, but the two most common methods involve studying the velocity distribution and/or clustering of VP components.

4.3.1. Voigt Profile Components

To compare to the intermediate ions studied by Werk et al. (2013), we present the kinematics of our Mg II absorbers as a function of galaxy rest-frame $B-K$ color, redshift, $z_{\rm gal}$, and impact parameter, D, in Figure 4.3 for all 47 absorber-galaxy pairs with a high-resolution quasar spectrum. We show a simplified spectrum of each Mg II absorber as a function of D, with a velocity zero point at $z_{\rm abs}$ (panel (a)) and at $z_{\rm gal}$ (panel (b)), where the latter is comparable to Werk et al. (2013). VP components (clouds) are plotted as points centered at their fitted line-of-sight velocity and on the impact parameter at which the host galaxy's CGM is probed. The spread in velocity of the absorbers is plotted as vertical lines and represents only the largest deviations from $z_{\rm abs}$; gaps between equivalent width regions and regions whose equivalent widths are below our sensitiviy cut are not presented here. Point colors indicate the rest-frame $B-K$ color of the host galaxy (a proxy for star formation rate), with blue points representing galaxies with $B-K<1.4$, and red points as galaxies with $B-K\geq 1.4$, while black points are those galaxies that do not have a $B-K$ measurement (8 galaxies). Point types indicate whether the host galaxy is located at low redshift (circles, $z_{\rm gal}<0.656$), or high redshift (triangles, $z_{\rm gal}\geq 0.656$). Finally, filled points indicate galaxies for which we have a good measurement on $z_{\rm gal}$ (where $\sigma_{(z_{\rm gal})}\leq 30$ km s^{-1}comoving, 29 galaxies, 27 of

which also have galaxy colors) and open points are galaxies for which we have less precise measurements on $z_{\rm gal}$ (where 30 km s^{-1}< $\sigma_{(z_{\rm gal})}$ $\leq$ 300 km s^{-1}comoving, 18 galaxies).

We find several general trends in the data. In Figure 4.3(a), VP components are mostly found within $v_{\rm cloud} = \pm 150$ km s^{-1} of the absorber systemic velocity. The absorbers may be more extended in velocity for blue galaxies than red and for low redshift than high redshift. The spread in velocity for absorbers may also be larger when absorption is probed closer to the galaxy at smaller D. In Figure 4.3(b), absorbers tend to be found within $v_{\rm cloud-galaxy} = \pm 200$ km s^{-1} relative to the galaxy and span the galaxy systemic velocity. This is consistent with the findings of Werk et al. (2013). We also find that red galaxies tend to have absorption at larger velocities relative to the galaxy than in blue galaxies. Absorption that is found closer to galaxies (smaller D) also appears to have larger velocities relative to the galaxy than at large D. The differences in kinematics for different redshifts seem to depend on galaxy color.

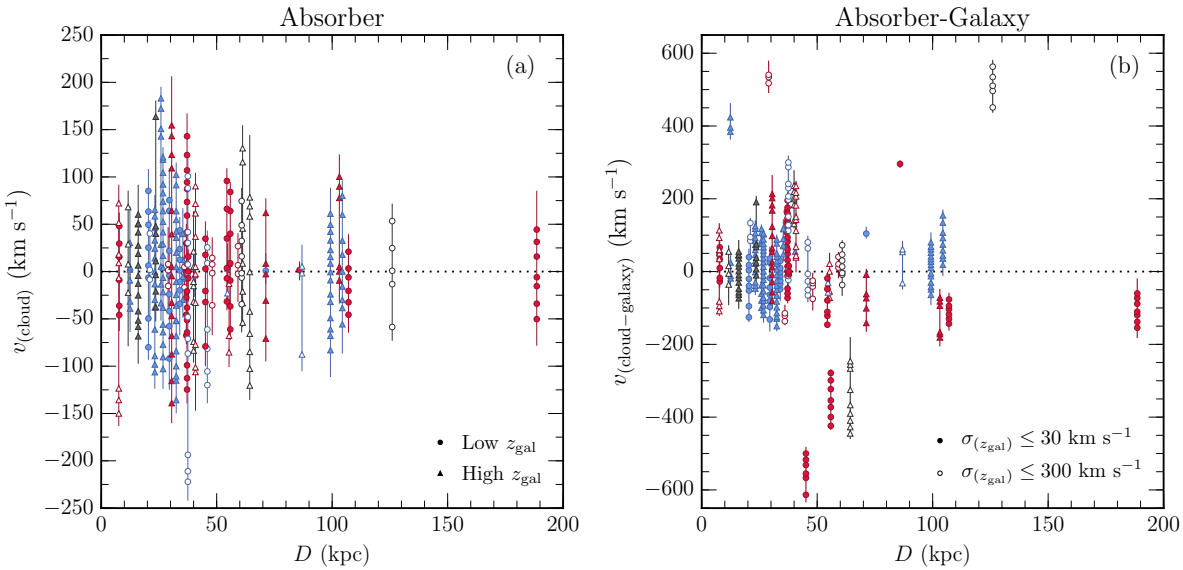

Fig. 4.3.— Velocity distributions of clouds (Voigt profile components) in the absorption profiles as a function of impact parameter. (a) Cloud velocities measured using Voigt profile fitting analysis, $v_{(\mathrm{cloud})}$. (b) Cloud velocities shifted to the galaxy redshift, $v_{(\mathrm{cloud-galaxy})}$. Points represent each individual fitted cloud while vertical lines show the extremes in velocity of each profile, ignoring any outlying clouds that have been dropped from the sample due to our equivalent width sensitivity cut. Point colors represent host galaxy colors, where blue points represent blue galaxies with $B-K<1.4$ and red points are red galaxies with $B-K\geq 1.4$. Galaxies for which we do not have a $B-K$ color are presented as black points. The redshift of the associated galaxy is represented by point types, where circles are galaxies at $z_{\mathrm{gal}}<0.656$ and triangles are $z_{\mathrm{gal}}\geq 0.656$. Open points indicate galaxies for which the uncertainty in z_{gal} is less than ~ 300 km s^{-1} comoving, while filled points are those with good measurements on z_{gal} ($\sigma_{z_{\mathrm{gal}}}\leq 30$ km s^{-1} comoving). In panel (a), most absorption is found within ± 150 km s^{-1} of z_{abs} and absorbers located at smaller impact parameters appear to have broader profiles in velocity space than those further away. Conversely, in panel (b), most absorption is found within ± 200 km s^{-1} of the galaxy systemic velocity. Higher velocity (with respect to z_{gal}) absorbers tend to be located at smaller impact parameters, whereas absorbers found near or which span z_{gal} are found at all impact parameters.

4.3.2. Pixel Velocity Two-Point Correlation Functions

We continue the line of work started by Petitjean & Bergeron (1990) by examining the pixel velocity two-point correlation function (TPCF) for various galaxy subsamples and compare the resultant line of sight velocity dispersions. Previous works constructed absorber TPCFs using cloud (VP component) velocities, while we use the velocities of pixels in regions of the spectrum which contribute to the overall Mg II equivalent width (i.e., equivalent width regions). Pixel velocities better represent the spread in absorption, provide more velocity pairs for better statistics, and can be compared more easily to simulations since the profiles do not need to be Voigt profile modeled. They are also model-independent, i.e., they do not depend on the fitting method used and the resulting fit. We study several different velocity dispersions: the absorber TPCF, the absorber-galaxy TPCF, and normalized absorber and absorber-galaxy TPCFs. We present the normalized TPCFs in Appendix D for comparison with simulations.

To construct the absorber TPCF, which is a measure of the internal absorber velocity dispersion, we define a subsample of galaxies (for example, blue galaxies) and assume we have many lines of sight through one galaxy. We take the absorption profiles for each spectrum, where $v = 0$ km s^{-1} represents $z_{\rm abs}$, and obtain the velocities of all pixels within equivalent width regions (gray shaded region of Figure 4.2(a)), pooling all of the pixels from every line of sight in the galaxy subsample together. We then calculate the absolute value of the velocity differences of each possible pair of pixels, $\Delta v_{\rm pixel}$, and bin them up, normalizing by the number of pixel pairs for comparison between different galaxy subsamples. We use a bin size of 10 km s^{-1} which corresponds to roughly one resolution ele-

ment of both the HIRES/Keck and UVES/VLT spectrographs (three pixels per resolution element, with a resolution of ~ 6.6 km s^{-1}).

To determine the uncertainties on the TPCFs, we conduct a bootstrap analysis. We randomly draw with replacement a sample of equivalent width regions from the subsample we are examining which contains the same number of regions as the original data and construct the TPCF. We do this for 1000 bootstrap realizations and then calculate the 1σ standard deviations from the mean of the realizations in each TPCF bin. The bootstrap uncertainties are plotted as shaded regions.

We also characterize the TPCFs by measuring the velocity separations within which 50% and 90% of the data reside, $\Delta v(50)$ and $\Delta v(90)$, respectively. Uncertainties on these values are obtained from the bootstrap analysis and represent 1σ deviations from the mean. These values and their uncertainties are presented in Table 4.1 for each subsample.

We present the absorber TPCFs comparing blue and red galaxies in Figure 4.4(a). Blue galaxies are presented as the thick, blue line with blue shaded areas indicating the bootstrap uncertainties, while the thin, red line and shading represents red galaxies. In this panel, we find that the absorption associated with blue galaxies has a larger velocity dispersion than with red galaxies. To test whether the two samples were drawn from the same population, we ran a chi-square test on the binned TPCFs and find that the null hypothesis that the samples were drawn from the same population can be ruled out at the 3.3σ level. We present the significance, σ, the reduced chi-square, χ^2_ν, and the number of degrees of freedom, ν, in each panel of Figure 4.4. For Figure 4.4(a), we find that

Table 4.1. TPCF $\Delta v(50)$ and $\Delta v(90)$ Measurements

		Absorber				Absorber-Galaxy			
Sample	Cut	Cut	# Gals	$\Delta v(50)$[a]	$\Delta v(90)$[a]	Cut	# Gals	$\Delta v(50)$[a]	$\Delta v(90)$[a]
				Figure 4.4					
Blue	$B-K<1.4$	···	19	72^{+6}_{-7}	186^{+15}_{-20}	···	14	43^{+5}_{-5}	119^{+148}_{-54}
Red	$B-K\geq 1.4$	···	20	60^{+5}_{-6}	151^{+11}_{-14}	···	13	95^{+42}_{-28}	460^{+52}_{-129}
				Figure 4.5					
Blue - Low $z_{\rm gal}$	$B-K<1.4$	$z_{\rm gal}<0.656$	7	78^{+9}_{-13}	199^{+20}_{-37}	$z_{\rm gal}<0.762$	7	49^{+17}_{-14}	340^{+50}_{-202}
Blue - High $z_{\rm gal}$	$B-K<1.4$	$z_{\rm gal}\geq 0.656$	12	65^{+5}_{-8}	168^{+12}_{-20}	$z_{\rm gal}\geq 0.762$	7	39^{+1}_{-3}	90^{+5}_{-5}
Red - Low $z_{\rm gal}$	$B-K\geq 1.4$	$z_{\rm gal}<0.656$	14	49^{+7}_{-8}	123^{+17}_{-22}	$z_{\rm gal}<0.498$	6	$215^{+0.3}_{-107}$	483^{+39}_{-120}
Red - High $z_{\rm gal}$	$B-K\geq 1.4$	$z_{\rm gal}\geq 0.656$	6	73^{+6}_{-7}	177^{+13}_{-16}	$z_{\rm gal}\geq 0.498$	7	60^{+2}_{-5}	142^{+8}_{-11}
				Figure 4.6					
Blue - Low $D/R_{\rm vir}$	$B-K<1.4$	$D/R_{\rm vir}<0.24$	9	64^{+6}_{-10}	169^{+14}_{-22}	$D/R_{\rm vir}<0.24$	7	45^{+11}_{-9}	307^{+60}_{-172}
Blue - High $D/R_{\rm vir}$	$B-K<1.4$	$D/R_{\rm vir}\geq 0.24$	10	75^{+8}_{-10}	186^{+20}_{-27}	$D/R_{\rm vir}\geq 0.24$	7	40^{+3}_{-5}	100^{+7}_{-11}
Red - Low $D/R_{\rm vir}$	$B-K\geq 1.4$	$D/R_{\rm vir}<0.24$	10	72^{+7}_{-10}	174^{+14}_{-18}	$D/R_{\rm vir}<0.28$	6[b]	59^{+5}_{-8}	148^{+13}_{-15}
Red - High $D/R_{\rm vir}$	$B-K\geq 1.4$	$D/R_{\rm vir}\geq 0.24$	10	48^{+2}_{-3}	114^{+4}_{-7}	$D/R_{\rm vir}\geq 0.28$	7	135^{+48}_{-57}	473^{+45}_{-123}

[a] km s^{-1}
[b] This subsample only has six equivalent width regions on which we can conduct our bootstrap analysis; the rest have at least seven regions.

the $\Delta v(50)$ measurements for both TPCFs are consistent with each other, while $\Delta v(90)$ is greater for blue galaxies than red, indicating that the significant difference we find in the chi-square test is due to a longer tail of velocity separations in blue galaxies.

For the absorber-galaxy TPCF, which examines the velocity dispersion of absorbers around the galaxy, we add two steps to our calculations before we determine the velocity differences. First we shift the pixel velocities to the redshift of the host galaxy. In this case $v = 0$ km s^{-1} represents the galaxy systemic velocity, or $z_{\rm gal}$. Then we take the absolute value of the pixel velocities since we do not know where the lines of sight are probing each galaxy. The rest of the process proceeds as detailed above, starting with calculating pixel velocity separations, $\Delta v_{\rm pixel-gal}$. We only consider galaxies for which we have more precise measurements on $z_{\rm gal}$ (uncertainties $\sigma_{(z_{\rm gal})} \leq 30$ km s^{-1} comoving). This prevents large uncertainties in the velocity separations and allows us to use bin sizes of roughly 30 km s^{-1}. In nearly all cases, we run 1000 bootstraps for our uncertainty calculations, but because of the reduced sample from which we can slice into subsamples for the absorber-galaxy TPCFs, we only run 100 bootstraps when a subsample consists of only six equivalent width regions. Six regions only allows for a maximum of 462 possible combinations. The sole case where this applies is noted in Table 4.1.

The absorber-galaxy TPCF comparing blue and red galaxies is presented in Figure 4.4(b). We find a significant difference between the TPCFs for blue and red galaxies (4.5σ). In red galaxies, the absorbers have large velocity dispersions around the galaxy, which is less present in blue galaxies. The peak in blue galaxies at $v \sim 350$ km s^{-1} is due to one equivalent width region or galaxy. These results

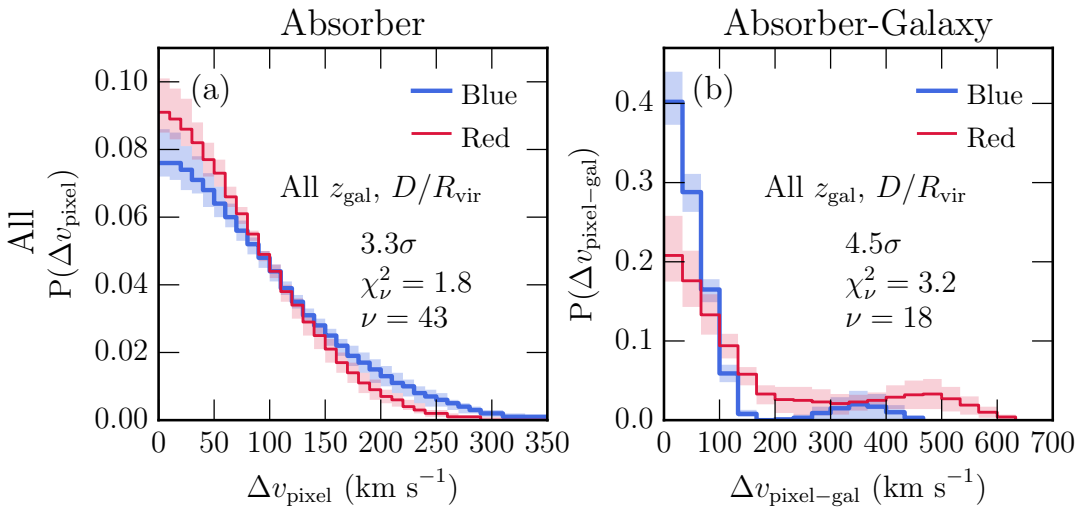

Fig. 4.4.— Pixel velocity two-point correlation functions for blue (blue lines and shading) and red (red lines and shading) galaxies using pixel velocities with respect to (a) the absorption redshift, $z_{\rm abs}$ and (b) the galaxy redshift, $z_{\rm gal}$. Shaded regions represent the 1σ uncertainties around the data (solid lines) from a bootstrap analysis. The significance of a χ^2 test comparing the distributions of the blue and red TPCFs is listed on each panel. In panel (a), we find that blue galaxies tend to have larger velocity dispersions than red galaxies. However, in panel (b), red galaxies have larger absorber-galaxy velocity dispersions than blue galaxies.

are also present in the measurements of $\Delta v(50)$ and $\Delta v(90)$, where the values are larger for red galaxies than blue. We also find large upward uncertainties in blue galaxies for $\Delta v(90)$, consistent with having only one equivalent width region at large velocities.

4.4. TPCFs: Multivariate Analysis

In this section, we report on a multivariate analysis of the absorber, absorber-galaxy, and normalized absorber-galaxy TPCFs for blue and red galaxies cut by (1) galaxy redshift, $z_{\rm gal}$, and (2) the projected radial distance normalized by the virial radius, $D/R_{\rm vir}$.

4.4.1. Redshift Evolution

While we find significant differences between blue and red galaxies in the absorber and absorber-galaxy TPCFs in Figure 4.4, the differences may be washed out by other effects. One such effect is the fact that the star formation rate has decreased over time from $z \sim 2-3$. Therefore, we slice our blue and red subsamples into low and high $z_{\rm gal}$. We present the TPCFs for $B-K$ and $z_{\rm gal}$ subsamples in Figure 4.5, where solid lines are the TPCF for each subsample and the shaded regions are the 1σ bootstrap uncertainties. On the plot, we list the significance of a chi-square test between subsample pairs as well as the reduced chi-square, χ^2_ν, and the degrees of freedom, ν for each panel. Absorber TPCFs are presented in panels (a), (b), (c), and (d), while absorber-galaxy TPCFs are plotted in panels (e), (f), (g), and (h). Measurements of $\Delta v(50)$ and $\Delta v(90)$ are presented in Table 4.1.

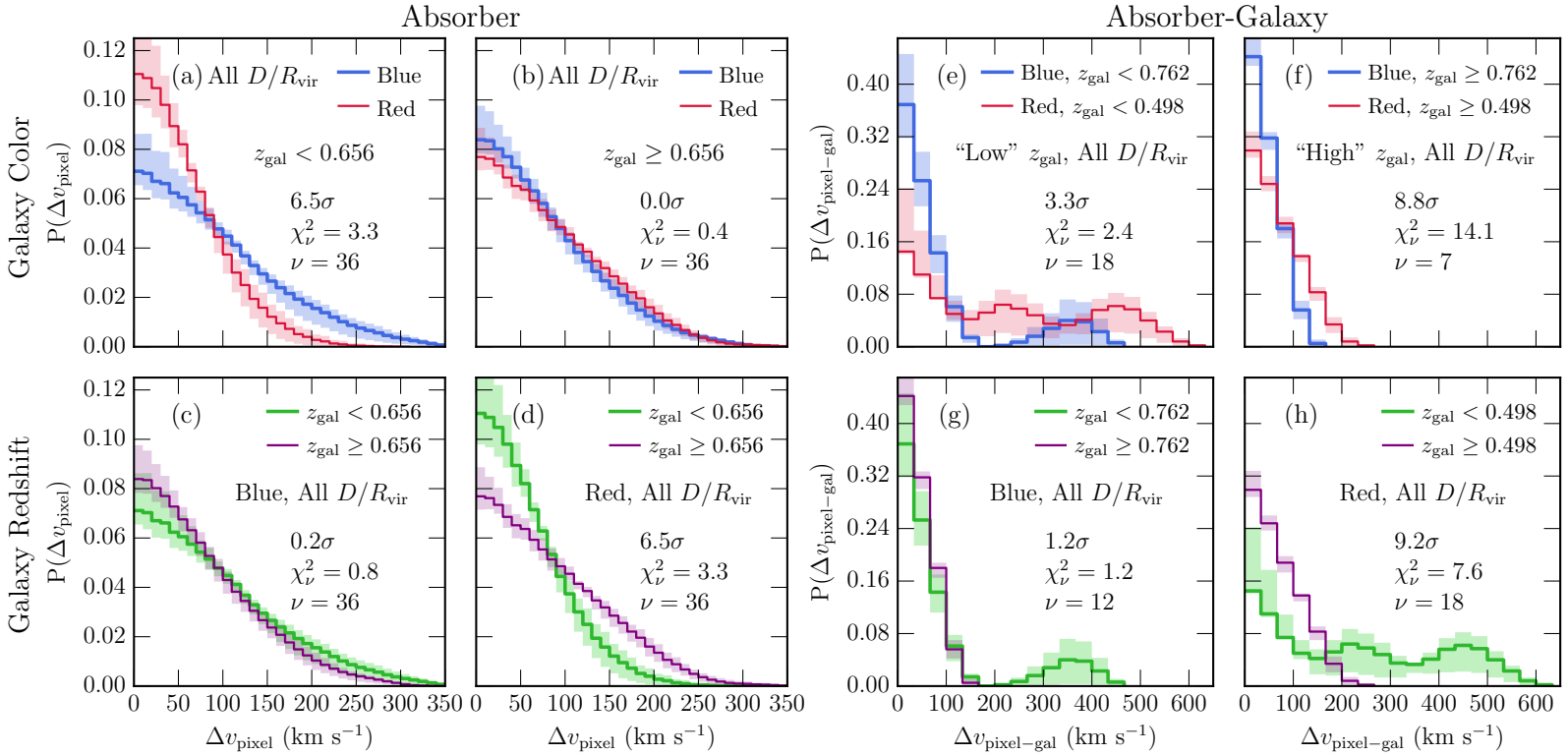

Fig. 4.5.— Pixel velocity two-point correlation functions examining dependencies of the absorber (panels (a), (b), (c), and (d)), and absorber-galaxy (panels (e), (f), (g), and (h)) TPCFs on color and redshift. Solid lines are the TPCFs while shaded regions are the 1σ bootstrap uncertainties. We list the significance, the reduced chi-square value, χ^2_ν, and the degrees of freedom, ν, from a chi-square test comparing subsamples in each panel. In each case, blue galaxies have $B-K<1.4$ and red galaxies have $B-K\geq 1.4$. For the absorber TPCFs, we slice the samples into low ($z_{\rm gal}<0.656$) and high ($z_{\rm gal}\geq 0.656$) redshift. For the absorber-galaxy TPCFs, a significant anti-correlation between $B-K$ and $z_{\rm gal}$ (3.1σ) requires that we slice the blue and red galaxies into redshift subsamples with $\langle z_{\rm gal}\rangle = 0.762$ and $\langle z_{\rm gal}\rangle = 0.498$, respectively. We find that red, low $z_{\rm gal}$ galaxies have significantly smaller absorber velocity dispersions than red, high $z_{\rm gal}$ galaxies or blue galaxies (panels (a) and (d)), whereas there are no differences in the velocity dispersions for blue galaxies (panel (c)) or at high $z_{\rm gal}$ (panel (b)). For the absorber-galaxy TPCFs, we find significant differences for each subsample pair, with the exception of blue galaxies at low and high $z_{\rm gal}$ (panel (g)).

For the absorber TPCFs, we use median cuts of $\langle B-K\rangle = 1.4$ and $\langle z_{\rm gal}\rangle = 0.656$ as defined in Table 4.1. We find that the TPCF for the red, low $z_{\rm gal}$ subsample is an outlier. In this case, the absorber velocity dispersion for red galaxies evolves with redshift over a span of roughly 2 Gyrs (6.5σ, Figure 4.5(d)), while there is no such evolution for blue galaxies (0.2σ, Figure 4.5(c)). At high $z_{\rm gal}$, absorption in red galaxies has similar dispersions as in blue galaxies (0.0σ, Figure 4.5(b)), but decreases as $z_{\rm gal}$ decreases whereas the dispersion for blue galaxies remains constant (6.5σ, Figure 4.5(a)). In the $\Delta v(50)$ and $\Delta v(90)$ measurements, all absorber TPCFs are consistent within uncertainties except the red, low $z_{\rm gal}$ subsample, which has smaller values, confirming the low velocity dispersions.

For the absorber-galaxy TPCFs, we find that we have too few galaxies in the blue, low $z_{\rm gal}$ and red, high $z_{\rm gal}$ galaxy subsamples. We performed a Kendall-τ rank correlation test between $B-K$ and $z_{\rm gal}$ and find an anti-correlation such that bluer galaxies are found at larger $z_{\rm gal}$ (3.1σ). In this case, we split the sample by $\langle B-K\rangle = 1.4$ first, then determine the median $z_{\rm gal}$ for each color subsample. This results in a median value of $\langle z_{\rm gal}\rangle = 0.762$ for blue galaxies and $\langle z_{\rm gal}\rangle = 0.498$ for red galaxies, which we use as the redshift cuts for those subsamples.

When we examine the velocity dispersions of absorbers with respect to $z_{\rm gal}$, we find prominent high velocity peaks in the TPCF at large velocity splittings for low $z_{\rm gal}$ only in both the blue and red subsamples (Figure 4.5(e)). This is represented as large values in $\Delta v(90)$ for these subsamples. The absorber-galaxy velocity dispersions for the red galaxy subsamples appear to be larger than the blue galaxy subsamples regardless of redshift (3.3σ for Figure 4.5(e) and 8.8σ for Figure 4.5(f)). For blue galaxies, we find no significant difference (1.2σ) between low and high redshift despite a peak in the low $z_{\rm gal}$ TPCF at $\sim$ 380 km s^{-1}

(Figure 4.5(g)). We note that this peak is due to one equivalent width region since the bootstrap uncertainties drop to zero, i.e., this feature is not present in many bootstrap realizations. Conversely, the absorber-galaxy velocity dispersions for red galaxies appear to undergo redshift evolution (9.2σ, Figure 4.5(h)) where the dispersion becomes larger as $z_{\rm gal}$ decreases. This is in contrast to the absorber TPCFs in Figure 4.5(d).

4.4.2. Radial Dependence

Another effect that may be washing out differences in the TPCFs of blue and red galaxies is the projected radial distance at which absorption is found. Many previous works have studied the well-known anti-correlation between $W_r(2796)$ and D, which is significant to the 8σ level (see Nielsen et al. 2013b, and references therein). Furthermore, since galaxies span a range of masses, Churchill et al. (2013b) normalized D by the virial radius to account for the mass of the host galaxy and found an even stronger anti-correlation between $W_r(2796)$ and $D/R_{\rm vir}$ (9σ) (also see Churchill et al. 2013c). Since $W_r(2796)$ depends on column densities and/or velocity spreads (the latter being similar to what is studied in this paper), any differences in the TPCFs as a function of $D/R_{\rm vir}$ may be related to the $W_r(2796) - D/R_{\rm vir}$ anti-correlation. We present absorber and absorber-galaxy TPCFs in Figure 4.6. We note that though the results in this section are similar to those examining redshift evolution, we find no significant anti-correlation from a Kendall-τ rank correlation test between $z_{\rm gal}$ and $D/R_{\rm vir}$ to the 1.8σ level.

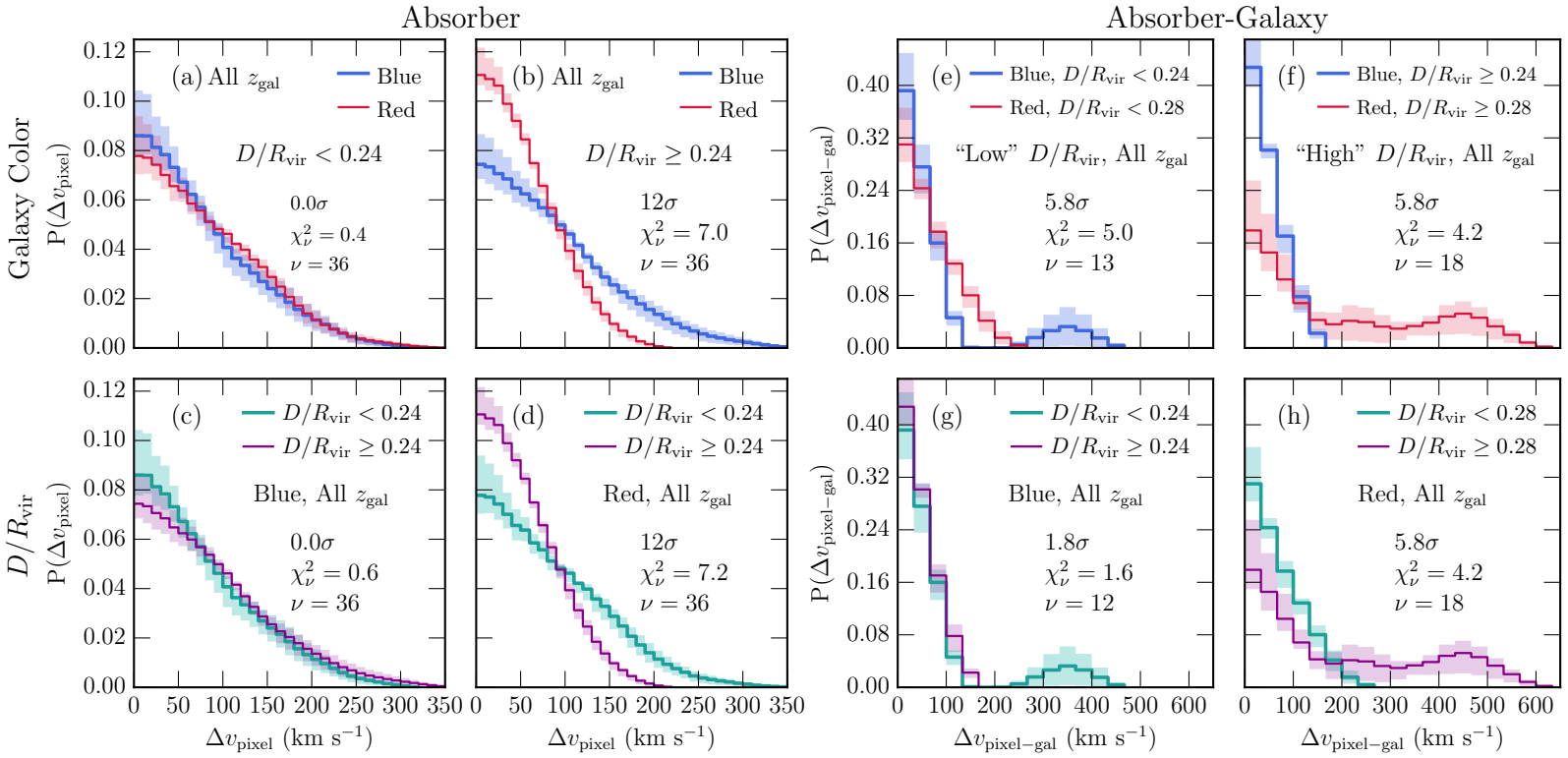

Fig. 4.6.— TPCFs for subsamples sliced by galaxy color, $B - K$, and virial radius-normalized impact parameter, $D/R_{\rm vir}$. Absorber TPCFs sliced by $\langle B - K \rangle = 1.4$ and $\langle D/R_{\rm vir} \rangle = 0.24$ are presented in panels (a), (b), (c), and (d). Absorber-galaxy TPCFs are presented in panels (e), (f), (g), and (h), with subsamples sliced by $B - K = 1.4$ and $D/R_{\rm vir} = 0.24$ for blue galaxies or $D/R_{\rm vir} = 0.28$ for red galaxies. Lines, shading, and chi-square test results are similar to those listed in Figure 4.5. We find that the red, low $D/R_{\rm vir}$ subsample is a significant outlier such that it has a smaller absorber velocity dispersion than the rest of the absorber TPCFs (12σ in both panels (b) and (d)). In the absorber-galaxy TPCFs, we find significant differences between every subsample pair except for blue galaxies at low and high $D/R_{\rm vir}$ (panel (g)).

In panels (a), (b), (c), and (d) of Figure 4.6, we plot absorber TPCFs for subsamples sliced by $\langle B-K \rangle = 1.4$ and $\langle D/R_{\rm vir} \rangle = 0.24$. We find that the internal velocity dispersion of absorbers (absorber TPCF) around blue galaxies does not depend on where the absorbers are located in projected distance away from the galaxy (0σ, panel (c)), but the dispersion does if the absorbers are located around red galaxies (12σ, panel (d)). In red galaxies, the internal dispersion of absorbers at low $D/R_{\rm vir}$ is comparable to absorbers in blue galaxies, regardless of where they are being probed (0σ, panel (a)). The outlier of the absorber TPCFs is the high $D/R_{\rm vir}$, red galaxy subsample, which has a significantly smaller dispersion than the absorber TPCF for blue, high $D/R_{\rm vir}$ galaxies (11σ, panel (b)), or for red, low $D/R_{\rm vir}$ galaxies (12σ, panel (d)).

We plot absorber-galaxy TPCFs in Figures 4.6(e), (f), (g), and (h), where subsamples are cut by $\langle B-K \rangle = 1.4$ and $\langle D/R_{\rm vir} \rangle = 0.24$ for blue galaxies or $\langle D/R_{\rm vir} \rangle = 0.28$ for red galaxies. We use different median cuts in $D/R_{\rm vir}$ for blue and red galaxies in order to more evenly distribute the galaxies in our sample. Unlike with galaxy color and redshift, we do not find a correlation between $B-K$ and $D/R_{\rm vir}$ (a Kendall-τ rank correlation test results in an insignificant anti-correlation with 0.8σ). It is the act of cutting the sample we are working with down to only those galaxies with more precise redshift measurements that preferentially removes galaxies from the red, low $D/R_{\rm vir}$ subsample. We only have six galaxies, corresponding to six equivalent width regions in this subsample. The maximum number of combinations for a sample of six with replacement is 462. As a result, we only run 100 bootstrap realizations on the red, low $D/R_{\rm vir}$ subsample in order to prevent too many repeated realizations in our uncertainty calculations.

We find that the absorbers around blue galaxies have similar absorber-galaxy

velocity dispersions regardless of the $D/R_{\rm vir}$ at which absorption is probed (panel (g)). Again, the peak at high velocity for the blue, low $D/R_{\rm vir}$ subsample is due to one equivalent width region. In the other panels, we find a 5.8σ significance from the chi-square test indicating that (e) blue galaxies have a larger absorber-galaxy velocity dispersion than red galaxies at "low" $D/R_{\rm vir}$, (f) red galaxies have a larger dispersion than blue at "high" $D/R_{\rm vir}$, and (h) red galaxies probed high $D/R_{\rm vir}$ have larger dispersions than red galaxies probed at low $D/R_{\rm vir}$. In panel (e), the absence of the high-velocity equivalent width region for blue galaxies would result in the velocity dispersion to be larger for red galaxies.

4.5. Discussion

The strong dependencies of the Mg II kinematics on galaxy color, redshift, and $D/R_{\rm vir}$ indicate that evolutionary processes may be changing the velocity structure of the gas, and this is most easily observed in the absorber TPCFs.

That we find redshift evolution of the absorber velocity dispersions for red galaxies in Figure 4.5(d) but not for blue galaxies in Figure 4.5(c) may suggest we are observing the consequences of quenching on the red galaxies over time, while ongoing star formation continues in blue galaxies. This is supported by the fact that the global star formation rate peaks at about $z \sim 2-3$, decreasing with lower redshift (e.g., Hopkins & Beacom 2006; Behroozi et al. 2013). If star formation in the red galaxies was active in the past, but has since been quenched, we would expect the absorber velocity dispersions to decrease over time due to a lack of outflows stirring up the absorbers. It's also possible that the kinematically hot material is removed by some mechanism, whether it is heated to temperatures that

do not allow for detectable Mg II absorption (i.e., shock heating) or it is ejected from the galaxy by a strong burst of star formation which removes much of the galaxy's gas supply (e.g., Dekel & Birnboim 2006; Dekel et al. 2009; Schawinski et al. 2014). However, the fact that we observe cool, Mg II gas in red, likely quenched galaxies indicates that some material remains in the CGM. The high velocity dispersions in the absorber-galaxy TPCFs of the red, low $z_{\rm gal}$ subsample (green line in Figure 4.5(h)) suggest that while the velocity dispersion of the absorbers is fairly small, the absorbers themselves will not accrete onto the galaxy due to their large velocities with respect to the galaxy. However, we only have a few galaxies with absorption at these large velocities.

At high redshift in Figure 4.5(b), the absorber velocity dispersions are similar regardless of galaxy color, indicating that the red galaxies we observe in the high redshift subsample may have undergone star formation driven outflows, but have since shut off at lower redshifts. In contrast to the red galaxies, the absorber velocity dispersions for blue galaxies remain fairly constant. The active star formation driven outflows in these blue galaxies may continuously stir up the absorbers so that they remain kinematically hot, but their velocities with respect to the galaxy systemic velocity tend to be small (Figure 4.5(g)). Therefore, while the absorbers themselves are disturbed for blue galaxies, their low absorber-galaxy velocities may allow them to reaccrete (or accrete for the first time if we are probing cold accretion) back onto the galaxy in the future.

The large velocity peaks in the low redshift, blue and red galaxy subsamples (Figures 4.5(e)) may be due to outflowing material from the host galaxy itself, and/or from satellite galaxies. These merging satellite galaxies may also be caught in the act of being tidally stripped by the host galaxy. Outflows tend to have

velocities on the order of hundreds of km s^{-1} with respect to z_{gal} (e.g., Rupke et al. 2005; Weiner et al. 2009; Steidel et al. 2010; Martin et al. 2012; Rubin et al. 2010; Bordoloi et al. 2014c; Rubin et al. 2014), which is consistent with the velocities of the peaks in both of our low redshift subsamples. Satellites may be less likely to be the source of this material due to the fact that we do not directly observe any in our galaxy images (most of which have been observed with *HST* and modeled to obtain galaxy morphologies, therefore satellites would have been observed in the model residuals) and the catalog from which we obtain the absorber-galaxy pairs (MAGIICAT) is an isolated galaxy sample. However, any satellites we may be probing are likely below the detection threshold of our data (roughly $L_B/L_B^* > 0.1$, for details, see Nielsen et al. 2013b) so we cannot rule them out completely. Very few satellites have been observed and found to be the source of high velocity absorbing material due to detection limits at the redshifts we are examining. Martin et al. (2012) attributed high velocity ($\sim$ 400 km s^{-1}) absorption in one of their galaxy spectra as being due to a nearby satellite which was directly imaged in their campaign. This velocity is consistent with the high velocity peaks in our sample.

The puzzling aspect of the absorber-galaxy TPCFs in Figure 4.5 is that the high velocity peaks are present in the low redshift subsamples for both blue and red galaxies. Both outflows and merging events tend to be more common at higher redshift so we would expect the high velocity peaks in the high redshift subsample. However, since our red galaxies tend to be located in more overdense regions, merging satellites should be observed more often around the red galaxies than blue and we do find more large velocity dispersion peaks in red galaxies than blue. Oppenheimer et al. (2010) and (Mathes et al. 2014) find that gas tends to

escape low mass galaxies more easily than high mass galaxies due to their lower gravitational potential. Since our red galaxies tend to be more massive than our blue galaxies, it's unexpected that we see high velocity peaks in the red galaxy subsample. We note that when we normalize these absorber-galaxy TPCFs by the host galaxy maximum circular velocity to take into account the mass of the host galaxy (see Appendix D and Figure D.2), the results remain unchanged. However, the high velocity peaks have velocities greater than the maximum circular velocity, $V_{\rm circ}$, indicating that this material is likely outflowing Trujillo-Gomez (2014).

Variations in the TPCFs with projected $D/R_{\rm vir}$ as presented in Figure 4.6 are important given the history of absorber-galaxy studies, which have found a strongly anti-correlated relationship between Mg II equivalent width, $W_r(2796)$, and projected impact parameter, D. In Nielsen et al. (2013b), we found this anti-correlation is significant to the $\sim 8\sigma$ level. More recently, Churchill et al. (2013b) and Churchill et al. (2013c) found that the anti-correlation strengthens when normalizing the impact parameter, D, by the virial radius, $R_{\rm vir}$, of the host galaxy to become significant to nearly 9σ. It is important to keep in mind that the equivalent width depends on the velocity spread of absorption, and/or the cloud column densities. Since our TPCFs provide a measure of the velocity dispersion of the absorbers, and is also related to the velocity spread, we have the opportunity to examine this relation in more detail.

As might be expected from the anti-correlation, we find that the absorber velocity dispersions of red galaxies tend to be larger at smaller $D/R_{\rm vir}$ than at larger $D/R_{\rm vir}$ in Figure 4.6(d). However, we find no such difference in the blue galaxies in Figure 4.6(c). In this case, red galaxies seem to show the $W_r(2796)$-$D/R_{\rm vir}$ anti-correlation, whereas blue galaxies do not. We suggest that this is

again due to quenching in red galaxies, but ongoing star formation in blue. The absorbers located nearer to red galaxies may have been more recently stirred up than those further away due to the last burst of star formation before the gas supply was removed. In the blue galaxies, not only is star formation ongoing, but it may also be stronger than in the red galaxies due to higher star formation rates, causing the disturbed absorbers to be pushed further out into the CGM. On the other hand, since the blue galaxies tend to be less massive than red galaxies, the large dispersions at high $D/R_{\rm vir}$ could also be due to differential kinematics in which outflows from lower mass galaxies have a greater likelihood to escape the gravitational potential well than for higher mass galaxies (Oppenheimer et al. 2010; Mathes et al. 2014).

Churchill et al. (2013c) show in their Figure 5 that the mean $W_r(2796)$ is independent of the galaxy mass for $D/R_{\rm vir} \leq 0.3$, which is slightly larger than our cut. This is consistent with what we find in Figure 4.6(a) where blue and red galaxies (i.e., low and high mass galaxies) have nearly identical TPCFs at low $D/R_{\rm vir}$. For $D/R_{\rm vir} > 0.3$, Churchill et al. (2013c) find that, with the exception of the lowest mass bin which is due to a single galaxy, all masses have values of $W_r(2796)$ which are consistent within uncertainties. This is inconsistent with what we find in Figure 4.6(b) for our high $D/R_{\rm vir}$ subsample where redder (more massive) galaxies have smaller velocity dispersions than bluer (less massive) galaxies. It's possible that the individual cloud column densities for the red galaxies are larger than in the blue galaxies to balance out the equivalent widths.

We find more quandaries when examining the absorber-galaxy TPCFs sliced by galaxy color and $D/R_{\rm vir}$ in Figure 4.6. If gas is more likely to escape lower mass (bluer) galaxies than higher mass (redder) galaxies as reported by Oppenheimer

et al. (2010) and Mathes et al. (2014), then we would expect to see large velocity dispersions with respect to the galaxy for all $D/R_{\rm vir}$ in blue galaxies, but not in red galaxies (or perhaps only for the low $D/R_{\rm vir}$ subsample in red galaxies as the material would have been decelerated by the time it reached higher $D/R_{\rm vir}$). We actually find that the dispersions for blue galaxies are smaller and do not depend on $D/R_{\rm vir}$, but tend to be large for red galaxies, with the largest dispersions at high $D/R_{\rm vir}$. If we take into account $V_{\rm circ}$ in Figure D.3, the general results do not change. In this Figure, red galaxies at high $D/R_{\rm vir}$ have peaks in the TPCF distribution that indicate they have velocities greater than $V_{\rm circ}$.

The results in the absorber-galaxy TPCFs for Figure 4.6 are similar to those in Figure 4.5. Therefore, we could also attribute the high velocity peaks to outflows and/or merging satellites as before. In this case, we would expect to see outflows more often in blue galaxies than red, but satellites more often in red galaxies (more massive) than blue. With the data we currently have, we cannot distinguish between the two scenarios. However, we expect that the high velocity material around red galaxies at high $D/R_{\rm vir}$ is more likely to be satellites than outflows since outflowing material will likely have been decelerated at high $D/R_{\rm vir}$ due to the large potential well.

4.6. Summary and Conclusions

Using a subset of MAGIICAT galaxies with associated MgII absorption in high-resolution quasar spectra, we examined the kinematics of gas in the CGM as a function of galaxy color, redshift, and virial radius-normalized impact parameter. We studied both the internal kinematics of the absorbers and the kinematics

with respect to the galaxy systemic redshift in a statistical fashion with the pixel velocity two-point correlation functions, which provide a measure of the velocity dispersions. In this work, we find:

1. Redshift evolution in the kinematics for absorbers hosted by red galaxies, but not hosted by blue galaxies. We suggest this is due to ongoing evolution in blue galaxies in the form of outflows which keeps stirring up the absorbers, but the quenching of star formation in red galaxies where the velocity dispersions decrease with decreasing redshift.

2. Redshift evolution in the absorber-galaxy kinematics for red galaxies such that the dispersions are greater at lower redshift. We find no such evolution for blue galaxies. Also, the dispersions for red galaxies are larger than for blue galaxies at all redshifts. These results are puzzling given that outflows and merging events are more common at higher redshifts, though outflows should be more likely in blue galaxies due to their higher star formation rates and satellites should be more likely in red galaxies due to living in more overdense environments.

3. Differences in the kinematics with $D/R_{\rm vir}$ for red galaxies such that the absorber velocity dispersions are greater at low $D/R_{\rm vir}$ than at high $D/R_{\rm vir}$, but no differences for blue galaxies. In this case, red galaxies appear to follow the trends found on the $W_r(2796)$-D and $W_r(2796)$-$D/R_{\rm vir}$ planes as found in Nielsen et al. (2013a) and Churchill et al. (2013b), but blue galaxies do not. This may be due to the fact that our blue galaxies tend to be less massive, and therefore the absorbers that have been stirred up by outflows may be distributed further from the galaxy.

4. Larger velocity dispersions in the absorber-galaxy TPCFs for red galaxies at low $D/R_{\rm vir}$, but no radial dependence for blue galaxies. Again, the high velocity peaks in these TPCFs could be due to either outflows or satellites, but it is difficult to tell since the velocities in the TPCFs are comparable to both the satellite galaxy and outflow velocity offsets found in studies using a down-the-barrel approach. Improving our galaxy redshift estimates will help clear up the absorber-galaxy TPCFs by increasing the number of galaxies with more precise redshifts and allow for finer binning on the TPCFs.

This work constitutes our first examination of the kinematics of Mg II absorbers as a function of galaxy properties. Previous works had examined the kinematics of the absorbers but hadn't connected their results to the host galaxy properties beyond making predictions. Other works have examined the gas kinematics with respect to the systemic velocity of the host galaxy, but did not have the high resolution spectra that we have. While the work we present here improves on previous studies, we lack the full three-dimensional kinematics and locations of the absorbing gas. There is plenty of evidence showing that the orientation of the galaxy is important when considering the physical mechanism which may be causing the gas we are probing to behave in certain ways (e.g., Bordoloi et al. 2011; Bouché et al. 2012; Kacprzak et al. 2012a; Bordoloi et al. 2014c; Lan et al. 2014; Rubin et al. 2014). We take the work we present here and expand upon the absorber TPCFs by examining their dependence on galaxy color and orientation in a companion paper Nielsen et al. (2015a) using the same dataset we present here.

To improve on the absorber-galaxy TPCFs we present in Section 4.4, we need more galaxies with better redshift estimates to make the absorber-galaxy TPCFs with smaller velocity separation bins and to increase our galaxy sample. For all of our results, it would also be useful to measure star formation rates for the galaxies rather than relying on galaxy color as a proxy. Metallicities of the absorbers would be interesting to examine as they may show a gradient with impact parameter and may differ at low and high redshifts. Lastly, our results help constrain the CGM in simulations and by analyzing mock quasar absorption lines, we could obtain a more physical picture for the processes occurring in the CGM.

We thank C. Steidel and J.-R. Gauthier for providing reduced HIRES/Keck quasar spectra. This work benefited from discussions with A. Klypin and J. Primack. This material is based upon work supported by the National Science Foundation under Grant No. 1210200 (NSF East Asia and Pacific Summer Institutes). This research was primarily supported through grant HST-AR-12646 provided by NASA via the Space Telescope Science Institute, which is operated by the Association of Universities for Research in Astronomy (AURA) under NASA contract NAS 5-26555 and by the Research Enhancement Program provided by NASA's New Mexico Space Grant Consortium (NMSGC). N.M.N. was also partially supported through a NMSGC Graduate Fellowship and a Graduate Research Enhancement Grant (GREG) sponsored by the Office of the Vice President for Research at New Mexico State University. M.T.M. thanks the Australian Research Council for Discovery Project grant DP130100568 which supported this work.

5. MAGIICAT V. OUTFLOW AND ACCRETION SIGNATURES IN ABSORBER KINEMATICS WITH ORIENTATION

The contents of this chapter have been submitted for publication in the Astrophysical Journal as Nielsen, N. M., Churchill, C. W., Kacprzak, G. G., Murphy, M. T., & Evans, J. L. 2015, ApJ

We examine the kinematics and column densities of a subsample of isolated MAGIICAT galaxies at $0.3 < z_{\rm gal} < 1.0$ for which we have modeled galaxy orientations and high-resolution quasar spectra covering Mg II $\lambda\lambda 2796, 2803$ doublet absorption within $D = 110$ kpc. We find that the velocity structure of the absorbers in the form of pixel velocity two-point correlation functions, and the cloud column densities both depend strongly on galaxy color and orientation. Slicing the sample by galaxy color, $B-K$, inclination, i, and azimuthal angle, Φ, we find suggestions of outflowing and accreting material consistent with previous works. While we do not directly observe satellite galaxies, we do not expect them to be the dominant source of this absorption. We attribute the largest absorber velocity dispersions in blue ($B-K < 1.4$), face-on ($i < 57^\circ$) galaxies to looking down into a bipolar outflow that is pointed towards the observer. The smaller dispersions in blue, edge-on ($i \geq 57^\circ$) galaxies along the minor axis ($\Phi \geq 45^\circ$) are likely due to probing across outflowing material which is moving more perpendicular to our line of sight. The absorbers in face-on galaxies generally have smaller cloud column densities, suggesting that outflowing material is fragmented. Small velocity dispersions in red ($B-K \geq 1.4$), face-on galaxies indicate that star formation has been quenched and outflows are not actively stirring up the Mg II absorbers. We also find evidence for accreting and/or rotating material in edge-on, major axis ($\Phi < 45^\circ$) galaxies regardless of galaxy color. This accreting material tends to have larger cloud column densities than in outflows, possibly revealing more

coherent structures.

5.1. Introduction

The circumgalactic medium (CGM) is generally defined as the bound gaseous halo surrounding galaxies and extends out to a few hundred kiloparsecs (e.g., Steidel et al. 2010; Tumlinson et al. 2011; Rudie et al. 2012; Nielsen et al. 2013a; Werk et al. 2013; Tumlinson et al. 2013; Mathes et al. 2014). This region has increasingly been found to host some of the most important mechanisms involved in galaxy evolution through the baryon cycle. The diffuse, multiphase nature of the CGM lends itself to study by way of absorption lines found in bright, background objects such as quasars or galaxies, or even in the spectrum of the host galaxy itself (i.e., the "down-the-barrel" approach). Most work examining the low-ionization, cool ($T \sim 10^4$ K) component has been focused on Mg II $\lambda\lambda 2796, 2803$ doublet absorption in background quasar spectra as it is easily observed in the optical at redshifts $0.1 < z < 2.5$ (e.g., Bergeron & Boissé 1991; Steidel et al. 1994; Guillemin & Bergeron 1997; Steidel et al. 1997; Churchill et al. 2005; Kacprzak et al. 2011b; Lan et al. 2014), and for a range of H I column densities ($16 \leq \log N(\mathrm{H\,I}) \leq 22$, e.g., Bergeron & Stasińska 1986; Steidel & Sargent 1992; Churchill et al. 2000; Rao & Turnshek 2000; Rigby et al. 2002). The Mg II ion is well-known to be a tracer of the steps involved in the baryon cycle including accretion, rotating material merging onto the galaxy, and outflows. Mg II absorbing gas may also be associated with merging satellites which are in the process of being tidally stripped and/or have ongoing star formation driven outflows.

Accreting gas in the form of filaments from the cosmic web and/or recycled

accretion from past outflows has been found to lie near the plane of the galaxy disk (e.g., Stewart et al. 2011; Martin et al. 2012; Rubin et al. 2012; Ford et al. 2014) and forms an extended (out to $\sim 0.3R_{\rm vir}$), warped disk that co-rotates with the galaxy when viewed in edge-on orientations (e.g., Stewart et al. 2011; Danovich et al. 2012, 2014). In individual galaxies which have been observed down-the-barrel, Rubin et al. (2012) found redshifted absorption interpreted as accretion in 6 galaxies, 5 of which are edge-on galaxies. Direct observations of infalling material have been few due to the small covering fraction of the accreting material (at least 6%; e.g., Martin et al. 2012; Rubin et al. 2012) and because outflows dominate the absorption profile. Nonetheless, accretion signatures may include velocities that are bound to the host galaxy, but are greater than or comparable to rotational velocities of the disk for edge-on galaxies probed along the projected major axis.

Outflows from galactic-scale winds due to star formation and/or supernovae feedback are often invoked to explain the presence of Mg II absorption (e.g., Rubin et al. 2010; Bouché et al. 2012; Martin et al. 2012; Bordoloi et al. 2014a,c; Rubin et al. 2014). A down-the-barrel approach was used in Weiner et al. (2009) and Rubin et al. (2010) which show that, in stacked galaxy spectra, outflows are easily observed in face-on orientations due to the observed blueshift of material being pushed out of the host galaxy in the direction of the observer. Using spectra of individual galaxies in a down-the-barrel experiment, Rubin et al. (2014) found that outflowing material is much more likely to be observed in face-on galaxies than edge-on (89% detection rate versus 45%, for face-on and edge-on respectively). By stacking galaxy spectra (background and down-the-barrel), Bordoloi et al. have consistently shown that the Mg II equivalent widths along the minor axis for edge-on galaxies are stronger than those along the major axis, and the equivalent width

for blue galaxies is greater than for red galaxies, both of which are attributed to outflows (Bordoloi et al. 2011, 2014c,a). All of this work is consistent with the picture of biconical, polar outflows whose signatures include broad, complex absorption profiles spanning hundreds of km s^{-1} that cannot be explained by rotation (Veilleux et al. 2005).

Merging satellite galaxies may also be a source of Mg II absorption in the CGM, however, due to the redshifts at which the absorbers typically lie and the low luminosities of satellite galaxies, it is difficult to directly observe such satellites. In fact, Martin et al. (2012) found a redshifted absorber with respect to the targeted galaxy and associated it with a satellite that was clearly detected in their galaxy images, but this was the only case out of their sample of over 200 galaxies. Examining the azimuthal angle dependence of satellites around host galaxies, Yang et al. (2006) found that satellites tend to be isotropically distributed around blue galaxies, but are preferentially located along the major axis of red galaxies. This result has been found with a variety of data sets, which are summarized in Yang et al. (2006), as well as in simulations (most recently by Dong et al. 2014).

Detailed absorber kinematics for a large absorber-galaxy sample, which are required to provide insight into the motions of the gas involved in the baryon cycle and constrain simulations, have thus far remained elusive due to the need to stack spectra because of low-resolution spectroscopy on the background source (whether it was a background galaxy, quasar, or the host galaxy itself). Even without needing to stack the spectra, much of the velocity structure is washed out in low-resolution spectra. Most of the previous work examining Mg II absorbers associated with baryon cycle processes have reported that the Mg II equivalent

width depends strongly on inclination and/or azimuthal angle, however this measurement does not provide a very detailed picture of the gas kinematics. This is especially true since equivalent width depends on the velocity spread of absorption and the column densities, which in turn depend on the geometry, metallicity, and ionization conditions of the absorbers. We therefore make use of a subsample of galaxies in MAGIICAT (Nielsen et al. 2013a,b; Churchill et al. 2013c) for which we have high-resolution ($R \sim 45,000$) background quasar spectra, in addition to detailed colors and orientations of the galaxies themselves. With these spectra, we can study the detailed kinematics of MgII absorbers and examine if the enhanced detection rates and larger equivalent widths for particular orientations are due to velocity spreads, column densities, or both.

In a previous work, Kacprzak et al. (2012a) examined the locations of a subset of MAGIICAT pairs by modeling the galaxies and measuring the azimuthal angles at which background quasars probe the CGM. They found that MgII absorption prefers to be located along the major and minor axes of blue galaxies, while there is no such preference for absorbers located around red galaxies (a result confirmed with a larger, statistical sample by Lan et al. 2014), or for sightlines in which no absorption is detected (nonabsorbers) regardless of galaxy color. They also found a tendency for MgII equivalent widths to be larger along the minor axis than the major axis, possibly an indication of probing more enriched outflowing material in the minor axis.

In this paper, we expand upon our previous work and examine how the MgII absorber pixel velocity two-point correlation functions (TPCFs, described in detail by Nielsen et al. 2015b) and cloud column densities depend on galaxy color and orientation using galaxies from MAGIICAT. The paper is organized as fol-

lows. Section 5.2 describes the sample, our methods for analyzing the spectra and data, and how we calculate the TPCFs. Section 5.3 details how the TPCFs and cloud column densities differ for galaxies of various colors, azimuthal angles, and inclinations. In Section 5.4 we place our kinematics results in the context of the baryon cycle and discuss the implications. Finally, we summarize and conclude our findings in Section 5.5. We adopt a ΛCDM cosmology ($H_0 = 70$ km s^{-1} Mpc^{-1}, $\Omega_M = 0.3$, $\Omega_\Lambda = 0.7$) throughout this paper.

5.2. Sample and Data Analysis

We use a sample of 30 spectroscopically confirmed ($0.3 < z_{\rm gal} < 1.0$) Mg II absorption-selected galaxies from the Mg II Absorber-Galaxy Catalog (MAGIICAT; Nielsen et al. 2013a,b). The galaxies are isolated to the limits of the data, where isolation is defined as having no spectroscopically identified neighbor within a projected distance of 100 kpc or a line-of-sight velocity of 500 km s^{-1}. Each galaxy has been imaged with WFPC2/*HST* in the F702W band and we have a rest-frame $B - K$ color for each galaxy which was determined as described in Nielsen et al. (2013b).

All galaxies were modeled using GIM2D (Simard et al. 2002) to obtain morphologies, inclinations, and position angles. Full details of the method used and the morphological properties of most galaxies in our sample are presented in Kacprzak et al. (2011b). We define inclinations of $i = 0°$ as face-on and $i = 90°$ as edge-on. We convert position angles to an "azimuthal angle" which describes where a background quasar sightline is located with respect to the major axis of the galaxy. An azimuthal angle of $\Phi = 0°$ is defined as having the quasar line of

sight along the projected galaxy major axis and $\Phi = 90^\circ$ as having the sightline along the projected minor axis.

Additionally, the CGM of each galaxy is probed by a nearby (projected on the sky distance of $20 < D < 110$ kpc) background quasar for which we have a high-resolution HIRES/Keck or UVES/VLT spectrum. We refer the reader to Churchill (1997), Churchill et al. (2003), Evans (2011), and Kacprzak et al. (2011b) for the spectra, full details of the reduction and analysis of the quasar spectra, and the detection and Voigt profile (VP) fitting of Mg II $\lambda\lambda 2796, 2803$ absorption. We measure Mg II equivalent widths and, from the VP fitting, we obtain VP component (cloud) column densities, velocities, and Doppler b parameters. For our TPCF analysis we use absorber pixel velocities in regions which contribute to the Mg II equivalent width. Equivalent width regions must have $W_r(2796) \geq 0.07$ Å to be included in our sample to account for differences in the quality of our spectra (Nielsen et al. 2015b). Velocity zero points are defined as the median velocity of the apparent optical depth distribution of Mg II absorption (Churchill 1997).

We slice the sample into several subsamples based on galaxy rest-frame $B-K$ color, inclination, i, and azimuthal angle, Φ. We tabulate the characteristics of each subsample in Table 5.1 including the subsample names, number of galaxies in each subsample, and the median value(s) by which the sample was cut. The subsample names listed are used throughout this paper. We caution that a weak trend exists between $B-K$ and $\log(M_{\rm h}/M_\odot)$ (Kendall τ rank correlation test, 2.1σ) where redder galaxies tend to be more massive. We find that, with the exception of eight galaxies, blue galaxies tend to be low mass while red galaxies tend to be high mass (also see Nielsen et al. 2015b). There are no significant differences in the TPCFs if we slice by color or mass. Therefore, the color dependencies in

our results are more accurately color-mass dependencies.

To rule out the possibility that any differences in our results are due to biased distributions of azimuthal angle and inclination, we ran a one-dimensional Kolmogorov-Smirnov (KS) test for both orientation measures. We find that the azimuthal angles and inclinations of galaxies in our sample are consistent with unbiased samples at the 0.6σ and 2.3σ levels, respectively. Additionally, rank-correlation tests between Φ or i and galaxy properties such as rest-frame $B-K$ color show no correlations. Therefore, any differences we see in our results are likely due to different physical processes rather than underlying sample biases.

We calculate pixel velocity two-point correlation functions (TPCFs) following the methods of Nielsen et al. (2015b), focusing only on the absorber TPCFs, defined as a measure of the *internal absorber velocity dispersion*. To summarize, we obtain the velocities of each pixel in the absorption equivalent width regions of a sample of galaxies and calculate the velocity separations of every possible pair of pixels. We bin up the absolute value of the separations and normalize by the number of pixel pairs in the sample. To obtain the uncertainties on the TPCF, we conduct a bootstrap analysis for 100 realizations, where the maximum number of realizations allowed for a sample size of five (our smallest sample) with replacement is 126. More realizations than this begin repeating permutations too often. The 1σ uncertainties are plotted as shaded regions. Additionally, we characterize the TPCFs by measuring the velocity separations within which 50% and 90% of the data are located, $\Delta v(50)$ and $\Delta v(90)$, respectively. These values are tabulated in Table 5.1 for each subsample.

Table 5.1. TPCF Velocity Measurements

Sample	# Gals	Cut	Cut	$\Delta v(50)^{a}$	$\Delta v(90)^{a}$
		Figure 5.1			
Edge-on	13	$i \geq 57°$	$\cdots$	64^{+4}_{-5}	149^{+9}_{-12}
Face-on	17	$i < 57°$	$\cdots$	67^{+6}_{-12}	192^{+14}_{-31}
Minor Axis	15	$\Phi \geq 45°$	$\cdots$	72^{+5}_{-7}	188^{+13}_{-22}
Major Axis	15	$\Phi < 45°$	$\cdots$	52^{+8}_{-11}	131^{+17}_{-26}
Edge-on - Minor Axis	8	$i \geq 57°$	$\Phi \geq 45°$	60^{+3}_{-4}	141^{+7}_{-10}
Edge-on - Major Axis	5	$i \geq 57°$	$\Phi < 45°$	73^{+11}_{-19}	171^{+25}_{-44}
Face-on - Minor Axis	7	$i < 57°$	$\Phi \geq 45°$	83^{+9}_{-11}	216^{+13}_{-22}
Face-on - Major Axis	10	$i < 57°$	$\Phi < 45°$	39^{+3}_{-4}	96^{+6}_{-8}
		Figure 5.2			
Blue - Minor Axis	10	$B-K < 1.4$	$\Phi \geq 45°$	80^{+7}_{-8}	204^{+16}_{-21}
Blue - Major Axis	5	$B-K < 1.4$	$\Phi < 45°$	52^{+8}_{-16}	124^{+16}_{-37}
Red - Minor Axis	5	$B-K \geq 1.4$	$\Phi \geq 45°$	52^{+2}_{-5}	123^{+4}_{-11}
Red - Major Axis	10	$B-K \geq 1.4$	$\Phi < 45°$	51^{+10}_{-15}	135^{+19}_{-38}
Blue - Face-on	8	$B-K < 1.4$	$i < 57°$	86^{+8}_{-14}	220^{+14}_{-31}
Blue - Edge-on	7	$B-K < 1.4$	$i \geq 57°$	61^{+5}_{-8}	143^{+10}_{-18}
Red - Face-on	9	$B-K \geq 1.4$	$i < 57°$	40^{+2}_{-4}	97^{+4}_{-9}
Red - Edge-on	6	$B-K \geq 1.4$	$i \geq 57°$	62^{+6}_{-13}	147^{+15}_{-30}

[a]km s^{-1}

5.3. Results

5.3.1. TPCFs: Galaxy Inclinations and Azimuthal Angles

In Figures 5.1(a) and (d) we examine bivariate trends in the absorber TPCFs for galaxies probed at different inclinations and azimuthal angles. We present "face-on" ($i < 57°$) and "edge-on" ($i \geq 57°$) galaxies probed at all azimuthal angles and colors in panel (a). Absorbers in face-on galaxies have larger velocity dispersions than those in edge-on galaxies. We ran a chi-square test on the binned TPCFs and find that the null hypothesis that the TPCFs are drawn from the same population can be ruled out at the 5.4σ level. The results of the test including the significance, reduced chi-square value, χ^2_ν, and degrees of freedom, ν, are listed in each panel. While the chi-square test result is significant, we find that the $\Delta v(50)$ measurements are within uncertainties for face-on and edge-on galaxies but the value of $\Delta v(90)$ is larger for face-on galaxies. Therefore, the difference between these two distributions is due to the large velocity separation tail in face-on galaxies.

We also examine absorption associated with galaxies probed along the "major axis" ($\Phi < 45°$) and "minor axis" ($\Phi \geq 45°$) in Figure 5.1(d) for all inclinations and colors and find that absorbers located in galaxies probed along the minor axis have larger velocity dispersions than those along the major axis (6.1σ). Values of $\Delta v(50)$ and $\Delta v(90)$ are larger for the minor axis sample than the major axis. For this TPCF pair and the rest in this paper, the measurements of both $\Delta v(50)$ and $\Delta v(90)$ reflect the chi-square results, i.e., where we find an insignificant chi-square value when comparing galaxy subsamples, we also find values of $\Delta v(50)$ and $\Delta v(90)$ that are consistent within uncertainties between subsamples and vice

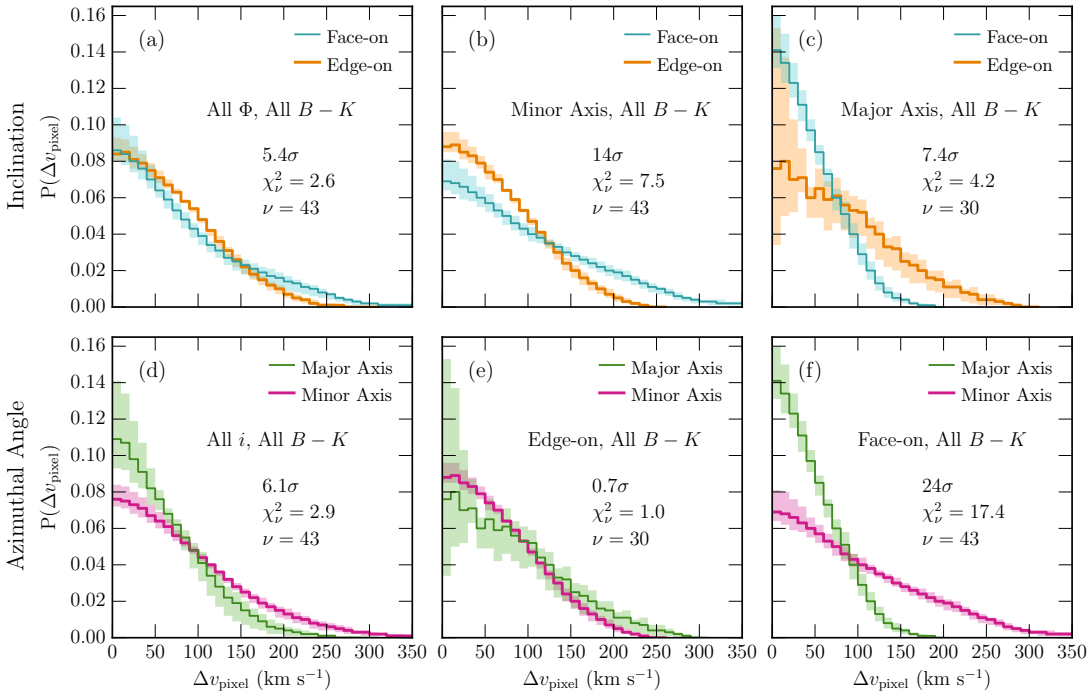

Fig. 5.1.— Two-point correlation functions examining how the spread in the pixel velocities of absorbers differs when probing galaxies of different inclinations and azimuthal angles (for all galaxy colors, $B-K$). Panels (a), (b), and (c) compare TPCFs of face-on ($i < 57°$) and edge-on ($i \geq 57°$) galaxies for all Φ, $\Phi \geq 45°$, and $\Phi < 45°$, respectively. Panels (d), (e), and (f) examine how the TPCFs along the major axis ($\Phi < 45°$) and minor axis ($\Phi \geq 45°$) differ for all i, $i \geq 57°$, and $i < 57°$, respectively. In each panel the TPCF is represented as a solid line while shaded regions are the 1σ bootstrap uncertainties. We list the significance of a chi-square test comparing the TPCFs in each panel in addition to the reduced chi-square value, χ^2_ν, and the degrees of freedom, ν. We see a broader velocity dispersion for face-on galaxies than for edge-on galaxies when all azimuthal angles are considered (panel (a)). We also see a larger velocity dispersion for minor axis projections than major axis projections when all inclinations are considered (panel (d)). This latter result becomes highly significant for face-on galaxies where the minor axis dispersion is greater than that for the major axis (panel (f)). Conversely, there is no difference in the dispersion with azimuthal angle for edge-on orientations (panel (e)). Thus, the velocity dispersion is greatest for face-on galaxies probed along the projected minor axis.

versa.

While we find significant differences in the absorber TPCFs with inclination or azimuthal angle, both orientation measures are important for describing the precise location of an absorber around a galaxy. Therefore, in Figure 5.1 we present a multivariate analysis comparing the absorber TPCFs for face-on and edge-on galaxies probed along (b) the minor axis and (c) the major axis. We also compare absorber TPCFs for galaxies probed along the major and minor axes for (e) edge-on galaxies and (f) face-on galaxies. We find that absorbers located in edge-on galaxies have similar velocity dispersions regardless of the azimuthal angle at which the galaxy is probed (panel (e), 0.7σ). We also find a highly significant difference (24σ) for face-on galaxies probed along the major and minor axes in Figure 5.1(f) where the absorber velocity dispersions are much greater along the minor axis than the major axis. In fact, both $\Delta v(50)$ and $\Delta v(90)$ for the face-on, minor axis subsample are roughly twice as large as those along the major axis. For absorption probed along the minor axis (Figure 5.1(b)) and the major axis (Figure 5.1(c)), face-on samples are significantly different from the edge-on samples. Along the minor (major) axis, the velocity dispersion of absorbers is greater (smaller) for face-on galaxies than edge-on with a significance of 14σ (7.4σ).

5.3.2. TPCFs: Galaxy Colors and Orientations

We also study the differences in absorber TPCFs for galaxies of various orientations with galaxy color in Figure 5.2. Panels (a), (b), (c), and (d) present azimuthal angle and color subsamples (for all inclinations) while panels (e), (f),

(g), and (h) present subsamples sliced by inclination and galaxy color (for all azimuthal angles).

Comparing the absorber TPCFs for subsamples sliced by azimuthal angle and $B-K$ color in the left panels of Figure 5.2, we find no significant difference (0σ) in absorber velocity dispersions along the major axis in blue and red galaxies (panel (a)) or for absorbers hosted by red galaxies along the major and minor axes (panel (d)). The only TPCF that is significantly different from the rest in this set is the blue, minor axis subsample which has a significantly larger absorber velocity dispersion than either the red, minor axis subsample (panel (b), 16σ) or the blue, major axis subsample (panel (c), 10σ). While $\Delta v(50)$ and $\Delta v(90)$ are nearly identical for the red, major axis subsample, the red, minor axis subsample, and the blue, major axis subsample, the measurements for the blue, minor axis subsample are two times larger than the rest.

In the right panels of Figure 5.2 where we examine absorber TPCFs of subsamples sliced by inclination and $B-K$ color, we find that the absorbers located around edge-on galaxies have similar velocity dispersions regardless of galaxy color (0σ, Figure 5.2(f)). The values of $\Delta v(50)$ and $\Delta v(90)$ for these two subsamples are nearly identical and consistent well within uncertainties. On the other hand, absorbers around face-on galaxies at all azimuthal angles in Figure 5.2(e) are dramatically different for blue and red galaxies. The absorber velocity dispersions are much greater (21σ) in face-on, blue galaxies than in face-on, red galaxies which are more highly peaked at low velocity separations. The $\Delta v(50)$ and $\Delta v(90)$ measurements are roughly twice as large for the blue subsample than the red subsample. The velocity dispersions of absorbers hosted by both blue and red galaxies in Figures 5.2(g) and 5.2(h) depend on the observed inclination.

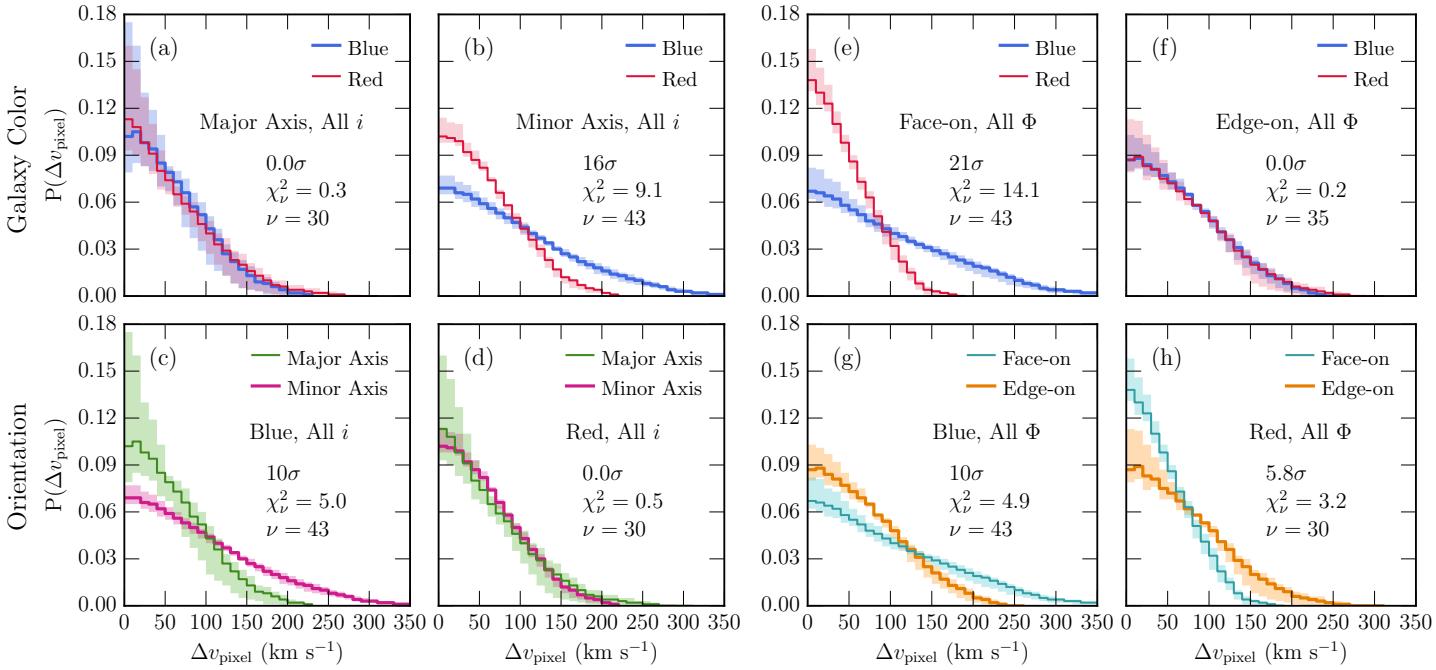

Fig. 5.2.— Velocity two-point correlation functions for subsamples cut by galaxy rest-frame $B-K$ color, azimuthal angle, and inclination. Lines, shading, and the results of a chi-square test comparing subsamples are plotted as in Figure 5.1. For all inclinations, blue and red galaxy TPCFs are compared along the major axis ($\Phi < 45°$) and minor axis ($\Phi \geq 45°$) in panels (a) and (b). Panels (c) and (d) present the TPCFs of blue and red galaxies, respectively, at different azimuthal angles. For all azimuthal angles, we compare the absorber velocity dispersions of blue and red face-on ($i < 57°$) galaxies in panel (e) and edge-on ($i \geq 57°$) galaxies in panel (f). Finally, panels (g) and (h) present TPCFs of blue and red galaxies, respectively, at different inclinations. The velocity dispersions for blue and red galaxies probed at different azimuthal angles are all statistically consistent (panels (a) and (d)) with the exception of large dispersions for the blue, minor axis subsample. We also find dramatic differences between the absorber velocity dispersions for blue and red galaxies in face-on orientations (panel (e)) where blue galaxies have much larger dispersions than red, but no differences for edge-on orientations (panel (f)).

5.3.3. Cloud Column Densities and Velocities

To obtain further understanding of the material being probed for each orientation presented in the TPCFs, we plot cloud (VP component) column densities and velocities in Figure 5.3, where clouds plotted in panel (a) are associated with galaxies probed along the minor axis and in panel (b) with galaxies probed along the major axis. Scatter plots show the cloud column densities and velocities from Voigt profile fitting, where vertical dashed lines on the scatter plots at ± 100 km s^{-1} are to help guide the eye between panels. Points are colored by galaxy color, $B-K$, while point types represent galaxy inclination, i. Histograms to the left and right in each panel present the distribution of cloud column densities for galaxies sliced by (left) galaxy color and (right) inclination, where the indicated significance is the result of a KS test between subsamples for the unbinned data. Finally, the histograms on top and bottom show the distribution of *pixel* velocities used to calculate the TPCFs for subsamples cut by (bottom) galaxy color and (top) inclination. The result of an F-test between the unbinned pixel velocities of each subsample pair is indicated next to the top and bottom histograms. In each case, the pixel velocity F-test results show similar results as the TPCF chi-square test, i.e., a significant chi-square test corresponds to a significant F-test and vice versa.

In general, we find that higher velocity material has lower column density values, while higher column density material is only found at lower velocity. This is consistent with previous works (e.g., Churchill et al. 2003) and is largely due to the fact that $v = 0$ km s^{-1} is defined by the optical depth median of the absorption. The highest velocity ($v > |100|$ km s^{-1}), low column density clouds

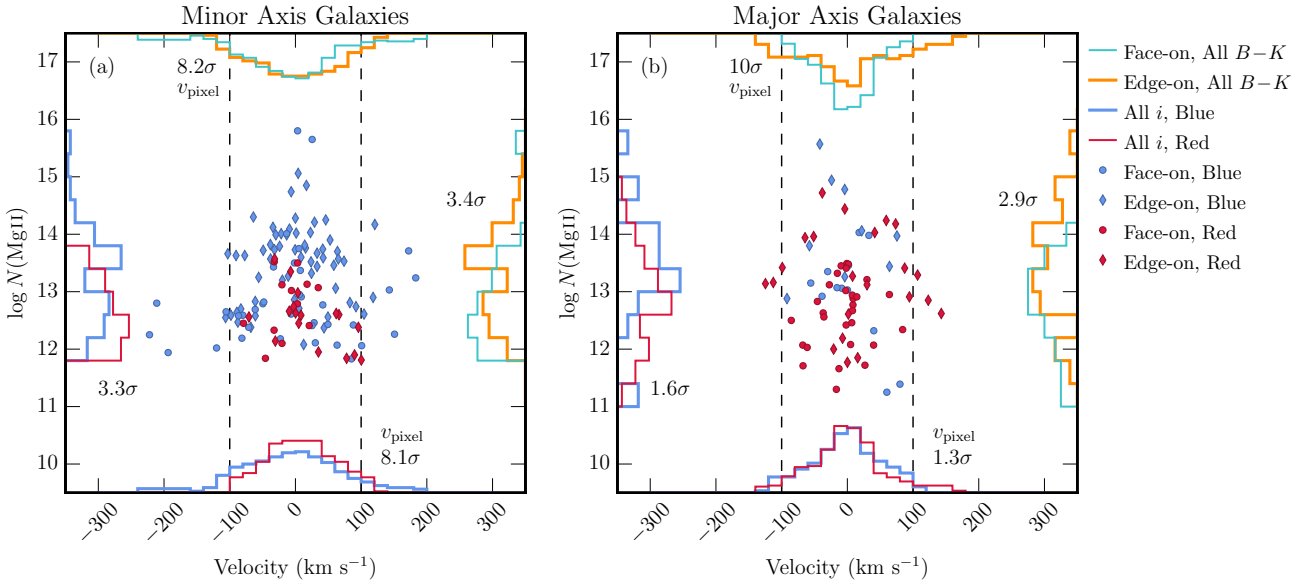

Fig. 5.3.— Cloud (VP component) column densities and velocities, and pixel velocities for galaxy subsamples sliced by inclination and galaxy color for galaxies probed along (a) the minor axis ($\Phi \geq 45°$) and (b) the major axis ($\Phi < 45°$). Scatter plots show the modeled cloud velocities and column densities. Blue points represent blue galaxies, red points are red galaxies, circles are face-on galaxies, and diamonds are edge-on galaxies. Vertical dashed lines at ± 100 km s^{-1} are provided to help guide the reader's eye between panels. Histograms on the left and right of each panel show the distribution of cloud column densities for subsamples sliced by (left) galaxy color, $B - K$, and (right) inclination, i. The quoted significance near the column density histograms is the result of a KS test between plotted subsamples. Top and bottom histograms of each panel present the distribution of *pixel* velocities for subsamples cut by (bottom) galaxy color and (top) inclination. The significances quoted for the top and bottom histograms are for an F-test comparing the variance in the distribution of pixel velocities for each pair of plotted subsamples. All histograms are normalized by the total number of data points in each subsample. In general, we find that clouds with larger velocities have smaller column densities, while those with larger column densities have smaller velocities. We find that the cloud column density distributions are statistically consistent for galaxies probed along the major axis (panel (b)), regardless of whether we compare subsamples sliced by galaxy color or inclination. However, we find statistically larger column densities for blue and face-on galaxies probed along the minor axis (panel (a)).

are mostly associated with blue, face-on galaxies probed along the minor axis. There is also a population of $v \sim |100|$ km s^{-1} clouds that are associated with edge-on galaxies probed along the minor axis, though we find a few for major axis galaxies as well. All of these clouds at high velocity are found in absorbers which have higher column density material located near the velocity zero point. about it

For minor axis galaxies in Figure 5.3(a), we find that blue galaxies have significantly larger column densities than red galaxies (3.3σ) and edge-on galaxies have significantly larger column densities than face-on galaxies (3.4σ). However, these results are mostly due to a lack of large column density clouds around face-on galaxies and red galaxies. For major axis galaxies in Figure 5.3(b), we only find a suggestion of larger column densities for edge-on galaxies than face-on galaxies (2.9σ), though clouds at $\log N(\mathrm{Mg\,II}) > 14$ are mainly hosted by edge-on galaxies. Conversely, we find no difference between blue and red galaxies (1.6σ) along the major axis.

In Figure 5.4 we compare the cloud column densities and velocities, and the pixel velocities for (a) face-on galaxies and (b) edge-on galaxies, slicing the samples by galaxy color and azimuthal angle. Similar to Figure 5.3, point colors and the left and bottom histograms represent blue and red galaxy subsamples, while point types and top and right histograms represent major axis and minor axis subsamples. The indicated significances correspond to the same statistical tests as in Figure 5.3. Again, the pixel velocity F-test results follow the TPCF chi-square test results, with the exception of the test comparing edge-on galaxies probed along the major and minor axes (panel (b)). In this case the F-test result is significant, but due to the large bootstrap uncertainties on the major axis

TPCF, the chi-square test on the corresponding TPCFs is not significant (see Figure 5.1(e)).

We find that absorbers around face-on galaxies consist of clouds with column densities that rarely exceed $\log N(\mathrm{Mg\,II}) = 14$. This is in contrast to edge-on galaxies which are more likely to have these high column density clouds. For face-on galaxies, the column densities of blue and red galaxies are statistically consistent (0.4σ). Comparing blue galaxies with face-on and edge-on inclinations, we find that the column densities of the edge-on subsample are larger than those in the face-on subsample (4.5σ, not plotted). We also find that the column densities of the blue, edge-on subsample are larger than the red, edge-on sample (4.0σ). There are no such differences in the column densities between galaxies probed along the major and minor axes for face-on (0.7σ), edge-on (0.9σ), blue (1.7σ, not plotted) or red (1.5σ, not plotted) galaxies.

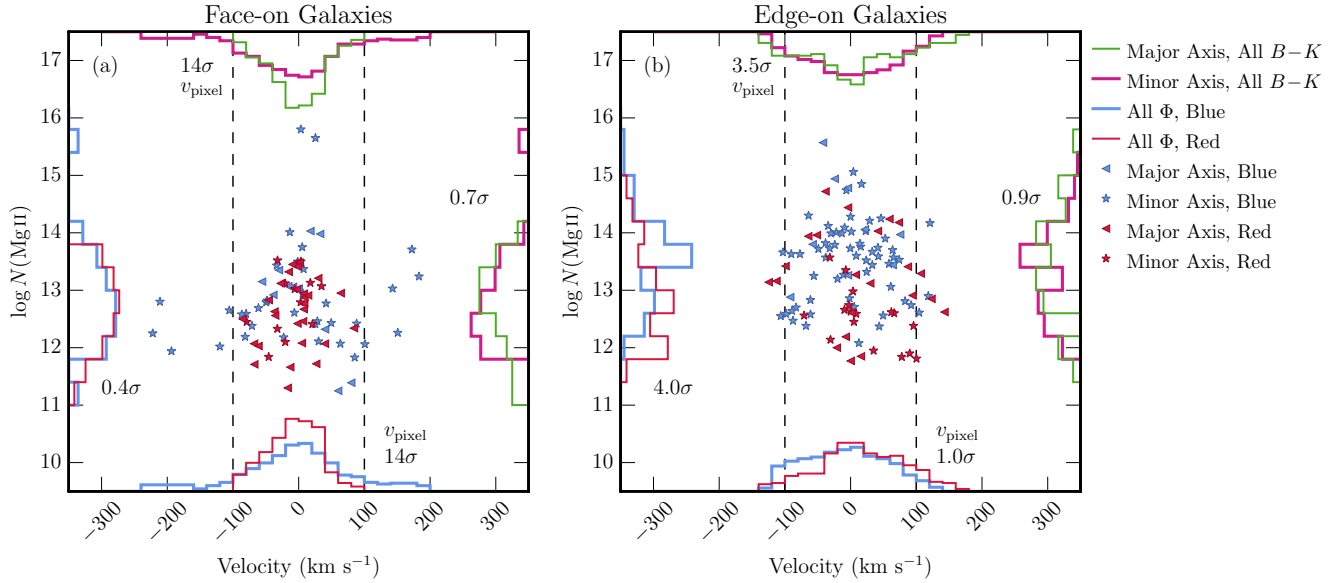

Fig. 5.4.— Cloud column densities and velocities, and pixel velocities for (a) face-on galaxies ($i < 57°$) and (b) edge-on galaxies ($i \geq 57°$) split by galaxy color and azimuthal angle. Blue galaxies are represented as blue points, red galaxies as red points, galaxies probed along the major axis as triangles, and galaxies probed along the minor axis as stars. Vertical dashed lines are plotted to help guide the reader's eye between panels. Histograms in each panel represent the distributions of cloud column densities split by (left) galaxy color, $B - K$, (right) azimuthal angle, Φ, and *pixel* velocities split by (bottom) galaxy color, and (top) azimuthal angle. The quoted significances near the histograms report the results of a KS test between plotted subsamples for the cloud column densities (left and right) and the results of an F-test comparing the variance in the pixel velocity distributions between plotted subsamples for the top and bottom histograms. We find that the cloud column densities for absorbers around face-on galaxies rarely exceed $\log N(\mathrm{Mg\,II}) = 14$ (panel (a)), in contrast to edge-on galaxies (panel (b)). In both face-on and edge-on galaxies, we see no difference in the column densities with regard to the azimuthal angle (right histograms). Lastly, we find that the cloud column densities in absorbers around blue galaxies with edge-on inclinations are greater than those for absorbers around blue, face-on galaxies (4.5σ, not plotted) or red, edge-on galaxies (4.0σ, panel (b)).

5.4. Discussion

The results in the previous section demonstrate that absorber velocity dispersions and column densities of the gas traced by Mg II absorption depend strongly on where the gas is located around the galaxy. Mechanisms in the baryon cycle which could give rise to this material include (1) merging satellite galaxies whose gas is either being ejected due to star formation or being stripped by tidal forces, (2) IGM accretion, recycled accretion, and/or rotating material merging onto the galaxy disk, and (3) outflowing gas in star-forming galaxies. In this section, we discuss which mechanisms are most likely contributing to the differences in the observed velocity dispersions and cloud column densities as a function of host galaxy color (as a proxy for star formation) and orientation.

5.4.1. Merging Satellite Galaxies

Many previous works have investigated the preferential location of satellite galaxies around a larger, host galaxy. The consensus appears to be that, for red galaxies, satellites within the virial radius are aligned with the central galaxy's major axis, while there is no preferred alignment for satellites around blue galaxies (with the exception of galaxies in the Local Group; Yang et al. 2006, and references therein). This has been confirmed in recent simulations by Dong et al. (2014). Our color cut defining blue and red galaxies is bluer than that used by Yang et al. (2006) (our $B - K = 1.399$ cut corresponds to $g - r = 0.62$, compared to their $g - r = 0.83$). Since the blue galaxies in Yang et al. (2006) have been found to have an isotropic distribution of satellites, our bluer color cut may result in more blue galaxies in our "red" sample than in the Yang red sample, and therefore a

more isotropic distribution of satellites around red galaxies for our sample.

We may be observing Mg II absorption due to satellites, but even though satellites align with the major axis of red galaxies, we see no difference between the TPCFs or column densities of our red galaxy samples along the major and minor axes. Also, the isotropic distribution of satellites around blue galaxies is not consistent with the highly significant differences between the TPCFs of our blue galaxy samples along the major and minor axes. If satellites are the dominant source of Mg II absorption, we would expect the TPCFs to show differences along the major and minor axes in red galaxies (or no differences due to our bluer color cut), but show no differences in blue galaxies.

We do not have velocity information on the host galaxy-satellite galaxy samples published in Yang et al. (2006). However, the velocity distribution of the satellites around galaxies is unlikely to be the cause of the different absorber kinematic distributions for several reasons. We are looking at the velocity dispersions of the absorbers themselves, not of the material with respect to the galaxy systemic velocity. We assume our sightlines are unlikely to pass through multiple satellites at once so the internal gas velocity distributions of the satellite galaxies would have to show differences for blue host galaxies (to match the TPCFs), but not for red. However, if Mg II absorption is due to tidal stripping of or outflows from the satellites, we would expect the satellites around red galaxies to be more disturbed and therefore have larger absorber velocity dispersions because they live in more massive halos than if they were located around blue galaxies. Therefore, we suggest that satellites are not the dominant source of Mg II absorption.

The galaxies in our sample were drawn from MAGIICAT (Nielsen et al.

2013b), which contains only galaxies that are isolated to the limits of the data, where no spectroscopically identified neighbor was found within $D < 100$ kpc or a line-of-sight velocity of 500 km s^{-1}. If satellites are present in our sample, they are undetected within both velocity space and impact parameter. Additionally, all of the galaxies were imaged with *HST* and satellite galaxies were not detected in any of the images which were carefully examined when the galaxies were modeled for their orientations. If satellites were present, they would have been detected in the model residuals. Therefore, if we are probing satellite galaxies, they are below our detection limits (i.e., below roughly $0.1L_B/L_B^*$ Nielsen et al. 2013b).

5.4.2. Accretion and Rotation

Previous work examining the low-ionization CGM has found accreting and/or rotating material in the form of blueshifted absorption for edge-on galaxies probed along the projected major axis (e.g., Bouché et al. 2012; Rubin et al. 2012). This is also commonly observed in simulations (e.g., Stewart et al. 2011). Since we do not know whether our absorbers are blueshifted or redshifted with respect to the galaxy as can be determined through the down-the-barrel approach used by Rubin et al. (2012), we cannot say for certain whether our absorbers are accreting or rotating. However, we can examine the possible properties of this material in absorber velocity dispersions and cloud column densities for orientations in which accreting and rotating material is expected to be found.

Edge-on galaxies probed along the major axis are most likely to exhibit accreting or rotating material and are the least likely orientation to be contaminated with outflowing material. Also, the velocity along the line-of-sight is greatest for

rotation in edge-on galaxies. In our sample, this orientation is dominated by absorbers that contain clouds with larger column densities ($\log N(\mathrm{Mg\,II}) > 13$), most of which have velocities $v < |100|$ km s^{-1}. This is most easily seen as the diamond points in Figure 5.3(b). We might expect to only see blue galaxies with absorption in this orientation due to the red galaxies having their star formation quenched from a lack of a gas reservoir, but the subsample is populated by both blue and red galaxies. We could be seeing recycled accretion in galaxies of all colors from past outflows, especially since, according to theory, cold-mode accretion is expected to be mostly non-existent for halo masses $\log(M_{\rm h}/M_{\odot}) > 12$ (e.g., Kereš et al. 2005, 2009; Dekel & Birnboim 2006). Nearly all of the red galaxies in our sample are in fact above this mass limit, and therefore should not have cold-mode accretion from the IGM, but instead may have recycled accretion. It is also possible that some of the red galaxies we have observed are in fact dusty, star-forming galaxies that are currently accreting material, especially since our $B-K$ color cut does include Sbc SED types in with the "red" galaxy subsample (see Nielsen et al. 2013b, for details concerning our $B-K$ color calculations). This is less likely because we would have observed signatures of outflows in both blue and red galaxies, unless dusty, star-forming galaxies are rare in our sample. We do not yet have the information needed to calculate the star formation rates to determine if we have dusty, star-forming galaxies in our sample.

It is interesting that we find no significant difference in the TPCFs of blue and red galaxies probed along the major axis (for all i) or in edge-on inclinations (for all Φ) in Figures 5.2(a) and (f), respectively. This suggests that the velocity structure of absorbers along the major axis or for edge-on galaxies does not depend on the star formation rate of the host galaxy. This fits in with the accretion or rotating

gas picture which, unlike outflows, should not depend on the star formation rate unless the star formation rate is so great as to prevent accretion and/or remove the gas reservoir. Also interesting is that the absorber velocity dispersions depend on inclination for the major axis sample in Figure 5.1(c). The absorber velocity dispersion is greater for edge-on galaxies than for face-on galaxies along the major axis, and this may be due to rotating gas whose line-of-sight velocity is maximized in edge-on inclinations. The column densities may also be greater for edge-on galaxies than for face-on galaxies along the major axis (Figure 5.3(b)). This could indicate that the accreting or rotating material for the edge-on galaxies is more coherent, i.e., the path lengths or amount of material are larger than for face-on galaxies.

5.4.3. Outflows

Absorption line studies have frequently found evidence for outflows as blueshifted absorption in face-on galaxies (e.g., Rubin et al. 2014) or as enhanced equivalent widths along the projected minor axis for edge-on galaxies (e.g., Bordoloi et al. 2011). We therefore also associate the kinematics results for our blue, face-on and minor axis subsamples with outflows. Again, we cannot say for certain if our absorbers are actually entrained in outflowing material so we instead focus on possible absorption properties of the absorbers for orientations in which outflows are most likely to occur.

For blue, edge-on galaxies probed along the minor axis (blue diamonds in Figure 5.3(a)), we found a group of lower column density ($\log N(\mathrm{Mg\,II}) < 13$), higher velocity ($v \lesssim |100|$ km s^{-1}) material. This is similar to Fox et al. (2015)

who used a background quasar whose line of sight passes through the biconical Fermi Bubbles at the Milky Way galactic center, where the Milky Way in this case is similar to our edge-on, minor axis subsample. They reported a complex absorption profile with two high-velocity metal absorption components at $v_{\rm LSR} \sim \pm 250$ km s^{-1} with $\log N({\rm S\,II}) \sim 13.2$. They associate these components with cool gas that has been entrained in the near and far sides of an outflow from the galactic center. In our sample, comparable components have similar column densities, but a lower velocity with respect to the bulk of the absorption, which may be due to the fact that we are probing outflows at much larger impact parameters than Fox et al. (2015); $D > 20$ kpc compared to $D = 2.3$ kpc. This suggests that the low column density clouds we find in our edge-on, minor axis galaxies are also associated with fragmented cool gas entrained in outflows.

In our subsample consisting of blue, face-on galaxies probed along the minor axis (blue circles in Figure 5.3(a)), the absorbers are dominated by low column density ($\log N({\rm Mg\,II}) < 14$) material (where most of the clouds are $\log N({\rm Mg\,II}) \leq 13$), with high velocity components at $v > |100|$ km s^{-1}. This material is also similar to the absorber found by Fox et al. (2015). We suggest that the velocities are larger for our face-on galaxies than for our edge-on galaxies along the minor axis because we are observing down into the outflow (i.e., the down-the-barrel approach) as opposed to across the outflow. We expect the line-of-sight velocity dispersions to be larger for the face-on sample as the biconical outflows are pointed toward (or away from) the observer, and this is observed in our face-on, blue galaxy subsample TPCFs.

The larger column density ($\log N({\rm Mg\,II}) > 13$), lower velocity ($v \lesssim |50|$ km s^{-1}) clouds for blue, edge-on galaxies probed along the minor axis (seen in Figure 5.3(a)

as blue diamonds), suggest that we are observing more material, a larger path length, a larger metallicity, or ionization conditions that are more conducive to MgII absorption than for face-on, minor axis galaxies. Since the material probed in both of these orientations is most likely outflows, we do not expect the metallicity or the ionization conditions to depend on orientation, and therefore should not be the cause of the enhanced column densities for the edge-on sample compared to the face-on sample. However, Veilleux et al. (2005) listed large variations in the metallicity and ionization levels between clouds as a possible signature of outflows in quasar absorption lines. If this were the case here, we should also see the large column density clouds for face-on galaxies, but they are nonexistent in our sample. Differences in the column densities with inclination therefore hint at probing larger amounts of gas or larger path lengths for the lowest velocity clouds associated with outflows in edge-on galaxies, an effect that may be due to the geometry of the clouds.

In contrast to the blue galaxies, we find very small absorber velocity dispersions for red galaxies in face-on, minor axis orientations (red circles in Figure 5.3(a)). We suggest that this is due to a lack of current outflows stirring up the MgII absorbers. This is supported by the fact that redder galaxies tend to have lower star formation rates and don't typically drive outflows. We caution that this subsample is small, which may indicate that outflows in red galaxies for this orientation are rare rather than nonexistent. The red, edge-on galaxies probed along the minor axis (red diamonds in Figure 5.3(a)) have clouds with velocities and column densities similar to the low column density clouds found around blue galaxies in the same orientation, suggesting that we do see fragmented, outflowing material in red galaxies, but again, it is rare.

5.5. Summary and Conclusions

We have examined the dependence of absorber velocity dispersions and cloud column densities on galaxy rest-frame $B - K$ color, azimuthal angle, and inclination for a subset of 30 isolated MAGIICAT galaxies. Each of these galaxies was imaged with *HST* and has been modeled to obtain galaxy orientations. In each case, we have a high-resolution spectrum of the associated background quasar for detailed kinematic analysis. Our findings include the following:

1. Merging satellite galaxies may contribute to the observed Mg II absorption, but are not expected to dominate. If they did dominate, then we would expect differences in the TPCFs to correspond to the preferred locations of the satellites around galaxies (isotropic distribution for blue galaxies and along the major axis for red galaxies), but this is not the case. We also do not expect the velocities of the satellites to have much of an effect on our TPCFs because it is unlikely that our sightlines are hitting multiple satellites at once, and we would expect larger absorber velocity dispersions for satellites hosted by red galaxies due to the larger mass of red galaxies than blue, which was not found.

2. We find possible evidence for coherent accretion and/or rotation in edge-on galaxies probed along the major axis, the signatures of which are average absorber velocity dispersions and larger column density clouds at low velocity. These signatures do not appear to depend on galaxy color, and therefore star formation rate. The fact that the column densities are larger and this material is observed for all galaxy colors may also indicate that this material is more likely recycled accretion from past outflows rather than cold-mode

accretion.

3. We see suggestions of outflows in the form of large absorber velocity dispersions and smaller column density clouds at higher velocity in blue, face-on galaxies probed along the minor axis and for blue, edge-on galaxies along the minor axis. Both of these orientation combinations are consistent with the location of bipolar outflows. These outflow signatures may be an indication that the material probed by Mg II absorption is fragmented material entrained in outflows. Larger column density clouds at low velocity are also present in the blue, edge-on galaxies probed along the minor axis. Since comparable components are lacking in the face-on sample, we suggest that the path lengths of these clouds are larger, suggesting a geometry effect. For the smallest column density clouds ($\log N(\mathrm{Mg\,II}) \lesssim 13$), the cloud velocities (and absorber velocity dispersions) are greater for the face-on galaxies than edge-on galaxies. We attribute this to looking down into the outflow for face-on galaxies, and across the outflow for edge-on galaxies. Conversely, the very small absorber velocity dispersions for red galaxies at these orientations suggests that outflows are not active, a result of star formation having been quenched.

This work shows that the velocity structure and cloud column densities of Mg II absorbers depend on a combination of galaxy orientations and colors (and likely other galaxy properties not included in this work), not just one or two properties at a time as has been commonly examined in the past. For example, when observing edge-on galaxies, absorption could be probing accretion along the major axis, or outflows along the minor axis. In this case, the outflows will

dominate the absorption signature and the information for accretion will likely be lost, which may contribute to the low covering fractions found for accreting material.

We also find that while the equivalent width of an absorption profile provides a useful diagnostic for generally determining what type of material is being studied, considering both the velocity structure (in terms of the velocity spread or dispersion) and cloud column densities of absorbers with galaxy orientation is important for probing the details of gas flows. This is evident in the fact that absorbers probing outflows in face-on galaxies may have large equivalent widths because of the large velocity spread in the absorbers, whereas outflows in edge-on, minor axis galaxies may have large equivalent widths mainly due to large column density clouds. Modeling the ionization conditions and metallicities in the clouds would also be beneficial, as large cloud-cloud variations in outflows have been suggested by Veilleux et al. (2005), but this is beyond the scope of the present work.

Future work might include examining mock quasar absorption line spectra in simulations for a variety of galaxy colors (or star formation rate and mass) and orientations to better understand the origin of the absorber velocity structure and cloud column densities. By applying our analysis to simulations, we not only obtain a more physical explanation for what we observe, but we also help constrain the CGM in simulations. Observationally, a larger sample of galaxies with *HST* images and high-resolution spectra would allow us to slice the sample by galaxy color, azimuthal angle, *and* inclination to better explore the multivariate dependence of absorber properties on the host galaxy and its baryon cycle. Our current sample is only large enough to slice by two galaxy properties in the TPCFs,

though we have presented all three properties in Figures 5.3 and 5.4.

It would also be useful to obtain estimates of the absorber metallicities to further understand whether we are probing cold-mode accretion, recycled accretion, satellite material, and/or outflows. Metallicities are important to help distinguish between accretion and outflows, where accreting material is expected to have lower metallicities than outflowing material (see Lehner et al. 2013, and references therein). Comparable metallicities across all galaxy orientations might indicate that Mg II absorption is primarily associated with outflows and recycled accretion, not cold-mode accretion. Lastly, determining the star formation rates of the galaxies in our sample is important to identify any possible dusty, star forming galaxies which may be contaminating the results of our red galaxy samples. The galaxy star formation rates provide a more physical indicator of ongoing star formation than galaxy color.

This material is based upon work supported by the National Science Foundation under Grant No. 1210200 (NSF East Asia and Pacific Summer Institutes). This research was primarily supported through grant HST-AR-12646 provided by NASA via the Space Telescope Science Institute, which is operated by the Association of Universities for Research in Astronomy (AURA) under NASA contract NAS 5-26555. N.M.N. was also partially supported through a NMSGC Graduate Fellowship and a Graduate Research Enhancement Grant (GREG) sponsored by the Office of the Vice President for Research at New Mexico State University. M.T.M. thanks the Australian Research Council for Discovery Project grant DP130100568 which supported this work.

6. CONCLUSIONS

6.1. Summary

While each preceding chapter contains a summary and conclusions, we list the most significant findings here to summarize the full body of work.

1. We compiled 182 Mg II absorber-galaxy pairs from literature spanning nearly three decades and standardized all galaxy properties to a single cosmology and filter set for direct comparisons between different surveys. The Mg II Absorber-Galaxy Catalog, MAGIICAT, is an isolated galaxy sample spanning a redshift range of $0.07 < z_{\rm gal} < 1.1$. For each galaxy in the catalog, we have spectroscopic redshifts ($z_{\rm gal}$), B- and K-band absolute magnitudes and luminosities, $B-K$ rest-frame colors, and a measurement or a 3σ upper limit on the associated Mg II absorption from a background quasar spectrum probing the CGM of each galaxy within $D = 200$ kpc.

2. We find a strong anti-correlation between Mg II absorbing strength, $W_r(2796)$, and projected impact parameter, D, which is significant to the 7.9σ level. As we probe further from the host galaxy, the amount of absorbing gas decreases and this is best parameterized as a log-linear relation. The scatter around this relation is most strongly due to the luminosity of the host galaxies, rather than the galaxy color (as a proxy for star formation rate) or redshift. In this case, more luminous galaxies have larger Mg II equivalent width measurements than less luminous galaxies at the same impact parameter.

3. The covering fraction, or the probability of detecting absorbing gas, de-

creases with increasing impact parameter and for increasing equivalent width cut from unity to nearly zero. We find that more luminous galaxies have larger covering fractions at all impact parameters than for less luminous galaxies, though this difference is reduced for the largest equivalent width cuts. In fact, low luminosity galaxies do not have absorption outside of $D = 100$ kpc in contrast to the higher luminosity galaxies. Bluer and higher redshift galaxies may also have larger covering fractions at all D and equivalent width cuts than red and lower redshift galaxies, respectively. Both red and low redshift galaxies have no absorption outside of $D = 100$ kpc.

4. To estimate the radial extent of the CGM as a function of galaxy luminosity, we fit values of R_* (the characteristic halo absorption radius for an L^* galaxy) and β (the luminosity scaling) for the "halo absorption radius," $R(L) = R_*(L/L^*)^\beta$, in both the B- and K-bands. We find that this outer envelope of absorption depends on both Mg II absorption strength and luminosity, where more luminous galaxies have larger values of $R(L)$ than less luminous galaxies. In the B-band, we find R_* ranges from $\sim$ 75 kpc to $\sim$ 80 kpc with a luminosity scaling of $\beta \sim 0.3$ to 0.4 and in the K-band, we find R_* ranges from $\sim$ 60 kpc to $\sim$ 80 kpc with $\beta \sim 0.2$ to 0.3 for the K-band. Redder galaxies tend to have larger values of R_* and steeper β than bluer galaxies, possibly due to the larger halo mass of red galaxies. Finally, in the B-band, higher redshift galaxies have a shallower dependence on luminosity (smaller values of β) than for lower redshift galaxies, but no differences in the K-band. Because the covering fractions for this sample are not unity at large D, we interpret $R(L)$ as more of a "fuzzy" boundary.

5. For the first time, we find direct, observational evidence for the evolution of the kinematics of the gas traced by Mg II absorption in both redshift and $D/R_{\rm vir}$ space, depending on whether the galaxy is expected to be star-forming (blue galaxies) or passive (red galaxies). The kinematics of absorbers hosted by blue galaxies do not appear to change over redshift or $D/R_{\rm vir}$, suggesting that ongoing evolution in the form of accreting and/or outflowing gas is retaining the structure of the CGM. On the other hand, the kinematics of absorbers hosted by red galaxies show redshift evolution, where the kinematics decrease in complexity towards lower redshifts and larger $D/R_{\rm vir}$, suggesting that red galaxies do not have the star formation required to continue replenishing the CGM of cool, Mg II absorbing gas at lower redshifts. We also find that the velocities of the absorbers with respect to the galaxy tend to be larger at lower redshift and higher $D/R_{\rm vir}$ in red galaxies, but not in blue. In this case, we may be observing satellite galaxies that are in the process of merging onto the host galaxy, or the absorbers in red galaxies have been stirred up due to quenching processes such that they will not (re-)accrete onto the galaxy in the future, as may be expected in blue galaxies.

6. We find evidence for merging satellite galaxies, accretion, and rotating gas structures in the velocity dispersions of absorbers hosted by galaxies of various colors and inclinations, and probed at a range of azimuthal angles. We do not expect satellite galaxies to dominate our kinematics signatures, however, as the differences in the pixel velocity two-point correlation functions do not follow the preferred locations of satellites around blue and red galaxies. On the other hand, accretion or a rotating gas disk should most

easily be observed in edge-on, major axis galaxies subsample. Signatures of accreting and/or rotating gas in the form of moderate velocity dispersions in the TPCFs and larger column density clouds at low velocity may indicate that this material is coherent and likely to be recycled accretion from past outflows.

7. Since bipolar outflows are expected to dominate the face-on, blue galaxies subsample and the edge-on, blue galaxies probed along the minor axis subsample, we also find evidence for outflows in our absorber kinematics. In our results, outflows show different signatures depending on the inclination of the galaxy. For face-on galaxies, absorbers assumed to be entrained in outflowing material tend to have lower column density clouds at high velocity. For edge-on galaxies probed along the minor axis, the clouds have larger column densities than for face-on subsamples, and high velocity material which is more consistent with the velocities found in accreting/rotating gas. This suggests we are observing an outflow directed towards the observer in face-on galaxies, and probing across the outflow for edge-on galaxies. We suggest the very small absorber velocity dispersions for red galaxies in orientations consistent with outflows suggests that star formation has been quenched, and therefore outflows are not active for this subsample.

We also obtained halo masses for the MAGIICAT galaxies and this work is presented in Churchill et al. (2013b) and Churchill et al. (2013c, Paper III). In these works, we calculated halo masses for each galaxy using halo abundance matching, following the methods described in Trujillo-Gomez et al. (2011). In summary, we compared the luminosity of each galaxy in the SDSS r-band to the

Wolf et al. (2003) galaxy luminosity functions for the corresponding redshift bins. Then we compared the associated number density for galaxies of that luminosity to the distribution of galaxy maximum circular velocities in the Bolshoi N-body cosmological simulation (Klypin et al. 2011), which then correspond to a given halo mass, $\log(M_{\rm h}/M_{\odot})$. Full details are presented in Churchill et al. (2013c). While we do not present the masses in this dissertation, we use the masses, virial radii, and maximum circular velocities for our kinematics analyses in Chapters 4 and 5.

The main result found in Churchill et al. (2013b) was that the CGM is self-similar with mass, where the Mg II equivalent width of higher mass galaxies is larger than for lower mass galaxies at a given impact parameter. When we examined the $W_r(2706)$-$D/R_{\rm vir}$ plane (which takes into account the fact that larger mass galaxies tend to have larger radii), we find an anti-correlation at the 9σ level and the mass segregation found on the $W_r(2796)$-D plane vanishes. We also found that any differences in the covering fraction for low and high mass galaxies are eliminated when normalizing D by the virial radius. Predictions of a drop in the covering fraction above a halo mass of $\log(M_{\rm h}/M_{\odot}) = 12$ from simulations (e.g., Stewart et al. 2011) of accreting gas in galaxies are not observed with MAGIICAT. In this case, we find that accretion is still present in these high mass galaxies or some mechanism besides accretion, such as outflows or merging sub-halos, is contributing to absorption signatures.

In Churchill et al. (2013c), we found that the majority of Mg II absorbing gas is found within the inner 30% of the virial radius regardless of absorption strength. This boundary is "fuzzy" due to large upward uncertainties on the absorption radius measurement, similar to the work in Chapter 3.3.5 which looked at galaxy

luminosity instead of mass, and due to non-unity covering fractions. Additionally, the authors found that the mean $W_r(2796)$ within $D \simeq 0.3R_{\rm vir}$ (and likely for $D/R_{\rm vir} \leq 1$) is independent of halo mass, contrary to cross-correlation studies between absorbers and their associated galaxies which found an anti-correlation such that smaller mass galaxies hosted absorbers with larger equivalent widths.

Using the MAGIICAT sample, Kacprzak et al. (2012a) modeled the orientations for galaxies imaged with either the Sloan Digital Sky Survey or the *Hubble Space Telescope*. By examining the number of galaxies with detected Mg II absorbing gas as a function of azimuthal angle, the authors found that Mg II absorption prefers to be located along the galaxy projected major and minor axes, whereas sightlines in which no absorption is detected are distributed evenly for all azimuthal angles. Comparing the azimuthal angle distribution between blue and red galaxies in which absorption was detected, they also found that absorption around blue galaxies shows an azimuthal angle preference whereas absorbers around red galaxies have no such preference. This work provided motivation to examine the kinematics of Mg II absorbers as a function of galaxy orientation.

6.2. The Big Picture

As outlined in Chapter 1, the CGM is an extremely important component of galaxies due to the role it plays in galaxy evolution and due to it being the interface between the gas in galaxies (the ISM) and the gas between or outside galaxies (the IGM). The work presented in this dissertation has made several predictions for future work and provides important observational constraints for simulations in their endeavor to create realistic galaxies.

An interesting prediction made in Chapter 3 for the strength of Mg II absorption is that it should level off at low impact parameters and remain roughly constant below $D = 10$ kpc as the impact parameter decreases. Since the work in Chapter 3 was published, Kacprzak et al. (2013) obtained six additional galaxies with background quasar sightlines $D < 6$ kpc from a foreground galaxy. Each galaxy was found to have associated Mg II absorption in the background quasar spectra. When placing these six absorption systems on the equivalent width-impact parameter plane, the authors found that these absorbers followed the log-linear relation found in Nielsen et al. (2013a, Chapter 3). Because of the low impact parameters at which these new absorbers lie and their equivalent width values, Kacprzak et al. (2013) report that they are probing ISM material, whereas beyond $D \sim 6$ kpc, quasar sightlines are more likely probing halo gas. This result implies a smooth gas distribution from the ISM, to extra-planar gas, to the CGM, and provides first steps towards connecting studies using quasar absorption lines and those using H I.

The CGM field has long been moving towards understanding the gas properties in the context of the host galaxy properties and understanding the ionization structure of the absorption. The work presented here is in line with this movement and provides detailed predictions for the motions of Mg II absorbing gas. In fact, up until now, disentangling which absorption systems may be associated with accretion or outflows has been difficult (Barnes et al. 2014). The work we present in Chapter 4 and especially Chapter 5 has made steps towards resolving this problem by comparing the detailed kinematics and column densities of Mg II absorbers to their locations around host galaxies. In these chapters, we provided several predictions which can be further examined in simulations and with other

data sets.

Finally, the work we present here helps tie Mg II absorption to the baryon cycle and galaxy evolution by studying absorption properties for galaxies undergoing a range of evolutionary processes as defined by their redshift, color, luminosity, and mass. Throughout this dissertation, we find evidence for the quenching of star formation in red, passive galaxies, but continued evolution in blue galaxies which keeps the structure of the CGM fairly similar over time. We also find that the CGM is complicated and messy due to the variety of baryon cycle processes occurring in this region around galaxies. While we have presented evidence for accretion and outflows in certain regions of the CGM, it is still difficult to disentangle without consulting detailed simulations. However, the work presented here provides a benchmark to which the simulations can aim.

6.3. Future Work

A first step to improving the dataset to provide more physical interpretations is to obtain more data on the galaxies and the absorbers in our sample. In particular, we wish to measure galaxy star formation rates (SFRs) and obtain better estimates of the galaxy redshifts. While galaxy color is a useful proxy for SFR, color does not indicate if a galaxy has a low SFR, or is a dusty star-forming galaxy. Having the SFRs in hand would reduce this degeneracy. Better estimates on the galaxy redshifts for our sample is important when comparing the motions of the gas with respect to the galaxy to determine if the gas is likely entrained in outflows or is infalling as accretion. Reducing the uncertainties on our redshift measurements also makes our kinematic analysis more sensitive by allowing for

smaller velocity separation bins in the absorber-galaxy TPCFs.

Metallicities of both the host galaxy and the absorbing gas is also important. By comparing the metallicities, we would be able to determine if a gradient is present with impact parameter and to determine if the material we are probing is likely accreting (whether it's more pristine or recycled) or outflowing. We could also compare our absorber metallicities to the work of Lehner et al. (2013) who find a bimodality in lyman limit systems, which is likely due to probing accreting and outflowing material.

Another useful next step towards understanding galaxy evolution by way of the CGM is to conduct our analysis using mock quasar absorption lines in realistic simulated galaxies of a variety of star formation rates, masses, redshifts, and orientations. Not only do our observations constrain the CGM in simulations to form better simulated galaxies, but simulations would improve our interpretations by providing a more physical picture of the processes occurring in our galaxies.

While compiling MAGiiCAT, we removed any absorber-galaxy pairs which were located in group environments. Therefore, we have in hand a sample of 16 MgII absorbers associated with group environments consisting of 33 galaxies. Due to the complicated nature of interacting galaxies, we have thus far avoided examining the circumgalactic medium of these galaxies. However, we plan to compare this sample to our isolated MAGiiCAT galaxies to examine the effect that living in a group environment has on the CGM. Previous works have indicated that the CGM tends to extend further for the same equivalent width than for isolated galaxies and may have larger covering fractions (e.g., Chen et al. 2010a; Bordoloi et al. 2011). We expect to find a more extended, complex, and kinematically hot

CGM for this group galaxy sample than for our isolated galaxy sample.

It is important to keep in mind that while Mg II $\lambda\lambda 2796, 2803$ absorption is a great tracer for the cool CGM and is associated with many of the processes that contribute to the evolution of galaxies, the CGM is more accurately a complex, multiphase reservoir. With this in mind, we intend to conduct our kinematic analysis with other ions such as H I which traces cool gas, C IV which traces gas at $T \sim 10^{4.6}$ K (photoionized) and $T = 10^{5.0}$ K (collisionally ionized), and O VI tracing $T = 10^{4.8}$ K (photoionized) and $T = 10^{5.5}$ K (collisionally ionized). Moving to progressively higher ionization stages probes gas at larger impact parameters. We have just finished collecting quasar spectra covering ultraviolet transitions for a range of ionization stages from a large program using the Cosmic Origins Spectrograph on *HST* and will soon begin analyzing the data.

Finally, we intend to expand MAGIICAT to larger redshifts up to nearly $z = 2.5$ by identifying the galaxies hosting the Mg II absorption found in quasar spectra as identified by Evans (2011, red histogram in Figure 1.1). This will be a long-term campaign in which we will use the MOSFIRE (Multi-Object Spectrometer for Infra-Red Exploration) instrument on Keck to obtain the redshifts, star formation rates, and metallicities for galaxies in the quasar fields studied by Evans (2011). Since the Mg II absorption profiles have already been modeled, expanding MAGIICAT to higher redshifts provides more leverage on the redshift evolution of the absorbers found in the kinematics of Chapter 4, especially since there is mounting evidence that the strongest Mg II absorbers trace the cosmic star formation rate (e.g., Matejek & Simcoe 2012). With this program, we intend to increase MAGIICAT by adding up to 120 absorber-galaxy pairs, nearly doubling the sample, and increasing our kinematics sample immensely.

APPENDICES

APPENDIX A. K-CORRECTIONS

The contents of this appendix were originally published as Nielsen, N. M., Churchill, C. W., Kacprzak, G. G., & Murphy, M. T. 2013, ApJ, 776, 114.

For a galaxy at redshift z and observed in bandpass y, the K-correction between bandpass y and desired bandpass x is:

$$K_{xy} = 2.5\log(1+z) + 2.5\log\left[\frac{\int R_x(\lambda)\,\lambda\,f_\lambda(\lambda)\;d\lambda}{\int R_y(\lambda)\,\lambda\,f_\lambda(\lambda/[1+z])\;d\lambda}\right] + 2.5\log\left[\frac{\int R_y(\lambda)\,\lambda\,f^s_\lambda(\lambda)\;d\lambda}{\int R_x(\lambda)\,\lambda\,f^s_\lambda(\lambda)\;d\lambda}\right], \quad \text{(A.1)}$$

where $R_y(\lambda)$ is the response curve of the y-band, $R_x(\lambda)$ is the response of the x-band, $f_\lambda(\lambda)$ is the flux density of the object being observed in the object's rest frame, $f_\lambda(\lambda/[1+z])$ is the flux density of the redshifted object in the observer frame, and $f^s_\lambda(\lambda)$ is the standard Vega or AB spectrum. The first two terms of the K-correction correct for the fact that the observed object's spectrum is stretched and shifted redwards at larger z. The last term is the color term which corrects for different observed (y) and desired (x) bandpasses. If these bandpasses are identical, the color term cancels out.

We obtained the required filter response curves, $R_x(\lambda)$ and $R_y(\lambda)$, from the website associated with the facility used to observe a given galaxy, or from the author of the work. Chuck Steidel (private communication) kindly provided us both the R_s and the K_s response curves while Jacqueline Bergeron (private communication) provided the $R_{\rm EFOSC}$ response curve. We also used the Spanish Virtual Observatory Filter Profile Service[1]. We retrieved the Vega composite flux stan-

[1]http://svo2.cab.inta-csic.es/theory/fps/

dard spectrum "alpha_lyr_stis_005" from the STScI Calibration Database System, Calspec[2]. For AB magnitudes, we calculated a standard AB spectrum, defined as a hypothetical source with $F_\nu^{(\mathrm{AB})} = 3.63x10^{-20}$ [erg s^{-1} cm^{-2} Hz^{-1}].

Figure A.1 presents the K-correction for each SED as a function of redshift for Vega magnitudes F702W and K_s, and AB magnitudes g and r, the four most common bandpasses in MAGIICAT. Vega magnitudes F702W and K_s were corrected to Vega magnitudes B and K, respectively, while AB magnitudes g and r were corrected to AB magnitudes B and R, respectively. The lighter gray shading indicates the full galaxy redshift range over which the K-corrections were applied for that band. The darker gray shading indicates where the central 68% of the galaxies reside.

We determined the constants of conversion between Vega and AB magnitudes by calculating the B- and K-band absolute magnitudes for a given SED alternately using the Vega spectrum and the AB spectrum. Taking the difference of the Vega and AB magnitudes in each band produced the conversions $B(\mathrm{AB}) = B(\mathrm{V}) - 0.0873$ and $K(\mathrm{AB}) = K(\mathrm{V}) + 1.8266$. These constants are comparable to the values -0.09 (B-band) and 1.85 (K-band) which are presented in Table 1 of Blanton & Roweis (2007). We applied these constants to the K-corrected apparent magnitudes when necessary.

[2]http://www.stsci.edu/hst/observatory/cdbs/calspec.html

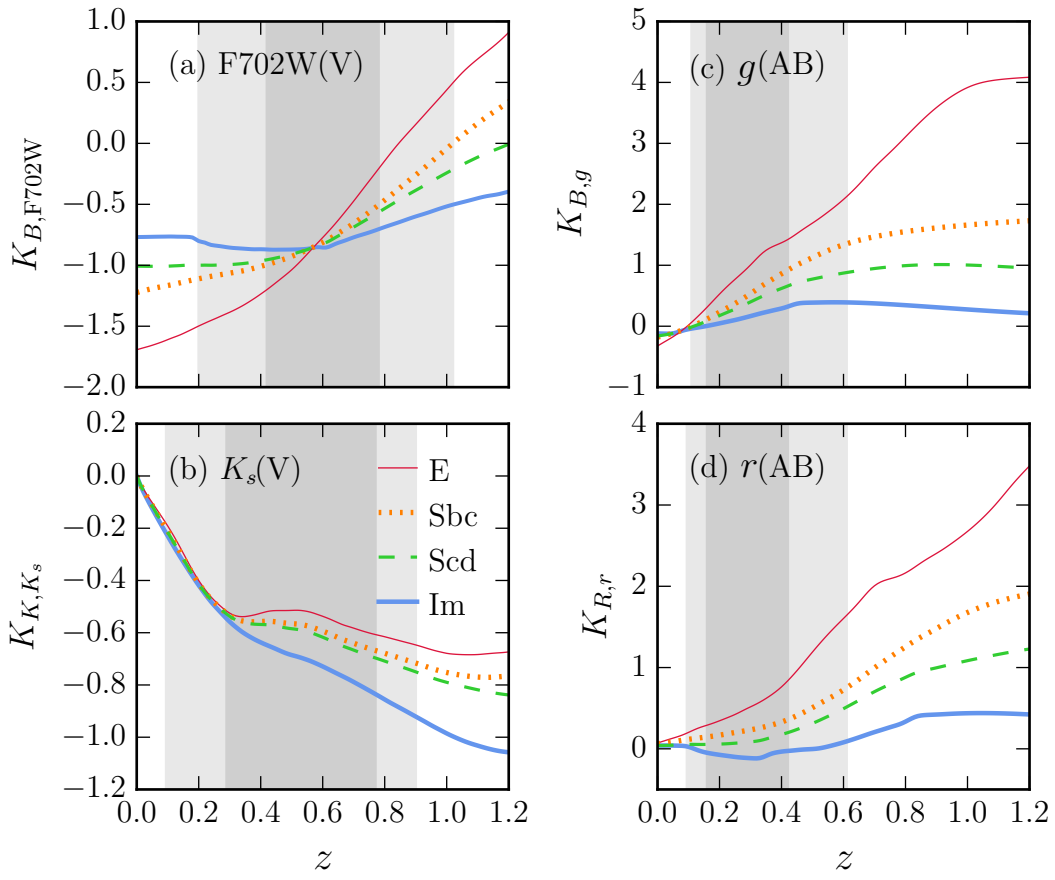

Fig. A.1.— K-corrections between various bands as a function of redshift for spectral energy distributions E, Sbc, Scd, and Im. Apparent magnitudes in the F702W(Vega) and g(AB) bands were K-corrected to the B-band, K_s(Vega) to the K-band, and r(AB) to the R-band. The lighter gray shading indicates the full redshift region over which the K-corrections were applied while the darker gray shading indicates where the central 68% of the galaxies reside.

APPENDIX B. SELECTING SPECTRAL ENERGY DISTRIBUTIONS FOR K-CORRECTIONS

The contents of this appendix were originally published as Nielsen, N. M., Churchill, C. W., Kacprzak, G. G., & Murphy, M. T. 2013, ApJ, 776, 114.

For $f_\lambda(\lambda)$ in Equation A.1, we did not have direct access to the galaxy spectra for MAGIICAT galaxies. Therefore we rely on Coleman et al. (1980) spectral energy distribution (SED) templates which were extended to shorter and longer wavelengths by Bolzonella et al. (2000) using synthetic spectra created with the GISSEL98 code (Bruzual A. & Charlot 1993). These SEDs were distributed with and used by the HYPERZ[1] photometric redshift code (Bolzonella et al. 2000).

To select which K-correction to apply, we determined which SED each galaxy in MAGIICAT most closely resembles. We compared the observed colors of the galaxy to each SED type at the galaxy's redshift. In cases where the observed galaxy color was in between the color of two different SEDs, the closest SED was selected. Where no observed colors were available due to a lack of a second band, the galaxy was classified as an Sbc galaxy, the average type for Mg II absorbing galaxies (SDP94; Zibetti et al. 2007).

We calculated the SED observed colors by first determining the rest-frame colors of each SED. This was done by calculating the appropriate apparent magnitudes of the SEDs at $z = 0$ and taking the difference of the magnitudes, making sure to use the correct filter and AB/Vega combinations. We then calculated the necessary K-corrections at redshifts $0 < z < 1.2$ with the methods described

[1]http://webast.ast.obs-mip.fr/hyperz/

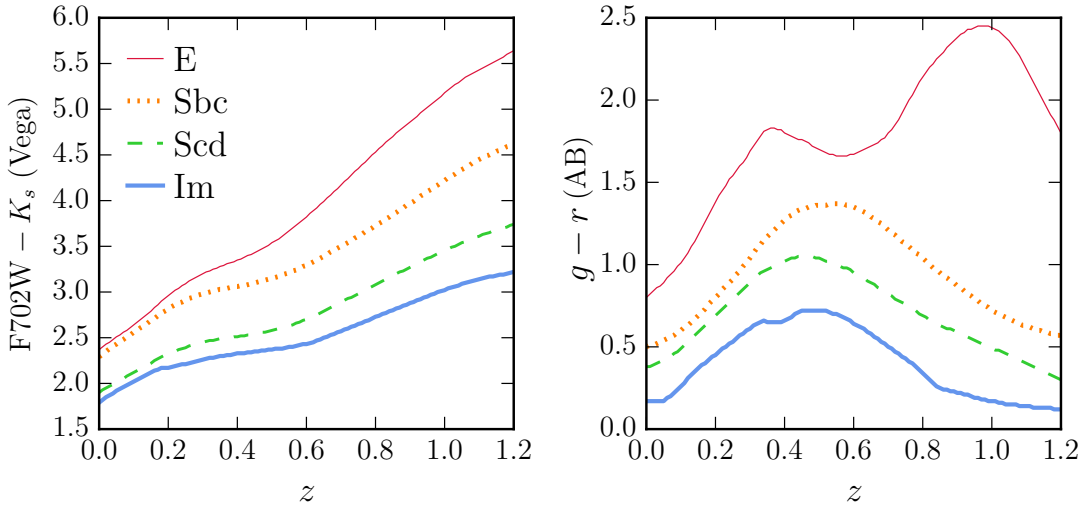

Fig. B.1.— Observed colors, F702W $- K_s$ (Vega) and $g - r$ (AB), for the galaxy SEDs as a function of redshift. These two colors are the most common observed colors in MAGIICAT. The rest of the colors follow the same trend as F702W $- K_s$.

in Appendix A. To obtain the observed SED colors for the redshift range of MAGIICAT, we combined these K-corrections with the rest-frame SED colors, e.g., $(\mathrm{F702W} - K_s)_{z>0} = (\mathrm{F702W} - K_s)_{z=0} + [K_{Ks}(z) - K_{F702W}(z)]$, where the terms in the square brackets are the K-corrections for the K_s and F702W bands, respectively, for $z > 0$.

The two most common observed colors in the sample are F702W $- K_s$ (Vega), and $g - r$ (AB). These colors are presented in Figure B.1 for all SEDs. The rest of the observed colors follow the trend of F702W $- K_s$ due to a combination of a red band with an infrared band. Our $g - r$ colors are consistent with Hewett et al. (2006), who present $g - r$ for the extended Coleman SEDs.

APPENDIX C. $B-R$ TO $B-K$ REST-FRAME COLOR CONVERSION

The contents of this appendix were originally published as Nielsen, N. M., Churchill, C. W., Kacprzak, G. G., & Murphy, M. T. 2013, ApJ, 776, 114.

For SDSS galaxies which did not have a K-band magnitude available, we determined M_K indirectly by using a conversion between rest-frame colors $B-R$ and $B-K$. We calculated the rest-frame $B-K$ and $B-R$ colors for each SED using the methods applied in Appendix B. The points in Figure C.1 present the rest-frame colors for each SED. The SED colors appear to follow a linear trend so a linear least-squares fit was performed. The fit has the form $(B-K) = 1.86(B-R) + 0.02$ and is presented as the solid line in Figure C.1. We therefore obtained absolute K-band magnitudes, M_K, for each SDSS galaxy by applying the equation $M_K = M_B - (B-K) = M_B - 1.86(B-R) - 0.02$.

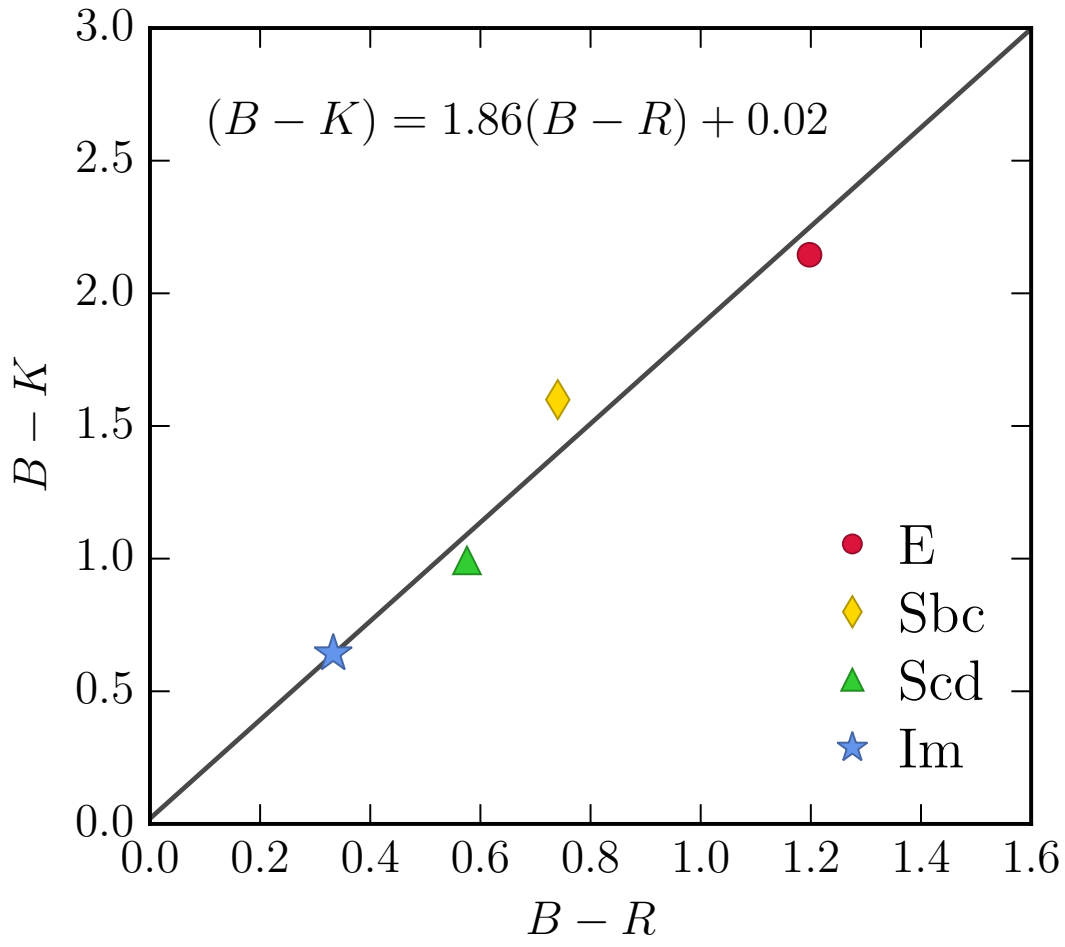

Fig. C.1.— Relationship between rest-frame colors $B-K$ and $B-R$ for the SEDs. Point types and colors indicate the SED type. The data appear to follow the linear relation listed on the figure.

APPENDIX D. MASS-NORMALIZED PIXEL VELOCITY TPCFS

The contents of this appendix have been submitted for publication in the Astrophysical Journal as Nielsen, N. M., Churchill, C. W., Kacprzak, G. G., Murphy, M. T., & Evans, J. L. 2013, ApJ

In order to compare to simulations and to account for the mass of the galaxy hosting absorption, we normalize the pixel velocities by the maximum circular velocity, $V_{\rm circ}$, of the host galaxy. We do this because our sample spans a range of galaxy halo masses and because of the fact that our red galaxies tend to be more massive than our blue galaxies (see Chapter 4.2 and Figure 4.1). Here we present methods for calculating normalized absorber and absorber-galaxy TPCFs and the results of cutting the sample into subsamples similar to the unnormalized TPCFs presented in Chapter 4.4.

We calculate the mass-normalized absorber TPCF using a similar procedure as the unnormalized absorber TPCF. Before we calculate the pixel pair velocity separations for a given subsample, we normalize each pixel velocity by the maximum circular velocity, $V_{\rm circ}$, of the host galaxy. After determining the velocity separations, $\Delta(v_{\rm pixel}/V_{\rm circ})$, we bin up the values using the same methods used for the absorber TPCFs. The normalized absorber TPCF for blue and red galaxies is presented in Figure D.1(a). The general result in this panel that blue galaxies have a larger absorber velocity dispersion than red galaxies does not differ from the unnormalized absorber TPCF in Figure 4.4(a), but the significance of the chi-square test is greater here. We also present measurements of $\Delta v(50)$ and $\Delta v(90)$ for each subsample in Table D.1. The subsample cuts and number of galaxies in each subsample are the same as those presented in Table 4.1, therefore we exclude these values from the table in this appendix.

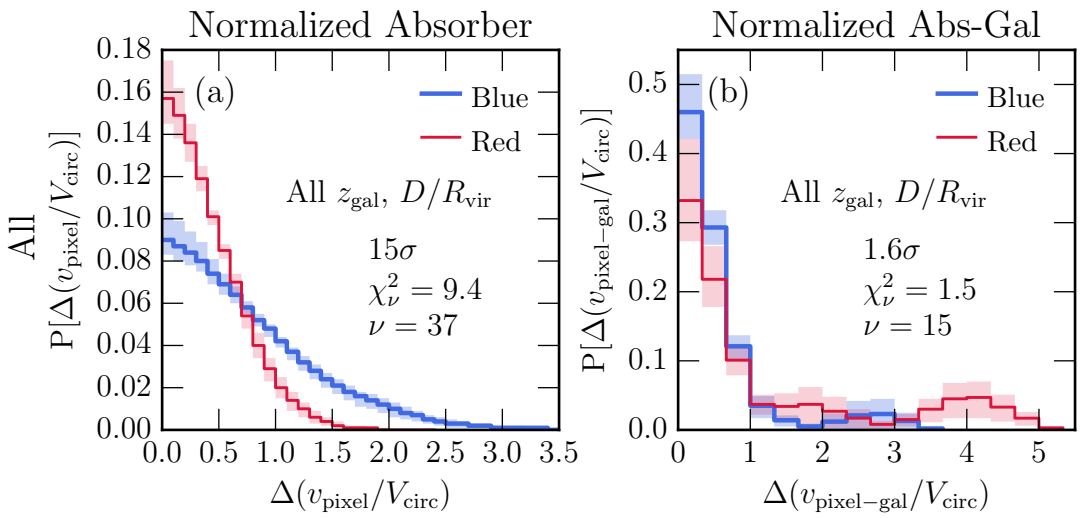

Fig. D.1.— Mass-normalized two-point correlation functions for the subsamples plotted in Figure 4.4. In panel(a), blue galaxies have a larger velocity dispersion than red galaxies which is the same result found for the unnormalized TPCFs, but the significance is much greater when the velocities are normalized by $V_{\rm circ}$. These red galaxies have absorber velocity separations that mostly lie within $V_{\rm circ}$. For the absorber-galaxy TPCF in panel (b), the significant difference between blue and red galaxies vanishes compared to the unnormalized dispersion, however red galaxies may still have a larger velocity dispersion due to the peak at roughly $\Delta(v_{\rm pixel-gal}/V_{\rm circ}) = 4$. For both blue and red absorber-galaxy TPCFs, most velocity separations are within $V_{\rm circ}$, with the exception of several high velocity separation peaks.

Table D.1. Mass-Normalized TPCF $\Delta v(50)$ and $\Delta v(90)$ Measurements

	Norm Absorber		Norm Abs-Gal	
Sample[a]	$\Delta v(50)$[b]	$\Delta v(90)$[b]	$\Delta v(50)$[b]	$\Delta v(90)$[b]
	Figure D.1			
Blue	$0.62^{+0.06}_{-0.08}$	$1.65^{+0.14}_{-0.21}$	$0.37^{+0.05}_{-0.05}$	$1.20^{+0.90}_{-0.52}$
Red	$0.35^{+0.03}_{-0.03}$	$0.87^{+0.07}_{-0.08}$	$0.57^{+0.36}_{-0.23}$	$4.00^{+0.48}_{-1.55}$
	Figure D.2			
Blue - Low $z_{\rm gal}$	$0.70^{+0.09}_{-0.14}$	$1.84^{+0.22}_{-0.38}$	$0.48^{+0.16}_{-0.13}$	$2.50^{+0.38}_{-1.21}$
Blue - High $z_{\rm gal}$	$0.55^{+0.06}_{-0.08}$	$1.42^{+0.11}_{-0.16}$	$0.30^{+0.01}_{-0.02}$	$0.70^{+0.04}_{-0.05}$
Red - Low $z_{\rm gal}$	$0.29^{+0.03}_{-0.05}$	$0.73^{+0.07}_{-0.11}$	$1.82^{+0.10}_{-0.98}$	$4.22^{+0.36}_{-1.09}$
Red - High $z_{\rm gal}$	$0.41^{+0.04}_{-0.05}$	$1.00^{+0.10}_{-0.13}$	$0.36^{+0.02}_{-0.04}$	$0.86^{+0.08}_{-0.09}$
	Figure D.3			
Blue - Low $D/R_{\rm vir}$	$0.55^{+0.05}_{-0.07}$	$1.38^{+0.09}_{-0.15}$	$0.36^{+0.10}_{-0.09}$	$2.33^{+0.44}_{-1.33}$
Blue - High $D/R_{\rm vir}$	$0.68^{+0.10}_{-0.13}$	$1.78^{+0.21}_{-0.33}$	$0.38^{+0.04}_{-0.06}$	$1.02^{+0.10}_{-0.19}$
Red - Low $D/R_{\rm vir}$	$0.37^{+0.05}_{-0.06}$	$0.95^{+0.11}_{-0.14}$	$0.34^{+0.03}_{-0.08}$	$0.87^{+0.13}_{-0.19}$
Red - High $D/R_{\rm vir}$	$0.31^{+0.02}_{-0.03}$	$0.75^{+0.04}_{-0.06}$	$0.95^{+0.57}_{-0.47}$	$4.12^{+0.47}_{-1.13}$

[a]Subsample cuts are the same as those presented in Table 4.1
[b]km s^{-1}

The mass-normalized absorber-galaxy TPCF is similar to the absorber-galaxy TPCF described in Chapter 4.3.2 except we add an additional step. We first shift the pixel velocities to $z_{\rm gal}$ and take the absolute value of the shifted velocities because we do not know whether the absorbers are in front of or behind the host galaxy based on the velocity alone. Then we normalize the velocities by the maximum circular velocity, $V_{\rm circ}$, of the host galaxy to obtain $v_{\rm pixel-gal}/V_{\rm circ}$. We then take the velocity separations of each normalized pixel velocity pair to obtain $\Delta(v_{\rm pixel-gal}/V_{\rm circ})$, and bin up the values to calculate the TPCF. Again, we only include galaxies with $\sigma_{(z_{\rm gal})} \leq 30$ km s^{-1} comoving since we are examining a normalized version of the absorber-galaxy TPCFs. We compare the normalized absorber-galaxy TPCFs for the full sample of blue and red galaxies in Figure D.1(b). Absorption around red galaxies may have larger velocity dispersions than blue galaxies, though this result is insignificant (1.7σ). This is in contrast to the unnormalized absorber-galaxy TPCF which found a significant difference in the same direction.

We also calculate the normalized absorber and normalized absorber-galaxy TPCFs for subsamples cut by galaxy color and redshift (Figure D.2) and cut by galaxy color and virial radius-normalized impact parameter (Figure D.3). The $\Delta v(50)$ and $\Delta v(90)$ values for these figures are also tabulated in Table D.1. In general, we find that most pixel velocity separations are less than $V_{\rm circ}$ and this is reflected in the $\Delta v(50)$ and $\Delta v(90)$ measurements. Comparing these TPCFs to those presented in Chapter 4.4, we find that our results remain mostly the same. Where the chi-square test results in a significance difference (greater than 3.0σ) between subsamples for the unnormalized TPCFs, we also find significant differences for the normalized TPCFs in the same direction (e.g., blue galaxies

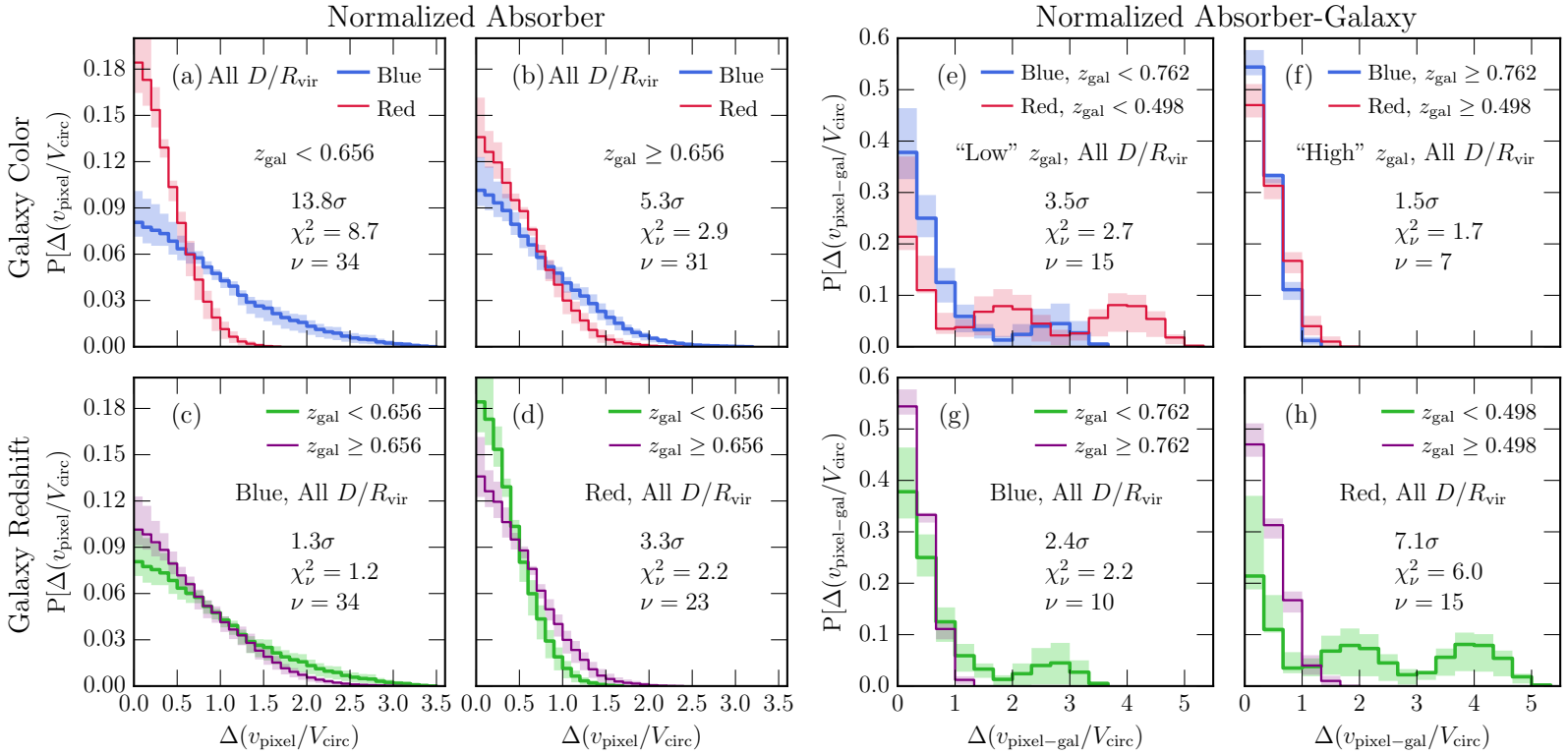

Fig. D.2.— Pixel velocity two-point correlation functions that have been normalized by the virial radius of the host galaxy. Subsamples presented are the same as those in Figure 4.5. For the absorber TPCFs, normalizing the velocities by $V_{\rm circ}$ does not change the results presented in Figure 4.5, with the exception of the high redshift samples in panel (b). In this panel, we find that blue galaxies have a larger absorber velocity dispersion than red galaxies, in contrast to no difference for the unnormalized TPCFs. For the normalized absorber-galaxy TPCFs, we again find no differences in the results when comparing to the unnormalized absorber-galaxy TPCFs, with the exception of panel (f). The significant difference between blue and red galaxies at "high" redshift drops to an insignificant difference when the velocities are normalized to $V_{\rm circ}$, where blue and red galaxies have similar velocity dispersions. Nearly all TPCFs presented here have velocity dispersions within $V_{\rm circ}$.

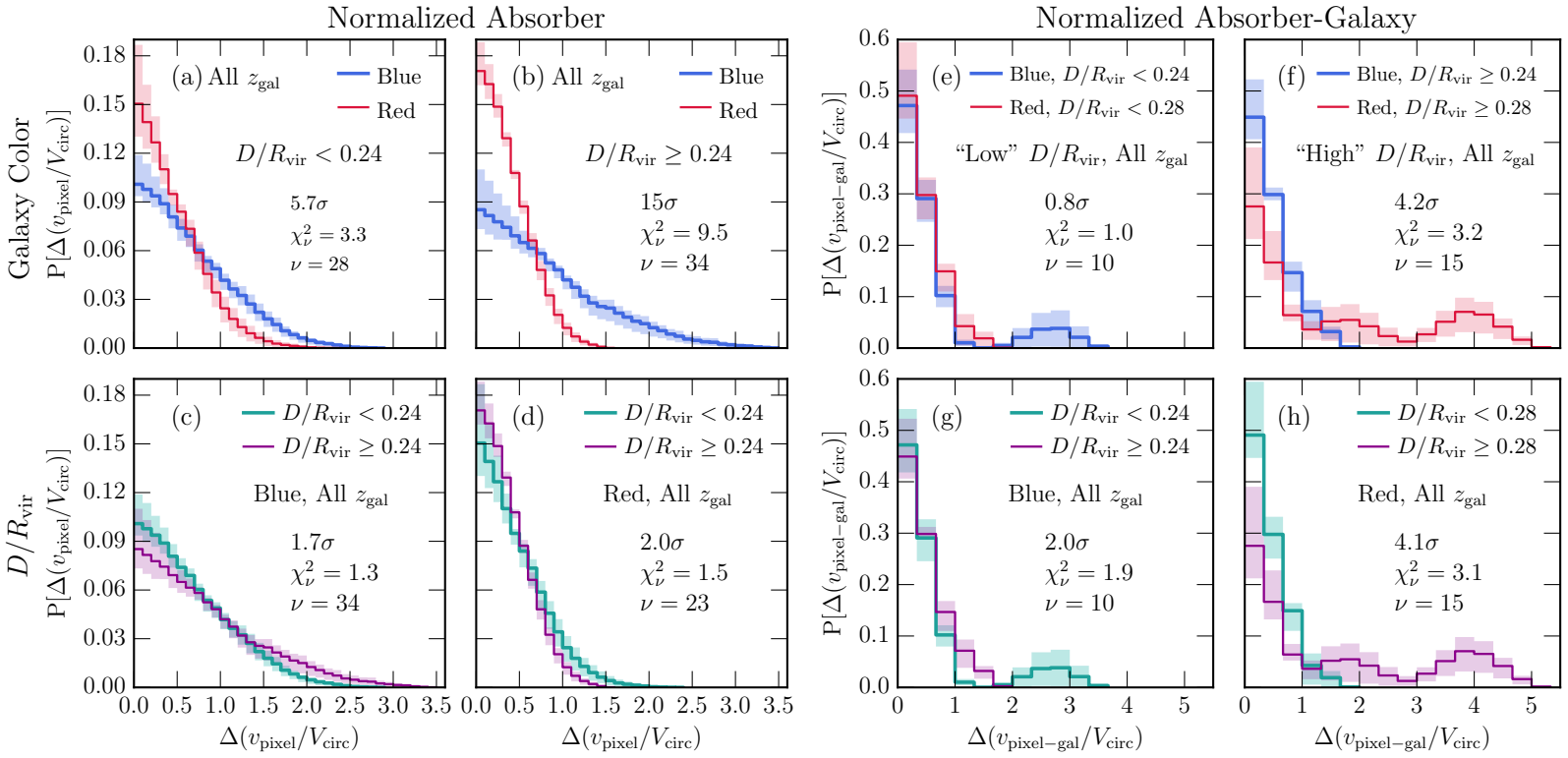

Fig. D.3.— Mass-normalized TPCFs for the subsamples plotted in Figure 4.6. Contrary to the results with the unnormalized absorber TPCFs, we find no redshift evolution for either blue or red galaxies in panels (c) and (d), respectively, however red galaxies have smaller absorber velocity dispersions than blue galaxies at all redshifts (panels (a) and (b)). For the normalized absorber-galaxy TPCFs, we find similar results as the unnormalized TPCFs in Figure 4.6, except for panel (e) which presents blue and red galaxies at "low" $D/R_{\rm vir}$. In this case, we find no significant difference between blue and red galaxies. Most of the velocity dispersions for these TPCFs are located within $V_{\rm circ}$.

have larger dispersions than red galaxies for both normalized and unnormalized TPCFs), however the actual significance values may differ.

In a very few cases, we find different results when we normalize the TPCFs. For the high redshift sample in Figure D.2(b), we now find a significant difference for the normalized TPCFs where blue galaxies have a larger dispersion than red galaxies (5.3σ), whereas there is no difference between blue and red absorber velocity dispersions for unnormalized TPCFs. For blue and red "high" redshift galaxies, we find no significant difference between the normalized absorber-galaxy TPCFs in Figure D.2(f), in contrast to a larger dispersion for red galaxies for the unnormalized absorber-galaxy TPCFs. For Figure D.3, we find that normalizing the TPCFs by $V_{\rm circ}$ removes the significant redshift evolution we found in red galaxies (panel (d)), but does not affect the blue galaxies. In fact, the normalized absorber TPCFs now show that red galaxies have smaller velocity dispersions than blue galaxies for both low $D/R_{\rm vir}$ in panel (a) and high $D/R_{\rm vir}$ in panel (b). For the normalized absorber-galaxy TPCFs, we find no differences between blue and red galaxies at "low" $D/R_{\rm vir}$ in panel (e), which is not consistent with the larger dispersions found for red galaxies (ignoring the peak at high velocities for blue galaxies) with the unnormalized TPCFs.

Since the TPCF results are the same in most cases and the normalized velocities are less intuitive when looking at an absorption profile, we prefer the unnormalized TPCFs. Normalizing the velocity separations by $V_{\rm circ}$ preferentially decreases the velocities for absorbers associated with red galaxies because the red galaxies tend to be more massive. In fact, in every case where we find different results between the normalized and unnormalized TPCFs, the difference is mostly caused by the red galaxy subsample velocities being reduced more than the

blue galaxy subsample. A benefit to this normalization, however, is determining whether the gas probed by Mg II absorption is possibly escaping the galaxy or not, and is useful as a diagnostic for determining whether the material being probed is associated with outflows, which tend to have a wide range of velocities that can be greater than the maximum circular velocity, whereas accreting material has a maximum velocity at or below $V_{\rm circ}$ (Trujillo-Gomez 2014).

REFERENCES

Adelberger, K. L., Shapley, A. E., Steidel, C. C., Pettini, M., Erb, D. K., & Reddy, N. A. 2005, ApJ, 629, 636

Bahcall, J. N., & Spitzer, Jr., L. 1969, ApJ, 156, L63

Barnes, L. A., Garel, T., & Kacprzak, G. G. 2014, PASP, 126, 969

Barton, E. J., & Cooke, J. 2009, AJ, 138, 1817

Behroozi, P. S., Wechsler, R. H., & Conroy, C. 2013, ApJ, 770, 57

Benjamin, R. A., & Danly, L. 1997, ApJ, 481, 764

Bergeron, J. 1988, in IAU Symposium, Vol. 130, Large Scale Structures of the Universe, ed. J. Audouze, M.-C. Pelletan, A. Szalay, Y. B. Zel'dovich, & P. J. E. Peebles, 343

Bergeron, J., & Boissé, P. 1991, A&A, 243, 344

Bergeron, J., & Stasińska, G. 1986, A&A, 169, 1

Bergeron, J., et al. 1994, ApJ, 436, 33

Birnboim, Y., & Dekel, A. 2003, MNRAS, 345, 349

Birnboim, Y., Dekel, A., & Neistein, E. 2007, MNRAS, 380, 339

Blanton, M. R., & Roweis, S. 2007, AJ, 133, 734

Blumenthal, G. R., Faber, S. M., Flores, R., & Primack, J. R. 1986, ApJ, 301, 27

Blumenthal, G. R., Faber, S. M., Primack, J. R., & Rees, M. J. 1984, Nature, 311, 517

Bolzonella, M., Miralles, J.-M., & Pelló, R. 2000, A&A, 363, 476

Bordoloi, R., Lilly, S. J., Kacprzak, G. G., & Churchill, C. W. 2014a, ApJ, 784, 108

Bordoloi, R., et al. 2011, ApJ, 743, 10

—. 2014b, ApJ, 796, 136

—. 2014c, ApJ, 794, 130

Bouché, N., Hohensee, W., Vargas, R., Kacprzak, G. G., Martin, C. L., Cooke, J., & Churchill, C. W. 2012, MNRAS, 426, 801

Bouché, N., Murphy, M. T., Péroux, C., Csabai, I., & Wild, V. 2006, MNRAS, 371, 495

Bowen, D. V., & Chelouche, D. 2011, ApJ, 727, 47

Brown, B. W., Hollander, M., & Korwar, R. M. 1974, Reliability and Biometry, 327

Bruzual A., G., & Charlot, S. 1993, ApJ, 405, 538

Ceverino, D., & Klypin, A. 2009, ApJ, 695, 292

Ceverino, D., Klypin, A., Klimek, E. S., Trujillo-Gomez, S., Churchill, C. W., Primack, J., & Dekel, A. 2014, MNRAS, 442, 1545

Charlton, J. C., & Churchill, C. W. 1996, ApJ, 465, 631

—. 1998, ApJ, 499, 181

Chelouche, D., & Bowen, D. V. 2010, ApJ, 722, 1821

Chen, H.-W., Helsby, J. E., Gauthier, J.-R., Shectman, S. A., Thompson, I. B., & Tinker, J. L. 2010a, ApJ, 714, 1521

Chen, H.-W., Lanzetta, K. M., & Webb, J. K. 2001a, ApJ, 556, 158

Chen, H.-W., Lanzetta, K. M., Webb, J. K., & Barcons, X. 1998, ApJ, 498, 77

—. 2001b, ApJ, 559, 654

Chen, H.-W., & Tinker, J. L. 2008, ApJ, 687, 745

Chen, H.-W., Wild, V., Tinker, J. L., Gauthier, J.-R., Helsby, J. E., Shectman, S. A., & Thompson, I. B. 2010b, ApJ, 724, L176

Churchill, C. W. 1997, PhD thesis, University of California, Santa Cruz

Churchill, C. W., Kacprzak, G. G., Nielsen, N. M., Steidel, C. C., & Murphy, M. T. 2013a, ApJ, submitted

Churchill, C. W., Kacprzak, G. G., & Steidel, C. C. 2005, in IAU Colloq. 199: Probing Galaxies through Quasar Absorption Lines, ed. P. Williams, C.-G. Shu, & B. Menard, 24–41

Churchill, C. W., Kacprzak, G. G., Steidel, C. C., & Evans, J. L. 2007, ApJ, 661, 714

Churchill, C. W., Kacprzak, G. G., Steidel, C. C., Spitler, L. R., Holtzman, J., Nielsen, N. M., & Trujillo-Gomez, S. 2012, ApJ, 760, 68

Churchill, C. W., Mellon, R. R., Charlton, J. C., Jannuzi, B. T., Kirhakos, S., Steidel, C. C., & Schneider, D. P. 2000, ApJS, 130, 91

Churchill, C. W., Nielsen, N. M., Kacprzak, G. G., & Trujillo-Gomez, S. 2013b, ApJ, 763, L42

Churchill, C. W., Rigby, J. R., Charlton, J. C., & Vogt, S. S. 1999, ApJS, 120, 51

Churchill, C. W., Steidel, C. C., & Vogt, S. S. 1996, ApJ, 471, 164

Churchill, C. W., Trujillo-Gomez, S., Nielsen, N. M., & Kacprzak, G. G. 2013c, ApJ, 779, 87

Churchill, C. W., & Vogt, S. S. 2001, AJ, 122, 679

Churchill, C. W., Vogt, S. S., & Charlton, J. C. 2003, AJ, 125, 98

Cirasuolo, M., McLure, R. J., Dunlop, J. S., Almaini, O., Foucaud, S., & Simpson, C. 2010, MNRAS, 401, 1166

Coil, A. L., Weiner, B. J., Holz, D. E., Cooper, M. C., Yan, R., & Aird, J. 2011, ApJ, 743, 46

Coleman, G. D., Wu, C.-C., & Weedman, D. W. 1980, ApJS, 43, 393

Danovich, M., Dekel, A., Hahn, O., Ceverino, D., & Primack, J. 2014, ArXiv e-prints, 1407.7129

Danovich, M., Dekel, A., Hahn, O., & Teyssier, R. 2012, MNRAS, 422, 1732

Dekel, A., & Birnboim, Y. 2006, MNRAS, 368, 2

Dekel, A., & Silk, J. 1986, ApJ, 303, 39

Dekel, A., et al. 2009, Nature, 457, 451

Dekker, H., D'Odorico, S., Kaufer, A., Delabre, B., & Kotzlowski, H. 2000, in SPIE Conference Series, Vol. 4008, Optical and IR Telescope Instrumentation and Detectors, ed. M. Iye & A. F. Moorwood, 534–545

Dong, X. C., Lin, W. P., Kang, X., Ocean Wang, Y., Dutton, A. A., & Macciò, A. V. 2014, ApJ, 791, L33

Eggen, O. J., Lynden-Bell, D., & Sandage, A. R. 1962, ApJ, 136, 748

Ellis, R. S. 1997, ARA&A, 35, 389

Evans, J. L. 2011, PhD thesis, New Mexico State University

Faber, S. M., et al. 2007, ApJ, 665, 265

Ford, A. B., Davé, R., Oppenheimer, B. D., Katz, N., Kollmeier, J. A., Thompson, R., & Weinberg, D. H. 2014, MNRAS, 444, 1260

Fox, A. J., et al. 2014, ApJ, 787, 147

—. 2015, ApJ, 799, L7

Fried, J. W., et al. 2001, A&A, 367, 788

Gauthier, J.-R., & Chen, H.-W. 2011, MNRAS, 418, 2730

Gauthier, J.-R., Chen, H.-W., & Tinker, J. L. 2009, ApJ, 702, 50

Gehrels, N. 1986, ApJ, 303, 336

Guillemin, P., & Bergeron, J. 1997, A&A, 328, 499

Hewett, P. C., Warren, S. J., Leggett, S. K., & Hodgkin, S. T. 2006, MNRAS, 367, 454

Hopkins, A. M., & Beacom, J. F. 2006, ApJ, 651, 142

Kacprzak, G. G., Churchill, C. W., Barton, E. J., & Cooke, J. 2011a, ApJ, 733, 105

Kacprzak, G. G., Churchill, C. W., Ceverino, D., Steidel, C. C., Klypin, A., & Murphy, M. T. 2010a, ApJ, 711, 533

Kacprzak, G. G., Churchill, C. W., Evans, J. L., Murphy, M. T., & Steidel, C. C. 2011b, MNRAS, 416, 3118

Kacprzak, G. G., Churchill, C. W., & Nielsen, N. M. 2012a, ApJ, 760, L7

Kacprzak, G. G., Churchill, C. W., Steidel, C. C., & Murphy, M. T. 2008, AJ, 135, 922

Kacprzak, G. G., Churchill, C. W., Steidel, C. C., Murphy, M. T., & Evans, J. L. 2007, ApJ, 662, 909

Kacprzak, G. G., Churchill, C. W., Steidel, C. C., Spitler, L. R., & Holtzman, J. A. 2012b, MNRAS, 427, 3029

Kacprzak, G. G., Cooke, J., Churchill, C. W., Ryan-Weber, E. V., & Nielsen, N. M. 2013, ApJ, 777, L11

Kacprzak, G. G., Murphy, M. T., & Churchill, C. W. 2010b, MNRAS, 406, 445

Keeney, B. A., Stocke, J. T., Rosenberg, J. L., Danforth, C. W., Ryan-Weber, E. V., Shull, J. M., Savage, B. D., & Green, J. C. 2013, ApJ, 765, 27

Kereš, D., Katz, N., Fardal, M., Davé, R., & Weinberg, D. H. 2009, MNRAS, 395, 160

Kereš, D., Katz, N., Weinberg, D. H., & Davé, R. 2005, MNRAS, 363, 2

Kim, A., Goobar, A., & Perlmutter, S. 1996, PASP, 108, 190

Klypin, A. A., Trujillo-Gomez, S., & Primack, J. 2011, ApJ, 740, 102

Lan, T.-W., Ménard, B., & Zhu, G. 2014, ApJ, 795, 31

Lanzetta, K. M., & Bowen, D. 1990, ApJ, 357, 321

Lanzetta, K. M., & Bowen, D. V. 1992, ApJ, 391, 48

Lanzetta, K. M., Bowen, D. V., Tytler, D., & Webb, J. K. 1995, ApJ, 442, 538

Lehner, N., Howk, J. C., Thom, C., Fox, A. J., Tumlinson, J., Tripp, T. M., & Meiring, J. D. 2012, MNRAS, 424, 2896

Lehner, N., O'Meara, J. M., Fox, A. J., Howk, J. C., Prochaska, J. X., Burns, V., & Armstrong, A. A. 2014, ApJ, 788, 119

Lehner, N., et al. 2013, ApJ, 770, 138

Lilly, S. J., Tresse, L., Hammer, F., Crampton, D., & Le Fevre, O. 1995, ApJ, 455, 108

Lin, H., Yee, H. K. C., Carlberg, R. G., Morris, S. L., Sawicki, M., Patton, D. R., Wirth, G., & Shepherd, C. W. 1999, ApJ, 518, 533

Lundgren, B. F., et al. 2009, ApJ, 698, 819

Maller, A. H., & Bullock, J. S. 2004, MNRAS, 355, 694

Martin, C. L., & Bouché, N. 2009, ApJ, 703, 1394

Martin, C. L., Shapley, A. E., Coil, A. L., Kornei, K. A., Bundy, K., Weiner, B. J., Noeske, K. G., & Schiminovich, D. 2012, ApJ, 760, 127

Matejek, M. S., & Simcoe, R. A. 2012, ApJ, 761, 112

Matejek, M. S., Simcoe, R. A., Cooksey, K. L., & Seyffert, E. N. 2013, ApJ, 764, 9

Mathes, N. L., Churchill, C. W., Kacprzak, G. G., Nielsen, N. M., Trujillo-Gomez, S., Charlton, J., & Muzahid, S. 2014, ApJ, 792, 128

Ménard, B., Wild, V., Nestor, D., Quider, A., Zibetti, S., Rao, S., & Turnshek, D. 2011, MNRAS, 417, 801

Mo, H. J., & Miralda-Escude, J. 1996, ApJ, 469, 589

Navarro, J. F., Frenk, C. S., & White, S. D. M. 1996, ApJ, 462, 563

Nielsen, N. M., Churchill, C. W., & Kacprzak, G. G. 2013a, ApJ, 776, 115

Nielsen, N. M., Churchill, C. W., Kacprzak, G. G., & Murphy, M. T. 2013b, ApJ, 776, 114

Nielsen, N. M., Churchill, C. W., Kacprzak, G. G., Murphy, M. T., & Evans, J. L. 2015a, ApJ, submitted

—. 2015b, ApJ, submitted

Ocvirk, P., Pichon, C., & Teyssier, R. 2008, MNRAS, 390, 1326

Oppenheimer, B. D., Davé, R., Kereš, D., Fardal, M., Katz, N., Kollmeier, J. A., & Weinberg, D. H. 2010, MNRAS, 406, 2325

Petitjean, P., & Bergeron, J. 1990, A&A, 231, 309

Rao, S. M., Belfort-Mihalyi, M., Turnshek, D. A., Monier, E. M., Nestor, D. B., & Quider, A. 2011, MNRAS, 416, 1215

Rao, S. M., & Turnshek, D. A. 2000, ApJS, 130, 1

Ribaudo, J., Lehner, N., Howk, J. C., Werk, J. K., Tripp, T. M., Prochaska, J. X., Meiring, J. D., & Tumlinson, J. 2011, ApJ, 743, 207

Rigby, J. R., Charlton, J. C., & Churchill, C. W. 2002, ApJ, 565, 743

Rubin, K. H. R., Prochaska, J. X., Koo, D. C., & Phillips, A. C. 2012, ApJ, 747, L26

Rubin, K. H. R., Prochaska, J. X., Koo, D. C., Phillips, A. C., Martin, C. L., & Winstrom, L. O. 2014, ApJ, 794, 156

Rubin, K. H. R., Weiner, B. J., Koo, D. C., Martin, C. L., Prochaska, J. X., Coil, A. L., & Newman, J. A. 2010, ApJ, 719, 1503

Rudie, G. C., et al. 2012, ApJ, 750, 67

Rupke, D. S., Veilleux, S., & Sanders, D. B. 2005, ApJS, 160, 115

Sargent, W. L. W., Steidel, C. C., & Boksenberg, A. 1988, ApJ, 334, 22

Schawinski, K., et al. 2014, MNRAS, 440, 889

Schneider, D. P., et al. 1993, ApJS, 87, 45

Searle, L., & Zinn, R. 1978, ApJ, 225, 357

Silk, J., & Norman, C. 1981, ApJ, 247, 59

Simard, L., et al. 2002, ApJS, 142, 1

Simcoe, R. A., Sargent, W. L. W., Rauch, M., & Becker, G. 2006, ApJ, 637, 648

Spitzer, Jr., L. 1956, ApJ, 124, 20

Steidel, C. C. 1995, in QSO Absorption Lines, ed. G. Meylan, 139

Steidel, C. C., Dickinson, M., Meyer, D. M., Adelberger, K. L., & Sembach, K. R. 1997, ApJ, 480, 568

Steidel, C. C., Dickinson, M., & Persson, S. E. 1994, ApJ, 437, L75

Steidel, C. C., Erb, D. K., Shapley, A. E., Pettini, M., Reddy, N., Bogosavljević, M., Rudie, G. C., & Rakic, O. 2010, ApJ, 717, 289

Steidel, C. C., & Sargent, W. L. W. 1992, ApJS, 80, 1

Stewart, K. R., Kaufmann, T., Bullock, J. S., Barton, E. J., Maller, A. H., Diemand, J., & Wadsley, J. 2011, ApJ, 738, 39

Stocke, J. T., Keeney, B. A., Danforth, C. W., Shull, J. M., Froning, C. S., Green, J. C., Penton, S. V., & Savage, B. D. 2013, ApJ, 763, 148

Thom, C., Werk, J. K., Tumlinson, J., Prochaska, J. X., Meiring, J. D., Tripp, T. M., & Sembach, K. R. 2011, ApJ, 736, 1

Tinker, J. L., & Chen, H.-W. 2008, ApJ, 679, 1218

Tremonti, C. A., Moustakas, J., & Diamond-Stanic, A. M. 2007, ApJ, 663, L77

Trujillo-Gomez, S. 2014, PhD thesis, New Mexico State University

Trujillo-Gomez, S., Klypin, A., Primack, J., & Romanowsky, A. J. 2011, ApJ, 742, 16

Tumlinson, J., et al. 2011, Science, 334, 948

—. 2013, ApJ, 777, 59

Turnshek, D. A., Rao, S. M., Nestor, D. B., Belfort-Mihalyi, M., & Quider, A. M. 2005, in IAU Colloq. 199: Probing Galaxies through Quasar Absorption Lines, ed. P. Williams, C.-G. Shu, & B. Menard, 104–113

van de Voort, F., & Schaye, J. 2012, MNRAS, 423, 2991

van de Voort, F., Schaye, J., Booth, C. M., Haas, M. R., & Dalla Vecchia, C. 2011, MNRAS, 414, 2458

Veilleux, S., Cecil, G., & Bland-Hawthorn, J. 2005, ARA&A, 43, 769

Vogt, S. S., et al. 1994, in SPIE Conference Series, Vol. 2198, Instrumentation in Astronomy VIII, ed. D. L. Crawford & E. R. Craine, 362

Wang, W., & Wells, M. T. 2000, Statistica Sinicia, 10, 1199

Weiner, B. J., et al. 2009, ApJ, 692, 187

Weisheit, J. C. 1978, ApJ, 219, 829

Werk, J. K., Prochaska, J. X., Thom, C., Tumlinson, J., Tripp, T. M., O'Meara, J. M., & Peeples, M. S. 2013, ApJS, 204, 17

White, S. D. M., & Frenk, C. S. 1991, ApJ, 379, 52

White, S. D. M., & Rees, M. J. 1978, MNRAS, 183, 341

Wolf, C., Meisenheimer, K., Rix, H.-W., Borch, A., Dye, S., & Kleinheinrich, M. 2003, A&A, 401, 73

Wolynetz, M. S. 1979, J. R. Stat. Soc., 28, 195

Yang, X., van den Bosch, F. C., Mo, H. J., Mao, S., Kang, X., Weinmann, S. M., Guo, Y., & Jing, Y. P. 2006, MNRAS, 369, 1293

Zhu, G., & Ménard, B. 2013, ApJ, 770, 130

Zibetti, S., Ménard, B., Nestor, D. B., Quider, A. M., Rao, S. M., & Turnshek, D. A. 2007, ApJ, 658, 161